Structure and dynamics of the spin-orbit coupled ultra-dilute quantum droplets

A Thesis Submitted
in partial fulfilment of the requirements
for the degree of
Doctor of Philosophy

by

Km Sonali Gangwar

Roll No. 196121013

to the

DEPARTMENT OF PHYSICS

INDIAN INSTITUTE OF TECHNOLOGY GUWAHATI

October, 2024

Declaration

This is to certify that the work contained in this thesis entitled **"Structure and dynamics of the spin-orbit coupled ultra-dilute quantum droplets"** submitted by me to the Indian Institute of Technology, Guwahati, for the award of the degree of PhD, is a bonafide work carried out by me under the supervision of Dr. Pankaj Kumar Mishra and that this work has not been submitted elsewhere for a degree of diploma. I also wish to state that to the best of my knowledge and understanding nothing in this report amounts to plagiarism.

Km Sonali Gangwar
Department of Physics
Indian Institute of Technology
Guwahati

October, 2024

Certificate

It is certified that the work contained in this thesis entitled **"Structure and dynamics of the spin-orbit coupled ultra-dilute quantum droplets"** by **Km Sonali Gangwar**, has been carried out under my supervision, and this work has not been submitted elsewhere for a degree.

Dr. Pankaj Kumar Mishra
Associate Professor
Department of Physics
Indian Institute of Technology
Guwahati

October, 2024

Preface

In recent years, quantum droplets (QDs) have emerged as one of the novel matter forms of ultracold atoms, and the research is still at an infant stage. In general self-bound QDs are formed due to the interplay between attractive mean-field (MF) interactions and repulsive beyond mean-field (BMF) interactions caused by the quantum fluctuations. In one-dimensional systems, QDs in binary mixtures are predicted to arise from a different mechanism. Here, the formation of QDs takes place as a result of the balance between attractive BMF and repulsive MF interaction. The study of droplets in one dimension is particularly interesting because of the significant and nontrivial role of quantum fluctuations. One-dimensional droplets have captured the attention of researchers because they have long lifetimes and are more stable than their counterparts in higher dimensions. This advantage has led to a surge in the research of quasi-one dimensional QDs.

In this thesis, using the extended mean-field Gross-Ptaevskii model, we have investigated the ground state shape, size, stability, and dynamics of the ultra-dilute one-dimensional QDs for homonuclear BECs in the presence of spin-orbit and Rabi coupling. In the below, we present a brief summary of the key results of our thesis, which is mainly divided into seven chapters.

Chapter 1 provides a brief introduction of different kinds of condensates along with the MF model used to understand the structure and dynamics of these condensates. Further, we present the underlying Physics to understand the QDs formation with the main emphasis on the binary droplets. Subsequently, we have given an elaborated description of the modified MF model, also known as extended Gross-Pitaevskii equations (eGPEs) is used to model the structure and dynamics of the QDs. As our thesis work is based on the SO coupled BECs, we have also given a brief outline to get these eGPEs in the presence of SO coupling. It is followed by an extensive literature survey, including the seminal experimental, theoretical, and numerical works that have been performed in recent years to unravel different structures, shapes, phases, and dynamics of the QDs. The chapter ends with the main motivation of choosing this SO coupled droplet for our studies.

In **Chapter 2**, we provide the details of the numerical schemes employed to solve the dynamical equation (eGPEs) corresponding to SO coupled QDs. It begins with a brief description of the split-step Crank-Nicolson scheme, which is used to solve the time-dependent eGPEs in the presence of SO and Rabi coupling. Following this, we give a brief description of the imaginary time propagation scheme, which is used to obtain the ground state structure of the droplet. Subsequently, we outline various kinds of perturbation, such as velocity perturbation, quenching of the interaction, and coupling parameter, which have been used to generate the dynamics among the droplets. We present a brief description of the real-time propagation scheme that has been used to tackle the dynamical aspects of the droplets. The chapter ends with a demonstration to obtain a good converged ground state of the droplet.

In **Chapter 3**, we consider SO coupled droplet in quasi-one dimension for vanishingly small MF contribution (characterized by $\delta g = 0$), which is attained by taking equal and opposite contribution of the intra- and inter-species interaction. This results the QDs in the form as quantum soliton. We have obtained the analytical form for the quantum soliton with non-zero SO coupling. Depending upon the nature of SO coupling ground state either exhibits bright soliton or stripe soliton. For small velocity perturbation, soliton exhibits breather-like oscillation, while at large velocity perturbation, it exhibits moving soliton. For a given Rabi coupling, the breathing frequency increases upon increase in SO coupling, and it attains maximum value at the transition point where quantum bright to stripe soliton transition happens, after that, it decreases with increase in SO coupling. The transition from breather to moving soliton has been addressed by analyzing the different components of energy. The breathing soliton phase is dominated by the SO and Rabi energy, while in the moving soliton phase kinetic energy dominates. For instantaneous quenching of Rabi coupling results the dynamical phase transition from quantum bright soliton to the quantum stripe soliton and secondary soliton generation depending upon the quenching strength of Rabi coupling. However, the quenching of both SO and Rabi coupling facilitates several interesting dynamical phases like repulsive soliton, space-time breather, and filamentation of the soliton. Finally, by giving different instances of velocity perturbation, we have demonstrated that low velocity soliton goes inelastic collision while for high velocity, it exhibits elastic collision, which is quite consistent with experimental results.

In **Chapter 4**, we extend the analysis of the previous chapter of the droplet by considering the finite effective mean-field interaction using unequal intra- and interspecies interaction. We see a remarkably different nature of QDs in the presence of effective mean-field interaction compared to those that we have obtained with zero effective mean-

field interactions. We find that for $\delta g = 0$, the droplet has a sech-like shape, while with $\delta g \neq 0$, it exhibits a flat sech shape. Like $\delta g = 0$ here we also obtain systemic change from bright droplet to breathing droplet, which finally transforms to moving droplet upon increasing the velocity perturbation. The effect of the SO coupling parameter results in a decrease in the critical velocity at which the droplet gets transformed from a breather to a moving droplet. We find that the increase in effective mean-field interaction makes the transition from breathing to the moving droplet at a relatively lower velocity compared to those for lower effective mean-field interaction. Further, we have analyzed the quenching as well as collision dynamics for $\delta g \neq 0$. Interestingly, the inclusion of $\delta g \neq 0$ results in altering the nature of the collision from inelastic (for $\delta g = 0$) to elastic one.

In the previous two chapters, we fixed the atom numbers however, in **Chapter 5**, we extend our study by varying the atom number as well as effective mean-field interaction. In particular, we have presented a detailed exploration of the atom number, interaction strength, and coupling parameters that reveal various ground state structures of the droplet. We find that for small SO coupling, the droplet gets transformed from Gaussian to flat-top droplet upon increasing the atom numbers as well as effective mean-field interaction. Similar features have been observed with large SO coupling where the ground state displays a stripe phase that gets saturated to modulated flat-top droplet upon increasing the atom number. Using the Bogoliubov-de-Gennes analysis for the non-homogeneous ground state, we have demonstrated that relatively small SO coupling droplets are dynamically stable upon variation of the atom number and interaction. However, the stripe phase droplets are dynamically unstable. We also show the appearance of rich dynamical feathers of droplets using velocity imprinting and abrupt changes in interaction strength and coupling parameters. The characteristic dynamical features include breather droplets, moving droplets, asymmetric droplet fragmentation, the admixture of single and stripe droplets, erratic spatial distribution, etc.

Previous chapter works were based on the equal population among the two components. In **Chapter 6**, we extend the analysis for unequal population among the spin components, which has been achieved by considering the imbalanced intra-species interaction. We find that including the imbalanced interaction leads to a change in the structure as well as the population of the individual component of the droplet. We demonstrate beyond a threshold interaction between the components get transformed from flat-top to Gaussian-like droplet at large atom number. In addition, we have explored the effect of particle number, interaction strength and SO and Rabi coupling on the shape as well as population on the spin components. For finite SO coupling, we have observed that the population difference decreases among the components upon increasing the Rabi coupling,

and further beyond the threshold value of Rabi coupling, the population gets balanced. We have also considered the effect of harmonic trap on the shape of the imbalanced SO coupled droplet. In the presence of the trap, the shape of the droplet changes from Gaussian to broader-Gaussian on the increase in atom number from low to moderate atom number and at high atom number, transforms to trapped gas.

In **Chapter 7**, we provide a brief summary and conclusion of our thesis work, which is based on the structure and dynamics of the SO coupled QDs. We also present an outline of future extensions of the work performed in the thesis.

We hope that the present study offers novel insights into the behavior of SO coupled QDs and is timely, given the upcoming experimental investigations into one-dimensional droplets with SO and Rabi coupling. We believe our work will contribute significantly to the field and provide valuable guidance for future experiments.

Acknowledgements

The journey of my PhD, which began in 2019, has now reached its conclusion. It has truly been one of the most interesting and enriching experiences of my life. At this moment, I want to express my heartfelt gratitude and sincere thanks to all the incredible people who have played a vital role and have made this journey so memorable.

First and foremost, I would like to express my sincere gratitude to my thesis supervisor, Dr. Pankaj Kumar Mishra, for the incredible opportunity to work in the fascinating field of quantum droplets of newly evolving phenomena in ultracold matter. I am deeply thankful for his belief in my abilities and for granting me the freedom to explore various aspects of this exciting research area. I appreciate his unwavering support and cooperation throughout my PhD journey. The vibrant and thought-provoking scientific discussions we shared have consistently inspired and motivated me, especially during challenging times. Working with him has been a truly enriching experience, and I will always cherish these memories.

Thanks are due to my Doctoral Committee members, Prof. Kanhaiya Pandey, Prof. Amarendra K. Sarma, and Prof. Sumana Dutta, whose constant encouragement and inputs helped me to finish my PhD in the stipulated time period. In addition, I would like to acknowledge the support and guidance that I have received from former HoDs Prof. Subhradip Ghosh and Prof. Perumal Alagarsamy and current HoD Prof. Bosanta R. Boruah.

It is my pleasure to express my deep sense of gratitude to all of our group collaborators. I greatly benefitted from their expertise and experience during the course of my work. I would like to acknowledge Prof. Paulswamy Muruganandam (Bharathidasan University) for introducing me to different numerical techniques in the field of the mean-field model of Bose-Einstein condensate. I acknowledge him for sharing his rich experience in different fields of ultracold matter. I acknowledge my fruitful collaboration with Dr. R. Ravishankar. I acknowledge Dr. R. Ravishankar for introducing me to several software

packages, which are being used for my thesis work. Above all, I express my high regard for him for all the computation-related help that I received from him at the various stages of my work. I would like to acknowledge Prof. Simeon Mistakadis for his fruitful collaboration for the later part of my thesis work.

I acknowledge all the teachers of the Physics Department from whom I received rigorous training during my course work studies. Specifically, I would like to thank Prof. Saurabh Basu, Prof. Padmakumar Padmanabhan, and Prof. Pankaj Kumar Mishra for setting up an excellent base for basic Physics during my PhD course work in IIT Guwahati. I would especially like to thank Prof. Tapan Mishra and Prof. Pratima Agarwal, with whom I did not have the opportunity to take any course but with whom discussions at different moments have played a very crucial role in keeping up my enthusiasm and energy.

I thank all my lab mates −Rony Da, Swarup, Sanu, Shawan, Joya, Nalinikanta, Sumit, and Premabrata− for their cooperation and fruitful discussions at different stages.

I would like to acknowledge all the staff members of the Physics Department for their kind cooperation, support, and ever willingness to help no matter how difficult the problems were. My special thanks are due to Mr. Basab Bijoy Purkayastha and Mr. Ambarish Biswas for their kind cooperation on different official matters. I would like to thank Mr. Basab Bijoy Purkayastha for all the computation related help which I have received from him at different points of time.

During my brief stay at IIT Guwahati, I came across several friends who made the journey very pleasant and memorable. I acknowledge all the company of sorrow and joy that I have received from them at different stages of my PhD journey. I thank Amalika, Alolika, Esha, Gargi, Saraswati, Pooja, Soumen, Juhi, Jaishree, Himangshu, and many other friends whose company I really cherished during my PhD and whose memories will always be an integral part of my life. I would like to especially mention my childhood best friends, Dr. Jyoti Pandey, Dr. Rangeeta Dhaka, and Vidushi Saxena for their encouragement. My special thanks are due to Swarup and Rony Da for always showing his great interest to discuss several aspects of Physics whenever I approached him. I am very thankful to Manvendra for his suggestions and motivational conversation during tea time.

This work would not have been possible without the computational facilities at Param Ishan and Param Kamrupa, an IIT Guwahati. I would especially like to acknowledge our department's supercomputing facility, Newton Cluster. I am grateful to the University

Grants Commission (UGC), India, for providing financial support in the form of a scholarship under the NET-JRF scheme.

Above all, this PhD would not have been possible without the constant support, encouragement, and blessings of my family. I can never fully repay their unconditional love and the personal sacrifices they have made to help me achieve this goal. I am especially grateful to my Mummy, Papa, and younger brother, Dr. Anukool, for their unwavering support since my childhood. A heartfelt thank you to my Papa for encouraging me to pursue higher studies; I will always be indebted to him for this. I am thankful to my elder brother Dr. Surendra Gangwar for his support and care. I would also like to express my deep gratitude to my husband, Dr. Manvendra Singh Gangwar, for his unwavering faith in my abilities and for backing me wholeheartedly throughout this beautiful yet occasionally challenging journey due to my health. Additionally, I acknowledge my in-laws for their incredible support, especially my Papaji, Bhaiya, and Bhabhi, who have also been a great source of encouragement.

Km Sonali Gangwar

To my parents...

Publications

1. Dynamics of quantum solitons in Lee-Huang-Yang spin-orbit-coupled Bose-Einstein condensates, **S. Gangwar**, R. Ravisankar, P. Muruganandam, and P.K. Mishra , Phys. Rev. A **106**, 063315 (2022).

2. Exploring the Role of Beyond Mean-Field Interaction in the Structure and Dynamics of One-Dimensional Quantum Droplets **S. Gangwar**, R. Ravisankar, P. Muruganandam, and P.K. Mishra, Journal of Physics B: Atomic, Molecular and Optical Physics **56**, 165302 (2023).

3. Spectrum and quench-induced dynamics of spin-orbit coupled quantum droplets, **S. Gangwar**, R Ravisankar, S. I. Mistakidis, P Muruganandam, P.K. Mishra, Phys. Rev. A **109**, 013321 (2024).

4. Interaction imbalanced spin orbit coupled quantum droplet, **S. Gangwar**, R Ravisankar, S. I. Mistakidis, P Muruganandam, P.K. Mishra, arXiv:2409.01945 (2024)[Under Review].

Contents

List of Figures

Chapter 1

Introduction

Bose-Einstein Condensate (BEC) is a state of matter that occurs when a dilute gas of atoms is cooled to temperatures very close to absolute zero [1]. At these extremely low temperatures, the atoms collapse into the lowest possible energy state, resulting in a collective quantum state where all atoms occupy the same quantum level. The theoretical foundation for BEC was laid by Satyendra Nath Bose and Albert Einstein in the early 1920s [2, 3]. Historically, the realization of the condensation-like phenomena was experimentally realized in the case of liquid Helium upon cooling below the lambda transition temperature by Kaptiza and Allen and Misener in 1938 [4, 5]. This was recognized as the first realization of condensate-like phenomena for which London in 1938 showed an intimate relation between the condensation in liquid Helium and BEC [6]. Further, the condensate theory got more enriched with the work of Landau (1941) [7] and subsequently by Penrose and Onsager [8, 9] in the 1950s, who categorically showed the necessity of phase coherence at the macroscopic model to attain the BEC. However, it was realized that due to the strong interaction, only a tiny fraction of the particle remained in the condensate state in order to exhibit the superfluidity. On the other hand, BEC can be achieved only at lower temperature and lower densities.

The first successful demonstration of BEC was achieved by the research groups led by Eric Cornell and Carl Wieman at the University of Colorado, Boulder using ^{87}Rb atoms [10], and shortly thereafter by Wolfgang Ketterle at the Massachusetts Institute of Technology (MIT) [11] using ^{23}Na atoms. The realization of Bose-Einstein condensates (BECs) in laboratory experiments has brought great revolution in the research of ultracold gases and has become an important factor to explore many interesting and novel phenomena, including supersolids [12], Anderson localization [13], and self-bound quantum droplets (QDs) [14, 15]. Among these, QDs—a unique excited bound state of BECs—have drawn a significant attention of the researchers working in different fields of

condensed matter and quantum optics in recent years. These droplets emerge from an intricate balance between attractive mean-field (MF) interactions and repulsive beyond-mean-field (BMF) effects.

The first theoretical proposal for the quantum droplet (QD) phase of the condensate was laid by Dmitry S. Petrov in 2015 [14]. Following the BMF theory proposed in 1957 by Lee, Huang, and Yang [16, 17], Petrov theoretically showed that the attractive binary Bose-Bose mixture instead of collapsing can form a dilute liquid-like droplet, which is mainly stabilized by the quantum fluctuation. Following Petrov's groundbreaking proposal, a series of experimental efforts aimed at realizing this novel phase of quantum matter were initiated. Notably, two independent experiments successfully observed QDs: one led by Tilman Pfau [18, 19, 20, 21] in Stuttgart using dipolar atoms (specifically, Dysprosium) and the other by Francesca Ferlaino at the University of Innsbruck with Erbium [22]. These experiments confirmed that the competing short-range repulsion and long-range dipolar interaction can lead to the formation of the droplet. Following these experiments, the theoretical proposal for the droplet formation in the binary mixture was further confirmed by a group led by Leticia Tarruel from ICFO [15, 23], Spain and others by Macro Fattori [24] from Florence, Italy using the internal spin-state of the ^{39}K. These series of seminal experiments opened up new avenues for exploring the properties and dynamics of QDs in ultracold gases. Following these QDs were also realized in heteronuclear BECs [25, 26], and binary magnetic gases [27]. All the above mentioned experimental observations are quite recent, and many of the theoretical ideas pertaining to the structure and dynamics of these QDs are yet to be systematically explored. In this thesis, by using the modified MF model known as the extended Gross-Pitaevskii equation (eGPE), we have investigated the ground state shape, size, stability, and dynamics of these QDs for homonuclear BECs in the presence of spin-orbit (SO) and Rabi coupling.

In general, the nature of quantum fluctuations, mainly responsible for the appearance of QDs, has a strong dependence on the dimensionality of the condensate. They are attractive in nature for the two and three-dimensional condensate but repulsive in nature for the condensate in one dimension. Therefore, in one-dimensional systems, QDs in binary mixtures are predicted to arise from a different mechanism. Here, the formation of QDs takes place as a result of a balance between attractive BMF and repulsive MF interaction [28]. The study of droplets in one-dimension is particularly interesting because of the significant and nontrivial role of quantum fluctuations. One-dimensional droplets have captured the attention of researchers because they have long life-time and are more stable than their counterparts in higher dimensions [29]. This advantage has led to a surge in the research of quasi-one dimensional QDs from experimental [30], theoretical [31], and

numerical [32, 33] font. These numerical models are mainly confined to deal the droplet using the effective one component extended MF theory [32, 34], which compromises the detailed exploration of individual component dynamics of the droplet and thus puts up some limitations on the analysis. In this thesis work, we have been able to circumvent that sort of constraint by considering the SO and Rabi coupled QDs [33], which enabled us to explore much richer dynamics of this novel form of the ultracold matter.

The outline of the Chapter is as follows. First we discuss the theoretical formalism for the non-interacting scalar BEC. Following this we present the MF model Gross-Pitaevskii equation (GPE) of the interacting condensate. Further, we present the spinor binary BECs, which are followed by the synthetic SO and Rabi coupled BECs. We also present the different types of SO couplings. Subsequently, we provide the theoretical formalism of the stabilization of the QDs. Here we discuss the BMF theory and derive the eGPE for the droplets. Subsequently, we present the eGPE for the SO coupled QDs, which we have used in our thesis work. Further, we present the state-of-the-art research in the QDs, followed by the motivation of our current thesis work. Finally we end the chapter by giving the layout of the subsequent chapters.

1.1 Bose-Einstein condensation

The Bose-Einstein condensation is purely a quantum mechanical effect. As Bosons follow the Bose-Einstein statistics, unlike Fermions, there is no restriction of Bosons particles over occupying a given quantum state. At very low temperature, Bose atoms mainly occupy the lowest available energy state. The overall condensate behaviour can be understood using the phenomenological argument based on the wave-particle duality of the Bosons. At a given temperature, the de-Broglie wavelength (λ_{dB}) for the Boson particle is given by $\lambda_{dB} = (2\pi\hbar^2/mk_BT)^{1/2}$ where m is the mass of the Boson particle, k_B is the Boltzmann constant, and T is the temperature. At high temperature, λ_{dB} is smaller than the inter-particle separation, i.e., $n\lambda_{dB}^3 \ll 1$, where $n = N/V$ is the particle number density for a given particle number N of the Boson gas in a volume V. Upon decreasing the temperature, the λ_{dB} increases, and at the temperature when $n\lambda_{dB}^3 \approx 1$ holds, the Boson gas makes a transition to the condensate state. The condensate state can be represented by the giant macroscopic wave which forms as a result of the constructive interference between the de-Broglie wave of Boson particles. The condensate temperature

of non-interacting Bosons is given by

$$T_c = \frac{2\pi\hbar^2}{mk_B}\left(\frac{n}{\zeta(3/2)}\right)^{2/3}, \tag{1.1}$$

where $\zeta(3/2)$ is the Riemann zeta function. If we consider $n \approx 10^{19} - 10^{21}m^{-3}$ the condensation temperature ranges from $T_c \approx 50nK - 2\mu K$. In general, not all the atoms collapse to the ground state once condensate forms at finite temperature, but there is some finite fraction that remains in the excited state. The condensate fraction at a temperature is given by

$$\frac{N_0}{N} = 1 - \left(\frac{T}{T_c}\right)^3, \tag{1.2}$$

where N_0 is the number of condensate atoms. In Fig. 1.1 we show the condensate distribution for different temperature in the momentum space: Left for $T > T_c$, middle for $T = T_c$ and right for $T < T_C$ [35]. The condensate cloud has been obtained after the time of flight experiment. For $T > T_c$ the atoms show the Maxwell distribution. At $T = T_c$ (middle panel of Fig. 1.1), most of the atom accumulates near the zero momenta state, and below the critical temperature, almost all the particles go to the zero momenta state (right panel of the figure).

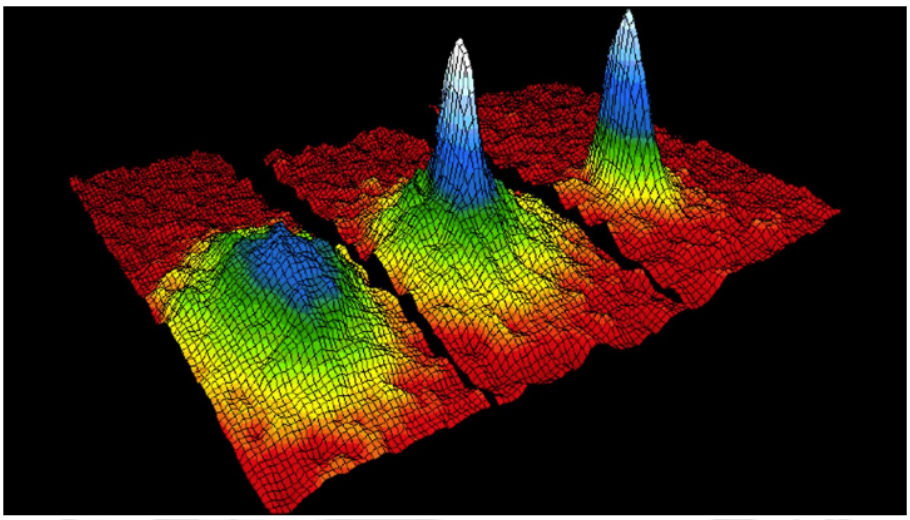

Figure 1.1: Velocity distribution of the trapped rubidium atoms at different temperature. The temperature in the left figure is above the critical temperature therefore, the cloud has only thermal Gaussian distribution. In the center figure, the temperature is lowered below the critical temperature, showing the maximum density of the condensate at $k = 0$. In the right figure, most of the condensate accumulates at zero momentum state. This Figure is taken from [35].

1.1.1 Short-range contact interaction

All the discussion made in the previous section was based on the non-interacting Boson gas. However, in the experiment, the collisional effect of the atoms at finite temperature becomes quite essential and can not be ignored. It is worthwhile to note that one of the experimental steps adopted to achieve BECs is the rethermalization of the gas during the evaporative cooling [11], which is only possible when the collision between atoms takes place due to the scattering events. Therefore, the interaction between the atoms in BECs becomes quite important to decide the structure of its ground state. In this section, we will discuss the effect of the finite interaction on the overall features of the condensate state.

Usually, the interaction between the neutral atoms can be modeled through the van der Waals interactions which is attractive for the larger separation and repulsive for the small separation between the atomic particles. However, the gas in the BEC state is quite dilute one. As a result of this the van der Waals interaction interactions are quite negligible. As an example, for Potassium atomic condensate, the van der Waals range is typically of the order of $r_0 \approx 3.5nm$ [15] while in the condensate, the dilute gas has the interparticle separation is $d \approx 8\mu m$ [11]. Therefore, the interaction between the particles can be approximated using the low-energy wave scattering contact potential as [36]

$$V_{int} = g\delta(\mathbf{r}), \tag{1.3}$$

where, $\delta(\mathbf{r})$ is the Dirac delta function, $g = \dfrac{4\pi\hbar^2 a}{m}$ is the contact interaction strength that depends on the scattering length a and mass m of the atom. Note that the above form of the potential is considered assuming the low energy s-wave scattering between the particle because the higher orbital waves like p-, d- or f- waves scattering get suppressed due to the ultradilute nature of the gas. Therefore, scattering length becomes the vital parameter while dealing with the ultradilute condensate gases. The scattering length can be either positive or negative, representing the repulsive or attractive nature of the interaction. In the experiment, the scattering length can be tuned using the Feshbach resonance[37]. The dependence of the scattering length on the magnetic field (B) is given by

$$a(B) = a^0\left(1 - \frac{\Delta}{B - B_0}\right), \tag{1.4}$$

where, a^0 is the background scattering length, Δ is the width of the resonance, and B_0 is the magnetic field at which the Feshbach resonance takes place. From the above expression, we see that as the $B > B_0$, the scattering length becomes lower than the

background scattering length a^0, while for $B < B_0$ the scattering length can be tuned higher than the a^0. In the following section, we discuss the mean-field dynamical equation for the weakly interacting condensate.

1.1.2 Mean-field model of weakly interacting Bose-Einstein condensates

A dilute condensate of weakly interacting gas can be represented with a second quantized field operator $\hat{\Psi}(r,t)$. The second quantized Hamiltonian for a weakly interacting Bosons in free space is given by

$$\hat{H} = \int dr\hat{\Psi}^\dagger(r)\left(-\frac{\hbar^2}{2m}\nabla^2 + V_{trap}(r)\right)\hat{\Psi}(r) + \frac{1}{2}\int\int drdr'\hat{\Psi}^\dagger(r)\hat{\Psi}^\dagger(r')V_{int}\left(r-r'\right)\hat{\Psi}(r')\hat{\Psi}(r), \tag{1.5}$$

where $\hat{\Psi}(r)$ and $\hat{\Psi}^\dagger(r)$ are the Boson field operators that annihilates and creates a particle at position r, respectively. Here $V_{int}(r-r')$ is the two-body interaction potential, and $V_{trap}(r)$ is the trapping potential. Considering the presence of low-energy s-wave scattering the V_{int} can be approximated as given in the Eq. (1.3) [36]. The Bosonic field operators satisfy the commutation relation given by

$$\begin{aligned}\left[\hat{\Psi}(r),\hat{\Psi}(r')\right] &= \left[\hat{\Psi}^\dagger(r),\hat{\Psi}^\dagger(r')\right] = 0,\\ \left[\hat{\Psi}(r),\hat{\Psi}^\dagger(r')\right] &= \delta(r-r'),\end{aligned} \tag{1.6}$$

and the corresponding density of the system is represented as $n =< \hat{\Psi}^\dagger(r)|\hat{\Psi}(r) >$ where $< . >$ represents the mean of the field operator.

Using the Heisenberg equation of motion $i\hbar\partial_t\hat{\Psi}(r,t) = \left[\hat{\Psi}(r,t),\hat{H}\right]$ and commutation relation between the operators (Eqs. 1.6), we get following equation for the field operators:

$$\mathrm{i}\hbar\frac{\partial}{\partial t}\hat{\Psi}(r,t) = \left[-\frac{\hbar^2}{2m}\nabla^2 + V_{trap}(r) + \int dr'\hat{\Psi}^\dagger(r',t)V_{int}\left(r-r'\right)\hat{\Psi}(r',t)\right]\hat{\Psi}(r,t). \tag{1.7}$$

The field operator is decomposed in the mean and fluctuating part as

$$\hat{\Psi}(r) = \psi(r) + \delta\hat{\Psi}(r), \tag{1.8}$$

here $\psi(r)$ corresponds to the mean part of the field wave function of the condensate

while $\delta\hat{\Psi}(r)$ corresponds to the fluctuating part of the field operator also inherits the contribution from the non-condensate part.

Under the MF approximation, we can ignore the contribution from the excited state which implies that $< \delta\hat{\Psi}(r) >= 0$. As we substitute the Eq. 1.8 into the Eq. 1.7, the mean-field dynamical equation of the condensate also known as Gross-Pitaevskii equation (GPE) is given by [38, 39]

$$\mathrm{i}\hbar\frac{\partial}{\partial t}\psi(\mathbf{r},t) = \left[-\frac{\hbar^2}{2m}\nabla^2 + V_{trap}(r) + g|\psi(\mathbf{r},t)|^2\right]\psi(\mathbf{r},t). \tag{1.9}$$

One can substitute the stationary state solution $\psi(r,t) = \psi(r)\exp(-\mathrm{i}\mu t/\hbar)$, with μ as the chemical potential into the Eq. 1.9 and obtain the energy and chemical potential as

$$\mu = \int d^3\mathbf{r}\left[|\nabla\psi(\mathbf{r})|^2 + V_{trap}(r)|\psi(\mathbf{r})|^2 + g|\psi(\mathbf{r})|^4\right] \tag{1.10}$$

$$E = \int d^3\mathbf{r}\left[|\nabla\psi(\mathbf{r})|^2 + V_{trap}(r)|\psi(\mathbf{r})|^2 + \frac{g}{2}|\psi(\mathbf{r})|^4\right] \tag{1.11}$$

Note that in the follow up discussion, for the sake of brevity, we consider $V_{trap} = 0$. After discussing the GPE of the scalar BEC, next we move our focus on the binary BEC, which is the main content of the following subsection.

1.2 Binary mixture of Bose-Einstein condensates

In the laboratory experiment, the binary BEC can be generated by either mixing two different atomic species or by mixing the two different hyperfine states of the same atom. After the experimental realization of BECs in 1995, researchers began to explore the more complex multi-component and multi-species BECs, enriching the system's dynamics and applications. In particular, in the last few decades, lots of efforts have been put up to realize the atomic BECs with internal spin degrees of freedom, also referred to as the spinor condensates, which offer a new avenue to create coherent matter with complex internal quantum structures.

Historically, the binary BEC using two hyperfine states of the ^{87}Rb was first reported in the Ref. [40], and subsequently, the states were coupled using the linear Rabi coupling [41]. Following this, the MIT group also realized the two-component BEC in the dilute atomic gases of sodium using its hyperfine spin $F = 1$ by transferring the spin-polarized condensates into a far-off resonant optical trap [42], which helps to liberate the spin degrees of freedom of the system. These experimental realizations opened up a gar-

den variety of opportunities for the researchers to explore the ground state, metastability, and quantum spin tunneling of the binary condensate [43, 44, 45] and have become one of the key tool for the upcoming quantum technology. Next, we will present a systematic discussion of the dynamical equation corresponding to the binary BEC in the similar line adopted for one component BEC in the previous section.

1.2.1 Gross-Pitaevskii equation of Binary mixture

Let us assume the ground state of the binary BEC at $T = 0$, which is composed by the two condensate wave functions corresponding to each component represented as $(\psi_\uparrow, \psi_\downarrow)$. The corresponding time-dependent coupled GPEs that deal with the spinor BECs are given by

$$\begin{aligned} \mathrm{i}\hbar\frac{\partial\psi_\uparrow(r,t)}{\partial t} &= \left[-\frac{\hbar^2}{2m_\uparrow}\nabla^2 + g_{\uparrow\uparrow}|\psi_\uparrow(r,t)|^2 + g_{\uparrow\downarrow}|\psi_\downarrow(r,t)|^2\right]\psi_\uparrow(r,t), \\ \mathrm{i}\hbar\frac{\partial\psi_\downarrow(r,t)}{\partial t} &= \left[-\frac{\hbar^2}{2m_\downarrow}\nabla^2 + g_{\downarrow\downarrow}|\psi_\downarrow(r,t)|^2 + g_{\uparrow\downarrow}|\psi_\uparrow(r,t)|^2\right]\psi_\downarrow(r,t). \end{aligned} \tag{1.12}$$

where $m_{\uparrow,\downarrow}$ denotes the masses corresponding to the up and down components, respectively. The intraspecies interaction is given by $g_{jj} = \frac{4\pi\hbar^2 a_{jj}}{2m_j}$ where $j \in \{\uparrow,\downarrow\}$ and the interspecies interaction is given by $g_{\uparrow\downarrow} = \frac{2\pi\hbar^2 a_{\uparrow\downarrow}}{m_r}$, where $m_r = m_\uparrow m_\downarrow/(m_\uparrow + m_\downarrow)$ denotes the reduced mass of the binary state. The normalization condensate of the individual component is given by

$$\int d^3\mathbf{r}|\psi_j(r,t)|^2 = N_j, \tag{1.13}$$

$$\int d^3\mathbf{r}|\psi_\uparrow(r,t)|^2 + |\psi_\downarrow(r,t)|^2 = N_{total}, \tag{1.14}$$

where $N_{total} = N_\uparrow + N_\downarrow$ denote the total number of particle in the condensate. Similar to the scalar condensate as discussed in the previous section, here also using the stationary state solution, the energy functional of the binary condensate can be expressed as

$$\begin{aligned} E\left[\psi_\uparrow,\psi_\downarrow\right] &= \int d^3\mathbf{r}\left[-\frac{\hbar^2}{2m_\uparrow}|\nabla\psi_\uparrow(\mathbf{r})|^2 + \frac{g_{\uparrow\uparrow}}{2}|\psi_\uparrow(r,t)|^4\right] \\ &+ \int d^3\mathbf{r}\left[-\frac{\hbar^2}{2m_\downarrow}|\nabla\psi_\downarrow(\mathbf{r})|^2 + \frac{g_{\downarrow\downarrow}}{2}|\psi_\downarrow(r,t)|^4\right] \\ &+ \int d^3\mathbf{r}\left[g_{\uparrow\downarrow}|\psi_\uparrow(r,t)|^2|\psi_\downarrow(r,t)|^2\right]. \end{aligned} \tag{1.15}$$

After discussing the binary BEC now, we move our focus to the more complex BEC, where the hyperfine state can be coupled with their momentum using the synthetic SO coupling.

1.3 Spin-orbit coupled Bose-Einstein condensates

Over the last few decades, in ultracold gases, using the light-matter interaction, there has been a proposal to combine the momentum of the condensate atom with the spin corresponding to the hyperfine states. These ideas are mainly based on the space-dependent coupling of the atom with the particular geometrical configuration of the laser beams. In this case, a synthetic gauge field appears when the system starts following adiabatically one of the local eigen states. On the other hand, an interesting situation arises when the local spin-dressed states are degenerate in nature that, yields the spin-orbit-like configuration. In this direction, the first experimental observation of SO coupled BEC was realized by the NIST group in 2011 [46] using the two coupled Raman lasers. Using the hyperfine state of ^{87}Rb atoms, they were able to engineer one-dimensional synthetic SO coupling, which can be characterized by the Rasbha [47] and Dresselhaus [48] SO coupling. At later stage, similar techniques were adopted to realize the SO coupled Fermi gases [49], spin-1 BEC [50], etc. As our thesis work is based on the SO coupled QDs, here in this section, we provide a very pedagogical level of description of SO coupled BECs.

Firstly, we discuss about the atomic SO coupling, which generally appears as a result of the coupling of the spin with its momentum. It is followed by a very brief overview of different kinds of SO coupling present in the bulk materials. Thereafter, we will provide a brief outline of the synthetic SO coupling observed in the experiment which is followed by the time-dependent SO and Rabi-coupled BECs.

1.3.1 Spin-orbit coupling of an atom

SO coupling generally arises as a result of coupling between the electron spin with its own orbital angular momentum. In condensed matter Physics, several phenomena such as spintronics, topological insulators [51], and spin-Hall effects are the direct manifestation of the SO coupling. The SO coupling of an atom can be physically described in the following way. For an electron moving with the velocity $\mathbf{v}$, the electrostatic field $\mathbf{E}$ gets transformed into an effective magnetic field $\mathbf{B_{eff}}$ in the electron rest frame. This transformation is based on the relativistic principle that an electric field is seen in one frame of reference can be perceived as the magnetic field in another frame of reference.

The effective magnetic field is given by

$$\mathbf{B_{eff}} = -\frac{\mathbf{v} \times \mathbf{E}}{c^2}, \tag{1.16}$$

where, $\mathbf{E}$ and $\mathbf{B_{eff}}$ represent the electric and magnetic field respectively while $\mathbf{v}$ denotes the orbital velocity of the electron and c is the light velocity in the vacuum. Considering the electric field as $\mathbf{E} = E_0\hat{z}$ the magnetic field gets coupled with the magnetic moment of the electron also termed as the SO coupling and the Hamiltonian is described as

$$H_{SO} = -\mu_s \cdot \mathbf{B_{eff}} \equiv -\frac{g_s\mu_B\mathbf{E_0}}{2mc^2}(\mathbf{k} \times \boldsymbol{\sigma}) \cdot \hat{z}, \tag{1.17}$$

Equivalently we can express the above Hamiltonian as

$$H_{SO} = -\alpha_{SO}(\mathbf{k} \times \boldsymbol{\sigma}) \cdot \hat{z}, \tag{1.18}$$

Here, $\alpha_{SO} = \frac{g_s\mu_B\mathbf{E_0}}{2mc^2}$ with μ_B as the Bohr's magneton, while g_s denotes the gyromagnetic ratio of the elctron and $\boldsymbol{\sigma}$ is the Pauli matrices. Different combinations of α_{SO} will be responsible for various types of SO coupling, such as Rashba, Dresselhaus, and their combination.

1.3.2 Different types of spin-orbit couplings

In this section, we present different types of SO coupling observed in the condensed matter system. In materials, SO coupling most often gets connected with the momentum dependent Zeeman energy, where the the momentum of the electron gets affected due to the presence of the effective magnetic field. The Rashba coupling originates as a result of the lack of mirror symmetry in a 2D system leading to the coupling between electron spin and its angular momentum.

The Hamiltonian corresponding to the Rashba SO coupling [47] is given by

$$H_R = \lambda_R \times (k_y\sigma_x - k_x\sigma_y), \tag{1.19}$$

Here, λ_R represents the coupling constant. Equivalently the above relation can be written as

$$H_R = \Xi_R(\mathbf{k}) \cdot \sigma, \tag{1.20}$$

where $\Xi_R(\mathbf{k}) = \lambda_R\,(-k_y, k_x, 0)$. k_x and k_y are the components of the electron's momentum.

However, the Dresselhaus SO coupling Hamiltonian [48] is given by

$$H_D = \lambda_D \times (-k_y\sigma_x - k_x\sigma_y), \tag{1.21}$$

The above relation can be expressed as

$$H_D = \Xi_D(\mathbf{k}) \cdot \sigma, \tag{1.22}$$

where $\Xi_D(\mathbf{k}) = \lambda_R\,(k_y, k_x, 0)$.

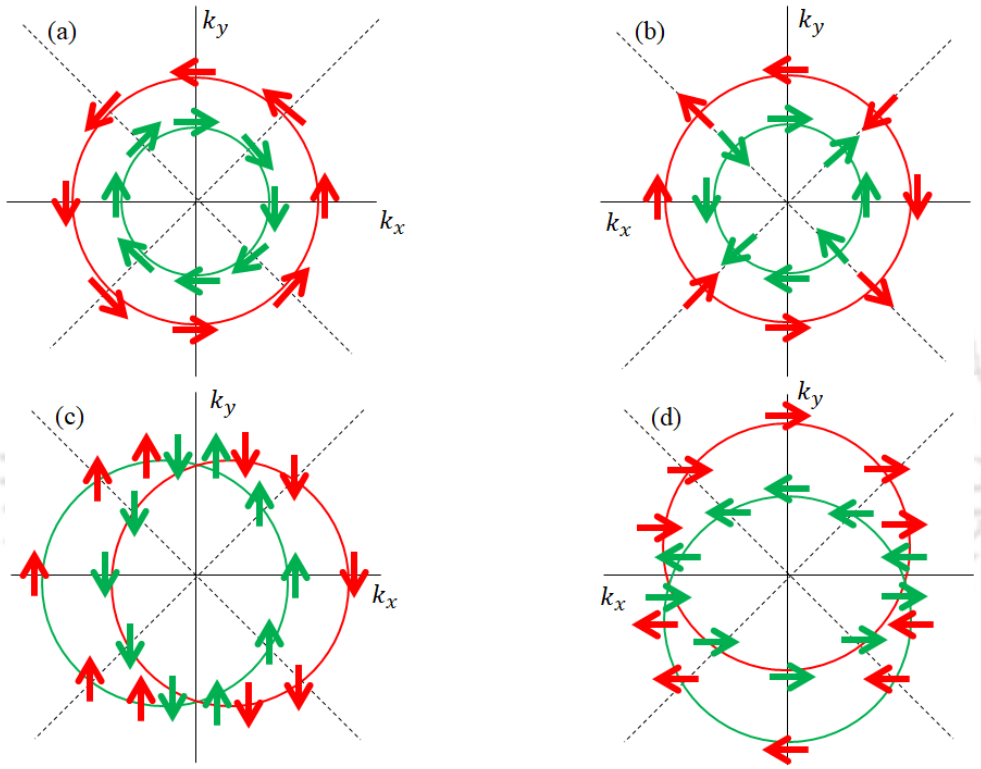

Figure 1.2: Spin orientation corresponding to the various SO coupling. (a) 2D Rashba SO coupling $\lambda_R \times (k_y\sigma_x - k_x\sigma_y)$ which lacks the mirror symmetry. (b)2D Dresselhaus SO coupling $\lambda_D \times (-k_y\sigma_x - k_x\sigma_y)$ having bulk inversion symmetry. (c) and (d) depict 1D SO coupling as a consequence of the equal combination of Rashba and Dressalhaus SO coupling corresponding to $-\lambda_{RD}k_x\sigma_y$ and $\lambda_{RD}k_y\sigma_x$ respectively. The arrow is used to show the spin orientation: red for the up-spin and green for the down-spin.

In Fig. 1.2(a) we depict the Rashba coupling $\Xi_R(\mathbf{k})$ configuration for the spin in 2D. The red and green colors represent the different spins. The Rashba SO coupling leads to a momentum dependent spin splitting, where the spin orientation depends on its momentum direction. We see the presence of mirror symmetry for the Rashba coupling configuration as depicted in Fig. 1.2(a). In Fig. 1.2(b), we show the spin configuration related to the Dresselhaus coupling $\Xi_R(\mathbf{k})$, which shows the bulk inversion symmetry. Upon linearly

combining the Dresselhaus and Rashba coupling, one can obtain the spin configuration corresponding to the one-dimensional SO coupling. In Fig. 1.2(c) and (d), we show the spin configurations corresponding to $H_R + H_D$ and $H_R - H_D$ state, respectively that represent the one-dimensional nature of the SO coupling.

1.3.3 Synthetic one-dimensional spin-orbit coupled Bose-Einstein condensates

SO coupling is typically observed in solid-state materials, where it is an intrinsic property. The presence of the SO coupling gives rise to various exotic phenomena such as topological insulators [51, 52], spin-Hall effect [53], spintronic devices [54], and quantum simulations [55, 56]. Ultracold Bose gases offer a highly controlled experimental environment to explore these many-body quantum effects. Therefore, it acts as a powerful quantum simulator for various quantum systems. In this context, researchers aim to mimic the SO coupling phenomenon in ultracold Bose gases with tunable coupling. However, a key challenge is that ultracold atoms are neutral particles and, thus, do not naturally experience SO coupling. As a result, SO coupling must be artificially engineered in these systems.

The first experimental observation of synthetic SO coupling in a BEC was observed by the NIST group in 2011 [46] using a method based on Raman coupling. In Fig. 1.3, we show the schematic diagram of the experiment. In this experiment, they used ^{87}Rb atoms, whose ground state electronic structure is $5S_{1/2}$. The total spin F is the sum of the total angular momentum J and the nuclear spin I. Since the orbital angular momentum of ^{87}Rb in the ground state is $l = 0$, which gives an angular momentum $J = 1/2$. With a nuclear spin $I = 3/2$, the total spin states F are separated by hyperfine coupling into two manifolds, $F = 1$ and $F = 2$. In their experiment, they considered ^{87}Rb in the $F = 1$ ground state hyperfine manifold, which is three-fold degenerate. Firstly, a bias magnetic field is applied along the y direction to break this degeneracy. This results in Zeeman splitting, which separates the levels into $|F = 1, m_F = +1\rangle$, $|F = 1, m_F = -1\rangle$, and $|F = 1, m_F = 0\rangle$, leading to the formation of multi-component BECs (See Fig. 1.3(b)). Next, the coupling between these states is introduced with the help of the two Raman lasers. Two Raman lasers with a wavelength of $\lambda = 804.1nm$ are positioned perpendicular to each other, propagating along the directions $y + x$ and $y - x$, with frequencies ω_L and $\omega_L + \Delta\omega_L$, respectively. In general, both the Raman lasers carry the same wavelength, and they are set offset from each other by a pair of acousto-optic modulators driven by two phase-locked frequency synthesizers that work near the $80MHz$ [46]. The

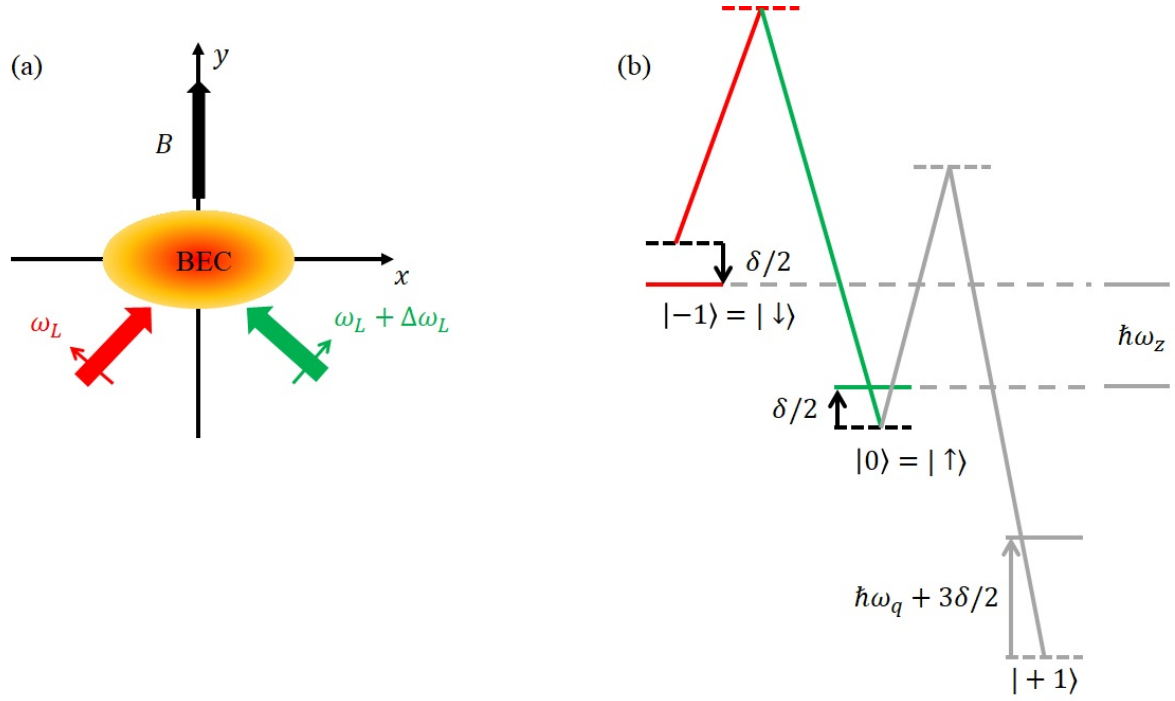

Figure 1.3: (a)Schematic of the experimental setup [46] for the realization of synthetic SO coupling when BEC cloud is subjected to the strong magnetic field and two Raman Laser beams. (b) Schematic of hyperfine state levels of ^{87}Rb. Two lasers couple the hyperfine states $|\uparrow\rangle$ and $|\downarrow\rangle$, differing in energy by $\hbar\omega_z$ Zeeman shift.

bias magnetic field induces a Zeeman shift $\hbar\omega_Z$ between the states $|F = 1, m_F = 0\rangle$, and $|F = 1, m_F = -1\rangle$, and this shift is equal to the frequency difference $\Delta\omega_L$ between the two lasers. However, the state $|F = 1, m = 1\rangle$ is effectively decoupled from the rest of the system due to the large quadratic Zeeman shift $\hbar\omega_q$. By neglecting this state, the system can be reduced to an effective spin-1/2 system, with the two remaining states represented as pseudo-spin-up $|\uparrow\rangle = |m_F = 0\rangle$ and pseudo-spin-down $|\downarrow\rangle = |m_F = -1\rangle$. These two states are coupled with a Rabi frequency Ω, which is determined by the laser intensity.

The single particle Hamiltonian for two-level synthetic guaged SO coupled BEC is given by

$$H = \frac{\hbar^2 k_x^2}{2m} + \frac{\hbar^2 k_L}{m} k_x \sigma_z + \hbar\Omega\sigma_x + \frac{\hbar\delta}{2}\sigma_z, \tag{1.23}$$

where, $k_L = \dfrac{\sqrt{2}\pi}{\lambda_L}$ with λ_L as the wavelength of the Raman lasers, m is the mass of the ^{87}Rb atoms, $(\sigma_x, \sigma_y, \sigma_z)$ are the Pauli spin matrices, Ω is the Rabi coupling strength between the two dressed states, and δ is detuning from the Raman resonance. Throughout the work we have considered $\delta = 0$.

The corresponding SO coupled GPE for the spin-up $(\psi_\uparrow)$ and spin-down $(\psi_\downarrow)$ states are given by

$$
\begin{aligned}
\mathrm{i}\hbar\frac{\partial\psi_{\uparrow}(x,t)}{\partial t} &= \left[-\frac{\hbar^2}{2m}\partial_x^2 - \mathrm{i}\frac{\hbar^2}{m}k_L\partial_x + g_{\uparrow\uparrow}|\psi_{\uparrow}(x,t)|^2 + g_{\uparrow\downarrow}|\psi_{\downarrow}(x,t)|^2\right]\psi_{\uparrow}(x,t) + \hbar\Omega\psi_{\downarrow}(x,t),\\
\mathrm{i}\hbar\frac{\partial\psi_{\downarrow}(x,t)}{\partial t} &= \left[-\frac{\hbar^2}{2m}\partial_x^2 + \mathrm{i}\frac{\hbar^2}{m}k_L\partial_x + g_{\downarrow\downarrow}|\psi_{\downarrow}(x,t)|^2 + g_{\uparrow\downarrow}|\psi_{\uparrow}(x,t)|^2\right]\psi_{\downarrow}(x,t) + \hbar\Omega\psi_{\uparrow}(x,t).
\end{aligned}
\tag{1.24}
$$

After giving a brief overview of the SO coupled BECs now, we move on the theoretical description of QDs, which is the main point of attraction of my thesis work.

1.4 Theoretical formalism of the quantum droplets

In this section, we provide the theoretical framework related to the QDs. First, we give a brief overview of the BMF theory responsible for the formation of the QDs and proposed by Petrov in 2015. Following this, using Petrov's theory, we will derive the dynamical equation corresponding to the SO coupled QDs, which have been used as a key dynamical equation to obtain the structure and dynamics of the QDs presented in the thesis work.

1.4.1 Beyond mean-field approximation

The MF approximation discussed in Sec. 1.1.2 does not take account of the quantum fluctuation that mainly arises due to the contribution from the non-condensate. Here, we consider that fluctuation and derive the BMF contribution.

For a uniform Bose gas occupying a volume V, the field operator in the basis of the superposition of the plane waves can be expressed as

$$\hat{\Psi}(r) = \sum_p \frac{e^{\mathrm{i}pr/\hbar}}{\sqrt{V}}\hat{a}_p, \tag{1.25}$$

$$\hat{\Psi}^{\dagger}(r) = \sum_p \frac{e^{-\mathrm{i}pr/\hbar}}{\sqrt{V}}\hat{a}^{\dagger}{}_p, \tag{1.26}$$

where $\hat{a}_p$ and $\hat{a}_p^{\dagger}$ correspond to the annihilation and creation operators, respectively, that annihilate or create a particle in the state with momentum p. The operators $\hat{a}_p$ and $\hat{a}_p^{\dagger}$ follow the similar Bosonic commutation rule similar as of Eq. (1.6),

$$[\hat{a}_p, \hat{a}_{p'}] = \left[\hat{a}_p^\dagger, \hat{a}_{p'}^\dagger\right] = 0, \qquad \left[\hat{a}_p, \hat{a}_{p'}^\dagger\right] = \delta_{p,p'}. \tag{1.27}$$

Inserting Eqs. (1.25) and (1.26) into Eq. (1.5) and applying the pseudo potential approximation, the many-body Hamiltonian can be expressed in the momentum state as follows

$$\hat{H} = \sum_p \frac{p^2}{2m}\hat{a}_p^\dagger \hat{a}_p + \frac{g}{2V}\sum_{p_1,p_2} \hat{a}_{p_1}^\dagger \hat{a}_{p_2}^\dagger \hat{a}_{p_1}\hat{a}_{p_2}. \tag{1.28}$$

Below condensate temperature, we can assume the collision between the two groups of atoms in which one group has zero momenta ($p = 0$) and the other set of atoms has finite momenta. Among all the possible scattering processes between the two particles with different momenta p_1 and p_2, we only consider the net exchange of p momenta. In other words, the following set of exchange of momentum exchanges is allowed in the summation of Eq. 1.28 with four possible ways. (i)$p_1 = 0$ and $p_2 = p$ and no momentum transfer, (ii)$p_1 = 0$ and $p_2 = p$ and with p momentum transfer, (iii) $p_1 = p$ and $p_2 = 0$ and with no momentum transfer, and (iv) $p_1 = p$ and $p_2 = 0$ and with $-p$ momentum transfer. In the MF approximation, all the terms containing the field operators $\hat{a}_p$ and $\hat{a}_p^\dagger$ with $p \neq 0$ have been neglected. Now, we will extend the MF theory to take into account the field operators of the states with $p \neq 0$. We consider the Bogoliubov approximation and replace the $\hat{a}_0^\dagger$ and $\hat{a}_0$ with $\sqrt{N_0}$, which will give

$$\hat{H} = \sum_p \frac{p^2}{2m}\hat{a}_p^\dagger \hat{a}_p + \frac{g}{2V}\sum_{p\neq 0}\left(N_0^2 + 4N_0\hat{a}_p^\dagger\hat{a}_p + N_0\hat{a}_p^\dagger\hat{a}_{-p}^\dagger + N_0\hat{a}_p\hat{a}_{-p} + \mathcal{O}\left(\left(\hat{a}^\dagger\hat{a}\right)^2\right)\right). \tag{1.29}$$

From the normalization condition we have

$$N_0 = N - \sum_{p\neq 0}\hat{a}_p^\dagger\hat{a}_p, \tag{1.30}$$

Hence we have

$$N_0^2 = N^2 - 2N\sum_{p\neq 0}\hat{a}_p^\dagger\hat{a}_p + \mathcal{O}\left(\left(\hat{a}^\dagger\hat{a}\right)^2\right). \tag{1.31}$$

As we are mainly interested in the first non-vanishing correction to the MF energy, we omit the higher-order terms. By substituting Eq. (1.31) into the Hamiltonian Eq. (1.29)

we obtain

$$\hat{H} \simeq \sum_{p} \frac{p^2}{2m}\hat{a}_p^\dagger \hat{a}_p + \frac{gN^2}{2V} + \frac{gN}{2V}\sum_{p\neq 0}\left(2\hat{a}_p^\dagger \hat{a}_p + \hat{a}_p^\dagger \hat{a}_{-p}^\dagger + \hat{a}_p \hat{a}_{-p}\right), \tag{1.32}$$

where the first term in the above equation represents the kinetic energy, the second term denotes the energy corresponding to $p = 0$ state (ground state), and the third term depicts the excited state energy ($p \neq 0$). The many-body Hamiltonian (Eq. 1.32) is not diagonal as it have the terms like $\hat{a}_p^\dagger \hat{a}_{-p}^\dagger$ and $\hat{a}_p \hat{a}_{-p}$. It can be diagonalized by using the Bogoliubov transformation given below

$$\begin{aligned} \hat{a}_p &= u_p \hat{\beta}_p + v_{-p}^* \hat{\beta}_{-p}^\dagger, \\ \hat{a}_p^\dagger &= u_p^* \hat{\beta}_p^\dagger + v_{-p} \hat{\beta}_{-p}, \end{aligned} \tag{1.33}$$

where new set of operators $\hat{\beta}_p$ and $\hat{\beta}_p^\dagger$ can annihilate and create a quasi-particle of momentum p respectively.

The Bogoliubov coefficients u_p and v_{-p} can be determined by imposing the condition that the operators $\hat{\beta}_p$ and $\hat{\beta}_p^\dagger$ follow the same Bosonic commutation relation, i.e., $\left[\hat{\beta}_p, \hat{\beta}_{p'}^\dagger\right] = \delta_{p,p'}$ as the real field operator $\hat{a}_p$ and $\hat{a}_p^\dagger$. This condition gives

$$|u_p|^2 - |v_{-p}|^2 = 1. \tag{1.34}$$

Now we can choose the u_p and v_{-p} in such a way that it will follow the above constraint and make the non-diagonal terms of the Hamiltonian (Eq. 1.32) to be zero. The diagonalized Hamiltonian can be written as [1]

$$\hat{H} = \mathcal{E}_0 + \mathcal{E}_0^{(1)} + \sum_{p\neq 0} \epsilon(p)\hat{\beta}_p^\dagger \hat{\beta}_p, \tag{1.35}$$

where ϵp is the Bogoliubov dispersion relation given by

$$\epsilon(p) = \sqrt{\left(\frac{p^2}{2m}\right)^2 + p^2 \frac{gn}{m}}, \tag{1.36}$$

where, m is the mass and n is particle density of the condensate. On the other hand in Eq. (1.35) $\mathcal{E}_0$ is the MF ground state energy and $\mathcal{E}_0^{(1)}$ is the first order energy correction to the MF energy given by

$$\mathcal{E}_0 = \frac{gN^2}{2V}, \tag{1.37}$$

and,

$$\mathcal{E}_0^{(1)} = \frac{1}{2}\sum_{p\neq 0}\left(\epsilon(p) - gn - \frac{p^2}{2m} + \frac{mg^2n^2}{p^2}\right). \tag{1.38}$$

The first order correction term $\mathcal{E}_0^{(1)}$ that appears along with the ground state energy can be attributed due to the quantum fluctuation also popularized with the name Lee-Huang-Yang (LHY) correction to the MF energy [16, 17]. The first-order correction energy density in the thermodynamic limit reduces to

$$E_{LHY} \equiv \frac{\mathcal{E}_0^{(1)}}{V} \simeq \frac{64}{15\sqrt{\pi}} gn^{5/2}a^{3/2}, \tag{1.39}$$

where, to obtain the above equation we used $g = 4\pi\hbar^2 a/m$ with a as the scattering length.

So including the first-order correction in the ground state energy, the modified ground state energy density can be written as

$$E_0 = \frac{1}{2}gnN\left(1 + \frac{128}{15}\sqrt{\frac{na^3}{\pi}}\right). \tag{1.40}$$

The chemical potential can be obtained by using the relation $\partial E_0/\partial N$ and gives

$$\mu = gn\left(1 + \frac{32}{3}\sqrt{\frac{na^3}{\pi}}\right). \tag{1.41}$$

The LHY correction to the MF is proportional to $\propto \sqrt{na^3}$, so for the dilute system ($\sqrt{na^3} \ll 1$), the LHY term is typically very small compared to the MF term. As a result of this, if we consider the repulsive Bose gas, it will keep on expanding without the trap as the MF term is the dominating one. However, condensate will be collapsed for attractive interaction. Therefore, droplet formation is not possible for a single Bose gas without any long-range interaction. Petrov [14, 28] in his seminal paper, obtained the form of LHY correction to the MF energy for binary mixture and proposed the formation of the droplet for the binary condensate, which we discussed in the next section.

1.4.2 Quantum droplets in binary mixture

As my thesis work is based upon the binary BEC in which we consider the hyperfine states of the atom as the pseudo-spin state. In this section, we focus on deriving the BMF energy for the binary BEC constructed with the hyperfine states.

The MF interaction energy density for the binary mixture from the Eq. 1.15 can be written as

$$E_{MF}(n_\uparrow, n_\downarrow) = \frac{1}{2} g_{\uparrow\uparrow} {n_\uparrow}^2 + \frac{1}{2} g_{\downarrow\downarrow} {n_\downarrow}^2 + g_{\uparrow\downarrow} n_\uparrow n_\downarrow, \tag{1.42}$$

where the $\uparrow$ and $\downarrow$ are the spin-up and spin-down component of the condensate respectively, $n_{\uparrow,\downarrow}$ are the densities of each component, and $g_{\uparrow\uparrow}, g_{\downarrow\downarrow}$ correspond to the intraspecies coupling constant describing the interaction between the same spin states, while $g_{\uparrow\downarrow}$ corresponds to the interspecies coupling constant.

From Eq. (1.42) we see that as $g_{\uparrow\downarrow} < -\sqrt{g_{\uparrow\uparrow} g_{\downarrow\downarrow}}$, the condensate becomes unstable because the MF energy of mixture becomes negative. In the unstable regime of the MF, we can introduce a parameter near the collapse point represented as

$$\delta g = g_{\uparrow\downarrow} + \sqrt{g_{\uparrow\uparrow} g_{\downarrow\downarrow}}. \tag{1.43}$$

In Eq. (1.43), δg is the effective mean-field interaction and represents the imbalance between the MF contributions from the inter and intra-species interaction. For the unstable case $\delta g < 0$ as we consider δg small compared to $g_{\uparrow\uparrow}$, $g_{\downarrow\downarrow}$, i.e. $\delta g << \sqrt{g_{\uparrow\uparrow} g_{\downarrow\downarrow}}$, the MF energy density can be represented in terms of δg as

$$E_{MF}(n_\uparrow, n_\downarrow) = \frac{1}{2} \left(n_\uparrow \sqrt{g_{\uparrow\uparrow}} - n_\downarrow \sqrt{g_{\downarrow\downarrow}} \right)^2 + \delta g n_\uparrow n_\downarrow, \tag{1.44}$$

The first term in the MF energy can be minimized by considering a constant density ratio of the condensate $n_\downarrow / n_\uparrow = \sqrt{g_{\uparrow\uparrow} / g_{\downarrow\downarrow}} = \gamma$. Using this the MF energy density of the above Eq. (1.44) in terms of parameters γ and total density $n = n_\uparrow + n_\downarrow$ can be expressed as

$$E_{MF}(n) = \delta g \frac{\gamma}{(1+\gamma)^2} n^2. \tag{1.45}$$

On a similar line of one component BEC as discussed in the Sec. 1.4.1 Petrov [14] derived the LHY energy density for the binary mixture which is given by

$$E_{LHY} = \frac{8}{15\pi^2} \left(\frac{m_\uparrow}{\hbar^2} \right)^{3/2} (g_{\uparrow\uparrow} n_\uparrow)^{5/2} \mathcal{F} \left(z = \frac{m_\downarrow}{m_\uparrow}, x = \frac{g_{\uparrow\downarrow}^2}{g_{\uparrow\uparrow} g_{\downarrow\downarrow}}, y = \frac{g_{\downarrow\downarrow} n_\downarrow}{g_{\uparrow\uparrow} n_\uparrow} \right), \tag{1.46}$$

where $\mathcal{F}(z, x, y)$ is a positive dimensionless function. In the limit of the MF instability where $\delta g << \sqrt{g_{\uparrow\uparrow} g_{\downarrow\downarrow}}$, we can neglect the small contribution of δg ($\delta g = 0$) and set $g_{\uparrow\downarrow}^2 = g_{\uparrow\uparrow} g_{\downarrow\downarrow}$, i.e. $x = 1$. For the homonuclear mixture $m = m_\uparrow = m_\downarrow$, the function is

given by

$$\mathcal{F}(1,1,y) = (1+y)^{5/2}. \tag{1.47}$$

In these conditions, the LHY energy density can be written as:

$$E_{LHY} = \frac{8}{15\pi^2}\left(\frac{m}{\hbar^2}\right)^{3/2}(g_{\uparrow\uparrow}n_\uparrow + g_{\downarrow\downarrow}n_\downarrow)^{5/2}, \tag{1.48}$$

the above equation will be modified in terms of the total density n as

$$E_{LHY}(n) = \frac{8}{15\pi^2}\left(\frac{m}{\hbar^2}\right)^{3/2}(\gamma g_{\downarrow\downarrow})^{5/2}\, n^{5/2}. \tag{1.49}$$

After discussing the LHY correction for the binary BEC now, we move our focus to explain the experimental proposal that was put forward by Petrov, which was later realized in the laboratory experiment [15].

1.4.3 Proposal for quantum droplets in binary mixture

In the classical case the droplet formation can be understood as the balance between the attractive and repulsive term in the van der Waals interaction. In a similar line, Petrov [14] argued that in the presence of an attractive MF term, as the condensate starts collapsing, the density increases, and at a certain density, the LHY or BMF term starts stabilizing the condensate. As a result of the balance between attractive MF term and repulsive LHY term, the bound state forms in the condensate, which is also known as the QDs.

Cabrera et al. [15] performed the seminal experiment to observe QDs in a binary mixture. To create self-bound droplets, they used two hyperfine states of ^{39}K, namely $|F=1, m_F=0\rangle$ and $|F=1, m_F=-1\rangle$. In Fig. 1.4, we show the free evolution of the condensate after removing the radial confinement for different values of δg as observed in the experiment [15]. For ($\delta g > 0$) (first row), the condensate behaves like a gas and keeps on expanding in the absence of any trap. For attractive interaction ($\delta g < 0$) (second row), the condensate remains stable until $t \lesssim 25$ms indicates the formation of the QDs. Note that for $\delta g < 0$, MF interaction suggests the collapse of the condensate, however, due to the significant presence of the LHY contribution in this parameter range, the stable bound state in the form of a QDs appears. On the one hand, the attractive MF interaction in the binary mixture exhibits the stable droplet, however the same attractive interaction in the single component BEC shows a collapsing tendency for $g < 0$ as shown in the third

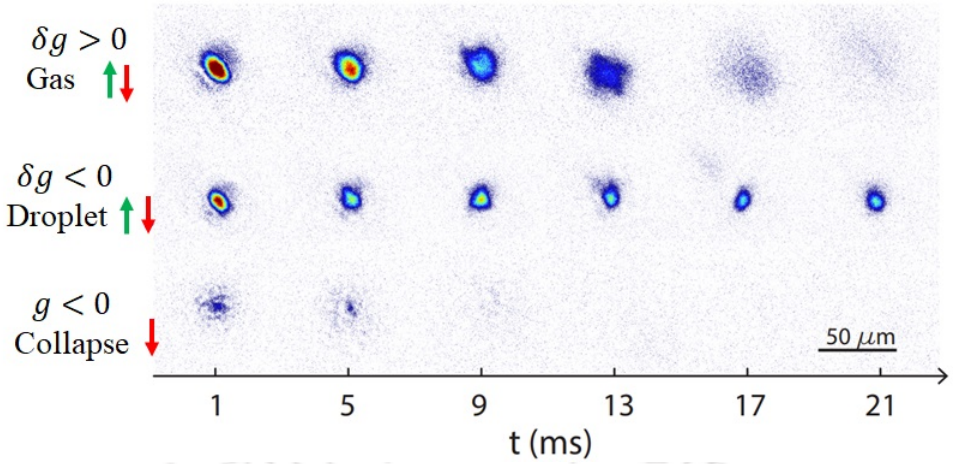

Figure 1.4: Time of flight experimental snaps of the condensate of atoms ^{39}K for different range of δg at different instants represented in the horizontal scale. For $\delta g > 0$ the condensate keeps on expanding like a gas. For single component $g < 0$ leads to the collapse of the condensate. However, for $\delta g < 0$ the condensate remains stable in the form of the droplet until $t \lesssim 25ms$. The figure is adapted from the Ref. [15].

panel of Fig. 1.4.

In a three-dimensional homogeneous binary mixture, if $\delta g < 0$, the BMF contribution becomes significant. For the binary mixture, the energy functional is given by adding a quantum fluctuation effect with the MF energy. This quantum fluctuation term is repulsive in nature. Using the Eq. (1.45) and Eq. (1.49) the total energy can be written as [14]

$$E_{total} = \delta g \frac{\gamma}{(1+\gamma)^2} n^2 + \frac{8}{15\pi^2} \left(\frac{m_\uparrow}{\hbar^2}\right)^{3/2} (\gamma g_{\downarrow\downarrow})^{5/2} n^{5/2}, \tag{1.50}$$

where $n = n_\uparrow + n_\downarrow$ is the total density of the condensate. In Eq. (1.50), the first term represents the MF term that depends on δg while the latter is the LHY term which depends only on the contact interaction. Therefore, near the collapse point, the MF energy is small while LHY energy is significant, and the BMF effect becomes important in binary mixture.

In Fig. 1.5 we schematically show the energy density variation as a function of the droplet density for $\delta g < 0$. In 3D, the MF contribution in energy density is attractive in nature, which is produced by all the zero-point energy of the Bogoliubov modes and varies as $-n^2$, as shown with the green line in the figure. However, the repulsive LHY or BMF term contribution in the energy density varies as $n^{5/2}$ shown with a brown line in the figure. For low condensate density, the MF term dominates overall energy, and due to its attractive nature, it destabilizes the condensate. As a result of this the condensate starts approaching towards the collapsed region with an increase in the density of the condensate.

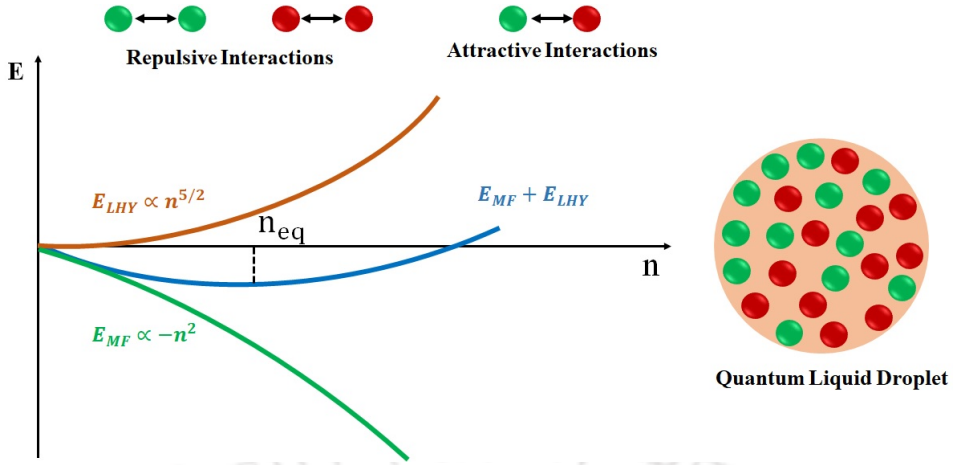

Figure 1.5: A pictorial representation of the stabilization mechanism. This Figure is taken from Ref. [57].

At large densities the LHY contribution starts playing the role which is positive in nature for 3D and which tries to stabilize the condensate. Like classical droplets, there is a tug of war between the attractive MF and repulsive LHY contribution to the energy density that leads to attaining the equilibrium density state of the condensate where the system is self-bound in nature. In the schematic diagram at the equilibrium density (n_{eq}), the total energy density shown with the blue line in the figure (MF+LHY) attains the minimum value. The bound state is also known as the QD as it comes due to the presence of LHY or BMF contribution, which is totally quantum in nature. Please note that the equilibrium density corresponding to the QD state is eighth-order less than the usual classical fluid. In this thesis, we are mainly interested to analyze the structure and dynamics of the droplet at $T = 0$.

Following the prediction of the droplet in three-dimensional, many experimental and theoretical studies were motivated by these interesting developments in the ultracold gases. We will discuss them in more detail in the later part of the Chapter. However, in 2016, Petrov also calculated the energy correction due to the BMF in lower dimensions such as 1D and 2D. He found that the BMF term is repulsive in nature in 2D while it is attractive in nature in 1D [28].

1.4.4 One-dimensional spin-orbit coupled quantum droplets

In this section, we derive the dynamical equations corresponding to the one-dimensional SO coupled QDs, which is also the main focus of my PhD thesis.

Following the energy density obtained in 3D for binary mixture Petrov extended the calculation for the zero-point contribution from the Bogoliubov modes for the 1D binary

QD. For the 1D case, the first-order correction due to the Bogoliubov modes vanishes, and the second-order energy correction survives as the next leading order term, which happens to be attractive in nature. Following the Petrov calculation the energy corresponding to one-dimensional QDs can be written as [28]

$$E_{1D} = \frac{\left(g_{\uparrow\uparrow}^{1/2} n_\uparrow - g_{\downarrow\downarrow}^{1/2} n_\downarrow\right)^2}{2} + \frac{g\delta g \left(g_{\downarrow\downarrow}^{1/2} n_\uparrow + g_{\uparrow\uparrow}^{1/2} n_\downarrow\right)^2}{\left(g_{\uparrow\uparrow} + g_{\downarrow\downarrow}\right)^2} - \frac{2}{3\pi}\left(g_{\uparrow\uparrow} n_\uparrow + g_{\downarrow\downarrow} n_\uparrow\right)^{3/2}, \quad (1.51)$$

where, the interaction parameter $g = \sqrt{g_{\uparrow\uparrow} g_{\downarrow\downarrow}}$ and the effective mean field interaction is $\delta g = g_{\uparrow\downarrow} + \sqrt{g_{\uparrow\uparrow} g_{\downarrow\downarrow}}$. For the symmetric interaction ($g_{\uparrow\uparrow} = g_{\downarrow\downarrow} = g$) if one considers the $n_\uparrow = n_\downarrow = n$ the energy in the above equation becomes

$$E_{1D} = \delta g n^2 - \frac{4\sqrt{2}}{3\pi} g^{3/2} n^{3/2}. \quad (1.52)$$

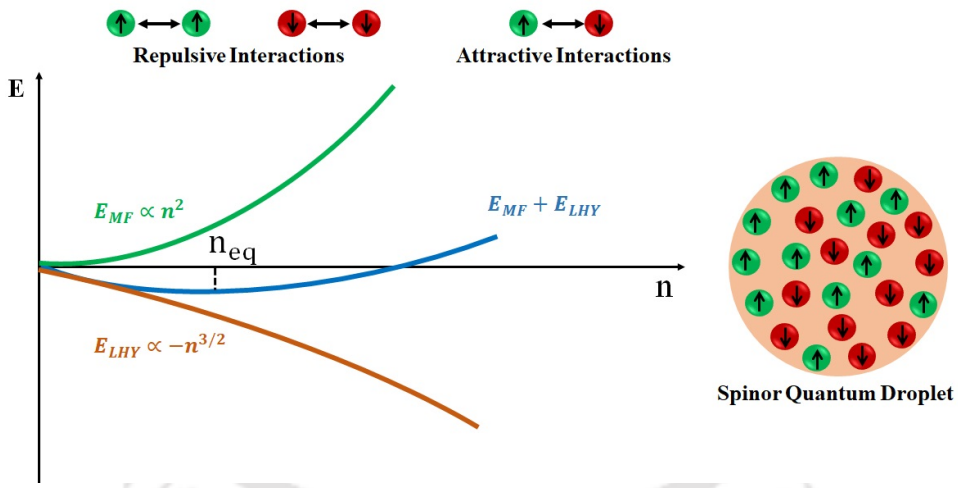

Figure 1.6: A schematic diagram depicting the variation of the E_{LHY} and E_{MF} with the density (in the left panel) and bound state of spinor QD (right panel) in one dimension.

For the symmetric case we find that $E_{LHY} \propto -n^{3/2}$ and $E_{MF} \propto n^2$. In a similar line, as shown for a 3D droplet in Fig. 1.6, we schematically show the variation of the E_{LHY} and E_{MF} as a function of density. For n_{eq} one can expect the formation of the droplet for 1D. In the thesis, we have mainly focused over the more generalized 1D droplet, which includes both symmetric and asymmetric cases for the droplet with SO and Rabi couplings.

So far the energy correction term has been obtained for the binary mixture of the droplet. However, the energy for synthetically SO coupling (with parameter k_L) and Rabi

(denoted with the parameter Ω) coupled QDs can be written in the following form [33]

$$\begin{aligned} E_{1D} &= \frac{\left(g_{\uparrow\uparrow}^{1/2}n_\uparrow - g_{\downarrow\downarrow}^{1/2}n_\downarrow\right)^2}{2} + \frac{g\delta g\left(g_{\downarrow\downarrow}^{1/2}n_\uparrow + g_{\uparrow\uparrow}^{1/2}n_\downarrow\right)^2}{(g_{\uparrow\uparrow}+g_{\downarrow\downarrow})^2} - \frac{2}{3\pi}\left(g_{\uparrow\uparrow}n_\uparrow + g_{\downarrow\downarrow}n_\uparrow\right)^{3/2} \\ &- ik_L\left[\psi_\uparrow^*\partial_x\psi_\uparrow - \psi_\downarrow^*\partial_x\psi_\downarrow\right] + \Omega\left[\psi_\uparrow^*\psi_\downarrow + \psi_\downarrow^*\psi_\uparrow\right]. \end{aligned} \tag{1.53}$$

Using Eq. (1.53) one can obtain dimensionless coupled eGPEs for the SO coupled QDs in one dimension which is given by [33]

$$\begin{aligned} \mathrm{i}\partial_t\psi_\uparrow = &\Bigg[-\frac{1}{2}\partial_x^2 - \mathrm{i}k_L\partial_x + g_{\uparrow\uparrow}|\psi_\uparrow|^2 - \sqrt{g_{\uparrow\uparrow}g_{\downarrow\downarrow}}|\psi_\downarrow|^2 + \frac{2\sqrt{g_{\uparrow\uparrow}g_{\downarrow\downarrow}}\delta g}{(g_{\uparrow\uparrow}+g_{\downarrow\downarrow})^2}\left(g_{\downarrow\downarrow}|\psi_\uparrow|^2 + \sqrt{g_{\uparrow\uparrow}g_{\downarrow\downarrow}}|\psi_\downarrow|^2\right) \\ &- \frac{g_{\uparrow\uparrow}}{\pi}\sqrt{g_{\uparrow\uparrow}|\psi_\uparrow|^2 + g_{\downarrow\downarrow}|\psi_\downarrow|^2}\Bigg]\psi_\uparrow + \Omega\psi_\downarrow, \end{aligned} \tag{1.54a}$$

$$\begin{aligned} \mathrm{i}\partial_t\psi_\downarrow = &\Bigg[-\frac{1}{2}\partial_x^2 + \mathrm{i}k_L\partial_x + g_{\downarrow\downarrow}|\psi_\downarrow|^2 - \sqrt{g_{\uparrow\uparrow}g_{\downarrow\downarrow}}|\psi_\uparrow|^2 + \frac{2\sqrt{g_{\uparrow\uparrow}g_{\downarrow\downarrow}}\delta g}{(g_{\uparrow\uparrow}+g_{\downarrow\downarrow})^2}\left(g_{\uparrow\uparrow}|\psi_\downarrow|^2 + \sqrt{g_{\uparrow\uparrow}g_{\downarrow\downarrow}}|\psi_\uparrow|^2\right) \\ &- \frac{g_{\downarrow\downarrow}}{\pi}\sqrt{g_{\uparrow\uparrow}|\psi_\uparrow|^2 + g_{\downarrow\downarrow}|\psi_\downarrow|^2}\Bigg]\psi_\downarrow + \Omega\psi_\uparrow. \end{aligned} \tag{1.54b}$$

where, $\psi_\uparrow$ and $\psi_\downarrow$ denote the 1D spin wave function and $\delta g = g_{\uparrow\downarrow} + \sqrt{g_{\uparrow\uparrow}g_{\downarrow\downarrow}}$ is the effective mean-field interaction parameter [28]. We have used the characteristic energy scale as $\hbar\omega_\perp$, where $\omega_\perp$ is the transverse trap frequency, time, and length respectively as $\omega_\perp^{-1}$ and $a_\perp = \sqrt{\hbar/(m\omega_\perp)}$ to obtain the above set of dynamical equations (Eqs. 1.54). Here the intracomponent interaction strengths $g_{\uparrow\uparrow} = 2N_\uparrow a_{\uparrow\uparrow}/a_\perp$ and $g_{\downarrow\downarrow} = 2N_\downarrow a_{\downarrow\downarrow}/a_\perp$, while the intercomponent one is $g_{\uparrow\downarrow} = 2N_\uparrow a_{\uparrow\downarrow}/a_\perp$ with $N_{\uparrow,\downarrow}$ being the particle number in each component.

Throughout the thesis work, we have used this equation under different constraints. For instance in Chapter 3 we have considered $\delta g = 0$ along with symmetric interaction condition. However, Chapters 4 and 5 are based on symmetric interaction with finite δg. Finally, in Chapter 6, we have considered the asymmetric interaction condition to analyze the behaviour of population imbalanced droplet.

1.5 State of the art research in quantum droplets

Formation of the QD in BECs, which appears in the form of small clusters of atoms bound together owing to the balance between the attractive and repulsive forces, has given a great boost to the field of ultracold gases in recent years. In a binary mixture of the condensate,

the QD manifests in a spherical shape due to the competition between the effective short-range attractive interaction between the atoms and the repulsive interaction arising solely due to quantum fluctuation or BMF, which is also responsible for its stabilization of the condensate [58]. Readers are referred to the previous section to get more concrete theoretical formalism related to the MF and BMF contribution to realize the droplet.

Despite being a relatively new field, the literature on QDs is quite vast, encompassing a wide range of experimental, numerical, and theoretical studies. In this section, we will briefly overview the current state of research on QDs, highlighting key findings and advancements. Following this overview, we will outline the motivation and objectives of our thesis, focusing on the structure and dynamics of SO coupled QDs. This exploration aims to deepen our understanding of the interplay between SO coupling and the unique properties of droplets, paving the way for potential applications in quantum technologies.

In the seminal theoretical work in 2015, Petrov analytically derived the condition for the stabilization of the collapsing attractive binary BECs [14]. He proposed that the phase is primarily stabilized by quantum fluctuations, which he calculated by considering the contributions of Bogoliubov modes to the zero-point energy of the condensate. BMF terms were corroborated first time in experiments with homogeneous and single component Bose gas of ^{85}Rb [59] and ^{7}Li [60], and recently in binary ^{39}K [61]. The first experimental observation of QDs was achieved using dipolar dysprosium (^{164}Dy) condensates, where the attractive long-range dipolar interaction was compensated by the repulsive short-range interaction arising due to both MF and BMF interaction. Overall, as a result of the anisotropic nature of the dipolar interaction, the droplet was of elongated shape [19, 20, 21]. Following up the experiment on dipolar dysprosium, a similar mechanism for the droplet formation was also reported in the erbium (^{166}Er) condensates, which stabilization was thoroughly confirmed by the collective excitation measurement [22].

Following up the theoretical proposal of the formation of binary droplets many research groups successfully demonstrated the appearance of QDs in a variety of binary condensate systems. For instance, Cabrera *et al.* used Zemman hyperfine states of ^{39}K and showed the appearance of the droplet state when the effective mean-field interaction was tuned to be negative, and condensate was allowed to expand freely after removing the radial trap [15]. In a follow up work, Semeghini *et al.* demonstrated the formation of the droplet in the free space with binary hyperfine states of ^{39}K condensate. Subsequent experimental work in this direction analyzed the dynamics of QDs in a binary mixture by allowing the droplets to make a collision with each other [62]. It was shown that the nature of collision very much depends on the velocity of the droplets. For low velocity, the collision is inelastic in nature, while the collision is elastic for high velocity. The experimental analysis further

computed the critical velocity for the transition between the elastic and inelastic collision and showed that it has a strong dependence on the number of atoms in the condensate. In free space, homonuclear droplets have only a few milliseconds of short lifetimes due to the three-body losses. However, by mixing the two different atoms, stable, long-lived droplets could be achieved. D'Errico et al.[25] observed the formation of the QDs in a heteronuclear bosonic mixture of ^{41}K and ^{87}Rb. They found that the strongly attractive mixture remains self-bound into several tens of milliseconds (400 ms) in the free space. Similar structural and dynamical features were also observed in different types of other binary droplets, such as Bose-Fermi mixtures [63] and binary magnetic gases [27].

In 2016, Petrov conducted the theoretical calculation of the droplets in lower dimensions, mainly in 1D and 2D, and found that the BMF terms appear to be dimension dependent. While the BMF term is repulsive with a logarithmic nature in 2D, the nature of BMF in 1D is attractive. In particular, the QDs are formed in 1D as a result of repulsive MF interaction which is proportional to (n), and the attractive BMF interaction proportional to $-n^{1/2}$ [28]. This proposal triggered a lot of interest among the ultracold community to understand the detailed structure, stability, and experimental exploration of the droplet in a lower dimension. In general, the QDs were reported in the three dimensions, however, there are some theoretical works which demonstrated that the droplets in 1D have lower equilibrium density than that of 3D droplets. This particular feature suggested to have a higher lifetime for the droplet in the lower dimension [29]. The lifetime of the droplets increases in the lower dimensions because of enhancement higher loss of the atoms due to three-body loss in the case of 3D to those in lower dimension [31]. These series of works generated a great enthusiasm among the researchers in the ultracold community to realize the 1D QDs in the experiment. In 2018 Cheiney *et al.* [23] used the strong transverse trap to generate the quasi 1D droplet which has a bright solitonic nature for the lower number of atoms and flat-top droplet nature for the higher number of atoms which density does not change upon increasing the number of atoms beyond a threshold value.

Following the seminal theoretical and experimental work on the droplets, many numerical investigations have been performed using the extended Gross-Pitaevskii MF model. Many of the work has been restricted to the effective one-component model where the density for both the binary components has been considered to be the same. For instance, Astrakharchik and Malomed [32] numerically investigated the structure and dynamics of QDs in one-dimension droplets and reported the transition from the Gaussian to the flat-top like structure of the droplet upon increase in the number of atoms. They considered the collisional dynamics between the droplets and found that it is quasi-elastic in nature

for the Gaussian-like droplet while it is inelastic for the flat-top droplet. It was shown that the inelastic collisions are accompanied with the matter wave interference patterns. Pathak and Nath [64] developed an analytical model to understand the structure of the QDs trapped in the harmonic potential and showed the transition from soliton to droplet. Additionally, they analyzed the effect of the trap strength on the dynamics of the droplet, which suggested the presence of droplet fragmentation with strong trapping potential.

However, there are other leagues of work that considered the binary droplet and have considered the impact of the effective mean-field interaction as well as the variation of the number of particles on the structure and dynamics of the binary droplet. For instance, Mistakidis *et al.* [65] numerically investigated the effect of LHY correction due to interspecies correlation for the one-dimensional QD's ground state and quenching dynamics. For the symmetric case, the ground state of droplets, upon increasing interspecies interaction, gradually changes from flat-top to localized Gaussian state. A flat-top ground state is found either for large particle numbers or small interspecies interactions. Further, they investigated the quenching dynamics of the QD by instantaneously changing the interspecies interaction that leads to the expansion of the Gaussian droplet state, which finally acquired the flat-top droplet state as the interaction strength is lowered from the initial value. Upon increasing the interaction strength, the interspecies interaction becomes more attractive after the quenching and mixture approaches to the MF balanced state and exhibits breather-like oscillation. There are some works that analyze the modulational instabilities involved in the binary mixture. For instance, Mithun et al. [66] explored the formation stability of the symmetric and asymmetric two-component one-dimensional droplet. Using the linear stability analysis, they reported that the plane wave with LHY term exhibits modulational instability for either a small number of atoms or a small effective mean-field interaction. On the other hand, there are some studies that show the formation of the droplet from the first principle simulation. For instance, Parisi and Giorgini [67] use the quantum Monte-Carlo simulation to analyze the structure and dynamics of the one-dimensional droplet using a generalized GPE. They investigated the finite-size effect by analyzing the energy per particle behavior of the droplet and calculated the surface energy as a function of the ratio of intraspecies and interspecies interaction strength.

The work discussed above mainly considered the equal population among the droplet components. However, in the binary droplet experiment the population of the component can be tuned either considering the Hetronuclear mixture [25] or varying the intraspecies interaction strengths [15]. Following this, there are several numerical works that have been undertaken for the imbalanced droplets. For instance, Englezos et al. [68] investigated

the ground state and dynamics of one-dimensional imbalanced droplets by introducing the unequal intraspecies interactions and found that component with higher intraspecies interaction exhibits flat-top nature, while other component exhibit the Gaussian profile. This led to the different structure of the components of the droplet. In a similar line, Flynn et al. [69] used different particle constraints on the component to create the imbalance and reported the effect of harmonic trap potential on the imbalanced droplets. For small trap strength, the flat-top state remains unaltered, while for large trap strength, the droplet state makes a transition to the trapped gas state.

Most of the numerical works described above, we find that they have mainly focused on the effective one-component droplet structure and their dynamics by considering the symmetric nature of the binary BECs. This assumption imposes the limitation on studying the dynamics of individual components of the QDs. However, in the experiment, the intercoupling between the components plays a very important role. Motivated by this we have chosen the SO and Rabi coupled spin-1/2 binary QDs for my thesis work. This particular model provides us great freedom to investigate the interwinding structure and dynamics of the binary droplets in a much more detailed way and allows us to obtain a large variety of interesting phenomena that have not been detected in the effective one-component binary mixture.

There is a handful of work that has been attempted in SO coupled droplets. E. Chiquillo [70] analytically calculated the quantum correction to the ground state energy for a one- and two-dimensional Rabi coupled binary mixture of BECs and theoretically proposed the formation and stability of the Rabi coupled QDs. He derived conditions for QD formation based on Rabi coupling and interaction strength and found that, in both one- and two-dimensional cases, there is a critical Rabi frequency above which the droplet becomes unstable. Following Petrov's work [14, 28] on the binary droplet, Tononi et al. [33] derived the dynamical equation corresponding to the SO coupled QD and numerically investigated the structure and dynamics of the droplet for the vanishingly small MF interaction strength. They reported the transition from the bright soliton to the stripe phase of the droplet. However, several questions like dynamical stability, the detailed effect of the different sorts of perturbations, and their impact on the structure and dynamics were not studied with the same rigor as it was available for the binary droplet in the literature. Therefore, we have chosen this particular model for our thesis work and have unraveled different facets of the structure and dynamics through our studies. We hope that our studies performed in the present thesis will be quite useful feedback for the future experiments in the field of droplets.

1.6 Layout of the thesis

The layout of the subsequent chapters is as follows.

In **Chapter 2**, we illustrate the details of the numerical algorithm implemented to solve the dynamical equation (eGPE) corresponding to SO coupled QDs. We outline the details of the split-step Crank-Nicolson scheme, which is used to solve the time dependent eGPE in the presence of SO and Rabi coupling. We have described the imaginary and real time propagation schemes which have been used respectively to obtain the ground state and analyze the dynamics of the condensate. We have also provided a brief outline of different perturbation schemes, such as velocity perturbation, quenching of the interaction, and coupling parameters, which are utilized to generate the dynamics. We also present an example to obtain a good converged ground state.

In **Chapter 3**, as a part of the first problem, we have analyzed the shape of the droplet in the absence of the MF contribution, which we achieve by considering equal and opposite inter- and intra-species interactions. As a result of that a localized self-bound solitonic state was obtained. We analytically derive the exact shape and size of the quantum soliton in the presence of SO coupling. Following this, we have explored several dynamical aspects of the quantum soliton, which have been obtained by several perturbations such as velocity perturbation, quenching the SO and Rabi coupling parameter, and collision of spin-component soliton by providing equal and opposite velocity.

In **Chapter 4**, As a second part of the problem, we have considered the effect of the effective mean-field interaction along with the BMF term on the structure and dynamics of the droplet. Here, in particular, we have investigated different aspects of droplet stability in the presence of effective mean-field interaction and how they are different than those observed without MF interaction.

In the previous two chapters, we fixed the atom numbers; however, in **Chapter 5**, we consider the interplay of effective mean-field interaction and a large number of condensate atoms on the structure and quench dynamics of the droplet. For the first time, we have developed an analytical framework using Bogoliubov-de-Gennes theory to determine the dynamical stability of the different phases of the droplet in the presence of SO and Rabi coupling.

In **Chapter 6**, as a part of the final problem of the thesis, we have extended our analysis for the imbalanced QDs and analyzed the effect of the extent of the imbalance on the structure and dynamics of the droplet. We have explicitly shown that adjusting the interaction imbalance alters the droplet shape from a flat-top to a Gaussian structure. Similarly, increasing the Rabi coupling induces comparable structural changes. We

identify the threshold interaction value where these shape transitions occur by analyzing changes in kinetic energy. Our study reveals how population exchange among spin components of the droplet is influenced by changes in Rabi or SO coupling. Further, we provide a detailed analysis of how trapping affects imbalanced droplets. Our findings indicate that increasing particle numbers can transition the system from a bound state to a trapped gas many-body state.

In **Chapter 7**, we provide a brief summary and conclusion of our thesis work which is based on the structure and dynamics of the SO coupled QDs. We also present an outline of future extensions of the work performed in the thesis.

Chapter 2

Numerical simulation of the extended Gross-Pitaevskii equation of spin-orbit coupled quantum droplets

In this Chapter, we provide the details of the numerical scheme used to solve the extended MF dynamical equations of the SO coupled QDs presented in the thesis work. Several numerical techniques are available in the literature to solve the ground state structure and dynamics of the BECs. However, we have mainly utilized the split-step Crank-Nicolson method to solve the eGPE pertaining to the SO and linear Rabi coupled QDs. The plan of the Chapter is as follows. First, we discuss the split-step Cranck-Nicolson scheme that we have used to get the numerical solution of the time-dependent eGPE of SO and Rabi coupled QDs. Following this, we discuss the imaginary and real-time propagation schemes which we have used to get the ground state and analyze the dynamical behaviour of QDs, respectively. Further, we present the convergence of the ground state for different spatial and temporal step sizes. Finally, we provide a detailed overview of the different protocols that have been used to generate the dynamics in the QDs.

2.1 Split-step Crank-Nicolson scheme

In this section, we present the numerical scheme that has been used to solve the eGPE of SO coupled QDs considered in the thesis work. The corresponding eGPE is given in the introduction Chapter. However, to make the Chapter self-contained, here we provide the

generalized eGPEs and further illustrate a systematic procedure involved in solving the time-dependent eGPEs. We also provide the details of the imaginary-time scheme used to obtain the ground state and the real-time propagation scheme used to investigate the dynamics of the droplet.

The time-dependent eGPEs in the dimensionless form (see Eqs. 1.54 in Chapter 1 for a detailed description) is given by the following set of equations:

$$\begin{aligned}\mathrm{i}\partial_t\psi_\uparrow = \Bigg[&-\frac{1}{2}\partial_x^2 - \mathrm{i}k_L\partial_x + g_{\uparrow\uparrow}|\psi_\uparrow|^2 - \sqrt{g_{\uparrow\uparrow}g_{\downarrow\downarrow}}|\psi_\downarrow|^2 \\ &+ \frac{2\sqrt{g_{\uparrow\uparrow}g_{\downarrow\downarrow}}\delta g}{(g_{\uparrow\uparrow}+g_{\downarrow\downarrow})^2}\left(g_{\downarrow\downarrow}|\psi_\uparrow|^2 + \sqrt{g_{\uparrow\uparrow}g_{\downarrow\downarrow}}|\psi_\downarrow|^2\right) - \frac{g_{\uparrow\uparrow}}{\pi}\sqrt{g_{\uparrow\uparrow}|\psi_\uparrow|^2 + g_{\downarrow\downarrow}|\psi_\downarrow|^2}\Bigg]\psi_\uparrow + \Omega\psi_\downarrow,\end{aligned} \tag{2.1a}$$

$$\begin{aligned}\mathrm{i}\partial_t\psi_\downarrow = \Bigg[&-\frac{1}{2}\partial_x^2 + \mathrm{i}k_L\partial_x + g_{\downarrow\downarrow}|\psi_\downarrow|^2 - \sqrt{g_{\uparrow\uparrow}g_{\downarrow\downarrow}}|\psi_\uparrow|^2 \\ &+ \frac{2\sqrt{g_{\uparrow\uparrow}g_{\downarrow\downarrow}}\delta g}{(g_{\uparrow\uparrow}+g_{\downarrow\downarrow})^2}\left(g_{\uparrow\uparrow}|\psi_\downarrow|^2 + \sqrt{g_{\uparrow\uparrow}g_{\downarrow\downarrow}}|\psi_\uparrow|^2\right) - \frac{g_{\downarrow\downarrow}}{\pi}\sqrt{g_{\uparrow\uparrow}|\psi_\uparrow|^2 + g_{\downarrow\downarrow}|\psi_\downarrow|^2}\Bigg]\psi_\downarrow + \Omega\psi_\uparrow.\end{aligned} \tag{2.1b}$$

We solve the above set of equations using the split-step Crank-Nicolson scheme in which the Hamiltonian corresponding to the GPE is split into two parts, namely, non-derivative and derivative parts. Firstly, we spatially discretize the non-derivative part, and following this, we obtain an intermediate solution with an initial trial condensate wavefunction function, which is generally Gaussian in nature. Then, the intermediate solution is considered as as an input wave function to obtain the final state wave function using the derivative part of the Hamiltonian. The derivative part of the eGPEs is integrated using the semi-implicit Crank-Nicolson method same as adopted in the references [71, 72, 73, 74]. The time integration is continued until the final converged solution has been attained. The main advantage of using split-step Crank-Nicolson is that, the non-derivative terms are treated alone and are not being mingled with the derivative part. This particular feature of the method helps to acquire an accurate and stable converged solution even with high nonlinearity. The other advantage lying in the fact that the normalization of the wave-function remains nicely conserved throughout all the iterations. In another aspect, the error involved in splitting the equations is of the order of Δ^2 where Δ represents the time resolution [71].

Under the Crank-Nicolson scheme, first, the equation (2.1) is written as a combination

of the derivative and non-derivative part in the form given below

$$\mathrm{i}\frac{\partial \Psi}{\partial t} = \left[H_{deriv} + H_{nonderiv}\right]\Psi, \tag{2.2}$$

where, H_{deriv} and $H_{nonderiv}$ represent the derivative and non-derivative part of the Hamiltonian operator respectively and $\Psi \equiv (\psi_\uparrow, \psi_\downarrow)^T$ with T is the transposition.

As a result of this, non-derivative and derivative parts of the Eq. (2.1a) can be written in the more explicit form respectively as given below:

$$\mathrm{i}\frac{\partial \psi_\uparrow}{\partial t} = \Bigg[g_{\uparrow\uparrow}|\psi_\uparrow|^2 - \sqrt{g_{\uparrow\uparrow}g_{\downarrow\downarrow}}|\psi_\downarrow|^2 + \frac{2\sqrt{g_{\uparrow\uparrow}g_{\downarrow\downarrow}}\delta g}{(g_{\uparrow\uparrow}+g_{\downarrow\downarrow})^2}\left(g_{\downarrow\downarrow}|\psi_\uparrow|^2 + \sqrt{g_{\uparrow\uparrow}g_{\downarrow\downarrow}}|\psi_\downarrow|^2\right) - \frac{g_{\uparrow\uparrow}}{\pi}\sqrt{g_{\uparrow\uparrow}|\psi_\uparrow|^2 + g_{\downarrow\downarrow}|\psi_\downarrow|^2}\Bigg]\psi_\uparrow + \Omega\psi_\downarrow \equiv H_{\uparrow A1}\psi_\uparrow + H_{\uparrow A2}\psi_\downarrow, \tag{2.3a}$$

$$\mathrm{i}\frac{\partial \psi_\uparrow}{\partial t} = -\frac{1}{2}\frac{\partial^2 \psi_\uparrow}{\partial x^2} - \mathrm{i}k_L\frac{\partial \psi_\uparrow}{\partial x} \equiv H_{\uparrow B}\psi_\uparrow, \tag{2.3b}$$

where different Hamiltonian terms are given by

$$H_{\uparrow A1} = \Bigg[g_{\uparrow\uparrow}|\psi_\uparrow|^2 - \sqrt{g_{\uparrow\uparrow}g_{\downarrow\downarrow}}|\psi_\downarrow|^2 + \frac{2\sqrt{g_{\uparrow\uparrow}g_{\downarrow\downarrow}}\delta g}{(g_{\uparrow\uparrow}+g_{\downarrow\downarrow})^2}\left(g_{\downarrow\downarrow}|\psi_\uparrow|^2 + \sqrt{g_{\uparrow\uparrow}g_{\downarrow\downarrow}}|\psi_\downarrow|^2\right) - \frac{g_{\uparrow\uparrow}}{\pi}\sqrt{g_{\uparrow\uparrow}|\psi_\uparrow|^2 + g_{\downarrow\downarrow}|\psi_\downarrow|^2}\Bigg], \tag{2.4a}$$

$$H_{\uparrow A2} = \Omega, \tag{2.4b}$$

$$H_{\uparrow B} = -\frac{1}{2}\frac{\partial^2}{\partial x^2} - \mathrm{i}k_L\frac{\partial}{\partial x}. \tag{2.4c}$$

In a similar line, the Eq. (2.1b) can be expressed in the non-derivative and derivative form of the Hamiltonian respectively, as given below:

$$\mathrm{i}\frac{\partial \psi_\downarrow}{\partial t} = \Bigg[g_{\downarrow\downarrow}|\psi_\downarrow|^2 - \sqrt{g_{\uparrow\uparrow}g_{\downarrow\downarrow}}|\psi_\uparrow|^2 + \frac{2\sqrt{g_{\uparrow\uparrow}g_{\downarrow\downarrow}}\delta g}{(g_{\uparrow\uparrow}+g_{\downarrow\downarrow})^2}\left(g_{\uparrow\uparrow}|\psi_\downarrow|^2 + \sqrt{g_{\uparrow\uparrow}g_{\downarrow\downarrow}}|\psi_\uparrow|^2\right) - \frac{g_{\downarrow\downarrow}}{\pi}\sqrt{g_{\uparrow\uparrow}|\psi_\uparrow|^2 + g_{\downarrow\downarrow}|\psi_\downarrow|^2}\Bigg]\psi_\downarrow + \Omega\psi_\uparrow \equiv H_{\downarrow A1}\psi_\downarrow + H_{\downarrow A2}\psi_\uparrow, \tag{2.5a}$$

$$\mathrm{i}\frac{\partial \psi_\downarrow}{\partial t} = -\frac{1}{2}\frac{\partial^2 \psi_\downarrow}{\partial x^2} + \mathrm{i}k_L\frac{\partial}{\partial x}\psi_\downarrow \equiv H_{\downarrow B}\psi_\downarrow, \tag{2.5b}$$

where different Hamiltonian terms are given by

$$H_{\downarrow A1} = \Bigg[g_{\downarrow\downarrow}|\psi_\downarrow|^2 - \sqrt{g_{\uparrow\uparrow}g_{\downarrow\downarrow}}|\psi_\uparrow|^2 + \frac{2\sqrt{g_{\uparrow\uparrow}g_{\downarrow\downarrow}}\delta g}{(g_{\uparrow\uparrow}+g_{\downarrow\downarrow})^2}\left(g_{\uparrow\uparrow}|\psi_\downarrow|^2 + \sqrt{g_{\uparrow\uparrow}g_{\downarrow\downarrow}}|\psi_\uparrow|^2\right) - \frac{g_{\downarrow\downarrow}}{\pi}\sqrt{g_{\uparrow\uparrow}|\psi_\uparrow|^2 + g_{\downarrow\downarrow}|\psi_\downarrow|^2}\Bigg], \tag{2.6a}$$

$$H_{\downarrow A2} = \Omega, \tag{2.6b}$$

$$H_{\downarrow B} = -\frac{1}{2}\frac{\partial^2}{\partial x^2} + \mathrm{i}k_L\frac{\partial}{\partial x}. \tag{2.6c}$$

To perform the time evolution of the wave function, first, we discretize the time into N_t number of time steps with a constant interval of length Δ. At any time t_0 we advance the wave function in time using the non-derivative part of the Hamiltonian to get the intermediate solution of the wave function at $t_0 + \Delta$. Following this the intermediate solution is used as an initial condition to get the solution of the propagation of the wave function with respect to the derivative part of the Hamiltonian at $t_0 + \Delta$. Through this, we finally obtain the solution at $t_0 + \Delta$. After giving a brief methodology of the split-step Cranck-Nicolson scheme below, we provide the description of the real-time propagation and imaginary-time propagation schemes in a more systematic way, which has been used respectively to investigate the non-equilibrium dynamics and attain the ground state of the droplets in our thesis work.

2.1.1 Real-time propagation

To study the non-equilibrium dynamics of the SO coupled spinor BECs, we have used the real-time propagation scheme. In this section, we provide the detailed steps involved in getting the solution of time-dependent eGPEs using the real-time propagation method. In brief first we solve Eqs. (2.3a) and (2.5a) with a trial solutions $\psi_\uparrow(x, t_0)$ and $\psi_\downarrow(x, t_0)$, respectively, at time $t = t_0$ to attain an intermediate solution at $t = t_0 + \Delta$, where Δ is the time step. Then such intermediate solution is applied as raw initial input to solve (2.3b) and (2.5b) generating the final solutions at $t = t_0 + \Delta$ as $\psi_\uparrow(x, t_0 + \Delta)$ and $\psi_\downarrow(x, t_0 + \Delta)$, respectively. This process is repeated n times to get the final converged solution at time $t_{\text{final}} = t_0 + N_t\Delta$.

Let's consider at time t_n the up-component of the condensate $(\psi_\uparrow^n, \psi_\downarrow^n)$ advanced first over the time step Δ by solving the Eqs. (2.3a) and (2.5a) to produce an intermediate solution $(\psi_\uparrow^{n+1/2}, \psi_\downarrow^{n+1/2})$. As there are no spatial derivative terms in Eqs. (2.3a) and (2.5a), the advancement in the wave function has been performed for small Δ using the

expression given below

$$\mathrm{i}\frac{\partial}{\partial t}\Psi^{n+1/2} = \mathcal{O}_{nd}(\mathbf{S})\Psi^{n}, \tag{2.7}$$

with

$$\mathbf{S} = \begin{pmatrix} H_{\uparrow A1} & H_{\uparrow A2} \\ H_{\downarrow A2} & H_{\downarrow A1} \end{pmatrix}, \tag{2.8}$$

where $\Psi = (\psi_\uparrow, \psi_\downarrow)^T$, $\mathcal{O}_{nd}(\mathbf{S})$ denotes time-evolution operation with the matrix $\mathbf{S}$ which elements are given in the Eqs. (2.6) and subscript 'nd' has been used to denote the non-derivative part of the Hamiltonian.

Due to the presence of Rabi coupling, the solution of the Eq. (2.7) will no more be as explicit as given for the scalar BECs as given in [71]. Therefore, we use the following methodology to solve the equation. First let's rewrite the equations (2.3a) and (2.5a) as

$$\mathrm{i}\frac{\partial \psi_\uparrow}{\partial t} = a\psi_\uparrow, + b\psi_\downarrow, \quad \mathrm{i}\frac{\partial \psi_\downarrow}{\partial t} = c\psi_\uparrow + d\psi_\downarrow, \tag{2.9}$$

where

$$a = \left[g_{\uparrow\uparrow}|\psi_\uparrow|^2 - \sqrt{g_{\uparrow\uparrow}g_{\downarrow\downarrow}}|\psi_\downarrow|^2 + \frac{2\sqrt{g_{\uparrow\uparrow}g_{\downarrow\downarrow}}\delta g}{(g_{\uparrow\uparrow}+g_{\downarrow\downarrow})^2}\left(g_{\downarrow\downarrow}|\psi_\uparrow|^2 + \sqrt{g_{\uparrow\uparrow}g_{\downarrow\downarrow}}|\psi_\downarrow|^2\right) - \frac{g_{\uparrow\uparrow}}{\pi}\sqrt{g_{\uparrow\uparrow}|\psi_\uparrow|^2 + g_{\downarrow\downarrow}|\psi_\downarrow|^2}\right],$$

$$d = \left[g_{\downarrow\downarrow}|\psi_\downarrow|^2 - \sqrt{g_{\uparrow\uparrow}g_{\downarrow\downarrow}}|\psi_\uparrow|^2 + \frac{2\sqrt{g_{\uparrow\uparrow}g_{\downarrow\downarrow}}\delta g}{(g_{\uparrow\uparrow}+g_{\downarrow\downarrow})^2}\left(g_{\uparrow\uparrow}|\psi_\downarrow|^2 + \sqrt{g_{\uparrow\uparrow}g_{\downarrow\downarrow}}|\psi_\uparrow|^2\right) - \frac{g_{\downarrow\downarrow}}{\pi}\sqrt{g_{\uparrow\uparrow}|\psi_\uparrow|^2 + g_{\downarrow\downarrow}|\psi_\downarrow|^2}\right],$$

$$b = c = \Omega.$$

The formal solution for the above equations can be written in terms of the discretized variables as given below:

$$\begin{pmatrix} \psi_\uparrow^{n+1/2} \\ \psi_\downarrow^{n+1/2} \end{pmatrix} = \frac{1}{2R}\mathrm{e}^{-\frac{\mathrm{i}}{2}\Delta(R+S)} \begin{pmatrix} A_R & B_R \\ C_R & D_R \end{pmatrix} \begin{pmatrix} \psi_\uparrow^{n} \\ \psi_\downarrow^{n} \end{pmatrix}, \tag{2.11}$$

where $S = a + d$ and $T = a - d$, $A_R = R\left[1 + \mathrm{e}^{\mathrm{i}R\Delta}\right] + T\left[1 - \mathrm{e}^{\mathrm{i}R\Delta}\right]$, $B_R = 2b\left[1 - \mathrm{e}^{\mathrm{i}R\Delta}\right]$, $C_R = 2c\left[1 - \mathrm{e}^{\mathrm{i}R\Delta}\right]$, $D_R = R\left[1 + \mathrm{e}^{\mathrm{i}R\Delta}\right] - T\left[1 - \mathrm{e}^{\mathrm{i}R\Delta}\right]$ and $R = \sqrt{(a-d)^2 + 4bc}$.

Next, we execute the time propagation corresponding to the operators H_{jB} numerically by the semi-implicit Crank-Nicolson method

$$\frac{\psi_j^{n+1} - \psi_j^{n+1/2}}{-\mathrm{i}\Delta} = \frac{1}{2} H_{jB}\left(\psi_j^{n+1} + \psi_j^{n+1/2}\right). \tag{2.12}$$

The formal solution to (2.12) is

$$\psi_j^{n+1} = \mathcal{O}_{CN}(H_{jB})\psi_j^{n+1} \equiv \frac{1 - \mathrm{i}\Delta H_{jB}/2}{1 + \mathrm{i}\Delta H_{jB}/2}\psi_j^{n+1/2}, \tag{2.13}$$

which combine with equation (2.7) provides

$$\Psi^{n+1} = \mathcal{O}_{CN}(H_{jB})\mathcal{O}_{nd}(\mathbf{S})\Psi^n, \tag{2.14}$$

where $j = \uparrow, \downarrow$, $\mathcal{O}_{CN}$ represents the time-evolution operation with H_{jB} and suffix 'CN' indicates the Crank-Nicolson algorithm. Operation $\mathcal{O}_{CN}$ is used to propagate the intermediate solution $\psi_j^{n+1/2}$ by the time step Δ to generate the solution ψ_j^{n+1} at the next time step $t_{n+1} = (n+1)\Delta$.

The time propagation of the remaining equations (2.3b) and (2.5b) are performed numerically by the semi-implicit Crank-Nicolson scheme [75]. For example, the Crank-Nicolson scheme is employed by mapping the equations (2.3b) and (2.5b) onto one-dimensional spatial grid points in x. The discretization of equations (2.3b) and (2.5b) along the spatial grid point x is carried out as follows [75, 76, 77]:

$$\begin{aligned}\frac{\mathrm{i}\left(\psi_{\uparrow,k}^{n+1} - \psi_{\uparrow,k}^{n+1/2}\right)}{\Delta} =& \frac{-1}{4h^2}\left[\left(\psi_{\uparrow,k+1}^{n+1} - 2\psi_{\uparrow,k}^{n+1} + \psi_{\uparrow,k-1}^{n+1}\right) + \left(\psi_{\uparrow,k+1}^{n+1/2} - 2\psi_{\uparrow,k}^{n+1/2} + \psi_{\uparrow,k-1}^{n+1/2}\right)\right] \\ & - \frac{\mathrm{i}k_L}{4h}\left[\left(\psi_{\uparrow,k+1}^{n+1} - \psi_{\uparrow,k-1}^{n+1}\right) + \left(\psi_{\uparrow,k+1}^{n+1/2} - \psi_{\uparrow,k-1}^{n+1/2}\right)\right], \end{aligned} \tag{2.15}$$

$$\begin{aligned}\frac{\mathrm{i}\left(\psi_{\downarrow,k}^{n+1} - \psi_{\downarrow,k}^{n+1/2}\right)}{\Delta} =& \frac{-1}{4h^2}\left[\left(\psi_{\downarrow,k+1}^{n+1} - 2\psi_{\downarrow,k}^{n+1} + \psi_{\downarrow,k-1}^{n+1}\right) + \left(\psi_{\downarrow,k+1}^{n+1/2} - 2\psi_{\downarrow,k}^{n+1/2} + \psi_{\downarrow,k-1}^{n+1/2}\right)\right] \\ & + \frac{\mathrm{i}k_L}{4h}\left[\left(\psi_{\downarrow,k+1}^{n+1} - \psi_{\downarrow,k-1}^{n+1}\right) + \left(\psi_{\downarrow,k+1}^{n+1/2} - \psi_{\downarrow,k-1}^{n+1/2}\right)\right], \end{aligned} \tag{2.16}$$

and rewrite as

$$\psi_{\uparrow,k}^{n+1}-\psi_{\uparrow,k}^{n+1/2}=\frac{\mathrm{i}\Delta}{4h^2}\left[\left(\psi_{\uparrow,k+1}^{n+1}-2\psi_{\uparrow,k}^{n+1}+\psi_{\uparrow,k-1}^{n+1}\right)+\left(\psi_{\uparrow,k+1}^{n+1/2}-2\psi_{\uparrow,k}^{n+1/2}+\psi_{\uparrow,k-1}^{n+1/2}\right)\right] - \frac{k_L\Delta}{4h}\left[\left(\psi_{\uparrow,k+1}^{n+1}-\psi_{\uparrow,k-1}^{n+1}\right)+\left(\psi_{\uparrow,k+1}^{n+1/2}-\psi_{\uparrow,k-1}^{n+1/2}\right)\right], \tag{2.17}$$

$$\psi_{\downarrow,k}^{n+1}-\psi_{\downarrow,k}^{n+1/2}=\frac{\mathrm{i}\Delta}{4h^2}\left[\left(\psi_{\downarrow,k+1}^{n+1}-2\psi_{\downarrow,k}^{n+1}+\psi_{\downarrow,k-1}^{n+1}\right)+\left(\psi_{\downarrow,k+1}^{n+1/2}-2\psi_{\downarrow,k}^{n+1/2}+\psi_{\downarrow,k-1}^{n+1/2}\right)\right] + \frac{k_L\Delta}{4h}\left[\left(\psi_{\downarrow,k+1}^{n+1}-\psi_{\downarrow,k-1}^{n+1}\right)+\left(\psi_{\downarrow,k+1}^{n+1/2}-\psi_{\downarrow,k-1}^{n+1/2}\right)\right], \tag{2.18}$$

where $\psi_{\uparrow,k}^{n}\equiv\psi_{\uparrow}(x_k,t_n)$ and $\psi_{\downarrow,k}^{n}\equiv\psi_{\downarrow}(x_k,t_n)$ represent the up and down component of the condensate respectively at spatial point x_k and at time t_n. For the discretization along x, we choose $x_k=-N_xh/2+kh$, $k=0,1,2,\ldots,N_x$ where N_x is the total number of grids in the x-direction and h is the spatial step. The above equations are essentially a set of algebraic equations of $\psi_{\uparrow,k+1}^{n+1}$, $\psi_{\uparrow,k}^{n+1}$, $\psi_{\uparrow,k-1}^{n+1}$, $\psi_{\downarrow,k+1}^{n+1}$, $\psi_{\downarrow,k}^{n+1}$ and $\psi_{\downarrow,k-1}^{n+1}$ at time t_{n+1}, which are solved using the closed boundary conditions. The algebraic equations emerging from (2.17) are written explicitly as [75]

$$A_k^-\psi_{\uparrow,k-1}^{n+1}+A_k^0\psi_{\uparrow,k}^{n+1}+A_k^+\psi_{\uparrow,k+1}^{n+1}=b_k, \tag{2.19a}$$

$$D_k^-\psi_{\downarrow,k-1}^{n+1}+D_k^0\psi_{\downarrow,k}^{n+1}+D_k^+\psi_{\downarrow,k+1}^{n+1}=d_k, \tag{2.19b}$$

where $A_k^0=D_k^0=1+\mathrm{i}\Delta/(2h^2)$, $A_k^+=D_i^-=k_L\Delta/(4h)-\mathrm{i}\Delta/(4h^2)$, and $A_k^-=D_k^+=-k_L\Delta/(4h)-\mathrm{i}\Delta/(4h^2)$ and

$$b_k=\frac{\mathrm{i}\Delta}{4h^2}\left(\psi_{\uparrow,k+1}^{n+1/2}-2\psi_{\uparrow,k}^{n+1/2}+\psi_{\uparrow,k-1}^{n+1/2}\right)-\frac{k_L\Delta}{4h}\left(\psi_{\uparrow,k+1}^{n+1/2}-\psi_{\uparrow,k-1}^{n+1/2}\right)+\psi_{\uparrow,k}^{n+1/2}, \tag{2.20a}$$

$$d_k=\frac{\mathrm{i}\Delta}{4h^2}\left(\psi_{\downarrow,k+1}^{n+1/2}-2\psi_{\downarrow,k}^{n+1/2}+\psi_{\downarrow,k-1}^{n+1/2}\right)+\frac{k_L\Delta}{4h}\left(\psi_{\downarrow,k+1}^{n+1/2}-\psi_{\downarrow,k-1}^{n+1/2}\right)+\psi_{\downarrow,k}^{n+1/2}. \tag{2.20b}$$

All quantities in b_k and d_k are referred to the time step $t_{n+1/2}$ which are known from the evolution using the non-derivative part of the Hamiltonian. The unknowns in (2.19) are the quantities like $\psi_{\uparrow,k\pm1}^{n+1}$, $\psi_{\uparrow,k}^{n+1}$, $\psi_{\downarrow,k\pm1}^{n+1}$ and $\psi_{\downarrow,k}^{n+1}$ at time step t_{n+1} which can be obtained by term using the forward recursion relation given by

$$\psi_{j,k+1}^{n+1}=\alpha_{j,k}\psi_{j,k}^{n+1}+\beta_{j,k}, \tag{2.21}$$

where, $j\equiv\{\uparrow,\downarrow\}$, and $\alpha_{j,k}$, $\beta_{j,k}$ are the coefficients that needs to be calculated. Substi-

tuting equation (2.21) in the equation (2.19) yields the solution given by,

$$\psi_{\uparrow,k}^{n+1} = \gamma_{\uparrow,k}(A_k^- \psi_{\uparrow,k-1}^{n+1} + A_k^+ \beta_{\uparrow,k} - b_k), \tag{2.22a}$$
$$\psi_{\downarrow,k}^{n+1} = \gamma_{\downarrow,k}(D_k^- \psi_{\downarrow,k-1}^{n+1} + D_k^+ \beta_{\downarrow,k} - d_k), \tag{2.22b}$$

with

$$\gamma_{\uparrow,k-1} = -1/(A_k^0 + A_k^+ \alpha_{\uparrow,k}), \tag{2.23a}$$
$$\gamma_{\downarrow,k-1} = -1/(D_k^0 + D_k^+ \alpha_{\downarrow,k}), \tag{2.23b}$$

$$\alpha_{\uparrow,k-1} = \gamma_{\uparrow,k} A_k^-, \qquad \beta_{\uparrow,k-1} = \gamma_{\uparrow,k}(A_k^+ \beta_{\uparrow,k} - b_k) \tag{2.24a}$$
$$\alpha_{\downarrow,k-1} = \gamma_{\downarrow,k} A_k^-, \qquad \beta_{\downarrow,k-1} = \gamma_{\downarrow,k}(D_k^+ \beta_{\downarrow,k} - d_k) \tag{2.24b}$$

by using the recursion relations (2.22), (2.23) and (2.24) we obtain $\alpha_{j,k}$ and $\beta_{j,k}$, where k is starting from $N_x - 2$ to 0. The initial values of $\alpha_{N_x-1} = 0$, $\beta_{j,N_x-1} = \psi_{j,N_x}^{n+1}$. Once the values of $\alpha_{j,k}$, $\beta_{j,k}$ and $\gamma_{j,k}$ are calculated, we find the solution using the relation (2.21) for the entire space starting from 0 to $N_x - 1$ with the proper boundary conditions as described in [71]. To find the solution for the entire space range using the initial spatial grid point where the wave function is $\psi_0^{n+1} = 0$ known from the boundary conditions. Also, the value at the last lattice point is zero. For real-time propagation, the initial solution at $t = 0$ is generally picked from an analytically known solution of the harmonic potential with zero nonlinearity $\alpha = \beta = 0$. Over the time iteration, the nonlinearity is ramped with a slow rate until the final nonlinearity is attained.

2.1.2 Imaginary-time propagation

To obtain a stable and exact ground state solution, we consider the imaginary-time propagation method. Under this scheme, the time in the eGPEs is transformed into an imaginary one by making a transformation as $t \to -it$, where t represents the time. This particular transformation ensures that the state with energy other than the ground state decays faster than the ground state and thus helps to converge to the ground state in a better way.

Even though real-time propagation has many advantages, which are described above, however, this method deals with complex wavefunction for non-stationary properties. For stationary ground state solution, we have to solve the equations (2.1a) and (2.1b) using

imaginary-time propagation. The wavefunction is fundamentally real for the stationary ground state and the imaginary-time propagation method dealing with real variables seems to be convenient. Which can be done by making time as imaginary, that is, $t \to -\mathrm{i}t$. In this case, first, the equations (2.9) can be rewritten as

$$-\frac{\partial \psi_\uparrow}{\partial t} = a\psi_\uparrow + b\psi_\downarrow, \quad -\frac{\partial \psi_\downarrow}{\partial t} = c\psi_\uparrow + d\psi_\downarrow, \tag{2.25}$$

where

$$\begin{aligned}
a = &\left[g_{\uparrow\uparrow}|\psi_\uparrow|^2 - \sqrt{g_{\uparrow\uparrow}g_{\downarrow\downarrow}}|\psi_\downarrow|^2 + \frac{2\sqrt{g_{\uparrow\uparrow}g_{\downarrow\downarrow}}\delta g}{(g_{\uparrow\uparrow}+g_{\downarrow\downarrow})^2}\left(g_{\downarrow\downarrow}|\psi_\uparrow|^2 + \sqrt{g_{\uparrow\uparrow}g_{\downarrow\downarrow}}|\psi_\downarrow|^2\right)\right. \\
&\left. - \frac{g_{\uparrow\uparrow}}{\pi}\sqrt{g_{\uparrow\uparrow}|\psi_\uparrow|^2 + g_{\downarrow\downarrow}|\psi_\downarrow|^2}\right], \\
d = &\left[g_{\downarrow\downarrow}|\psi_\downarrow|^2 - \sqrt{g_{\uparrow\uparrow}g_{\downarrow\downarrow}}|\psi_\uparrow|^2 + \frac{2\sqrt{g_{\uparrow\uparrow}g_{\downarrow\downarrow}}\delta g}{(g_{\uparrow\uparrow}+g_{\downarrow\downarrow})^2}\left(g_{\uparrow\uparrow}|\psi_\downarrow|^2 + \sqrt{g_{\uparrow\uparrow}g_{\downarrow\downarrow}}|\psi_\uparrow|^2\right)\right. \\
&\left. - \frac{g_{\downarrow\downarrow}}{\pi}\sqrt{g_{\uparrow\uparrow}|\psi_\uparrow|^2 + g_{\downarrow\downarrow}|\psi_\downarrow|^2}\right], \\
b = &\, c = \Omega.
\end{aligned}$$

Now the formal solution for the above equations can be written as (in terms of the discretized variables):

$$\begin{pmatrix} \psi_\uparrow^{n+1/2} \\ \psi_\downarrow^{n+1/2} \end{pmatrix} = \frac{1}{2R}\mathrm{e}^{-\frac{1}{2}\Delta(R+S)} \begin{pmatrix} A_I & B_I \\ C_I & D_I \end{pmatrix} \begin{pmatrix} \psi_\uparrow^{n} \\ \psi_\downarrow^{n} \end{pmatrix}, \tag{2.27}$$

where $R = \sqrt{(a-d)^2 + 4bc}$, $S = a + d$, $T = a - d$, $A_I = R\left[1 + \mathrm{e}^{R\Delta}\right] + T\left[1 - \mathrm{e}^{R\Delta}\right]$, $B_I = 2b\left[1 - \mathrm{e}^{R\Delta}\right]$, $C_I = 2c\left[1 - \mathrm{e}^{R\Delta}\right]$ and $D_I = R\left[1 + \mathrm{e}^{R\Delta}\right] - T\left[1 - \mathrm{e}^{R\Delta}\right]$. Similarly, equations (2.3) and (2.5) can be written as

$$\begin{aligned}
-\frac{\partial \psi_\uparrow}{\partial t} = &\left[g_{\uparrow\uparrow}|\psi_\uparrow|^2 - \sqrt{g_{\uparrow\uparrow}g_{\downarrow\downarrow}}|\psi_\downarrow|^2 + \frac{2\sqrt{g_{\uparrow\uparrow}g_{\downarrow\downarrow}}\delta g}{(g_{\uparrow\uparrow}+g_{\downarrow\downarrow})^2}\left(g_{\downarrow\downarrow}|\psi_\uparrow|^2 + \sqrt{g_{\uparrow\uparrow}g_{\downarrow\downarrow}}|\psi_\downarrow|^2\right)\right. \\
&\left. - \frac{g_{\uparrow\uparrow}}{\pi}\sqrt{g_{\uparrow\uparrow}|\psi_\uparrow|^2 + g_{\downarrow\downarrow}|\psi_\downarrow|^2}\right]\psi_\uparrow + \Omega\psi_\downarrow, \qquad (2.28a) \\
-\frac{\partial \psi_\uparrow}{\partial t} = &-\frac{1}{2}\frac{\partial^2 \psi_\uparrow}{\partial x^2} - \mathrm{i}k_L\frac{\partial \psi_\uparrow}{\partial x}, \qquad (2.28b)
\end{aligned}$$

and

$$-\frac{\partial\psi_\downarrow}{\partial t} = \Bigg[g_{\downarrow\downarrow}|\psi_\downarrow|^2 - \sqrt{g_{\uparrow\uparrow}g_{\downarrow\downarrow}}|\psi_\uparrow|^2 + \frac{2\sqrt{g_{\uparrow\uparrow}g_{\downarrow\downarrow}}\delta g}{(g_{\uparrow\uparrow}+g_{\downarrow\downarrow})^2}\left(g_{\uparrow\uparrow}|\psi_\downarrow|^2 + \sqrt{g_{\uparrow\uparrow}g_{\downarrow\downarrow}}|\psi_\uparrow|^2\right) - \frac{g_{\downarrow\downarrow}}{\pi}\sqrt{g_{\uparrow\uparrow}|\psi_\uparrow|^2 + g_{\downarrow\downarrow}|\psi_\downarrow|^2}\Bigg]\psi_\downarrow + \Omega\psi_\uparrow, \tag{2.29a}$$

$$-\frac{\partial\psi_\downarrow}{\partial t} = -\frac{1}{2}\frac{\partial^2\psi_\downarrow}{\partial x^2} + \mathrm{i}k_L\frac{\partial}{\partial x}\psi_\downarrow, \tag{2.29b}$$

respectively. Subsequently, equations (2.28b) and (2.29b) can be discretized using the Crank-Nicolson method similar to real-time propagation. The dynamics of the condensate wavefunction can be studied with the help of the ground state solution of the GPE.

2.1.3 Convergence of ground state

After providing a detailed overview about the real-time and Imaginary-time propagation schemes which have been used to get the ground state and dynamics of the QDs, respectively, now we move our focus to give the rational behind choosing the spatial and temporal steps for simulation runs presented in the thesis work. In what follows we dis-

dx	dt	μ	$\langle x\rangle$
0.1	0.01	−1.4504046	35.365491
0.08	0.005	−1.4503599	35.104702
0.06	0.001	−1.4503242	34.897462
0.05	0.0005	−1.4503199	34.871657
0.04	0.0001	−1.4503164	34.851026
0.025	0.00001	−1.4503158	34.846399

Table 2.1: Demonstration of convergence of simulation runs for different dx and dt for plane wave (PW) phase of QD. The imaginary-time scheme has been used to obtain the droplet with parameters $N = 100, \Omega = 1, k_L = 0.5, g_\uparrow = g_\downarrow = 1, g_{\uparrow\downarrow} = -0.9, \delta g = 0.1$. The chemical potential (μ) and rms size of droplet ($\langle x\rangle$) show convergence upto four decimal places upon changing the $dx \lesssim 0.05$.

cuss the grid independence test for our simulation results. In our work, we obtain the two states, namely plane wave (PW) for $\Omega \gtrsim k_L^2$ and modulated stripe wave (SW) phase of the droplet for $\Omega \lesssim k_L^2$.

To this end, first, we consider the case for the PW phase for which consider the droplet parameters as $N = 100, \Omega = 1, k_L = 0.5, g_\uparrow = g_\downarrow = 1, g_{\uparrow\downarrow} = -0.9, \delta g = 0.1$. Using the Imaginary-time scheme, we obtain the ground state for different values of spatial steps (dx) and time steps (dt) as mentioned in Table 2.1. For all the simulation runs the

Courant-Friedrichs-Lewy (CFL) condition ($dt/dx^2 \lesssim 1$) has been followed.

We find that for $dx \lesssim 0.05$, the chemical potential μ and the root-mean-square (rms) size of the droplet ($\langle x \rangle$) does not change. Therefore, for all the simulation runs presented

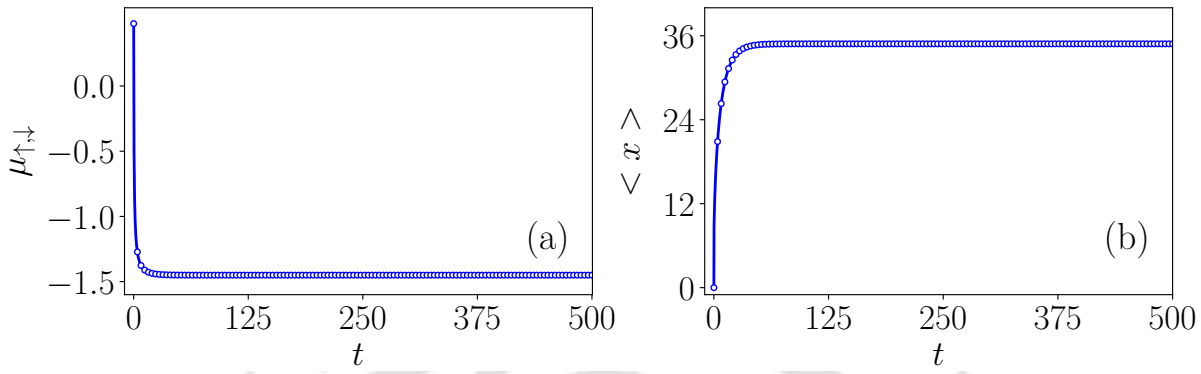

Figure 2.1: Imaginary-time propagation to obtain the ground state PW phase. (a) Temporal evolution of μ. (b) Temporal evolution of width of the condensate ($\langle x \rangle$) when the ground state is obtained using the imaginary time scheme. The parameters are the same as in Table 2.1.

in the thesis, we have chosen the optimum spatial step ($dx = 0.025$) and time step ($dt = 0.00001$) for the Imaginary as well as real-time propagation. In Fig. 2.1, we show the variation of the chemical potential of different components and rms size of the droplet with time for an imaginary-time propagation scheme. We find that $t \gtrsim 50$ both μ and $\langle x \rangle$ attain the steady state value, a signature of attaining the ground state for the droplet with parameters same as mentioned in Table 2.1. To test the stability of the ground

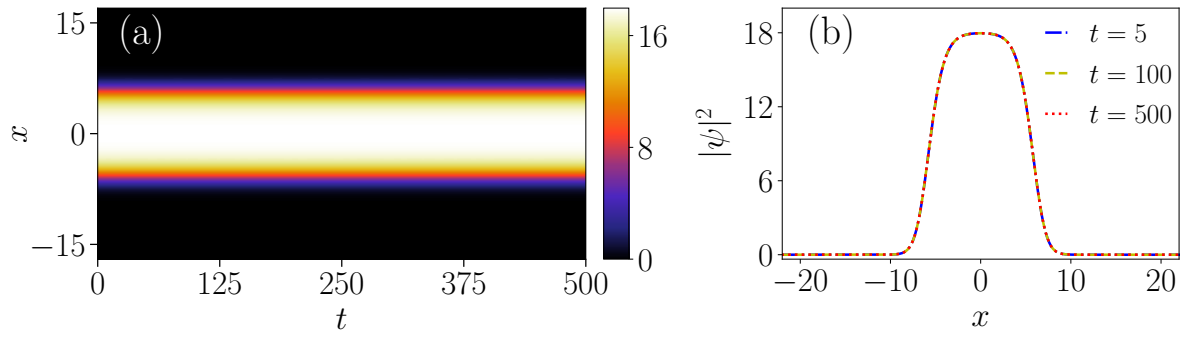

Figure 2.2: Stability check for the ground state of PW phase using real-time propagation scheme. (a) Pseudo color profile of the stationary state of the condensate during real-time propagation. (b) Profile of the condensate at different instants of time. No change in the profile of the condensate with the real-time propagation indicates the true stationary state behaviour of the condensate obtained using the imaginary-time scheme.

state solution, we consider the ground state obtained in Fig. 2.1 as an initial condition and evolve the state using the real-time propagation scheme. In Fig. 2.2(a), we show the evolution of the PW phase of the droplet using the real-time propagation scheme. In

Fig. 2.2(b), we show the profile for the different instants of time. Overall, we find that the droplet shape and size remain unaltered with time, confirming the good preparation of stationary ground state using our simulation. A similar feature of good convergence has been obtained for the stripe phase of the droplet.

2.1.4 Non-equilibrium dynamics of the spin-orbit coupled quantum droplets

In this section, we discuss different methodologies that have been adopted to analyze the dynamics of the SO coupled QDs. To generate the dynamics, we have adopted three protocols, which have been schematically depicted in Fig. 2.3. The main protocols are described below.

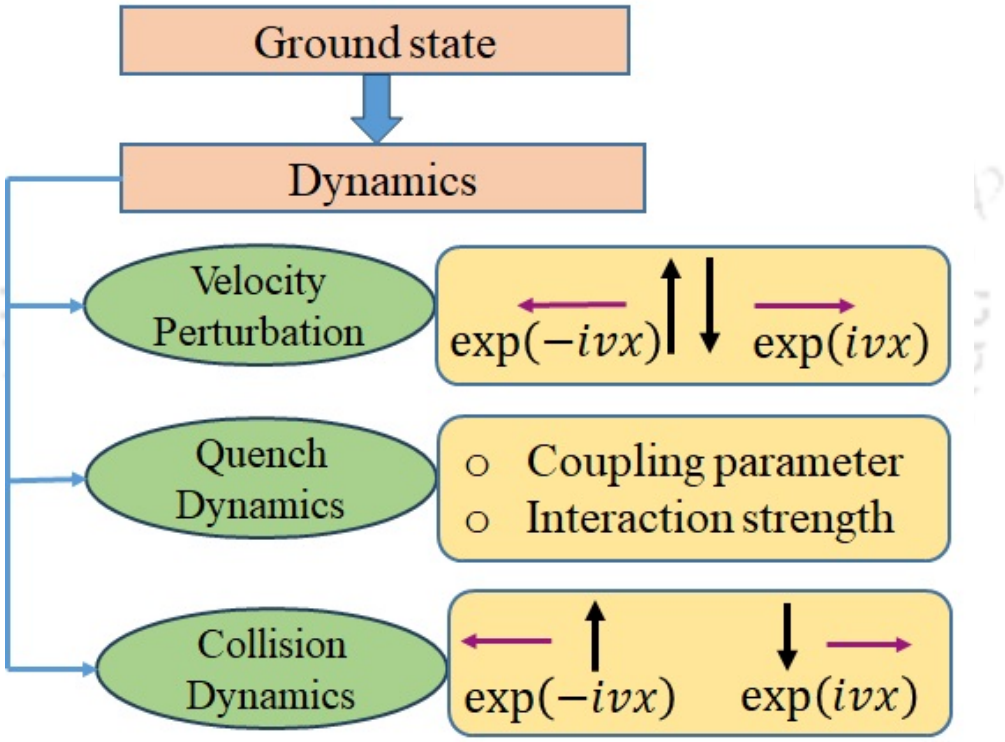

Figure 2.3: Schematic diagram for the different protocols adopted for generating the dynamics in the ground state of the condensate. These protocols are namely, (i) the velocity perturbation in which the spin-up component is supplied with the negative velocity while the spin-down component is given the positive velocity. This is achieved by uniformly changing the phase of the ground state wave function. (ii) quench dynamics, which has been achieved by instantaneously quenching either the interaction parameters, Rabi coupling, or SO coupling of the condensate ground state. (iii) The collision dynamics in which the spin-up and spin-down of the ground state are separated, and then given equal and opposite velocity.

1. First, we supply equal and opposite velocity to both the components by instantly

changing the phase of the condensate. Note that in the experiment the differential velocity to the components could be provided using the phase-imprinting technique [33, 78]. The result condensate wavefunction is $\psi_{\uparrow g} = \psi_{\uparrow g} e^{-ivx}$ and $\psi_{\downarrow g} = \psi_{\downarrow g} e^{ivx}$. Instant velocity perturbation excites the different modes of the condensate, leading to the display of many interesting feathers, like breathing oscillation at low velocity and the appearance of moving droplets at high velocity.

2. The second protocol involves instantaneous quenching of either the quenching SO and Rabi coupling or effective mean-field interaction. Under this protocol, we consider the ground state and change the coupling parameter in the next step of the simulation as the time step 10^{-5}, which corresponds to 10 nanoseconds in the real time. Note that if we change the rate of quench, the results remain unchanged.

3. Another third we generate the miscible ground state of the binary condensate. Following this, we separate the spin-up and spin-down components and keep them apart with a finite separation. Then, we supply equal and opposite velocity to the components and allow them to evolve during real-time propagation, which finally leads to the collision.

2.2 Summary and Conclusion

In this chapter, we have presented the numerical algorithm employed to solve the dimensionless one-dimensional SO and Rabi coupled eGPEs. We have given a brief overview of the detailed steps pertaining to the spit-step Crank-Nicolson method, which is used to obtain the ground state using the imaginary-time propagation scheme and dynamics using the real-time propagation scheme. We have given a collaborative overview to obtain a good converged ground state for different phases of the QDs. Finally, we give a brief sketch of the different protocols used to get the dynamics of the QDs presented in the thesis work.

Chapter 3

Quantum droplets with vanishingly small mean-field interaction

In this Chapter, we begin by considering the effective mean field term in the eGPEs to be zero. This particular feature allows us to investigate the effect of the BMF term on the structure and dynamics of SO coupled QDs [79]. In the absence of the MF term, the QDs exhibit the soliton like structure and thus display plenty of interesting structural phases and dynamical features for SO coupled QDs. The Chapter is organized as follows: first, we will present a brief introduction of the QDs, mainly in the quantum soliton state. Following this, we will present our MF based simulation results for the system under investigation. The work described here is published in Physical Review A [80].

3.1 Introduction

The introduction related to the QDs has been extensively discussed in Chapter 1. However, to make it self-contained here in this section, we will provide a brief overview of the QDs with a main emphasis over the solitonic phase of the droplet, which mainly appears either with small effective mean-field interaction or with small number of particles. After the theoretical perdiction of the QDs [14, 28, 58], the QDs were realized in the dipolar dysprosium (^{164}Dy) [19, 20, 21], erbium atoms (^{166}Er) [22] and in the binary mixtures of isotropic BECs [15, 23, 24, 62], Bose-Fermi mixture [63] and also in binary magnetic gases [27]. In general, the LHY correction term is attractive in quasi-one dimension, while it is repulsive in two and three dimension [14, 58]. These QDs are commonly observed in three dimensions, while it is possible to increase the lifetime of the droplets in the lower dimensions. The formation of one-dimensional QDs is due to the balance between the

repulsive MF contribution to the energy per particle, which is linear in the density (n) of the gas, and the attractive LHY correction, proportional to $-n^{1/2}$ [14, 28].

After the prediction of the non-trivial attractive nature of the LHY term in one-dimensional QD [28] a significant number of experimental [30], as well as theoretical and numerical works, have been performed in recent years using the effective one component [32], binary [65] and SO and Rabi coupled binary BECs [33, 81] that explored the structure and dynamics of the QD. Tononi et al., in SO coupled BECs, demonstrated that the self-bound states are solitonic in nature for vanishing MF contribution [33]. Depending upon the Rabi and SO coupling parameters range, these soliton-like states are either of single peak (bright soliton) or multiple peaks (stripe soliton) nature [33, 82]. Some of these works demonstrate the existence of soliton and droplet nature of the self-bound state for the effective-one component binary BECs in one dimension [64] as well as in the binary mixture with SO coupling in two dimension [81, 83]. The transition between the quantum soliton and QD regime depends on several parameters, like, the atom number (N), interaction strength, the strength of the confining potential, etc. [64]. For large N, a highly dense droplet solution exists, while low dense bright soliton occurs for small N [32]. A recent experiment shows that the attractive mixture of BECs confined in an optical waveguide could exhibit both quantum soliton and QDs. At large N, the droplet exhibits similar characteristics as those of the classical droplets [23].

Though lots of emphasis on exploring the structure and stability of QDs in the recent past, only a limited number of works are available in the literature that focus on the dynamical aspect of QDs. Ferioli et al. analyzed the dynamics of QDs in a binary mixture by allowing the droplets to collide with each other [62]. A few theoretical studies are available that establish the robustness of the quantum soliton or QD during the collision. For instance, Astrakharchik and Malomed numerically investigated the collision properties of two counter-propagating droplets [32] and the elastic nature of the collision for large velocity and inelastic nature of the collision for small velocity. Young and Adhikari numerically studied the collision properties of bright solitons in two-dimensional dipolar BECs [84].

In recent years, one may witness numerous theoretical and numerical works focusing on the structure and dynamics of the droplets in binary BECs. However, only a few studies are available on the droplets in the spinor BECs, especially in SO coupled binary BECs [33, 46]. In particular, the role of SO and Rabi coupling parameters in dictating the shape and dynamics of the QD is not well understood. In this Chapter, we present a detailed numerical investigation to understand the effect of the SO and Rabi coupling parameters on the stability and shape of the quantum soliton. Although Tononi *et al.* [33]

demonstrates the presence of the self-bound quantum soliton due to the LHY term with vanishing MF contributions, several aspects, like dynamical robustness of the ground state for different perturbations, have not been explored yet. In this Chapter, we show a systematic analysis of the impact of initial velocity, quenching of the SO and Rabi coupling parameters, and allowing the collision between the components by initially perturbing the components with equal and opposite speeds. All these protocols facilitate us to obtain a variety of dynamical phases that include breathing (both in space and time), repelling, multi-fragmented solitons, etc.

The structure of our Chapter is as follows. In Sec. 3.2, we present governing equations and numerical simulation details and outline a possible scenario to connect our numerical parameters with the experiment. We illustrate an analytical solution of the ground state of the quantum soliton in the presence of SO coupling in Sec. 3.4. Following this in Sec. 3.5, we present a detailed analysis of the ground state structure followed by its dynamics which are set up in the system by different procedures. First, we discuss the different sorts of dynamics that arise due to the initial velocity given to the soliton, followed by the dynamics due to the quenching of coupling parameters. Further, we highlight some of the pronounced dynamical behaviour shown by the solitons in the presence of collisions. Finally, we conclude our work in Sec. 3.6.

3.2 Beyond mean-field model for spin-orbit coupled BECs

As we are interested to investigate the structure of the droplet with vanishingly small MF interaction. For this we consider $g_{\uparrow\uparrow} = g_{\downarrow\downarrow} = g$ and effective mean-field interaction $\delta g = 0$ in Eq. 1.54 the dynamical equation gets reduced to the following dimensionless form [33]:

$$\mathrm{i}\partial_t\psi_\uparrow = \left[-\frac{1}{2}\partial_x^2 - \mathrm{i}k_L\partial_x + g|\psi_\uparrow|^2 + g_{\uparrow\downarrow}|\psi_\downarrow|^2 - \frac{g_{\mathrm{LHY}}^{3/2}}{\pi}\sqrt{|\psi_\uparrow|^2 + |\psi_\downarrow|^2}\right]\psi_\uparrow + \Omega\psi_\downarrow, \quad (3.1a)$$

$$\mathrm{i}\partial_t\psi_\downarrow = \left[-\frac{1}{2}\partial_x^2 + \mathrm{i}k_L\partial_x + g_{\downarrow\uparrow}|\psi_\uparrow|^2 + g|\psi_\downarrow|^2 - \frac{g_{\mathrm{LHY}}^{3/2}}{\pi}\sqrt{|\psi_\uparrow|^2 + |\psi_\downarrow|^2}\right]\psi_\downarrow + \Omega\psi_\uparrow. \quad (3.1b)$$

where $\psi_\uparrow$ and $\psi_\downarrow$ are the wavefunctions of the spin-up and spin-down components respectively, k_L is the SO coupling strength, Ω is the Rabi coupling frequency, g is the intraspecies interaction, and $g_{\uparrow\downarrow}$ are the interspecies interaction strengths. We consider the interaction term due to the LHY correction as $g_{\mathrm{LHY}} = g$. The wave functions are

subjected to the following normalization condition:

$$\int_{-\infty}^{\infty} \left(|\psi_\uparrow|^2 + |\psi_\downarrow|^2\right)\, dx = 2. \tag{3.2}$$

Equations (3.1) are non-dimensionalized using transverse harmonic oscillator length $a_\perp = \sqrt{\hbar/(m\omega_\perp)}$ as a characteristic length scale (where, $\omega_\perp$ is the trap frequency in the transverse direction), $\omega_\perp^{-1}$ as a time scale, and $\hbar\omega_\perp$ as an energy scale. The other interaction parameters are considered as $g = 2Na_{\uparrow\uparrow}/a_\perp$ and $g_{\uparrow\downarrow} = 2Na_{\uparrow\downarrow}/a_\perp$. Here, $a_{\uparrow\uparrow}$ and $a_{\uparrow\downarrow}$ represent the scattering length corresponding to intra and inter components, respectively. The SO and the Rabi coupling parameters have been rescaled as $k_L \to k_L a_\perp$ and $\Omega \to \Omega/\omega_\perp$, respectively, while the wave function is rescaled as $\psi_{\uparrow,\downarrow} = \psi_{\uparrow,\downarrow}\sqrt{a_\perp}$.

To make the numerical simulation experimentally viable, we choose the parameters same as considered in the recent realization of the QD in the binary hyperfine states mixture of ^{39}K condensates [15, 23, 62]. Following this we consider $N \sim 10^4$ atoms confined in the harmonic trap potential with frequencies $\omega_x = 2\pi \times 50\,\text{Hz}$, $\omega_\perp = 2\pi \times 800\,\text{Hz}$ in axial and perpendicular directions, respectively. Using this the characteristic length scale can be obtained as $a_\perp \sim 0.6\,\mu$m. Generally, in the experiment two internal hyperfine states $|F = 1, m_F = -1\rangle$ and $|F = 1, m_F = 0\rangle$ are considered which can be attributed, respectively, to the pseudo-spin up $|\uparrow\rangle$, and pseudo-spin down $|\downarrow\rangle$ states of our model. These two spin states have an equal number of atoms, and intra- and interspecies interaction strengths can be controlled by tuning s-wave scattering lengths through Feshbach resonance and by varying the magnetic field. Following the experiment we set $a_{\uparrow\uparrow} = a_{\downarrow\downarrow} = -a_{\uparrow\downarrow} = 0.2686a_0$ (a_0 is the Bohr radius) which gives the dimensionless interaction strengths as $g = g_{\text{LHY}} \approx 0.5$. Note that here we have taken all the scattering lengths to be the same to make the contribution of the MF term on the structure and dynamics of the soliton vanishingly small. Another parameter in this system is the Rabi coupling frequency (Ω), commonly used for coupling the spin states by tuning the frequency of Raman lasers ranging from $\Omega = 2\pi \times \{0.080 - 40\}$kHz, which implies that the dimensionless Rabi coupling frequency range as $\Omega = \{0.1, 50\}$. It is possible to vary the SO coupling strength (k_L) with the laser wavelength and their geometry. In the present work, we have considered the dimensionless SO coupling range $k_L = \{0.1, 8\}$, where the laser wavelength varies as $\lambda_L = 17.8\ \mu\text{m} - 223.2$ nm. Note that the LHY interaction is not equal to the MF interaction because the LHY nonlinear interaction term appears with an extra factor π. We have considered $g_{\text{LHY}} = g = 0.5$ and 1.0, for which the quantum fluctuation term contributes approximately of the order of 11% and 30% respectively.

Interestingly, albeit of small contribution, we have obtained a large variety of dynamical features for our system without any confinement.

We employ the imaginary-time propagation method with the aid of a split-step Crank-Nicolson scheme [71, 85, 86] to numerically solve the coupled eGPEs (3.1a) and (3.1b). The box size $[-153.6 : 153.6]$ with spatial resolution as $dx = 0.025$ is chosen for all the simulation runs, and we use the Gaussian initial condition with anti-symmetric profiles on the components, i.e., $\psi_\uparrow(x) = -\psi_\downarrow(-x)$. The time step is fixed at $dt = 10^{-5}$. We also consider various interaction strengths ($g = 0.5, 1, 2$) for our studies.

3.3 Calculation of energy in the spin-orbit coupled BECs with LHY correction

In this Section, we provide the detailed steps to obtain the total energy of the SO coupled BECs with LHY correction, which have been used to calculate the energy corresponding to the different term. The stationary state solution is given by

$$\psi_j(x, y) = \big(\psi_{jR} + \mathrm{i}\psi_{jI}\big)e^{-\mathrm{i}\mu_j t}, \tag{3.3}$$

where $j \in \{\uparrow, \downarrow\}$, ψ_{jR} and ψ_{jI} are the real and imaginary parts of the stationary wavefunction respectively, and $\mu_{\uparrow,\downarrow}$ are the chemical potential of the spin-up and down components respectively [74]. As we insert this solution in the Eqs. (3.1) we get

$$\mu_\uparrow\psi_{\uparrow R} = \left[-\frac{1}{2}\frac{\partial^2}{\partial x^2} + g|\psi_\uparrow|^2 + g_{\uparrow\downarrow}|\psi_\downarrow|^2 - \frac{g^{3/2}}{\pi}\sqrt{|\psi_\uparrow|^2 + |\psi_\downarrow|^2}\right]\psi_{\uparrow R} + k_L\left(\frac{\partial\psi_{\uparrow I}}{\partial x}\right) + \Omega\psi_{\downarrow R}, \tag{3.4a}$$

$$\mu_\downarrow\psi_{\downarrow R} = \left[-\frac{1}{2}\frac{\partial^2}{\partial x^2} + g|\psi_\downarrow|^2 + g_{\downarrow\uparrow}|\psi_\uparrow|^2 - \frac{g^{3/2}}{\pi}\sqrt{|\psi_\uparrow|^2 + |\psi_\downarrow|^2}\right]\psi_{\downarrow R} - k_L\left(\frac{\partial\psi_{\downarrow I}}{\partial x}\right) + \Omega\psi_{\uparrow R}, \tag{3.4b}$$

and for the imaginary parts we have

$$\mu_\uparrow\psi_{\uparrow I} = \left[-\frac{1}{2}\frac{\partial^2}{\partial x^2} + g|\psi_\uparrow|^2 + g_{\uparrow\downarrow}|\psi_\downarrow|^2 - \frac{g^{3/2}}{\pi}\sqrt{|\psi_\uparrow|^2 + |\psi_\downarrow|^2}\right]\psi_{\uparrow I} - k_L\left(\frac{\partial\psi_{\uparrow R}}{\partial x}\right) + \Omega\psi_{\downarrow I}, \tag{3.4c}$$

$$\mu_\downarrow\psi_{\downarrow I} = \left[-\frac{1}{2}\frac{\partial^2}{\partial x^2} + g|\psi_\downarrow|^2 + g_{\downarrow\uparrow}|\psi_\downarrow|^2 - \frac{g^{3/2}}{\pi}\sqrt{|\psi_\uparrow|^2 + |\psi_\downarrow|^2}\right]\psi_{\uparrow I} + k_L\left(\frac{\partial\psi_{\downarrow R}}{\partial x}\right) + \Omega\psi_{\uparrow I}, \tag{3.4d}$$

where $|\psi_\uparrow|^2 = \psi_{\uparrow R}^2 + \psi_{\uparrow I}^2$ and $|\psi_\downarrow|^2 = \psi_{\downarrow R}^2 + \psi_{\downarrow I}^2$. Multiplying Eq. (3.4a) with $\psi_{\uparrow R}$ and Eq. (3.4b) with $\psi_{\downarrow R}$, and integrating we get

$$\mu_\uparrow \int dx\, \psi_{\uparrow R}^2 = \int dx\, \psi_{\uparrow R} \left\{ \left[-\frac{1}{2}\frac{\partial^2}{\partial x^2} + g|\psi_\uparrow|^2 + g_{\uparrow\downarrow}|\psi_\downarrow|^2 - \frac{g^{3/2}}{\pi}\sqrt{|\psi_\uparrow|^2 + |\psi_\downarrow|^2} \right] \psi_{\uparrow R} \right\} + \int dx\, \psi_{\uparrow R} \left\{ k_L \left(\frac{\partial \psi_{\uparrow I}}{\partial x} \right) + \Omega \psi_{\downarrow R} \right\}, \tag{3.5a}$$

$$\mu_\downarrow \int dx\, \psi_{\downarrow R}^2 = \int dx\, \psi_{\downarrow R} \left\{ \left[-\frac{1}{2}\frac{\partial^2}{\partial x^2} + g|\psi_\downarrow|^2 + g_{\downarrow\uparrow}|\psi_\uparrow|^2 - \frac{g^{3/2}}{\pi}\sqrt{|\psi_\uparrow|^2 + |\psi_\downarrow|^2} \right] \psi_{\downarrow R} \right\} \int dx\, \psi_{\downarrow R} \left\{ -k_L \left(\frac{\partial \psi_{\downarrow I}}{\partial x} \right) + \Omega \psi_{\uparrow R} \right\}, \tag{3.5b}$$

Similarly, from the imaginary part equations (Eqs. 3.4c and 3.4d) we obtain

$$\mu_\uparrow \int dx\, \psi_{\uparrow I}^2 = \int dx\, \psi_{\uparrow I} \left\{ \left[-\frac{1}{2}\frac{\partial^2}{\partial x^2} + g|\psi_\uparrow|^2 + g_{\uparrow\downarrow}|\psi_\downarrow|^2 - \frac{g^{3/2}}{\pi}\sqrt{|\psi_\uparrow|^2 + |\psi_\downarrow|^2} \right] \psi_{\uparrow I} \right\} - \int dx\, \psi_{\uparrow I} \left\{ k_L \left(\frac{\partial \psi_{\uparrow R}}{\partial x} \right) + \Omega \psi_{\downarrow I} \right\}, \tag{3.6a}$$

$$\mu_\downarrow \int dx\, \psi_{\downarrow I}^2 = \int dx\, \psi_{\downarrow I} \left\{ \left[-\frac{1}{2}\frac{\partial^2}{\partial x^2} + g|\psi_\downarrow|^2 + g_{\downarrow\uparrow}|\psi_\uparrow|^2 - \frac{g^{3/2}}{\pi}\sqrt{|\psi_\uparrow|^2 + |\psi_\downarrow|^2} \right] \psi_{\downarrow I} \right\} + \int dx\, \psi_{\downarrow I} \left\{ k_L \left(\frac{\partial \psi_{\downarrow R}}{\partial x} \right) + \Omega \psi_{\uparrow I} \right\}, \tag{3.6b}$$

Upon rearranging the above equations (Eqs. 3.5b-3.6b) we obtain

$$\mu_\uparrow = \frac{1}{\int |\psi_\uparrow|^2 dx} \int \left[\frac{1}{2}\left| \frac{\partial \psi_\uparrow}{\partial x} \right|^2 + \left\{ g|\psi_\uparrow|^2 + g_{\uparrow\downarrow}|\psi_\downarrow|^2 - \frac{g^{3/2}}{\pi}\sqrt{|\psi_\uparrow|^2 + |\psi_\downarrow|^2} \right\} |\psi_\uparrow|^2 \right] dx + \frac{1}{\int |\psi_\uparrow|^2 dx} \int \left[k_L \left(\frac{\partial \psi_{\uparrow I}}{\partial x} \right) + \Omega \psi_{\downarrow R} \right] \psi_{\uparrow R} dx + \frac{1}{\int |\psi_\uparrow|^2 dx} \int \left[-k_L \left(\frac{\partial \psi_{\uparrow R}}{\partial x} \right) + \Omega \psi_{\downarrow I} \right] \psi_{\uparrow I} dx, \tag{3.7a}$$

$$\mu_\downarrow = \frac{1}{\int |\psi_\downarrow|^2 dx} \int \left[\frac{1}{2}\left| \frac{\partial \psi_\downarrow}{\partial x} \right|^2 + \left\{ g|\psi_\downarrow|^2 + g_{\downarrow\uparrow}|\psi_\uparrow|^2 - \frac{g^{3/2}}{\pi}\sqrt{|\psi_\uparrow|^2 + |\psi_\downarrow|^2} \right\} |\psi_\downarrow|^2 \right] dx + \frac{1}{\int |\psi_\downarrow|^2 dx} \int \left[-k_L \left(\frac{\partial \psi_{\downarrow I}}{\partial x} \right) + \Omega \psi_{\uparrow R} \right] \psi_{\downarrow R} dx + \frac{1}{\int |\psi_\downarrow|^2 dx} \int \left[k_L \left(\frac{\partial \psi_{\downarrow R}}{\partial x} \right) + \Omega \psi_{\uparrow I} \right] \psi_{\downarrow I} dx, \tag{3.7b}$$

From the above equations we obtain the different contributions in the energy as

$$E_{ki} = \int \left[\frac{1}{2\int|\psi_\uparrow|^2 dx} \left|\frac{\partial\psi_\uparrow}{\partial x}\right|^2 + \frac{1}{2\int|\psi_\downarrow|^2 dx} \left|\frac{\partial\psi_\downarrow}{\partial x}\right|^2 \right] dx \tag{3.8a}$$

$$E_{mf} = \int \left[\frac{1}{\int|\psi_\uparrow|^2 dx} \left[\frac{g}{2}|\psi_\uparrow|^2 + \frac{g_{\uparrow\downarrow}}{2}|\psi_\downarrow|^2\right] |\psi_\uparrow|^2 + \frac{1}{\int|\psi_\downarrow|^2 dx} \left[\frac{g_{\downarrow\uparrow}}{2}|\psi_\uparrow|^2 + \frac{g}{2}|\psi_\downarrow|^2\right] |\psi_\downarrow|^2 \right] dx \tag{3.8b}$$

$$\begin{aligned} E_{lhy} = &\int -\frac{1}{\int|\psi_\uparrow|^2 dx} \left[\frac{2}{3\pi} g^{3/2} \sqrt{|\psi_\uparrow|^2 + |\psi_\downarrow|^2}\right] |\psi_\uparrow|^2 dx \\ &- \int \frac{1}{\int|\psi_\downarrow|^2 dx} \left[\frac{2}{3\pi} g^{3/2} \sqrt{|\psi_\uparrow|^2 + |\psi_\downarrow|^2}\right] |\psi_\downarrow|^2 dx \end{aligned} \tag{3.8c}$$

$$\begin{aligned} E_{SO} = &\int \frac{1}{\int|\psi_\uparrow|^2 dx} \left[\left(k_L \frac{\partial\psi_{\uparrow I}}{\partial x}\right) \psi_{\uparrow R} + \left(-k_L \frac{\partial\psi_{\uparrow R}}{\partial x}\right) \psi_{\uparrow I} \right] dx \\ &+ \int \frac{1}{\int|\psi_\downarrow|^2 dx} \left[\left(-k_L \frac{\partial\psi_{\downarrow I}}{\partial x}\right) \psi_{\downarrow R} + \left(k_L \frac{\partial\psi_{\downarrow R}}{\partial x}\right) \psi_{\downarrow I} \right] dx \end{aligned} \tag{3.8d}$$

$$\begin{aligned} E_{Rabi} = &\int \frac{1}{\int|\psi_\uparrow|^2 dx} \left[(\Omega\psi_{\downarrow R})\, \psi_{\uparrow R} + (\Omega\psi_{\downarrow I})\, \psi_{\uparrow I} \right] dx \\ &+ \int \frac{1}{\int|\psi_\downarrow|^2 dx} \left[(\Omega\psi_{\uparrow R})\, \psi_{\downarrow R} + (\Omega\psi_{\uparrow I})\, \psi_{\downarrow I} \right] dx \end{aligned} \tag{3.8e}$$

where E_{ki} represents the kinetic energy, E_{mf} MF contribution, E_{lhy} is the energy due to the LHY correction, and E_{SO} is the contribution due to the SO coupling. The total energy $E_T = E_{ki} + E_{mf} + E_{lhy} + E_{SO}$.

3.4 Analytical soliton solution

Here, we present the analytical solution of the ground state for our model. For brevity, we wish to obtain a solution for zero Rabi coupling frequency ($\Omega = 0$) and finite k_L. For this purpose, we consider the following transformation to eliminate the SO coupling term from Eq. (3.1),

$$\psi_\uparrow(x,t) = \widetilde{\psi}_\uparrow(x,t) \exp\left[\frac{\mathrm{i}k_L}{2}(k_L t - 2x)\right], \tag{3.9a}$$

$$\psi_\downarrow(x,t) = \widetilde{\psi}_\downarrow(x,t) \exp\left[\frac{\mathrm{i}k_L}{2}(k_L t + 2x)\right]. \tag{3.9b}$$

Using the single field approximation we get $\widetilde{\psi}_\uparrow = \widetilde{\psi}_\downarrow = \phi(x)\exp(\mathrm{i}\mu t)$. Based on the system parameters $g_{\uparrow\downarrow} = -g$, we find that the MF interaction term cancels each other,

which yields the stationary state solution of the form

$$-\mu\phi = -\frac{1}{2}\partial_x^2\phi - \frac{\sqrt{2}}{\pi}g^{3/2}\phi^2, \tag{3.10}$$

which gives

$$\phi'^2 = \alpha\phi^2 - \beta\phi^3, \tag{3.11}$$

where prime ($'$) represents the spatial derivative with respect to x and $\alpha = 2\mu, \beta = 2\sqrt{2}g^{3/2}/3\pi$. Now the solution of the Eq. (3.11) becomes [33]

$$\phi(x) = \phi(0)\ \mathrm{sech}^2(\sqrt{\mu/2}\ x), \tag{3.12}$$

where, $\phi(0) = \alpha/\beta$. Here, the stationary state solution depends on the chemical potential. Using the normalization condition $\int|\psi_\uparrow|^2dx = \int|\psi_\downarrow|^2dx = 1$ we obtain $2|\mu| = (g^2/3^{2/3}\pi^{4/3})$. Thus the final solution of the Eq. (3.1) have the form as,

$$\begin{aligned}
\psi_\uparrow &= \left(\frac{\alpha}{\beta}\right)\mathrm{sech}^2\left(\sqrt{\frac{\mu}{2}}\ x\right)\exp\left[\frac{\mathrm{i}k_L}{2}(k_Lt - 2x) + \mathrm{i}\mu t\right], \\
\psi_\downarrow &= \left(\frac{\alpha}{\beta}\right)\mathrm{sech}^2\left(\sqrt{\frac{\mu}{2}}\ x\right)\exp\left[\frac{\mathrm{i}k_L}{2}(k_Lt + 2x) + \mathrm{i}\mu t\right].
\end{aligned} \tag{3.13}$$

In Fig. 3.1, we plot the analytical (red line) solution [Eqs. (3.13)] as well numerical simulation (black dots) results of the stationary ground state of the Eq. (3.1) for $g_{LHY} = g = 0.5$, with $\Omega = 0$ and $k_L = 1$. Both analytical and numerical simulation results match reasonably well for the real and imaginary parts and the total density of components.

In brief, we found the approximate soliton solution for the system of coupled Eqs. (3.1) by eliminating the SO coupling term using the transformation with zero Rabi coupling frequency. In the process, we have used single field approximation, which provides $\mathrm{sech}^2(x)$ soliton solution due to quadratic nonlinearity [33].

3.5 Numerical results

In this section, first, we present our numerical results for different ground state solitons obtained using the imaginary-time propagation scheme. Our main emphasis is to ascertain the role of MF and BMF or LHY terms on the overall shape and structure of the self-bound quantum soliton state. Following this, we focus on the soliton dynamics

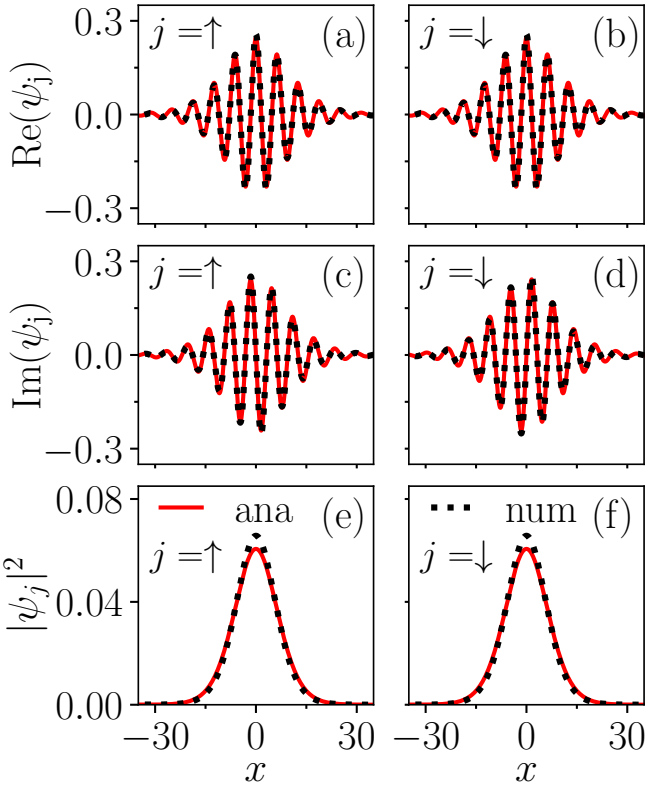

Figure 3.1: A comparison between the numerically obtained soliton profiles (dotted-black line) and analytical (solid-red line) solution (3.13) for interaction strengths $g = 0.5$, and coupling parameters $k_L = 1$ and $\Omega = 0$. Real parts of the spin components: (a) $\mathrm{Re}(\psi_\uparrow)$ and (b) $\mathrm{Re}(\psi_\downarrow)$, imaginary parts of the spin components: (c) $\mathrm{Im}(\psi_\uparrow)$ and (d) $\mathrm{Im}(\psi_\downarrow)$, and the densities of the (e) up $|\psi_\uparrow|^2$ and (f) down $|\psi_\downarrow|^2$ components.

by employing the real-time propagation of the governing dynamical eGPEs. Finally, we present a detailed analysis of the dynamics of quantum solitons by giving initial velocity, quenching the coupling parameters and allowing the collision between the components by initially imparting them with an equal speed in the opposite direction.

3.5.1 Stationary ground states of quantum solitons

To better understand the role of the BMF term (g_{LHY}) along with the SO and Rabi coupling frequency on the shape and size of the ground state, we now proceed to get the different ground state of the solitons by assuming $g = -g_{\uparrow\downarrow} = g_{\mathrm{LHY}}$. Here, we use MF and BMF acronyms to represent the ground states of the system in the absence ($g_{LHY} = 0$) and the presence of LHY correction ($g_{LHY} \neq 0$), respectively. In general, depending upon the coupling parameters range, the ground states are either bright soliton (BS) or stripe soliton (SS) in nature [33, 87].

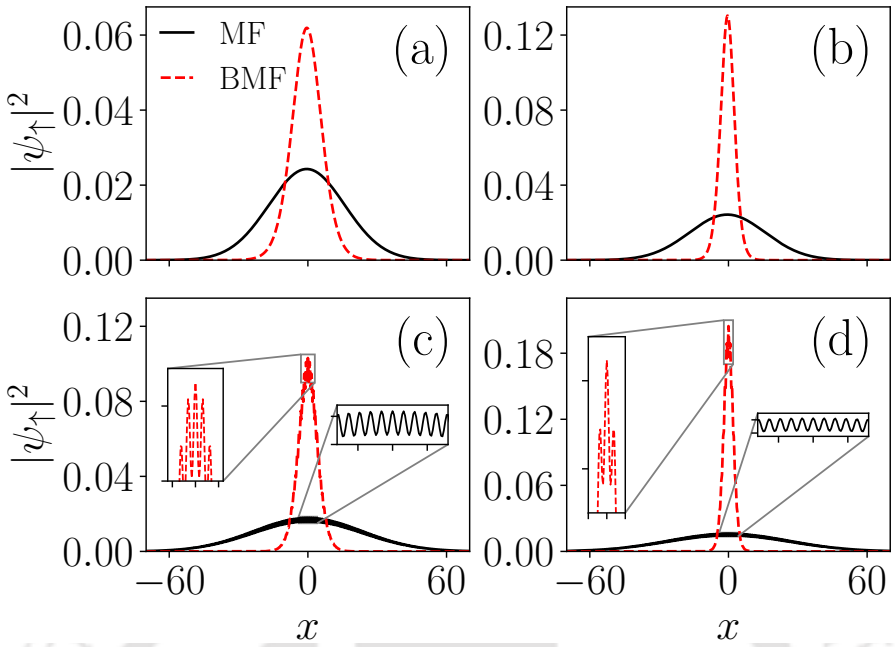

Figure 3.2: Ground state density profiles of the spin-up component in the presence and absence of LHY term. Bright soliton for $\Omega = 1$ and $k_L = 1$ with (a) $g = 0.5$ and (b) $g = 1.0$, and stripe soliton for $\Omega = 1$ and $k_L = 4$ with (c) $g = 0.5$ and (d) $g = 1.0$. The spin density gets more confined when the LHY term (dashed-red line) is present. The insets in (c) and (d) show the magnified views of the stripe patterns in the presence and absence of the LHY term.

We begin the analysis of the structure of BS in the absence of $g_{\rm LHY}$ (labeled as MF) for the fixed parameters $k_L = \Omega = 1$ and $g = -g_{\uparrow\downarrow} = 0.5$. In Fig. 3.2(a) we depict the density profile of the up component in absence (black line) and in presence (red dotted line) of the $g_{\rm LHY}$ for the BS state. In the presence of $g_{\rm LHY}$ (labeled as BMF) magnitude of the BS gets doubled, and it tends to become more localized even though the width of the soliton appears to get reduced, as represented by the dashed-red line in Fig. 3.2(a).

Further, upon increasing the interaction strengths to $g = -g_{\uparrow\downarrow} = 1$, we find a negligible change in the amplitude and width of the mean-field Bright soliton (MF-BS) [see Fig. 3.2(b) (solid-black line)]. However, in the presence of LHY interaction ($g_{\rm LHY} = 1$) a well localized quantum bright soliton (QBS) width gets reduced by half, while, its amplitude is increased by a factor ≈ 2.66 [see Fig. 3.2(b) (dashed-red line)].

Next, we consider the shape and structure of SS both in the presence and absence of the LHY correction term, which was obtained for $\Omega = 1$ and $k_L = 4$ at $g = 0.5, 1$. A phase transition from BS to SS states occurs as we change the SO coupling strength from $k_L = 1$ to $k_L = 4$. The fringes that appear in the density profiles characterize the stripe wave pattern. One may note that several local maxima appear in the density profile for both the MF and quantum solitons. In the presence of the LHY term with interaction strength

$g = 0.5$, the number of stripes, as well as the width, gets reduced, and amplitude gets doubled compared to those without LHY, indicating the localization of the soliton [see Fig. 3.2(c)]. On increasing the interaction strength to $g = 1$, we find that the mean-field stripe soliton (MF-SS) [shown with the black line in Fig. 3.2(d)] exhibits similar nature as those for $g = 0.5$. However, the LHY-SS or quantum SS (QSS) phase width gets reduced by half, and an increase in the amplitude by a factor ≈ 4, accompanied by a loss in the number of stripes and an increment in the localization [shown with the red line in Fig. 3.2(d)] is observed. Overall, we noticed that the condensate shape hardly changes upon increasing the MF interaction strengths. However, we note a significant change in the shape and amplitude when we consider the LHY correction ($g_{\rm LHY} \neq 0$). With the LHY correction on increasing the nonlinear interaction (g), the size of the soliton gets reduced while the amplitude increases.

3.5.2 Dynamics of different phases of quantum soliton

In this section, we present the dynamics of the ground state of the MF and quantum soliton by solving the governing equation [cf. Eqs. (3.1)] with the help of real-time propagation. The main aim here is to investigate the dynamics of the MF and BMF quantum solitons by giving some initial velocity to the condensate by making a uniform change in the phase of the soliton wavefunction [33, 88]. Further, we demonstrate appearance of breathing solitons, fragmented soliton, free expansion of soliton, etc., by manipulating the magnitude of the initial velocity.

Fig. 3.3(a-d) depicts the temporal evolution of BS for different velocities, $v = 0$, 0.2, 0.5 and 1, respectively, with $g = -g_{\uparrow\downarrow} = 0.5$ and $\Omega = k_L = 1$. For $v = 0$, the soliton propagates without any distortion [see Fig. 3.3(a)]. For a small but finite initial velocity (for example, $v = 0.2$), we notice setting up a time-dependent oscillation in the soliton that manifests as an undulating motion of the density in time and space. Beyond $t \sim 30$, the oscillation amplitude appears to vanish and stable soliton is observed [cf. Fig. 3.3(b)]. This oscillation can be associated with the instability that soliton displays upon making a sudden change in the phase by a factor $\exp(\pm ivx)$, where v is the resultant acquired velocity. Note that up-spin and down-spin component of the condensates have been given negative and positive x-direction velocity respectively. We also observe an expansion in the soliton upon waiting for a longer period. For $v = 0.5$, soliton appears to display breaking into secondary solitons and breathers-like oscillation in which it exhibits expansion followed by compression at a periodic time interval [see Fig. 3.3(c)]. The spin component exhibits interesting dynamical behaviour. We noticed the absence of the

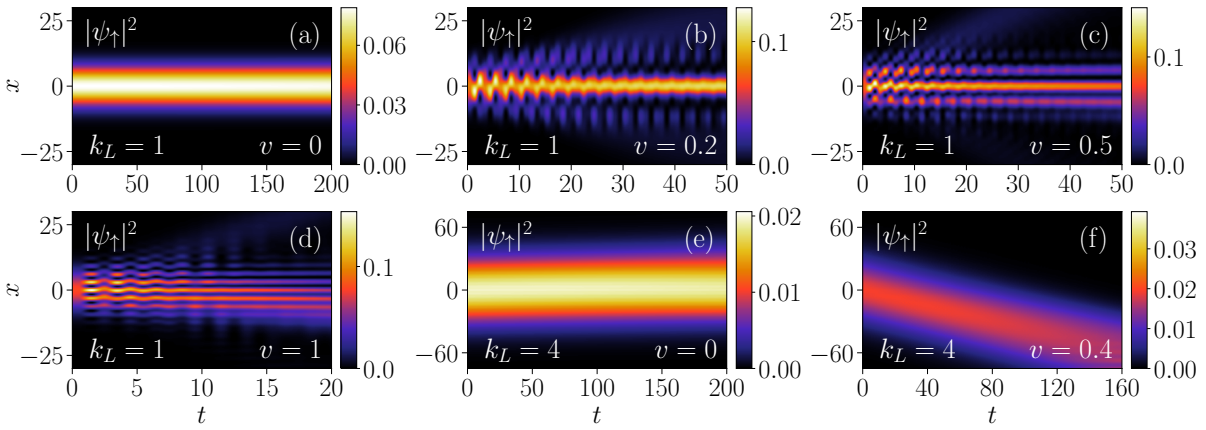

Figure 3.3: Temporal evolution of MF bright soliton (BS) at different initial velocities: (a) $v = 0$, (b) $v = 0.2$, (c) $v = 0.5$, and (d) $v = 1$ for $g = -g_{\uparrow\downarrow} = 0.5$ and $\Omega = k_L = 1$. Upon increasing the velocity from $v = 0$ to $v = 0.2$, a transition from the soliton to an oscillating soliton takes place. For large velocity multi-soliton (at $v = 0.5$) and bifurcated solitons (at $v = 1$) are observed. Temporal evolution of MF stripe soliton for different velocities: (e) $v = 0$ and (f) $v = 0.4$ with $g = -g_{\uparrow\downarrow} = 0.5$, $\Omega = 1$, and $k_L = 4$. For $v = 0$ shape of the soliton remains unchanged until $t \sim 200$. For finite velocity ($v = 0.4$), the stripe soliton shows propagation along the initial velocity direction.

breather on one side while it is present on the other side. However, the middle lobe exhibits oscillation for a shorter time and expansion in a long duration indicates the presence of an oscillation death-like behaviour in the soliton [87]. In addition, we also observe the presence of multi-soliton-like features. At $v = 1$, fragmented solitons with breather-like modes get generated and propagate in the respective directions for the spin components, accompanied by the appearance of bifurcation-like multi solitons [cf. Fig. 3.3(d)].

We observe similar nature of dynamical behaviour in the SS as those observed for BS in the absence of the LHY term. In Figs. 3.3(e)-(f), we show the temporal evolution of SS in the absence of LHY term for $\Omega = 1$ and $k_L = 4$ with $g = 0.5$ for (e) $v = 0$ and (f) $v = 0.4$. For $v = 0$, the SS state exhibits stripe solitonic feature. However, at higher velocity ($v = 0.4$), bifurcation of the stripe soliton into two propagating solitons occurs, which exhibits expansion with time.

After discussing the dynamics of the soliton in the presence of MF term only, we now analyse the dynamical evolution when we consider the BMF term along with MF term for both QBS and QSS. In Fig. 3.4, we illustrate the dynamics of QBS with the BMF (i.e., with LHY correction term) for different initial velocities $v = 0, 0.5$ and $v = 1.0$ at $g = -g_{\uparrow\downarrow} = 0.5$ and $\Omega = k_L = 1$. For zero velocity soliton exhibits stable nature with no change in its shape and size with time as depicted in Fig. 3.4(a) the feature is same as those for the MF bright soliton. On increasing the velocity to $v = 0.5$, the soliton displays breathers-like expansion and compression behaviour at periodic intervals, as shown in

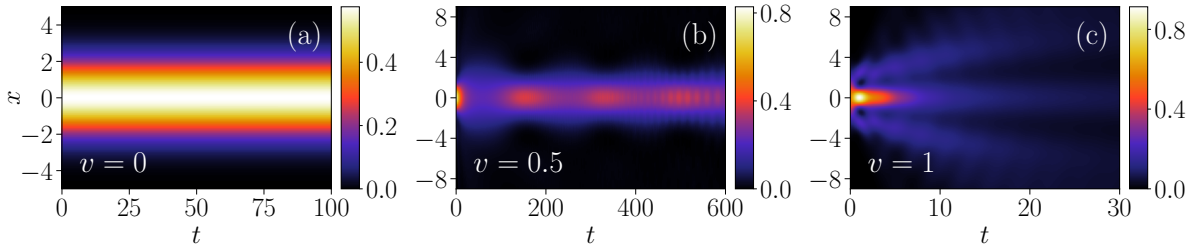

Figure 3.4: Plots of the total density, $\sum_{j=\uparrow,\downarrow}|\psi_j|^2$, showing dynamics of quantum bright soliton (QBS) with LHY correction for $g = -g_{\uparrow\downarrow} = 0.5$, $\Omega = 1$, $k_L = 1$ at different velocities: (a) soliton propagates with no shape change for $v = 0$, (b) breathers for finite velocity $v = 0.5$, and (c) oscillation and bifurcation for $v = 1.0$. Increase in the velocity leads transitions from bright soliton to breather which further gets transformed into multi-solitons.

Fig. 3.4(b). Here we find that the expansion of the condensate gets under control due to the presence of g_{LHY} interaction, stabilising the expanding condensate without any trap. The frequency of these breathing modes depends on the coupling parameters, which we shall discuss in detail in the later part of the Chapter. Note that Tononi et al. reported similar breathers like soliton [33], which was attained by a slight perturbation in the width of the ground state. As we increase the initial velocity to $v = 1$, the soliton develops periodic breather oscillations and exhibits bifurcation-like features in which the centre of the soliton moves in the $\pm x$ directions. Note that the up-spin component moves in the $-x$ direction while the other component moves in the $+x$ direction. This feature is noticeable for a finite time $t \lesssim 10$. Beyond this time, the breathers expand and span the entire space while the centred soliton exhibits expansion. Apart from this, we also notice that it exhibits bright-dark soliton for a shorter time, which finally gets converted into multi-soliton at a longer period [32] as displayed in Fig. 3.4(c).

Further, we focus on the dynamics of QSS with LHY correction at different velocities $v = 0, 0.2$, and 1.0 for the parameters $g = -g_{\uparrow\downarrow} = 0.5$, $\Omega = 1$, and $k_L = 4$. At $v = 0$, QSS remains stable and maintains its shape and size for a longer duration [see Fig. 3.5(a)]. However, with finite velocity ($v = 0.2$) QSS propagates for a while in the $\pm x$ directions, thereafter, for $t \gtrsim 50$ they start displaying decaying (dilatation) feature until $t \lesssim 300$. Following this the dilatation slowly gets diminished and for $t \gtrsim 500$ soliton gets revived [see Fig. 3.5(b)]. The whole revival and expansion of the soliton with time is similar to those obtained for the QBS [see Fig. 3.4(b)]. For $v > 0.5$, the QSS evolves with time in the respective directions, and after separation, they do not combine again, as shown for $v = 1.0$ in Fig. 3.5(c).

Next, we analyze the dependence of the breathing frequency for the quantum soliton as observed in Figs. 3.4(b) and 3.5(b) on the SO and Rabi coupling parameters. We compute the breathing frequency (ω_{bf}) using the time series of the density oscillation of

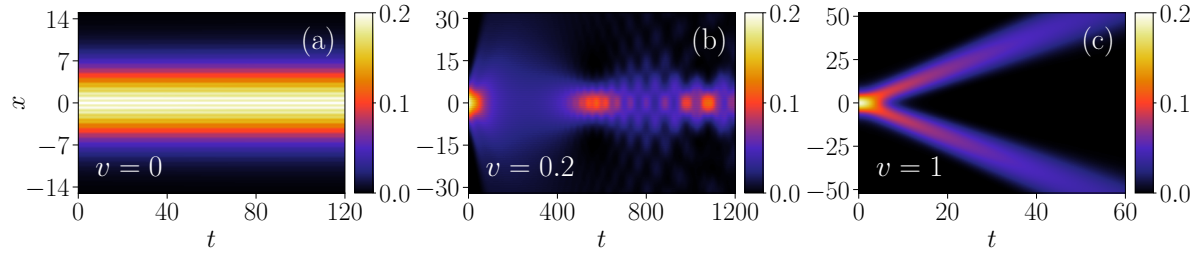

Figure 3.5: Plots of the total density, $\sum_{j=\uparrow,\downarrow}|\psi_j|^2$, showing the dynamics of quantum stripe soliton (QSS) with LHY correction at different velocities: (a) $v = 0$, (b) $v = 0.2$, and (c) $v = 1.0$ for $g = -g_{\uparrow\downarrow} = 0.5$ and $\Omega = 1$, $k_L = 4$. For $v = 0$ stable stripe soliton is observed. However, for finite velocity breathers ($v = 0.2$) and bifurcated ($v = 1.0$) solitons are observed.

the soliton. In Fig. 3.6(a) we show dependence of ω_{bf} on the SO couplings (k_L) for various Ω when the soliton was assigned the initial velocity as $v = 0.1$. Following Ref. [33], here we consider the initial wavefunction as Gaussian, which is different than that of the exact solution of the ground state. The breathing frequency is around 0.025 for $k_L = 0$ for all values of Ω. At $\Omega = 0$ the ω_{bf} remains unchanged upon increasing k_L. For finite Rabi coupling frequency ($\Omega = 1, 2, 4$), breather starts appearing at periodic intervals. For fixed Ω as $k_L^2 < \Omega$ the breathing frequency increases upon increasing in k_L. It attains the maximum at critical SO coupling ($k_L^2 = \Omega$) where the QBS to QSS phase transition occurs. For $k_L^2 > \Omega$, ω_{bf} decreases slowly in the regime of quantum stripe soliton. At higher k_L, ω_{bf} have the same value as those at $k_L \sim 0$ for all Ω. The critical breathing frequency (ω_{bf}^c) increases upon an increase in the Rabi frequency. Fig. 3.6(b) illustrates the variation of ω_{bf} with k_L for different velocities, $v = 0.1$ and 0.2, at $g = 0.5$. We have

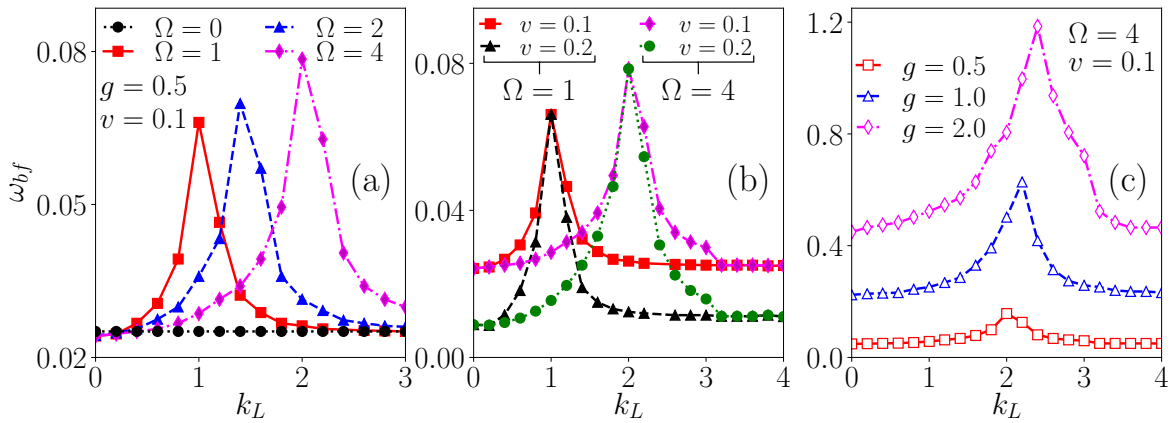

Figure 3.6: (a) Variation of breathing frequency (ω_{bf}) with the SO coupling strength (k_L) for different Ω with fixed velocity $v = 0.1$. (b) The Variation of ω_{bf} with k_L for different Rabi coupling ($\Omega = 1, 4$) and velocities $v = 0.1, 0.2$ with $g = 0.5$. At the critical k_L where BS-SS phase transition happens, ω_{bf}^c remains independent of the velocity. (c) Variation of ω_{bf} with k_L for different interaction strengths $g = 0.5$, 1.0, 2.0 at $\Omega = 4$ and $v = 0.1$. To bring the graph to the same scale, we multiply the data for $g = 0.5$ and $g = 1.0$ by a factor of two.

considered two sets of Rabi couplings $\Omega = 1$ and 4 for the analysis. The overall variation in ω_{bf} with k_L appears to be the same for both the velocities ($v = 0.1$ and 0.2), except that at lower velocity ($v = 0.1$) it has higher value compared to those at large velocity ($v = 0.2$). Interestingly, ω_{bf}^c remains the same for all the velocities ($v = 0.1$ and 0.2) as shown in Fig. 3.6 (b), indicating that the breathing frequency at the critical point remains unchanged upon increasing the velocity. To better understand the dependence of the ω_{bf} on the interaction strengths in Fig. 3.6(c) we show its variation with k_L for different g ($g = 0.5, 1.0, 2.0$) at $\Omega = 4$ and $v = 0.1$. We observe that the ω_{bf} for a given k_L shows increasing behaviour on increasing the interaction strength. The critical SO coupling (k_L^c) and corresponding critical breathing frequency (ω_{bf}^c) also increase upon the increase in g.

In Fig. 3.7(a), we plot the variation of ω_{bf}^c with Ω for $v = 0.1$. We find that ω_{bf}^c shows power law dependence on Ω with an exponent, 0.16. In Fig. 3.7(b), we plot the variation of ω_{bf} with initial velocity for fixed Rabi coupling ($\Omega = 2$) and for two sets of SO couplings $k_L = 1.2$ (solid red line) and $k_L = 1.8$ (dashed blue line). Here, we notice that ω_{bf} decreases upon increasing the initial velocity for both the k_L. The fall in the breathing frequency with the velocity becomes sharper upon the increase in k_L. However, for a given initial velocity, the ω_{bf} is small for $k_L = 1.8$, which happens to be in QSS than those for $k_L = 1.2$ at which we have QBS ground state. We note that the chemical potential in the QBS regime does not change with k_L until $k_L < k_L^c$, which indicates that the soliton is energetically stable in the BS regime. On the other hand, when we increase the Rabi frequency, Ω to 2, the critical k_L for the transition from the bright to stripe soliton also increases. Overall we find that the ground state energy of the quantum

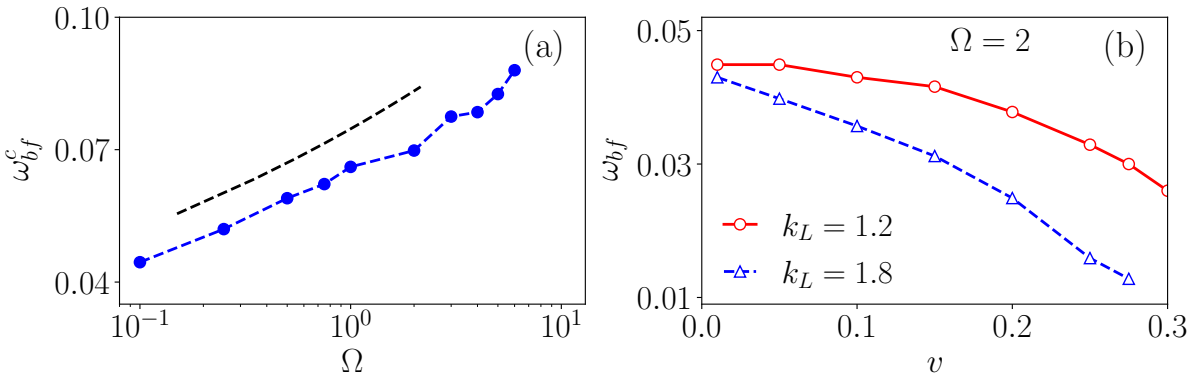

Figure 3.7: (a) Variation of breathing frequency (ω_{bf}^c) at critical k_L with Ω for fixed velocity $v = 0.1$. The other parameters are the same as those in Fig. 3.6. The critical breathing frequency increases and exhibits power law behaviour with Ω as $\omega_{bf}^c \sim \Omega^{0.16}$. The dashed line is drawn as a guide to the eye to show the power law nature of the ω_{bf}^c with Ω. (b) Variation of breathing frequency ω_{bf} with initial velocity v for different k_L keeping Rabi frequency fixed to $\Omega = 2$. The ω_{bf} is small for higher k_L for all the velocity.

soliton gets lower upon increasing Ω for a given k_L, suggesting a better way of obtaining an energetically stable soliton.

Another notable feature is the transition of the breathing soliton phase into the moving soliton upon the increase in the velocity as depicted in Figs. 3.4 and 3.5. Similar feature of the soliton with increase in the velocity has been reported in Ref. [32] for the binary mixture with an assumption of symmetric behaviour of the components. However, the presence of Rabi and SO coupling between the components make the nature of these breathing and moving solitons more complicated here. We can understand the instability that leads to the transition from breathers to the moving soliton by looking at the SO, Rabi, and the kinetic part of the chemical potential. While the kinetic term varies as v^2, the SO and Rabi parts will have linear and square dependence on the velocity, respectively. Due to this, one witnesses competition between the kinetic energy, which is positive and the SO and Rabi parts will have negative values upon changing the velocity. Overall, we expect the domination of the breathing soliton region by the SO and Rabi coupling contribution, while the moving soliton region kinetic energy dominates. The above also indicates that the chemical potential attains minimum at the critical velocity, which is consistent with our numerical observation.

After analyzing the dynamics of the solitons by imparting an initial velocity, in the following section, we present different dynamical features arising due to making an instantaneous quench in the coupling parameters (Ω and k_L).

3.5.3 Quench dynamics of quantum soliton

To better understand the effect of the SO and Rabi couplings on the overall dynamics (without giving any initial velocity) of the quantum solitons, in this section, we employ the instantaneous quench of the coupling parameters and analyze the resultant dynamics. With this protocol, we have obtained a variety of notable features like the generation of secondary and repulsive solitons, the dynamical phase transition from the QBS to the QSS and vice versa, etc.

In Fig. 3.8, we show the dynamical evolution of the soliton which generally arises due to the quench of Rabi coupling frequency by fixing the interaction strength to $g = -g_{\uparrow\downarrow} = 0.5$. The ground state soliton was initially prepared for $\Omega = 0, k_L = 2$. As we quench the Rabi frequency from $\Omega = 0 \rightarrow 1$ at finite time ($t \sim 20$) we notice that the QBS gets transformed to the QSS [see Figs. 3.8(a-c)]. However, upon employing $\Omega = 0 \rightarrow 5$, the QBS phase of the soliton gets transformed into a phase that displays expansion and certain characteristics of the repulsive soliton as shown in Figs. 3.8(d-f).

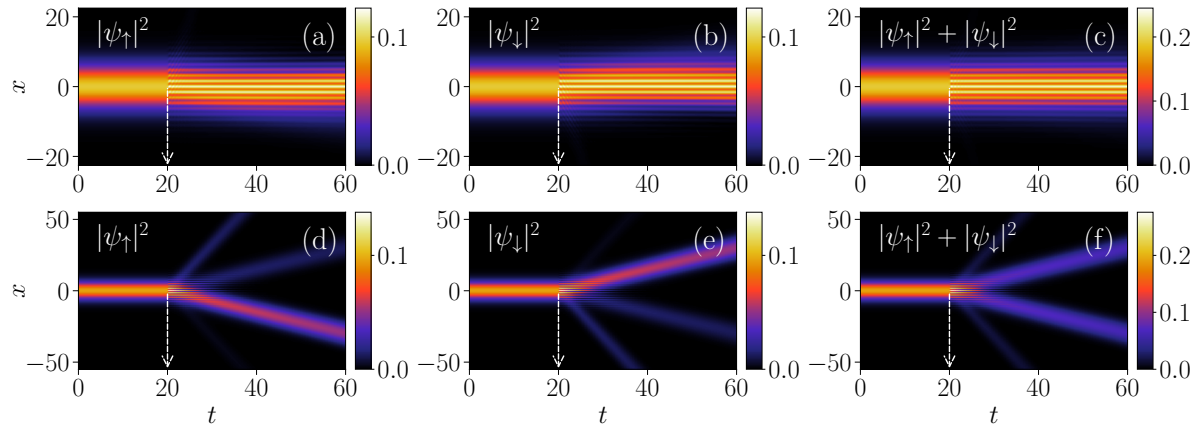

Figure 3.8: Dynamics of the quantum soliton appearing due to different quenching protocols at $g = -g_{\uparrow\downarrow} = 0.5$ as it was initially prepared for $\Omega = 0, k_L = 2$. (a)-(c): When the Rabi frequency is quenched as $\Omega = 0 \to 1$ at $t = 20$, the initial QBS phase changes to QSS, and (d)-(f): Quenching of Rabi frequency as $\Omega = 0 \to 5$ at $t = 20$ transforms the QBS phase into repulsive solitons.

In Fig. 3.9, we show the dynamical evolution of the solitons for two kinds of quenching protocols: (a-c) when $\Omega = 0 \to 50$ and $k_L = 2 \to 4$ and (d-f) when $\Omega = 0 \to 50, k_L = 2 \to 8$. In the first case, we find the appearance of multisolitons with interference-like patterns. Following the quenching, solitons get bifurcated into four that propagate away from each other and behave like repelling solitons. In the density profile, the outermost solitons show breathing-like features, and the innermost one inherits pure, stable soliton-like characteristics, i.e., they do not exhibit any change in shape and size with time as shown in Fig. 3.9(a-c). For the second quenching protocol ($\Omega = 0 \to 50$ and $k_L =$

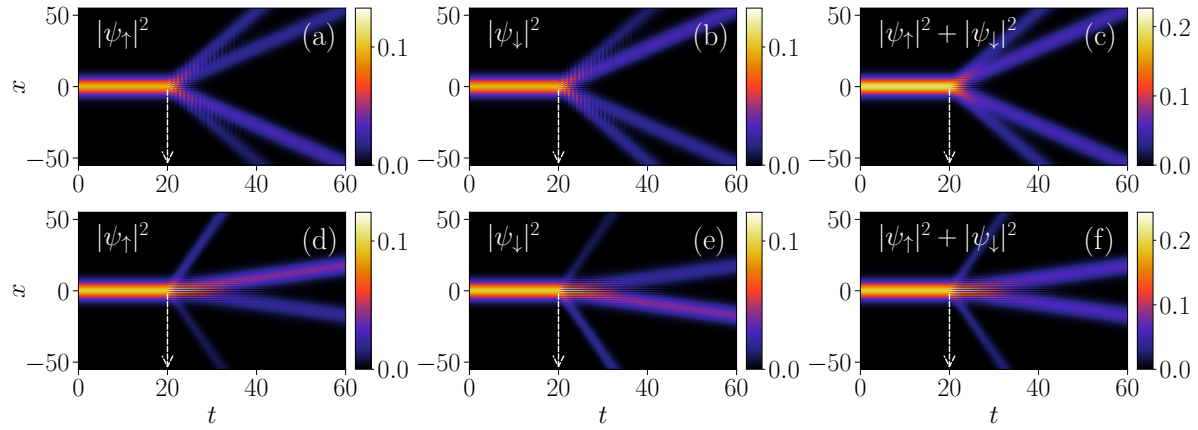

Figure 3.9: Dynamics of the quantum soliton appearing due to different quenching protocols at $t = 20$ with $g = -g_{\uparrow\downarrow} = 0.5$ as it was initially prepared for $\Omega = 0$, $k_L = 2$. (a)-(c): When both Rabi frequency and SO coupling are quenched as $\Omega = 0 \to 50, k_L = 2 \to 4$ at $t = 20$, which results the transformation of non-moving QBS soliton into moving multi soliton with large repulsion angle. (d)-(f): For quenching $\Omega = 0 \to 50, k_L = 2 \to 8$ at $t = 20$, QBS undergoes bifurcation into moving multi soliton state with small repulsive angle.

$2 \rightarrow 8$), again, multisoliton behaviour appears, which has some differences compared to the previous case. For this case, we notice that the outermost soliton-breather gets transformed into solitons with a relatively larger repulsive angle, while the innermost solitons transform into the stripe solitons and show attraction towards each other as depicted in Fig. 3.9(d)-(f). Thus, quenching of the coupling parameters (either one of Rabi and SO or both simultaneously) leads to generation of secondary solitons. Similar types of secondary solitons have been noticed experimentally as an excitation of the bright Matter wave solitons in quasi-one dimensional geometry [89].

Next, we discuss the effect of double quench protocols on the soliton dynamics. In Fig. 3.10, we show the dynamics of the quantum solitons as we implement double quenching protocols [90] of the coupling parameters for the initial ground state prepared at $\Omega = 0, k_L = 2$ for $g = -g_{\uparrow\downarrow} = 0.5$. In Fig. 3.10(a)-(c), we show the evolution when the first quench is performed by instantaneously switching off the SO coupling, that is, making the change $k_L = 2 \rightarrow 0$ at $t = 0$. Subsequently, we allow the soliton to evolve until $t = 20$ when we apply another quench by changing Rabi frequency as $\Omega = 0 \rightarrow 1$ and switching on the SO coupling as $k_L = 0 \rightarrow 2$. The first quenching, where we switch off the SO coupling, initially allows the solitons corresponding to the up and down components to display repulsive behaviour and move in the space until the application of a second quenching. After the second quench ($\Omega = 0 \rightarrow 1, k_L = 0 \rightarrow 2$) at $t = 20$, we notice a switching off the soliton position from $x = 0$ to some finite value which further remains invariant with time. Overall we see that the double quench protocol provides

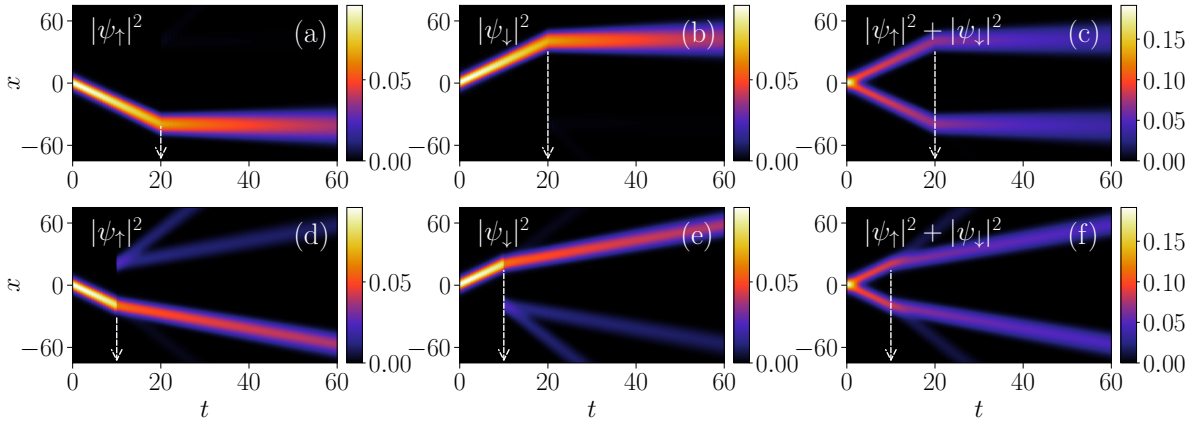

Figure 3.10: Dynamics of the quantum soliton prepared with $g = -g_{\uparrow\downarrow} = 0.5$, $\Omega = 0$, and $k_L = 2$ appearing due to double quenching protocols. (a)-(c): first quenching is performed at $t = 0$ with change in SO coupling ($k_L = 2 \rightarrow 0$) and second quenching is done at $t = 20$ when both coupling parameters are changed as $\Omega = 0 \rightarrow 1$ and $k_L = 0 \rightarrow 2$ which results as transforming the moving soliton to the stationary soliton. (d)-(f): At $t = 0$ first quenching is same as those in (a)-(c), while, at $t = 10$ second quenching is done as $\Omega = 0 \rightarrow 5$ that results transforming the moving soliton into soliton with secondary waves.

more stability to the solitons. This particular feature is one of the promising potential applications for quantum information and quantum computing which is based on the mixing and demixing of qubits [86, 91]. As we perform the first quenching the same as the previous case while in the second quench, only change in Rabi frequency is executed with $\Omega = 0 \to 5$ at $t = 10$ we find the appearance of moving BS with the generation of the second harmonics [see Fig. 3.10(d)-(f)].

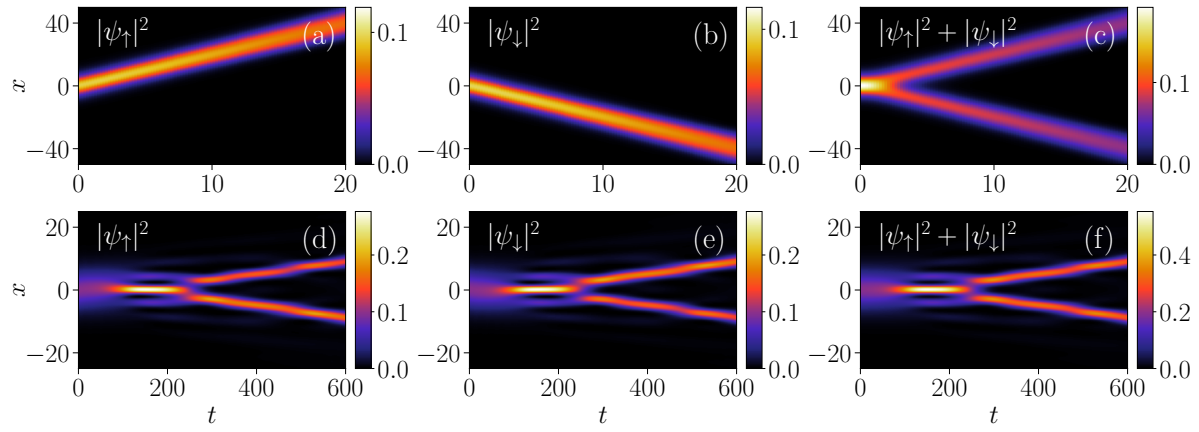

Figure 3.11: Dynamics of the quantum BS soliton prepared with $g = -g_{\uparrow\downarrow} = 0.5$ and $\Omega = 2$, $k_L = 0$ as quenching of both the coupling parameters are performed. (a)-(c): Quenching is done as $k_L = 0 \to 2$, $\Omega = 2 \to 0$ that results the transition of bright soliton into moving soliton. (d)-(f): With quenching $k_L = 0 \to 2$, $\Omega = 2 \to 4$ breather soliton gets bifurcated into filament like soliton beyond $t \sim 250$.

Further, we consider $\Omega = 2, k_L = 0$ with $v = 0$ which shows only the stable BS. As we quench $k_L = 0 \to 2$ and $\Omega = 2 \to 0$ the soliton repel each other [see Fig. 3.11(a)-(c)]. Upon quenching the Rabi coupling frequency from $\Omega = 2 \to 4$, we find that the soliton gets transformed into filaments after a finite time ($t \gtrsim 150$), which also appears to repel each other at ($t \gtrsim 250$) as depicted in Fig. 3.11 (d)-(f). The decay followed by the revival of the soliton along with multiple humps could be understood following the line of Ref. [87]. The main reason behind the fragmentation is the increase in the Rabi coupling while the change in the SO coupling triggers the movement of the soliton.

After discussing different dynamical behaviour arising in the quantum bright soliton due to the quench of the coupling parameter in what follows, we present the related dynamics for the quantum stripe soliton. In Fig. 3.12, we depict the dynamics that arise due to the quenching of both coupling parameters when the ground state is quantum stripe soliton nature.

In Figs. 3.12(a)-(c), we show the dynamics of soliton when quenching of both coupling parameters is performed at $t = 50$ for the initial state prepared with $g = -g_{\uparrow\downarrow} = 0.5$, $\Omega = 1, k_L = 2$. The quenching protocol for SO coupling is implemented as $k_L = 2 \to 0.2$, while

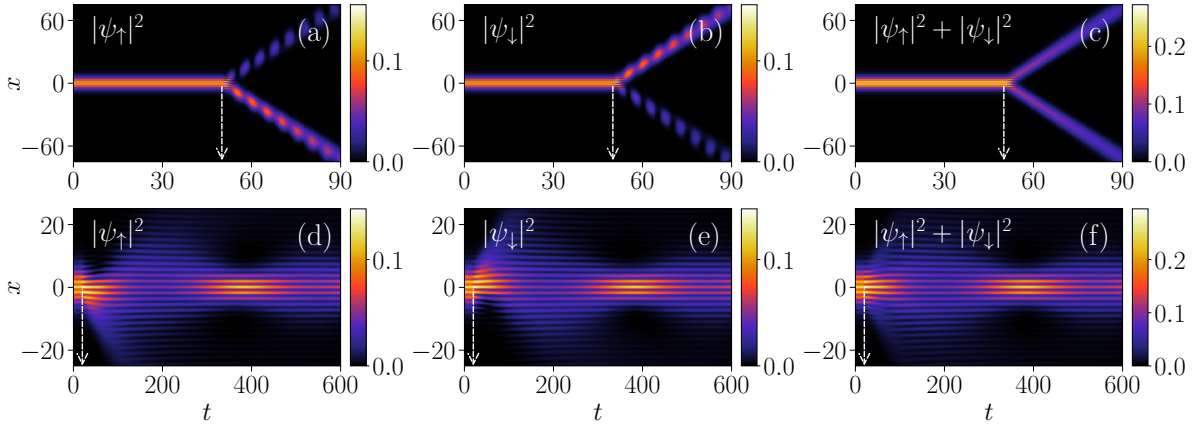

Figure 3.12: Dynamics of the quantum stripe soliton prepared with $g = -g_{\uparrow\downarrow} = 0.5$ and $\Omega = 1, k_L = 2$ and the quenching is performed at finite time. (a)-(c): Quenching is performed as $k_L = 2 \to 0.2, \Omega = 1 \to 0.5$ at $t = 50$ that results the transition from the stripe soliton to the space-time breather bright soliton. (d)-(f): Quenching is performed as $\Omega = 1 \to 2, k_L = 2$ at $t = 20$ resulting the transition from the stripe soliton to the breathing stripe soliton.

for Rabi coupling frequency, it is $\Omega = 1 \to 0.5$. We noticed that the quenching results in the bifurcation of stripe solitons into two parts wherein one shows weak breather-soliton while the other exhibits stronger behaviour. Interestingly, here we find that the quenching leads to the excitation mode that exhibits the spin-flipping characteristics, which is quite evident from the dynamical change in the population in the spin-up and spin-down state in the alternate fashion with time. The observed spin-flipping has been observed for the cases when Rabi coupling is quenched from the small ($\Omega < k_L^2$) to large ($\Omega > k_L^2$) value leading to the oscillatory instability. Similar observation has been made for the attractive binary mixture [87]. Note that the spin-flipping can also be observed by making an imbalance in the atomic population of the condensate state at the initial time [92]. Further, the decrease of Rabi coupling frequency leads to the disappearance of breathers and the generation of repulsive solitons. In Fig. 3.12(d)-(f), we depict the dynamics of soliton when quenching of Rabi coupling frequency is executed from $\Omega = 1 \to 2$ at $t = 20$. The quenching generates the stripe soliton breathers. Similar kinds of breathing solitons observed upon quenching the interaction strength so that the mean field contribution becomes small in the binary mixture of the condensates [65].

In Fig. 3.13, we show the dynamics that solely arises due to the quenching of the Rabi coupling for the ground states initially prepared for $g = -g_{\uparrow\downarrow} = 1.0$ and $\Omega = k_L = 2$. We quench the parameters as (a) $\Omega = 2 \to 1$ and in (b) $\Omega = 2 \to 3$ at $t = 10$. Here we notice that the stripe soliton exhibits expansion upon the quenching of the parameters. We find that the breathing oscillation frequency increases on increasing the interaction strength, as shown in Fig. 3.6(c). Further we consider another stripe soliton with $\Omega = k_L = 2$ in

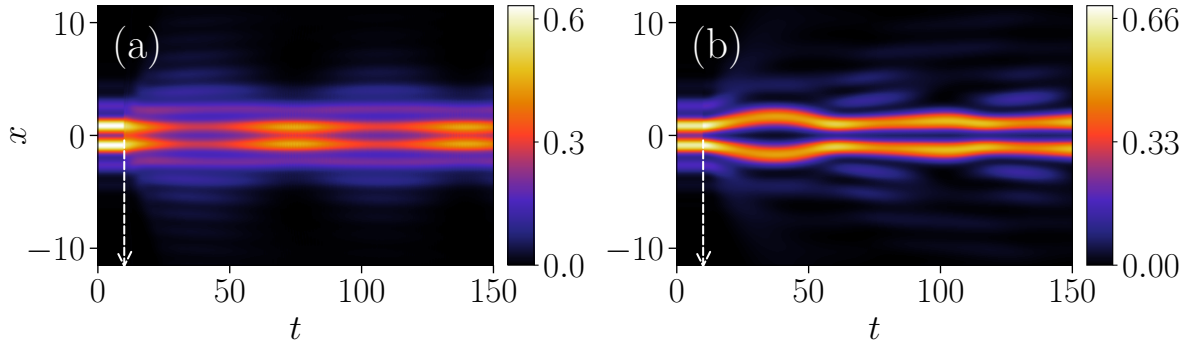

Figure 3.13: Dynamics of quantum stripe soliton prepared with $g = -g_{\uparrow\downarrow} = 1.0$ and $\Omega = k_L = 2$ as the quenching is performed on the Rabi frequency at $t = 10$. (a) Soliton gets bifurcated into repulsive and attractive solitons as Rabi coupling is quenched as (a) $\Omega = 2 \to 1$ and (b) $\Omega = 2 \to 3$.

which the Rabi coupling is quenched as $\Omega = 2 \to 1$. For this, we find that the frequency of the striped soliton breather becomes $\omega_{bf} \sim 0.08$ upon increasing the interaction strength. When we change $\Omega = 2 \to 3$, we obtain that the initial profile, which has two maximum peaks and two sidelobes, gets transformed into the multiple side lobes after the quench. Apart from this, the innermost soliton appears to repel each other after a finite time as they approach each other. A similar kind of dynamical behaviour gets repeated over time.

3.5.4 Collisional dynamics of quantum soliton

After studying the quenching dynamics of the quantum soliton by perturbing it with coupling parameters, in this section, we investigate how the solitons undergo different kinds of collisions that affect its overall stability depending upon the magnitude of the initial velocity. In particular, we find elastic, inelastic, repulsive and space-time breather soliton against collisions.

In absence of the trap, the quantum solitons are set in motion by giving an initial velocity $\mp v$ to the stationary ground state $(\psi_\uparrow, \psi_\downarrow)$ with a multiplier $\exp(\mp ivx)$ respectively [32]. Here we start for the case when the solitons are positioned at ± 50 for $g = -g_{\uparrow\downarrow} = 0.5$ and $\Omega = k_L = 0$. For a weak velocity ($v = 0.2$) the solitons undergo inelastic collision as depicted in Fig. 3.14(a). We find that the densities before the collision and after the collision are not the same. This indicates that after the collision, the solitons are unable to retain their shape and size same as those before the collision. As the initial positions of the soliton are at ± 50, the expected time for collision is $t = x/v = 250$, which can be clearly seen in Fig. 3.14(a). We find that after the collision ($t \sim 400$), the solitons start exhibiting the expansion, which makes them quite different in shape and size than they were before the collision. In order to understand the inelastic collision in a better

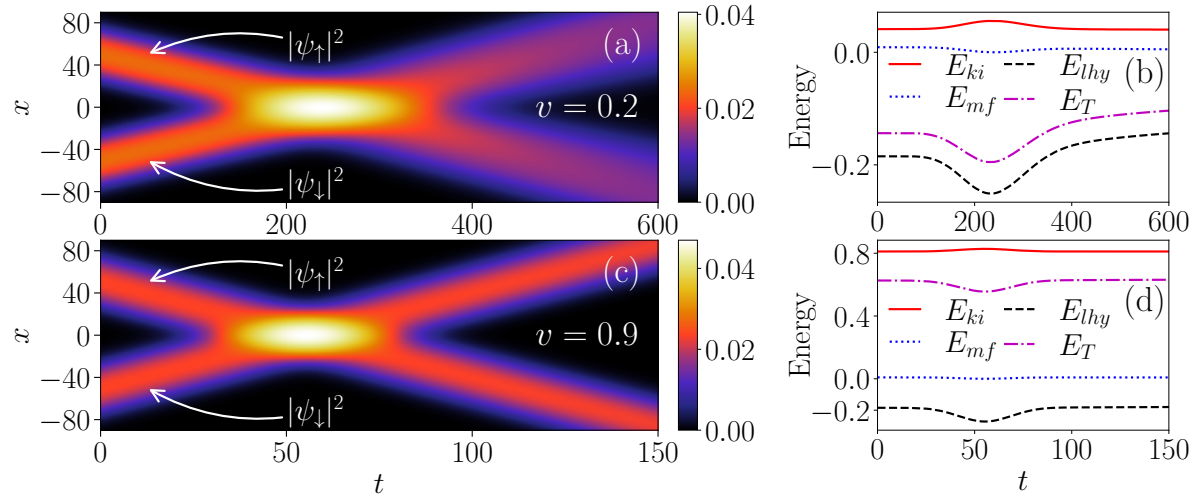

Figure 3.14: (a) The total density plots depicting the inelastic collision dynamics between the quantum soliton for $g = -g_{\uparrow\downarrow} = 0.5$ and $\Omega = k_L = 0$ as the velocity given to the up and down component is in the direction of $-x$ and x direction respectively, with magnitude $v = 0.2$. (b) Evolution of the different energies, E_{ki}, E_{lhy}, E_{mf} and total energy (E_T) with time for collision as shown in (a). There is a significant increase in the E_{lhy} and total energy (E_T) after the collision, indicating the inelastic nature of the same. (c) plots of the total density depicting the elastic collision dynamics of quantum soliton for $v = 0.9$. (d) Evolution of the different energies with time for the collision as shown in (c). Before and after the collision, all the energy remains the same, indicating the elastic collision nature.

way in Fig. 3.14(b) we plot the time evolution of the different energy contributions, like, kinetic energy (E_{ki}), MF energy (E_{mf}), LHY energy (E_{lhy}) and the total energy (E_T). The explicit form of energies is provided in the Eq. (3.8) of Sec. 3.3. We find that the MF energy, kinetic, LHY, and total energy after the collision do not remain the same as they are before the collision, which is consistent with the inelastic nature of the collision observed in the classical case.

For large velocity ($v = 0.9$), we observe the elastic collision with no change in the shape of the soliton after the collision. In Fig. 3.14 (c) we show the total density corresponding to the soliton when each component has been given an initial equal velocity ($v = 0.9$) but opposite direction with their initial positions at ± 50 for $g = -g_{\uparrow\downarrow} = 0.5$ and $\Omega = k_L = 0$. For this, the expected collision time will be at $t = 55.5$. We find that the densities before and after the collision are almost similar. In Fig. 3.14 (d), we plot the time evolution of the different energy contributions to confirm the elastic nature of the collision. It is observed that the MF energy, kinetic, LHY, and total energy remain the same after the collisions what they were before the collision, which are consistent with the elastic nature of the collision. This behaviour is consistent with the experimental observations of the collision between the QDs in three dimension [62]. Note that similar features of the collision between the QDs have been reported for the symmetric components of the

binary mixture with finite interaction [32].

So far, we have analyzed the collisional dynamics of the binary BECs with LHY correction and in the absence of Rabi and SO coupling parameters. However, as we consider it for finite SO and Rabi couplings, we find that the solitons get degenerated and thus, it could not provide the relevant collision dynamics. Considering what follows, we present the collision dynamics by keeping either SO or Rabi coupling frequency to be finite. Here as we obtain the spatially separated soliton, we employ the quenching of velocity and the coupling parameter, which was zero while preparing the states. To study the collisional dynamics with finite coupling parameters, we prepare the initial ground state with $\Omega = 1$ and $k_L = 0$. For this case, we find each spin component degenerates in the $\pm x$ direction and further exhibits the space-time breathers, which experience expansion after the finite time ($t \sim 40$). As we pass on the finite velocity, the solitons start interacting with each other. As for an example, for $v = 1$ the soliton starts moving towards each other that results in the elastic collision between them at $t \sim 20$. Note that here, after the collision, there is a small change in the density, which is different from the collision behaviour observed in Fig. 3.14(c). Therefore, we refer to this as the quasi-elastic collision. To avoid the repetition of depiction of the typical solitonic behaviour (like, space-time breathers and quasi-elastic collision) here we have not given any figure corresponding to this observation.

Next, we present the collisional dynamics by preparing the ground states with finite SO coupling and zero Rabi coupling frequency. We consider the system with $\Omega = 0$, $k_L = 0.5$ with $g = 0.5$ and finite velocity $v = 0.5$. Once we prepare the ground state, we analyse

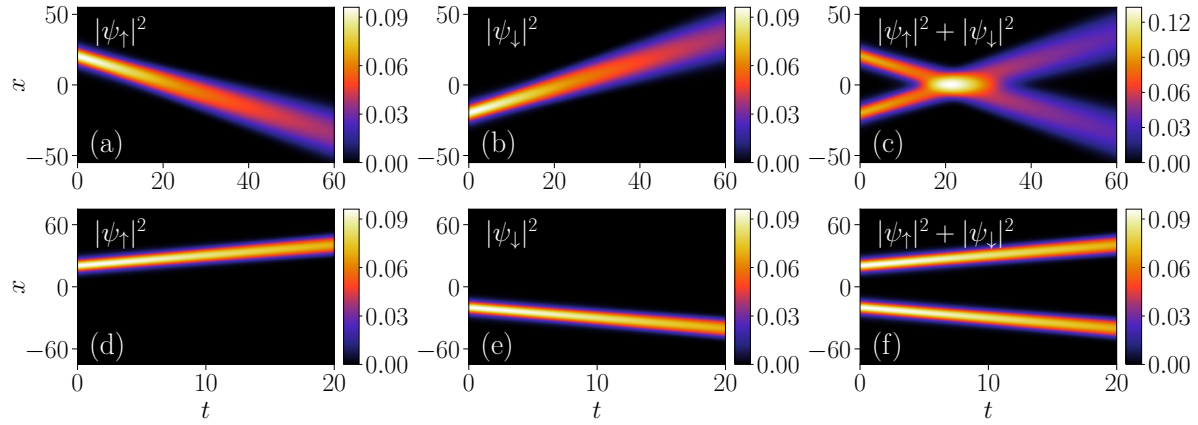

Figure 3.15: Collisional dynamics of the quantum solitons prepared with $g = -g_{\uparrow\downarrow} = 0.5$, $\Omega = 0$ and $k_L = 0.5$ and the individual components are given equal and opposite velocity ($v = 0.5$) at $t = 0$. Also, quenching on SO coupling parameter is performed as (a)-(c): $k_L = 0.5 \to 0.1$ and (d)-(f): $k_L = 0.5 \to 2$. Upon quenching the SO coupling, the solitons undergo inelastic collision in (a)-(c), while solitons repel each other for (d)-(f).

the collisional dynamics by quenching the SO coupling for two different situations. When $v > k_L/2$ non-degenerated soliton with decaying or expansion feature undergo inelastic collision as depicted in Fig. 3.15(a)-(c). However, for $v < k_L/2$ we observe that the soliton appears to repel each other upon progression of time [see Fig. 3.15(d)-(f)].

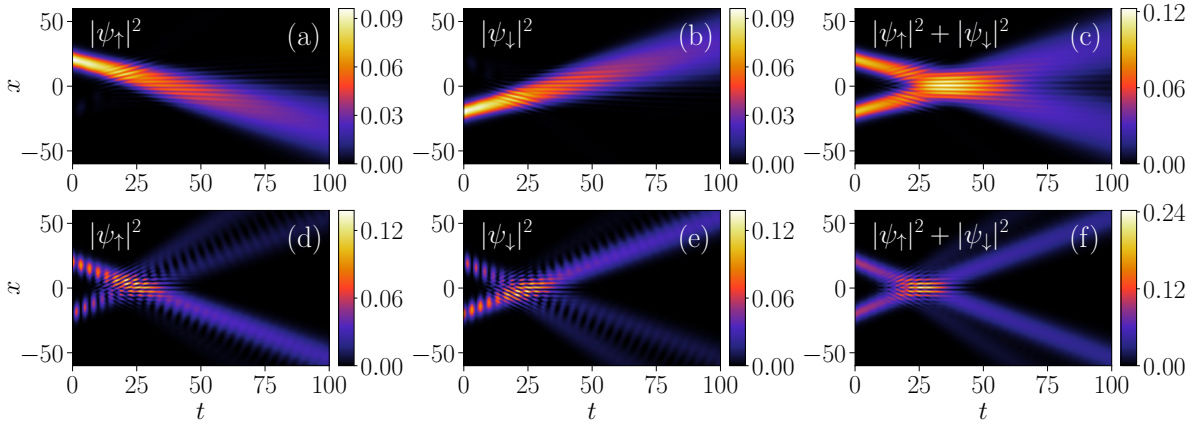

Figure 3.16: Collisional dynamics of the quantum solitons prepared with the same parameters and given same velocity at $t = 0$ as those for Fig. 3.15. At $t = 0$ the Rabi coupling is quenched as (a)-(c): $\Omega = 0 \to 0.1$ (d)-(f): $\Omega = 0 \to 0.8$. Upon quenching, Rabi coupling quantum soliton undergoes inelastic collision and displays an interference pattern (a)-(c). However, the soliton displays quasi-elastic collision with secondary solitons generation in (d)-(f).

Further, we analyse the collision dynamics by quenching the Rabi coupling. Like in the previous case, we study the dynamics of the solitons for two different situations. When $\Omega < k_L^2$ non-degenerated soliton undergo inelastic collision. They appear to show the stripe fringes as depicted in Fig. 3.16(a)-(c). For $\Omega > k_L^2$, we find a collision of bright soliton is quasi-elastic with the generation of interference stripe fringes. We also witness the generation of secondary solitons, as shown in Fig. 3.16(d)-(f).

3.6 Discussion and Conclusions

In this Chapter, using the MF model along with the LHY correction, we have numerically investigated the structure and dynamics of the ground state of the self-bound state in one-dimensional SO coupled BECs. Depending upon the nature of Rabi and SO couplings, the ground state is either quantum bright or stripe soliton. We have deduced an analytical solution of the quantum bright soliton without Rabi coupling. We have further studied the dynamics of the soliton using the three protocols, namely, by giving the initial velocity to the soliton, quenching the SO and Rabi coupling parameters, and allowing the component to collide by attributing an equal and opposite initial velocity.

We have obtained that the velocity perturbations generate breathing-like soliton. The breathing frequency increases upon the increase in the SO coupling for a given Rabi coupling frequency attains a maximum at the SO coupling, where the phase transition from the quantum bright to stripe soliton takes place. The magnitude of breathing frequency at critical SO coupling remains independent of the initial velocity and exhibits a power law dependence on the Rabi coupling frequency with an exponent ~ 0.16. We found that the critical breathing frequency increases upon increasing the interaction strengths. Using the contribution of the kinetic, SO, and Rabi energy terms, we find that while the domination of the breathing soliton phase by the SO and Rabi coupling, the moving soliton phase is the result of the kinetic energy part. This particular feature leads to the attainment of the minima of the chemical potential at the critical velocity where a change in the phase takes place. We have realized the presence of several dynamical phase transitions, like, QBS to QSS, and the multisoliton behaviour depending upon the quenching protocol of the Rabi coupling parameters. By quenching both Rabi and the SO couplings, we can control the direction/angle of the inner- and outer soliton. The quenching of Rabi and SO couplings facilitates several interesting dynamical phases like a repulsive soliton, space-time breathers, filamentation, etc.

We have also analyzed the collision dynamics of solitons. Depending upon the velocity of the soliton, we observed the presence of elastic and inelastic collisions. An inelastic collision occurs for low velocities, while it exhibits elastic collision at high velocities consistent with earlier experimental observations [62]. We have also complemented the collision dynamics by analyzing the nature of different energy terms like kinetic energy, MF energy, and LHY. Also, we analyzed the collision dynamics of the solitons by quenching either the velocity or the SO/Rabi coupling. For the former, we found the presence of quasi-elastic collision, while for the latter, we realized inelastic collision.

In this Chapter, we have considered the dynamical evolution of the quantum solitons for the situation when the MF contribution is negligible. In the next Chapter, we will explore the dynamics in the similar line presented in this Chapter in the presence of significant effective mean-field contribution along with the LHY correction in the quantum soliton.

Chapter 4

Effect of effective mean-field interaction on the structure and dynamics of the quantum droplets

Our work in the last Chapter (Chapter 3) was focused on analyzing the structure and dynamics of the droplet under the assumption of a vanishingly small effective mean-field interaction ($\delta g \approx 0$). However, achieving this precise situation in experimental settings is extremely challenging. Therefore, in this Chapter, we extend our analysis for the QD considering the finite effective mean-field interaction ($\delta g \neq 0$) and explore its impact on the structure and shape of the droplet. Wherever it is necessary, we also provide a one to one comparison between the behvaiour of the droplet in both with and without effective mean-field term. The Chapter is organized as follows: first, we give a brief introduction of the works done that have investigated the effect of the effective mean-field on the structure and dynamics of the droplet. Subsequently, we present our numerical results based on the MF model to simulate the SO coupled BECs. The work described here is published in Journal of Phys. B: Atomic, Molecular and Optical Physics [93].

4.1 Introduction

In this Section, we provide a very brief introduction to the effect of effective mean-field term on the shape, size, and dynamics of the QDs. The detailed introduction is given in the Chapter 1.

In general, subject to the MF contribution along with BMF, the condensate exhibits two types of self-bound states, such as a bright soliton with zero MF [79] and a flat-

top plateau droplet with a finite MF in one dimension. Depending upon the number of particles and interaction strength, Cheiney et al. experimentally observed the presence of these two self-bound states and explored a possible mechanism for this transition [23]. It exhibits a soliton-like ground state for a small number of atoms N, while for large N, a flat-top plateau droplet was realized. Following this, several numerical simulations were performed using the MF eGPEs with either the effective one-component BEC or binary BECs. Astrakharchik and Malomed considered the effective one-component eGPEs with finite MF contribution and identified the presence of Gaussian-like droplet for small N and flat-top droplet for large N [32]. However, Mistakidis et al. reported a similar type of QD in binary BECs in one dimension [65]. In a similar line, Li et al. reported the presence of stable QD with attractive intercomponent and repulsive intracomponent interaction for 2D SO coupled binary BECs with LHY and analyzed the effect of SO coupling terms on the stability of the droplet [94].

In the previous chapter 3, we have demonstrated that in the presence of the vanishingly MF contribution, the ground state of SO coupled BECs with the BMF term exhibits either quantum soliton or quantum stripe soliton. We demonstrated a systematic transition from the soliton into the breathing soliton, which further makes a transition into the moving soliton upon increasing the velocity perturbation in the ground state of the self-bound state. We also reported a large variety of novel features like the dynamical phase transition from plane to the stripe soliton, dynamical flipping of the spin state, generation of the secondary solitons, etc., when the dynamics are generated through the quenching of the coupling parameters. However, in the presence of effective mean-field terms, the dynamical robustness of the quantum soliton has not been investigated in great detail for the SO coupled BECs [80]. In this Chapter, we consider the effect of effective mean-field interaction on the overall structure and dynamics of the QD and show the transition from the quantum bright soliton to the QD (with flat top) state upon the increase in the MF contribution by keeping the LHY contribution fixed. We generate the dynamics in the droplet by either giving equal and opposite velocities to the components or quenching the interaction strength and coupling parameters. For small velocities, we find the presence of a breathing droplet, which eventually transforms into a moving droplet at large velocities for both the plane wave and stripe wave phases. The critical velocity at which moving droplets are observed decreases upon increasing the effective mean-field interaction ($\delta g/g$). For small interaction strengths, quenching the droplet leads to an expansion of the droplet, while for large quenchings, it triggers breathing-like oscillations. We demonstrate a significant role played by the effective mean-field contribution to the nature of the collision between the droplets. The collision is inelastic for vanishingly small MF con-

tributions, while for a higher value of the effective mean-field interaction, it is elastic in nature. Through this analysis, we have explored various intriguing features, such as the ability to control the critical velocity at which the transition from a breathing droplet to a moving droplet occurs by tuning the parameter $\delta g/g$ for both bright and stripe droplet phases.

The structure of this Chapter is as follows. In section 4.2, we present governing equations and numerical simulation details. Following this in section 4.3, we provide a detailed analysis of the ground state structure for a vanishingly small MF term and finite MF contribution followed by their dynamics, which have been set up in the system through different means. First, we present the different sorts of dynamics that appear in the system due to different velocities, followed by the dynamics due to the quenching of the nonlinear interactions. Further, we present some of the interesting dynamical behaviours that appear due to collision for both finite and zero MF terms. Finally, we conclude our work in section 4.4.

4.2 Beyond mean-field model for spin-orbit coupled BECs

For the symmetric condition $g_{\uparrow\uparrow} = g_{\downarrow\downarrow} = g$ and implementing effective mean-field interaction $\delta g = g + g_{\uparrow\downarrow}$, the Eq. 1.54 reduces to followings sets of coupled eGPEs in dimensionless form [33, 80]:

$$\begin{aligned} \mathrm{i}\partial_t\psi_\uparrow = \Bigg[& -\frac{1}{2}\partial_x^2 - \mathrm{i}k_L\partial_x + \frac{\delta g}{2}\left(|\psi_\uparrow|^2 - |\psi_\downarrow|^2\right) + g|\psi_\uparrow|^2 + g_{\uparrow\downarrow}|\psi_\downarrow|^2 \\ & - \frac{g_{\mathrm{LHY}}^{3/2}}{\pi}\sqrt{|\psi_\uparrow|^2 + |\psi_\downarrow|^2}\Bigg]\psi_\uparrow + \Omega\psi_\downarrow, \end{aligned} \tag{4.1a}$$

$$\begin{aligned} \mathrm{i}\partial_t\psi_\downarrow = \Bigg[& -\frac{1}{2}\partial_x^2 + \mathrm{i}k_L\partial_x + \frac{\delta g}{2}\left(|\psi_\downarrow|^2 - |\psi_\uparrow|^2\right) + g_{\downarrow\uparrow}|\psi_\uparrow|^2 + g|\psi_\downarrow|^2 \\ & - \frac{g_{\mathrm{LHY}}^{3/2}}{\pi}\sqrt{|\psi_\uparrow|^2 + |\psi_\downarrow|^2}\Bigg]\psi_\downarrow + \Omega\psi_\uparrow. \end{aligned} \tag{4.1b}$$

where $\psi_\uparrow$ and $\psi_\downarrow$ correspond to the wavefunctions of the spin-up and spin-down components, respectively, k_L is the SO coupling strength, Ω is the Rabi coupling frequency, g accounts the intraspecies interaction, and $g_{\uparrow\downarrow}$ represents interspecies interaction strength.

Here $g_{\rm LHY} = g$ is the interaction due to LHY correction, and $\delta g = g_{\uparrow\downarrow} + g$ represents the imbalance between the MF contributions from the inter and intra-species interactions. Note that for $g = -g_{\uparrow\downarrow}$ implies $\delta g = 0$, which has been used to analyze the self-bound state (quantum soliton) for the SO coupled BECs in Chapter 3. In this Chapter, we have considered the different ranges of $\delta g/g$, which yields the finite contribution from the overall effective mean-field term in the self-bound state. The normalization of the condensate wave function follows [33, 92, 95]:

$$\int_{-\infty}^{\infty} \left(|\psi_\uparrow|^2 + |\psi_\downarrow|^2\right) dx = 2. \tag{4.2}$$

We have chosen transverse harmonic oscillator length $a_\perp = \sqrt{\hbar/(m\omega_\perp)}$ as a characteristic length scale (where, $\omega_\perp$ is the trap frequency in the transverse direction), $\omega_\perp^{-1}$ as a time scale, and $\hbar\omega_\perp$ as an energy scale to obtain the non-dimensionalize equations (4.1). Here $g = 2Na_{\uparrow\uparrow}/a_\perp$ and $g_{\uparrow\downarrow} = 2Na_{\uparrow\downarrow}/a_\perp$ with N as number of particles, $a_{\uparrow\uparrow}$ and $a_{\uparrow\downarrow}$ being the scattering length corresponding to intra- and inter-species components, respectively. The corresponding adimensional scheme for the SO and Rabi coupling is $k_L \to k_L a_\perp$ and $\Omega \to \Omega/\omega_\perp$. The wave function is rescaled as $\psi_{\uparrow,\downarrow} = \psi_{\uparrow,\downarrow}\sqrt{a_\perp}$.

In order to closely replicate the model described in the Chapter with experimental conditions, we select parameters similar to those observed in droplets formed by a mixture of binary hyperfine states in ^{39}K condensates [15, 23, 62]. We assume a total particle number in the droplets of approximately $N \sim 10^4$. The droplet is confined within a harmonic trap potential with frequencies of $\omega_x = 2\pi \times 50$ Hz and $\omega_\perp = 2\pi \times 800$ Hz in the axial and perpendicular directions, respectively. Using these values, the characteristic length scale is determined to be $a_\perp = 0.568\,\mu$m.

The pseudo-spin states $|\uparrow\rangle$ and $|\downarrow\rangle$ in our model correspond to the two internal hyperfine states $|F = 1, m_F = -1\rangle$ and $|F = 1, m_F = 0\rangle$ of the ^{39}K atomic condensate. The interaction strengths for intra- and interspecies components can be adjusted using the Feshbach resonance of the s-wave scattering lengths. By choosing the scattering length values $a_{\uparrow\uparrow} = a_{\downarrow\downarrow} = -a_{\uparrow\downarrow} = 0.2686a_0$ (where a_0 is the Bohr radius), a nearly negligible MF interaction can be achieved, resulting in a dimensionless intracomponent interaction strength of $g = g_{\rm LHY} \approx 0.5$ with $\delta g = 0$. Introducing a finite δg, we consider the intercomponent interaction in the range of $g_{\uparrow\downarrow} = -0.5, -0.05$, allowing for variation in $\delta g = 0, 0.9$. This range of δg can be obtained by considering $a_{\uparrow\uparrow} = a_{\downarrow\downarrow} = 0.2686a_0$ and $a_{\uparrow\downarrow} = -0.2686, -0.0268$. The Rabi coupling frequency (Ω) depends on the intensity of the Raman lasers, which can be adjusted using the frequency with a typical experimental

value of $\Omega = 2\pi \times 0.8\,\text{kHz}$, resulting in a dimensionless Rabi coupling frequency of $\Omega = 1$. Additionally, the strengths of the SO coupling (k_L) depend on both the laser's geometry and wavelength. In the present study, we consider a dimensionless SO coupling range of $k_L = 0.5, 3$, with the laser wavelength varying from $\lambda_L = 5.047$ μm to 841nm [87]. The corresponding physical unit for the characteristic velocity would be $v \sim 3$ mm/sec.

The ground state is obtained by numerically solving the coupled eGPEs (4.1a) and (4.1b) using the imaginary-time method with the aid of split-step Crank-Nicolson scheme [74, 80, 86]. We consider the box size for all the simulations as $[-153.6 : 153.6]$ with a spatial resolution of $dx = 0.025$. We assume the Gaussian initial condition with anti-symmetric profiles on the components, i.e., $\psi_\uparrow(x) = -\psi_\downarrow(-x)$ to obtain all the ground states. For all the simulations, the time step is fixed at $dt = 10^{-5}$. We consider the interaction strength as $g = 0.5$ and take $\delta g/g = 0, 0.1, 0.5$.

4.3 Numerical results

In the previous Chapter (Chapter 3), we showed that for the vanishingly small MF contribution ($\delta g = 0$), depending upon the coupling parameters range, we may observe either a quantum-bright droplet (QBD) or quantum stripe droplet (QSD) for SO coupled BECs with LHY correction [80]. However, in the laboratory experiment, δg happens to be finite [30]. Also, some recent theoretical and experimental observations report the transition from the Gaussian-like droplet to the flat-top like droplets either upon increasing the $\delta g/g$ or increasing the number of particles [65, 66]. In continuation of the previous chapter's work on the structure of the droplets for $\delta g = 0$ (Chapter 3), in this section, we present the effect of finite but small $\delta g/g$ on the ground state phases of the SO coupled droplet. Further, we provide the dynamics of the droplet for different sorts of perturbations, namely by giving initial equal and opposite velocities to the components, quenching the interaction parameters, and allowing the condensate component to collide in the presence of $\delta g/g$ and analyzing the dynamics of the droplet for $\delta g/g \neq 0$.

4.3.1 Ground state structure of the quantum droplets with different phases

We now demonstrate the structure of the droplet by considering the deviation from the vanishingly small MF term ($\delta g = 0$). To make the $\delta g/g$ finite, however, $\delta g/g < 1$, one of the necessary arrangements used for the droplet formation [28], we have varied the interspecies interaction keeping intraspecies interaction fixed. We first consider the

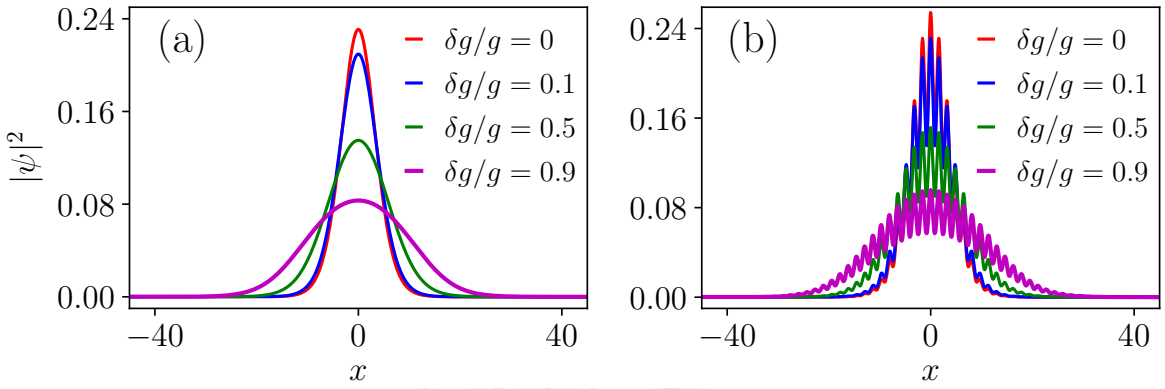

Figure 4.1: Ground state density profiles for (a) quantum bright droplet phase ($\Omega = 1$ and $k_L = 0.5$) and (b) quantum stripe droplet phase ($\Omega = 1$ and $k_L = 2$) for different $\delta g/g$. Upon increasing the $\delta g/g$, the peak density reduces, and the profile gets flattened in both phases.

quantum-bright droplets, which we prepared by assuming $g = 0.5$, $\Omega = 1$, $k_L = 0.5$, and $g_{\uparrow\downarrow} = -0.5, -0.45, -0.25, -0.05$ and employing $\delta g/g = 0, 0.1, 0.5, 0.9$, respectively. In figure 4.1(a), we show the ground states for different $\delta g/g$ ($\delta g/g = 0, 0.1, 0.5, 0.9$). We find that the ground state for the finite $\delta g/g$ shows QBD the same as those obtained for $\delta g/g = 0$. Upon increasing the $\delta g/g$, we notice a decrease in the density peak along with an increment in the shape of the droplets that leads to a transformation of the droplet from the sech-like shape to the broader sech-like [28, 65]. Figure 4.1(b) depicts the size of the QSD for different $\delta g/g$ with $\Omega = 1$ and $k_L = 2$. Similar to the change in shape and size of the QBD phase droplets upon the increase of $\delta g/g$, here we also find that the peak density of QD decreases upon increasing $\delta g/g$, while the size of the droplet gets bigger. The overall features of the droplets upon increasing $\delta g/g$ become consistent with those reported for the binary BECs [65].

4.3.2 Dynamics of the quantum droplets with varying external velocities

Next, we focus on analyzing the different sorts of dynamics of the droplet. We have attained the dynamics using the three protocols, namely, by giving a small initial velocity to each component, making a sudden quench in the nonlinear interaction parameters, and allowing the collision between the droplets. In what follows, we analyze these dynamics for $\delta g/g = 0$ and $\delta g/g \neq 0$. The dynamics of the ground state of QDs have been explored by numerically solving the eGPEs [cf. equations (4.1)] employing the real-time propagation scheme [80]. First, we explore the dynamics by providing initial velocity to the condensate. Note that here, we provide the velocity to the up and down components of the

droplet, respectively, in the negative and positive directions. This particular methodology is motivated by the generation of synthetic SO coupling in laboratory experiments [46], where the velocity of the individual component can be tuned by changing the SO coupling. For instance, the SO coupling imparts a positive velocity (k_L) to the up-component, while it imparts a negative velocity to the down-component. However, in our case, through phase imprinting, we can impart a negative velocity to the up-component and a positive velocity to the down-component [87]. Depending on the magnitude of the velocity, we obtain the appearance of different sorts of dynamics of the droplet, like breathing droplets, fragmented droplets, etc. [80].

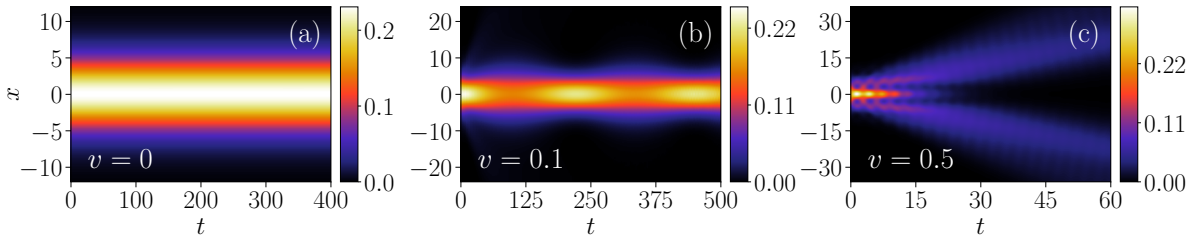

Figure 4.2: Dynamics of the quantum-bright droplet for different initial velocities for $\delta g/g = 0$: (a) $v = 0$ (b) $v = 0.1$ and (c) $v = 0.5$. The ground state was prepared with the interaction strength $g = -g_{\uparrow\downarrow} = 0.5$, $\Omega = 1$, and $k_L = 0.5$. For $v = 0$, no change in the shape and size of the density profile happens, while at $v = 0.1$, we notice a breathing droplet, which transforms into a moving droplet at $v = 0.5$.

In figure 4.2(a)-(c), we illustrate the temporal evolution of QBDs at different initial velocities $v = 0, 0.1$ and 0.5 as the ground state was prepared for $g = -g_{\uparrow\downarrow} = 0.5(\delta g/g = 0)$, $\Omega = 1$, and $k_L = 0.5$. Note that the up and down components have been given the velocity in the negative and positive direction respectively [80]. For $v = 0$, we do not find any change in the shape and size of the condensate as the system evolved with time [see figure 4.2(a)], indicating the solitonic nature of the droplet. However, for the finite but small velocity ($v = 0.1$), the droplet experiences a breathers-like excitation as shown in figure 4.2(b). Upon further increasing the v to 0.5, the droplet undergoes bifurcation into two droplets as depicted in figure 4.2(c). The two lobes of the fragmented droplet start moving in positive and negative directions leading to the appearance of moving droplets. Note that the presence of moving droplets is not trivial for the SO coupled BECs, as the SO coupling breaks the Galilean invariance of the system. However, here we find that the moving droplet starts existing beyond a critical velocity. Similar behaviour of the existence of moving solitonic states has been reported for the solitons moving below a critical velocity for two-dimensional SO coupled BECs [95].

In figure 4.3, we show the dynamics of QSDs for different velocities $v = 0, 0.1$ and 0.5 in which we prepare the ground state for $g = -g_{\uparrow\downarrow} = 0.5(\delta g/g = 0)$, $\Omega = 1$, and

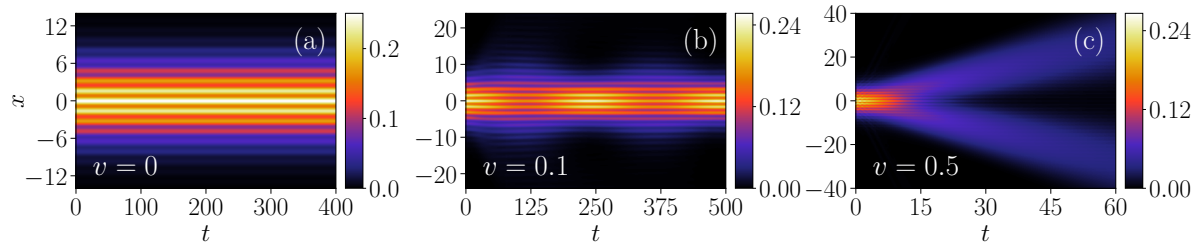

Figure 4.3: Dynamics of quantum stripe droplet at different initial velocities for $\delta g/g = 0$: (a) $v = 0$, (b) $v = 0.1$, and (c) $v = 0.5$. The other parameters are $\Omega = 1$ and $k_L = 2$. For $v = 0$, the soliton moves without any distortion in shape and size while we observe breathers for $v = 0.1$, which further transforms into a moving droplet for $v = 0.5$.

$k_L = 2$. For $v = 0$, the QSD propagates with no change in the shape and size as shown in figure 4.3(a). With a finite velocity $v = 0.1$, the stripe phase of the droplet exhibits breather-like expansion and compression [see figure 4.3(b)]. At $v = 0.5$, similar to the QBD stripe phase also has the presence of moving droplets [see figure 4.3(c)].

In both the quantum bright and stripe phases of the droplet, we find that the increase in the velocity results in the transition from the breathing droplet to the moving droplet. Astrakharchik and Malomed report a similar feature of the droplet with an increase in the velocity for the binary mixture with an assumption of symmetric behaviour of the components [32]. However, in the present study, we find the presence of Rabi and SO coupling between the components makes these breathing and moving nature of droplets more intricate. To probe the genesis of this peculiar feature, we compute the chemical potentials (μ) corresponding to the bright as well as stripe phase of the droplet and analyze the detailed behaviour. In figure 4.4, we show the variation of chemical potential (μ) with the velocity perturbation for different k_L keeping $\Omega = 1$ and $\delta g/g = 0$ parameters

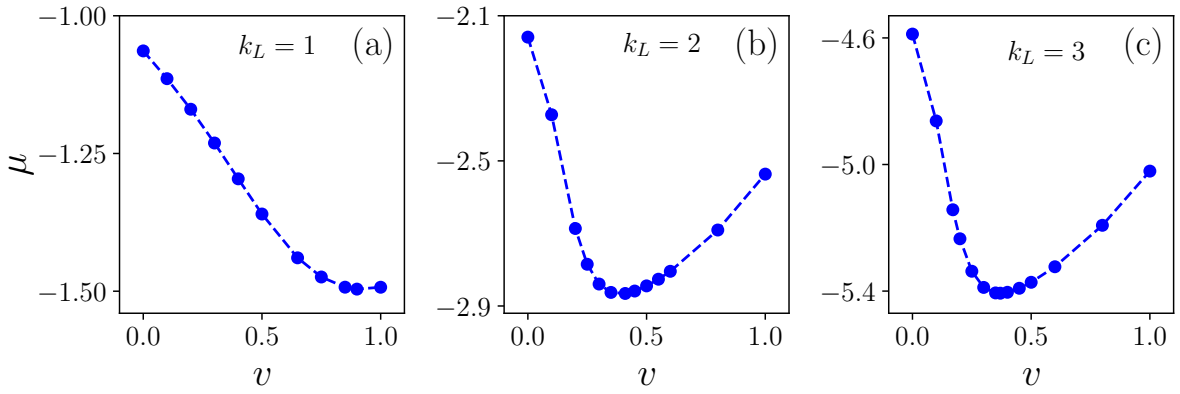

Figure 4.4: Variation of chemical potential μ with velocity for different k_L: (a)for $k_L = 1$, (b) for $k_L = 2$, and (c) for $k_L = 3$. Other parameters are $\delta g/g = 0$ and $\Omega = 1$. The velocity at which μ attains minima provides the critical velocity (v_c) at which the breather droplet transforms into a moving droplet. v_c decreases upon increasing the k_L.

fixed. We find that the chemical potential attains its minimum at the critical velocity (v_c) beyond which the droplet exhibits the bifurcation into the moving droplets. For critical velocity of the transition appears to be at $v_c \sim 0.9, 0.41$ and 0.37 respectively for $k_L = 1, 2$ and 3. The presence of two contrasting different dynamical regions of the droplets below and above the critical velocity can be understood as the domination of the breathing droplet region by the SO and Rabi coupling contribution, while the moving droplet region by the domination of the kinetic energy [80].

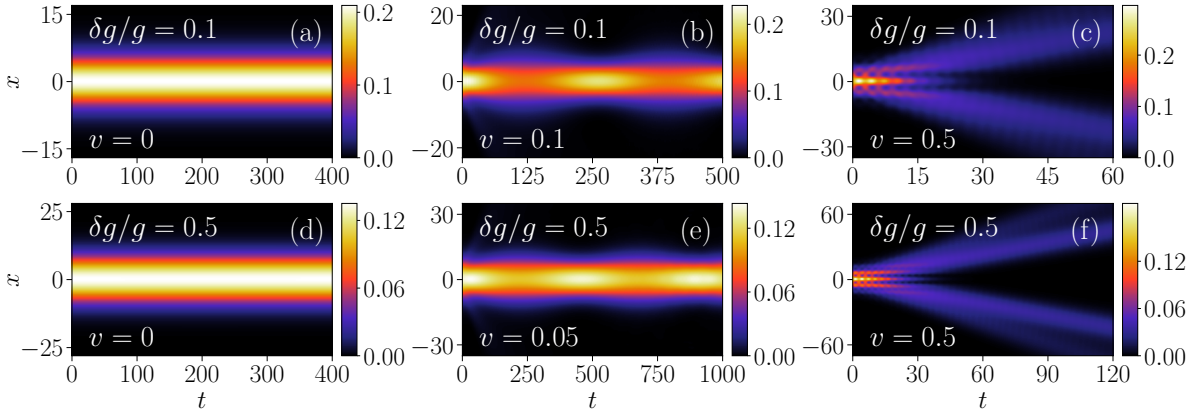

Figure 4.5: Dynamics of quantum droplet for finite $\delta g/g$ for $\Omega = 1$ and $k_L = 0.5$. (a)-(c) $\delta g/g = 0.1$ and velocity $v = 0, 0.1, 0.5$ respectively. (d)-(f) $\delta g/g = 0.5$ for different initial velocities, $v = 0, 0.05$ and 0.5 respectively. For both $\delta g/g$ at $v = 0$, the droplet remains stable, while for finite velocity ($v = 0.1, 0.05$), we observe a breather droplet, which converts into moving droplets upon increasing the velocity to $v = 0.5$. The breathing frequency appears to decrease compared to those for $\delta g/g = 0$ for the quantum bright droplet.

In figure 4.5, we illustrate the dynamics of QBD for finite $\delta g/g$: $\delta g/g = 0.1$ (in top panel) and $\delta g/g = 0.5$ (bottom panel) for different velocities. In figure 4.5(a)-(c), we fixed the interaction strength $g = 0.5$, $g_{\uparrow\downarrow} = -0.45$, while, in figure 4.5(d)-(f) $g = 0.5$, $g_{\uparrow\downarrow} = -0.25$, $\Omega = 1$, and $k_L = 0.5$. For $\delta g/g = 0.1$, the droplet exhibits solitonic nature at $v = 0$ same as those observed for $\delta g/g = 0$. Upon increasing the velocity to $v = 0.1$, the droplet exhibits breathing nature as shown in figure 4.5(b). However, the breathing frequency appears to be smaller for finite $\delta g/g$ than those for $\delta g/g = 0$ for the same velocity. At large velocity $v = 0.5$ droplet transforms into a moving droplet as depicted in figure 4.5(c). Interestingly with finite $\delta g/g$, the bifurcation of moving droplets takes place after a long time compared to those for $\delta g = 0$. Further, increase in $\delta g/g = 0.5$, we find a similar behaviour of the droplet with a change in the velocity as those observed for $\delta g/g = 0.1$. However, we observe two remarkable differences. First, the frequency of the breathing phase appears to be smaller than those for $\delta g/g = 0.1$, and the bifurcation of the droplet happens for an even larger time ($t \sim 25$) than those for $\delta g/g = 0.1$ which

is $t \sim 10$. Overall, we find that the increase in $\delta g/g$ leads to the enhancement in the dynamical stability of the droplet.

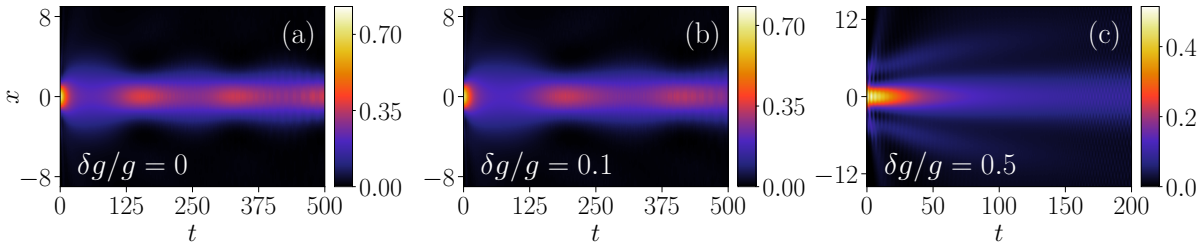

Figure 4.6: Dynamical evolution of total density of the quantum bright droplet for different $\delta g/g$: (a)$\delta g/g = 0$ (b) $\delta g/g = 0.1$ and (c) $\delta g/g = 0.5$ as the initial velocity given to the condensate is $v = 0.5$. The other parameters are $\Omega = 1, k_L = 1$ and $g = 0.5$. Upon increase in $\delta g/g$ leads to decrease in the breathing frequency and at high $\delta g/g (\sim 0.3)$ the droplet transforms into the moving droplet.

In figure 4.6, we show the dynamical evolution of the total density of the QBD by keeping the velocity fixed to $v = 0.5$ and varying the $\delta g/g$ keeping $g = 0.5$, $\Omega = 1$ and $k_L = 1$. At $\delta g/g = 0$, the droplet exhibits the breathing-like oscillation with time period $T \sim 154$, which decreases to $T \sim 220$ upon the increase of $\delta g/g = 0.1$. Upon further increase in $\delta g/g (= 0.5)$ results in the appearance of the moving droplets. Overall we find that the transition from the breathing to the moving droplet can be controlled by either tuning the velocity for a fixed MF interaction parameter $(\delta g/g)$ or by varying the $\delta g/g$ for fixed velocity. In order to get a comprehensive picture of the regime for the breathing and

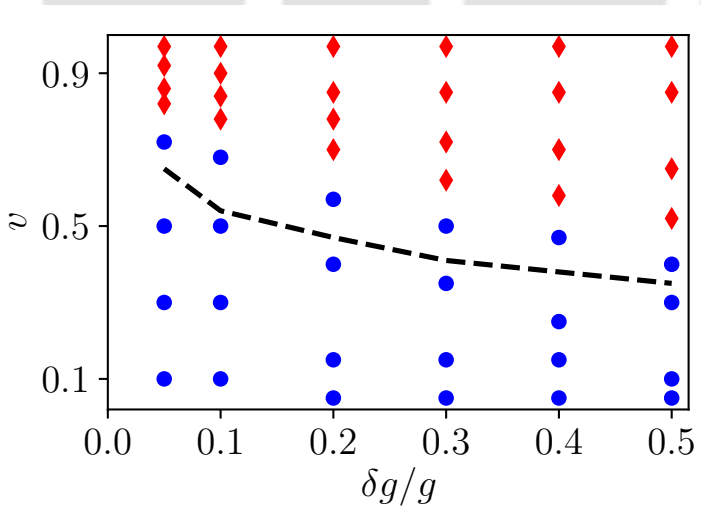

Figure 4.7: Plot showing the region of the breathing (blue dots) and moving (red diamond) droplets in the parameters space of v and $\delta g/g$ for the bright droplet region ($\Omega = 1, k_L = 1$ and $g = 0.5$). The velocity at which the transition from the breathing droplet to the moving droplet takes place for a given $\delta g/g$ decreases upon the increase in $\delta g/g$. The dashed black line shows the critical velocity for the transition from breathing to the moving droplet identified based on the velocity at which the MF energy attains the maximum value.

moving droplet we show them in the $\delta g/g$ and v parameter space in figure 4.7. The blue dots represent the breathing droplet region, while the red diamonds depict the moving droplet region, which has been obtained by analyzing the nature of the total density. We find that the increase in $\delta g/g$ makes the transition from breathing to the moving droplet at a relatively lower velocity compared to those for lower $\delta g/g$. This particular feature can be attributed to the decrease in the stiffness of the droplet upon the increase in $\delta g/g$ [32].

Following this, we aim to calculate the critical boundary that separates the breathing and moving droplets in the $v - \delta g/g$ plane. To achieve this, we determine the critical velocity at which the chemical potential reaches its minimum, similar to the approach used in figure 4.4, for various $\delta g/g$ values. This allows us to identify the threshold above which the droplet transitions from breathing to a moving state. Our investigation demonstrates that this method is reliable for droplets in the stripe phase ($k_L^2 > \Omega$). However, in the case of the plane wave phase, the strong influence of the Rabi term in the energy complicates the interpretation of the MF interaction and the LHY term, which are primarily responsible for the appearance of the critical velocity associated with the minimum chemical potential. For instance, when considering $k_L = 1$, we observe that the minima of the chemical potential, corresponding to the critical velocity does not significantly change with increasing $\delta g/g$. However, upon analyzing the individual contributions of the MF, SO, Rabi, and kinetic terms to the chemical potential, we find that the MF energy reaches its maximum value for the critical velocity at a given $\delta g/g$. Notably, the critical velocity associated with the maximum MF energy exhibits a substantial variation as $\delta g/g$ increases. Thus, we have adopted the criterion of the maximum MF term in the energy

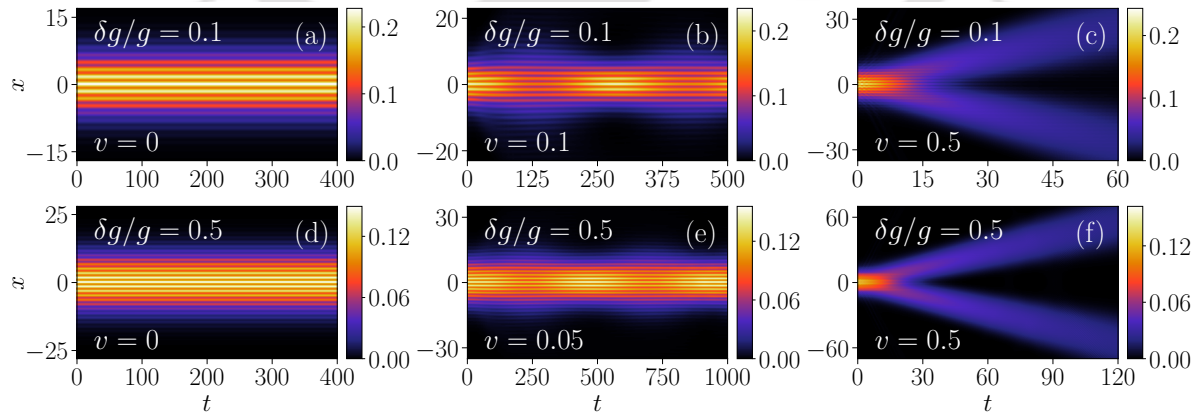

Figure 4.8: Dynamics of quantum stripe droplet for finite $\delta g/g$ for $\Omega = 1$ and $k_L = 2$. (a)-(c): $\delta g/g = 0.1$ and velocity $v = 0, 0.1, 0.5$ respectively. (d)-(f): $\delta g/g = 0.5$ for different initial velocities, $v = 0, 0.05$ and 0.5 respectively. Upon increasing the velocity from $v = 0$ to $v = 0.1$ for $\delta g/g = 0.1$ and from $v = 0$ to $v = 0.05$ for $\delta g/g = 0.5$, we observe a transition from solitonic droplet to breather droplet. For large velocity ($v = 0.5$), moving droplets are observed for both $\delta g/g$.

to determine the critical velocity for the transition from breathing to moving droplets. By employing this approach, we observe a significant variation in the critical velocity as $\delta g/g$ varies. Considering this aspect, we have represented the critical boundary between breathing and moving droplets using a dotted line in figure 4.7.

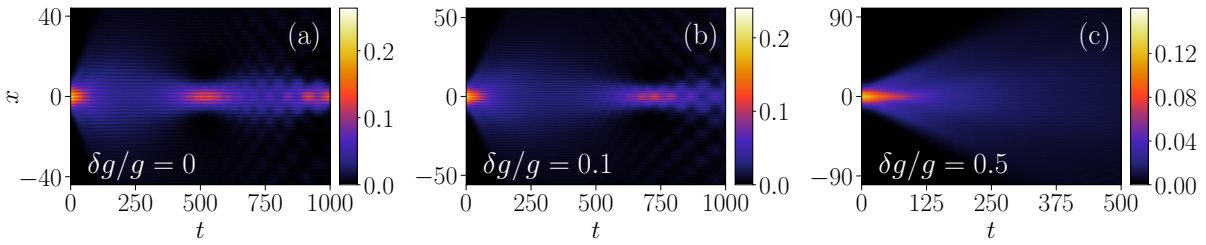

Figure 4.9: Dynamical evolution of total density of the quantum stripe droplet ($\Omega = 1$ and $k_L = 2$) for different $\delta g/g$: (a)$\delta g/g = 0$ (b) $\delta g/g = 0.1$ and (c) $\delta g/g = 0.5$ as the initial velocity given to the condensate is $v = 0.2$. The other parameters are same as in figure 4.8. Upon increase in $\delta g/g$ leads to decrease in the breathing frequency and at high $\delta g/g(\sim 0.2)$ the droplet transforms into the moving droplet.

The dynamics of the stripe phase have a similar nature for different $\delta g/g$ keeping $g = 0.5$, $\Omega = 1$, and $k_L = 2$ as those for the quantum bright phase, as discussed above. In figure 4.8(a)-(c), we show the dynamical evolution of the stripe phase of the droplet for $\delta g/g = 0.1$ for the different velocity $v = 0, 0.1$, and 0.5 respectively. We observe a solitonic nature of the droplet for $v = 0$, a breather for $v = 0.1$ and a moving droplet phase for $v = 0.5$. Similarly, with $\delta g/g = 0.5$, we also observe the solitonic, breather, and moving droplet phase for the velocities $v = 0, 0.05$, and 0.5, respectively (see figure 4.8(d)-(f)). Further, to probe the effect of MF interaction on the transition from breathing to moving droplet in the figure 4.9, we show the dynamical evolution of the stripe droplet

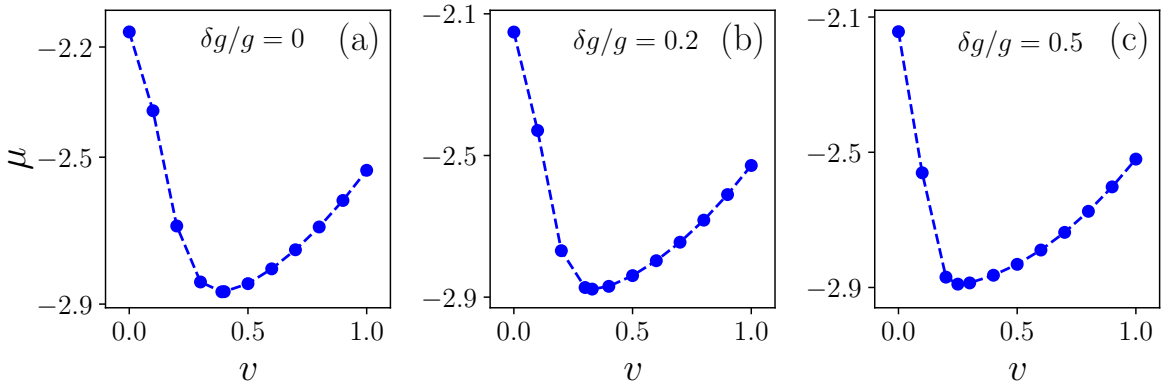

Figure 4.10: Variation of chemical potential (μ) with velocity for different $\delta g/g$: (a) for $\delta g/g = 0$, (b) for $\delta g/g = 0.2$, and (c) for $\delta g/g = 0.5$ in the stripe droplet region ($\Omega = 1$ and $k_L = 2$). Other parameters are same as in figure 4.8. The critical velocity at which μ attains separates the breathing droplet and moving droplet decreases upon increasing $\delta g/g$.

for various $\delta g/g$ by keeping the velocity fixed to $v = 0.2$. The other parameters have been kept the same as in figure 4.8. At $\delta g/g = 0$, the stripe droplet exhibits the breathing-like oscillation with period $T \sim 500$ (See figure 4.9(a)) which increases to $T \sim 750$ for $\delta g/g = 0.1$. Upon further increase in the $\delta g/g = 0.5$ results in the breaking of the droplet along with the presence of the moving droplet. The effect of $\delta g/g$ on the dynamical evolution of the droplet is similar to those of a bright droplet. We compute the critical velocity at which the transition from the breathing droplet to the moving droplet occurs for the stripe droplet region by analyzing the velocity at which the chemical potential attains the minimum [80]. In figure 4.10, we show the variation of the μ with v for

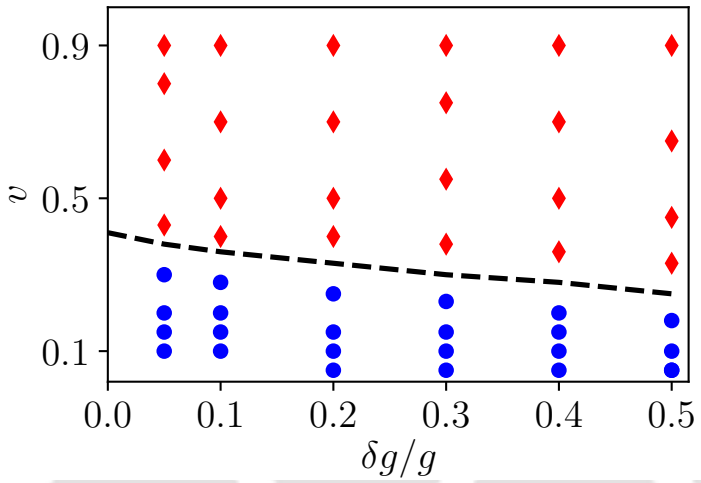

Figure 4.11: Plot showing the region of the breathing (blue dots) and moving (red diamonds) droplets in the parameters space of v and $\delta g/g$ for the stripe region. The dotted line represents the boundary between the two regimes decided analyzing the points at which the chemical potential attains the minimum. The other parameters are same as in Fig. 4.8.

different $\delta g/g$. The v_c are ~ 0.40, ~ 0.28 and ~ 0.14 respectively for $\delta g/g = 0, 0.2$ and 0.5. To make the analysis more complete in figure 4.11, we illustrate the breathing and moving stripe droplet regime with the blue dots and red diamonds, respectively, in the phase space $\delta g/g$ and v. We calculate the critical velocity by analyzing the minima of corresponding chemical potential and show those boundary regions with the dotted line in Fig. 4.11. We notice that the critical velocity for the transition decreases with the increase in $\delta g/g$ similar to those observed for the bright droplet regime. However, we find that the critical velocity for a given $\delta g/g$ is lower for the stripe droplet regime than that for the bright droplets.

Having analyzed the dynamics of the QD in detail by perturbing the condensate through a velocity, in the following, we investigate different dynamics by suddenly quenching the interaction strength.

4.3.3 Quench dynamics of quantum droplets

In the previous Chapter (Chapter 3) we carried out an extensive numerical simulation to analyze the effect of the quenching of coupling parameters on the overall dynamics of the bright and stripe phase of the QD with $\delta g = 0$. Where we reported a large variety of novel features, like the dynamical phase transition from plane to the stripe soliton, dynamical flipping of the spin state, generation of the secondary solitons, etc., by quenching, either the Rabi coupling or SO coupling [80]. Following this, we analyze the effect of the interaction strength quenching on the dynamics of the droplet for both zero and finite $\delta g/g$.

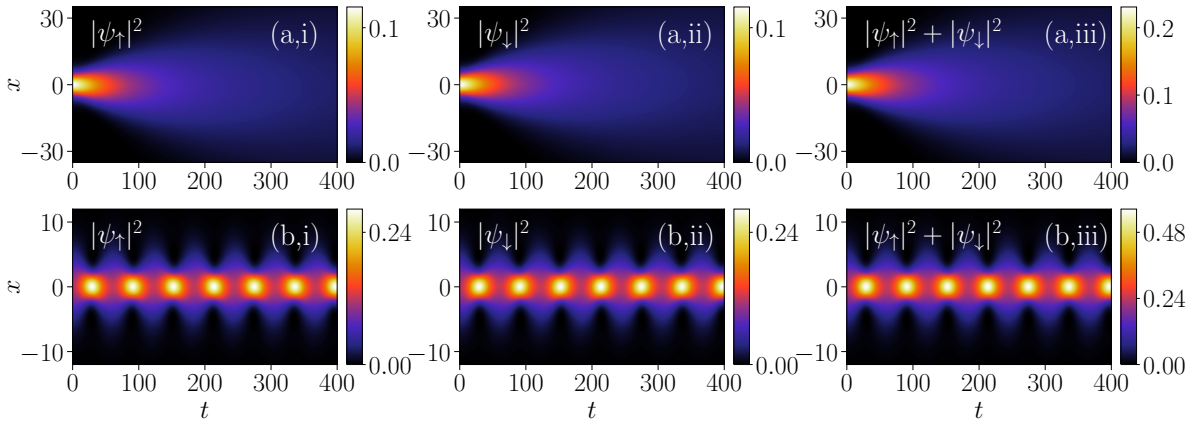

Figure 4.12: Dynamics of quantum droplet appearing due to sudden quenching in interaction strength as the ground states are prepared for $\Omega = 1$, $k_L = 0.5$, $g = -g_{\uparrow\downarrow} = 0.5$. (a,i)-(a,iii): for quenching from $g = -g_{\uparrow\downarrow} = 0.5 \rightarrow g = -g_{\uparrow\downarrow} = 0.1$. The quenching triggers the expansion in the droplet for a long time. (b,i)-(b,iii): for quenching from $g = -g_{\uparrow\downarrow} = 0.5 \rightarrow g = -g_{\uparrow\downarrow} = 1$. The quenching induces the appearance of breathing droplets.

Firstly, we analyze the quench dynamics by applying sudden changes in the interaction strength in both cases, $\delta g/g = 0$ and $\delta g/g \neq 0$. For this purpose, we prepare the ground state of the QD by fixing $g = -g_{\uparrow\downarrow} = 0.5$ and $\Omega = 1$, $k_L = 0.5$. As we make a sudden change in the interaction strength from higher to lower interaction ($g = 0.5 \rightarrow 0.1$), the QD shows an expansion immediately after the quenching [see figure 4.12(a,i)-(a,iii)]. However, when we quench from lower to higher interaction ($g = 0.5 \rightarrow 1$), the QD starts exhibiting breather-like oscillations as shown in figure 4.12(b,i)-(b,iii). This particular feature of the quenched behaviour of the QD demonstrates controlling the nature of the droplet from the expanding to the breathers by simply changing the quenching protocols.

In figure 4.13, we show the dynamical behaviour of the QD ensuing due to the quenching of interspecies interaction strength ($g_{\uparrow\downarrow}$). Like the case with $\delta g/g = 0$, here we also consider two types of quenching protocols, from large $g_{\uparrow\downarrow}$ to small and vice versa. We gen-

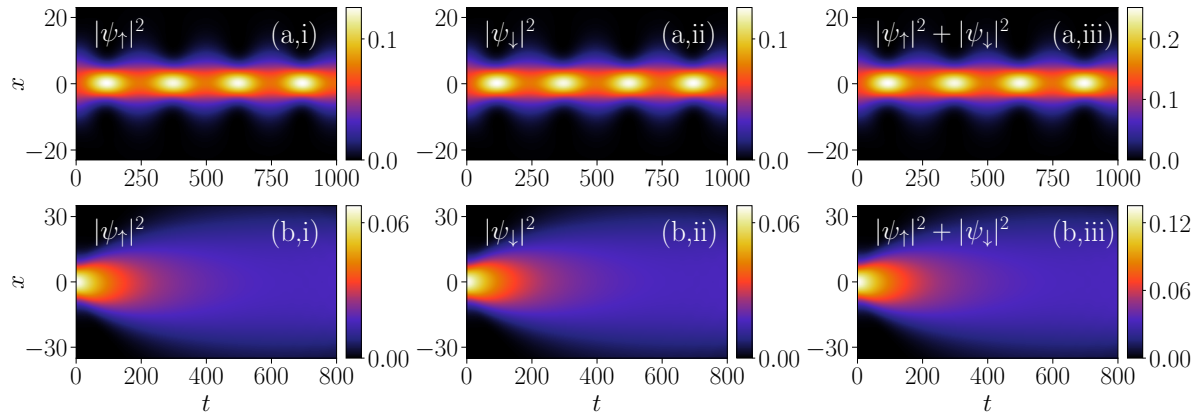

Figure 4.13: Quenching dynamics of the quantum droplet for the different quench protocols with the initial ground state prepared at $\Omega = 1$, $k_L = 0.5$, $g = 0.5$, $g_{\uparrow\downarrow} = -0.25$ ($\delta g/g = 0.5$). (a,i)-(a,iii): When the inter-species interaction strength is quenched as $g_{\uparrow\downarrow} = -0.25 \to -0.45$, ($\delta g/g = 0.5 \to 0.1$) breathing droplets are observed. (b,i)-(b,iii): quenching $g_{\uparrow\downarrow} = -0.25 \to -0.005$ ($\delta g/g = 0.5 \to 0.99$) results the droplets expansion after $t \sim 100$.

erate a ground state by fixing the interaction strength $g = 0.5$, $g_{\uparrow\downarrow} = -0.25$ ($\delta g/g = 0.5$), $\Omega = 1$ and $k_L = 0.5$. Upon quenching from a small $g_{\uparrow\downarrow}$ ($g_{\uparrow\downarrow} = -0.25$) to a large $g_{\uparrow\downarrow}$ ($g_{\uparrow\downarrow} = -0.45$), triggers the breathers like oscillation as shown in figure 4.13(a,i)-(a,iii). This particular feature can be attributed to the fact that upon increasing the attractive interspecies interaction may lead to the domination of LHY on the MF, which may result in these kinds of breathing behaviour [65]. In the reverse case, when we quench $g_{\uparrow\downarrow} = -0.25 \to -0.005$, the QDs undergo an expansion after $t = 100$ [see figure 4.13(b,i)-(b,iii)] which can be related to the domination of the MF term over LHY term [65]. As we compare the quench dynamics that we observe for $\delta g/g = 0$ to those for finite $\delta g/g$,

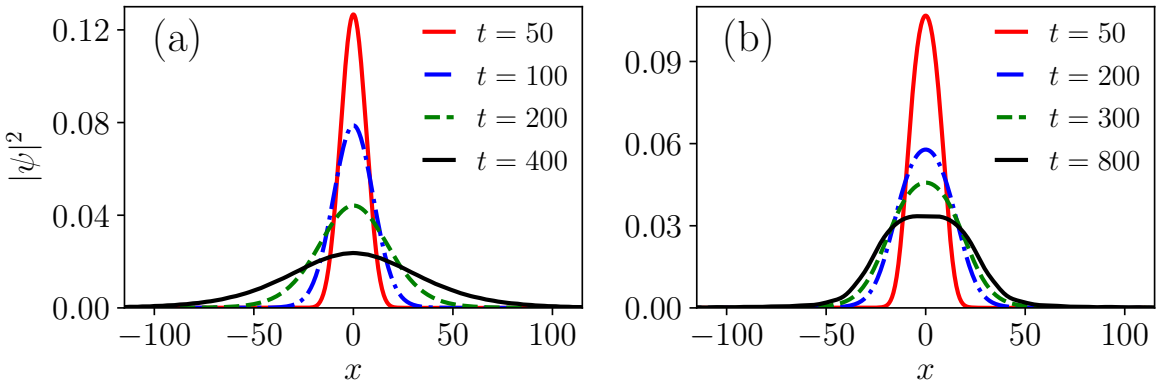

Figure 4.14: Temporal evolution of the total condensate density at different instants of time for the QD expansion of the quenching dynamics displayed in (a) figure 4.12(a) and (b)figure 4.13(b). The droplet exhibits a sech-like profile for an extended duration for $\delta g = 0$, as shown in (a). However, for finite values of $\delta g/g$, a transition from the sech-like profile to a broader sech-like profile has been observed for $t \sim 800$ in (b).

we find that both breathers and expansion dynamical features depend quite strongly on the $\delta g/g$. For $\delta g/g \neq 0$, this dynamical behaviour starts at a later time than that for $\delta g/g = 0$. Therefore the presence of the $\delta g/g$ can be associated with enhancing the dynamical stability of the droplet [66]. Another interesting aspect of having a finite $\delta g/g$ becomes apparent in the long-term dynamics of the droplet. For example, when $\delta g/g = 0$, a careful analysis of the droplet's profile over an extended period reveals that it maintains a sech-like shape while continuously expanding, accompanied by a decrease in peak density, as depicted in figure 4.14. In contrast, for a finite $\delta g/g$, the droplet's profile undergoes a dynamical phase transition from a sech-like shape to a flat sech-like profile after a prolonged evolution, as illustrated in figure 4.14 at $t = 800$.

Now we focus on analyzing the collision dynamics of the droplet for both $\delta g/g = 0$ and $\delta g/g \neq 0$. Previously, in Chapter 3 we presented extensive collision dynamics of the droplet for $\delta g = 0$ and found the presence of a variety of elastic and inelastic collisions of the droplet depending upon their velocities. Following this, here, we discuss the effect of the $\delta g/g$ on the collision dynamics that arises either by quenching the SO coupling parameter or by providing equal and opposite velocities to both components.

In figure 4.15, we show the collision dynamics for the droplet with the ground state prepared with $g = 0.5$, $g_{\uparrow\downarrow} = -0.25$ ($\delta g/g = 0.5$), and $\Omega = k_L = 0$. Further, the components were kept at ± 50 and were given the initial velocity $v = 1$ in the $-x$ (up-component) and $+x$ (down-component) direction. Following this, at $t = 0$ SO coupling was quenched from $k_L = 0 \to 0.5$ that resulted in the elastic collision between the droplets around $t \sim 80$ as shown in figure 4.15(a,i)-(a,iii). However, upon quenching the $k_L = 0 \to$

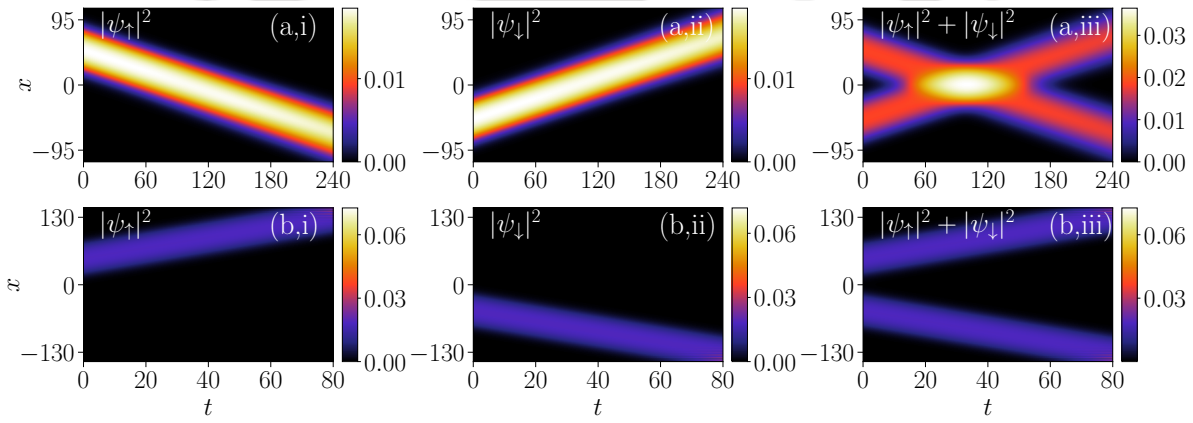

Figure 4.15: Collisional dynamics of the quantum droplet arising due to different quenching protocols. (a,i)-(a,iii): For quenching $k_L = 0 \to 0.5$, the droplet undergoes elastic collision and (b,i)-(b,iii): for quenching $k_L = 0 \to 2$, the droplets appear to repel each other and move in the opposite direction. The ground state was prepared with $g = 0.5, g_{\uparrow\downarrow} = -0.25$, $\Omega = 0$ and $k_L = 0$ and subsequently equal and opposite velocities with magnitude $v = 1$ was given to the individual components at $t = 0$.

2 results in a change in the direction of the motion of the components leading to their separation at a longer time [see figure 4.15(b,i)-(b,iii)]. The change in the direction of the velocity of the droplet component occurs when $v \lesssim k_L$ [87]. This characteristic becomes apparent as k_L determines the velocity of the up component in the positive direction and the down component in the negative direction. This opposes the direction of the velocity imparted to each individual component by the external velocity perturbation. The different features of the collision indicate that the collisional dynamics could be controlled by the quenching strength of the SO coupling parameters. Interestingly, for finite $\delta g/g$, the collision is elastic in nature while it is inelastic in nature for $\delta g = 0$ for the same SO quenching protocol [80].

Now we discuss the collisional dynamics for both $\delta g/g = 0$ and $\delta g/g \neq 0$ with finite Rabi coupling $\Omega = 1$ and $k_L = 0$. In figure 4.16, we show the collisional dynamics for $\delta g/g = 0$ with $g = -g_{\uparrow\downarrow} = 0.5$ for zero and finite ($v = 1$) velocity of the droplet. In

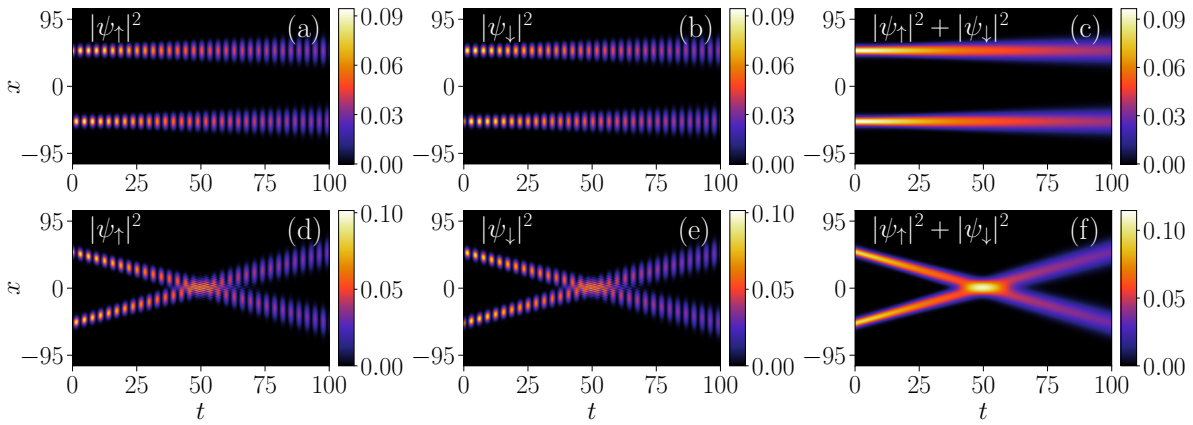

Figure 4.16: Collisional dynamics of the quantum droplet prepared with $g = -g_{\uparrow\downarrow} = 0.5$ and $\Omega = 1, k_L = 0$. (a,i-a,iii) $v = 0$ and (b,i-b,iii) $v = 1$. For $v = 0$, the droplet displays spin-flipping-like behaviour with no motion and shows expansion after $t \sim 50$. However, for $v = 1$, the droplet exhibits a space-time breather with the occurrence of an inelastic collision around $t \sim 50$.

figure 4.16(a,i)-(a,iii) we illustrate the evolution of the droplet for $v = 0$. For this case, the droplets are positioned at $x = \pm 50$. With time the droplet does not move from its initial position, however, the individual components show some sort of breathing like behaviour associated with spin-flipping-like dynamics. After some time ($t \sim 25$) the droplet undergoes expansion. A similar type of spin-flipping has also been realized for SO coupled BECs by making an atom number imbalance at the initial time [92].

As we consider the dynamics of the droplet by giving the velocity $v = 1$ to the individual components we find that the droplet undergoes inelastic collision at $t \sim 50$ [see figure 4.16(b,i)-(b,iii)]. To understand the nature of the collision more clearly in figure 4.17, we show the total density of the droplet before ($t = 15$), during ($t = 50$), and after

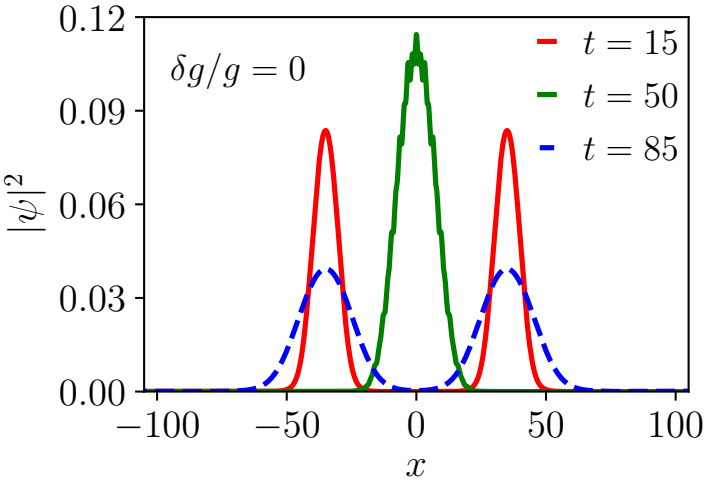

Figure 4.17: Total density plot at the different instant of time for the QD collision as shown in the figure 4.16: at $t = 15$ (before the collision), at $t = 50$ (during the collision) and at $t = 85$ (after the collision). The change in the amplitude and expansion of the density after the collision indicate the inelastic nature of the collision.

$(t = 85)$ the collision. The total density of the droplet shows expansion after the collision complementing the inelastic nature of the collision [84].

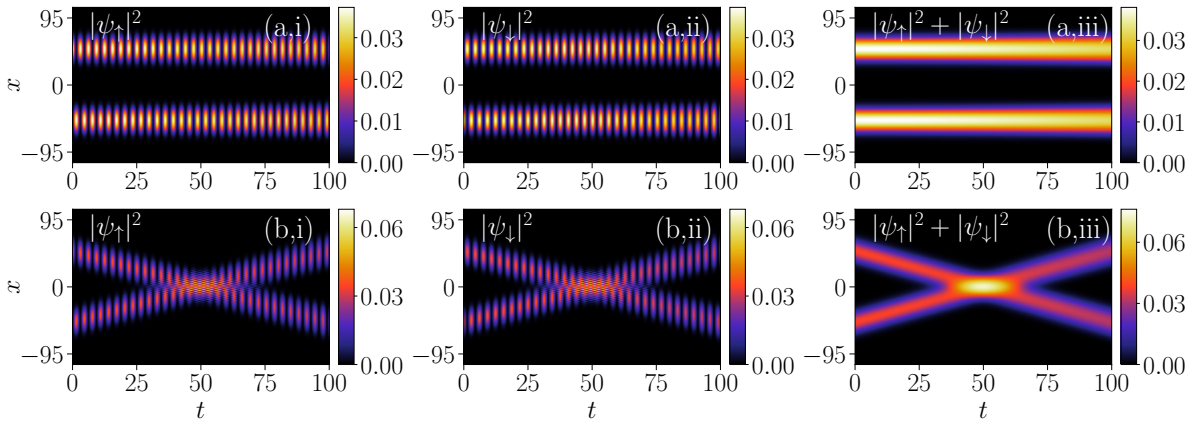

Figure 4.18: Collisional dynamics of the quantum droplet prepared with $g = 0.5$, $g_{\uparrow\downarrow} = -0.05$ $(\delta g/g = 0.9)$ and $\Omega = 1$, $k_L = 0$. (a,i)-(a,iii) For $v = 0$ droplet exhibits spin-flipping without expansion and (b,i)-(b,iii) for $v = 1$ droplet undergoes elastic collision at $t \sim 50$.

Further to probe the role of the finite contribution of the MF term on the collisional dynamics as discussed above we change the $\delta g/g = 0$ to $\delta g/g = 0.9$ by keeping the other parameters the same as those we

have in figure 4.16 and plot the time evolution of the individual components as well the total density in the figure 4.18(a,i-a,iii) for $v = 0$ and figure 4.18(b,i-b,iii) for $v = 1$. We find that the breathing along with the spin-flipping dynamics of the component remains the same as those we observed for $\delta g/g = 0$ for both the velocities. However, droplets

appear to be more stable for $\delta g/g = 0.9$. For instance, at $v = 0$ the droplets exhibit spin-flipping dynamics without any expansion for longer time [See figure 4.18(a,i-a,iii)]. However, for $v = 1$ the droplet appears to undergo elastic collision at $t \sim 50$. The elastic nature of the collision has been further established by analyzing the nature of the density of the droplet before and after the collision as shown in the figure 4.19. Overall we find that the presence of finite effective mean-field term enhances the overall dynamical stability of the droplet [66].

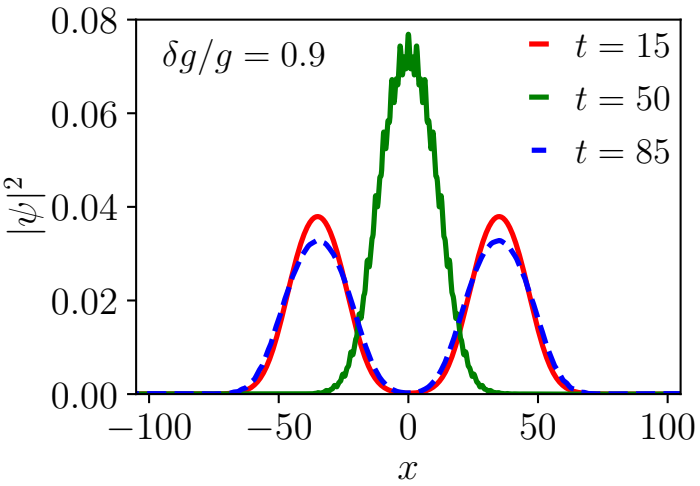

Figure 4.19: Total density plot at different instant of time for the QD collision as shown in the figure 4.18: before ($t = 15$), during ($t = 50$) and after the collision ($t = 85$). The density remains unchanged after the collision, inferring the elastic nature of the collision in the presence of finite $\delta g/g$.

4.4 Summary and Conclusions

In this Chapter, we have systematically analyzed the effect of the finite effective mean-field term on the structure and dynamics of different phases of the QD, namely, QBD and QSD. We found that the density of both bright droplet and stripe droplet phases decreases with enlargement in its size upon an increase in the effective mean-field contribution. Further, we have analyzed the effect of velocity perturbation on the dynamics of the droplet. Increasing the strength of the velocity perturbation to the initial ground state results in the appearance of breather droplets for low velocity, which transforms into the moving droplet at high velocities. The critical velocity at which the transition from the breather to the moving droplets occurs decreases upon increasing the SO coupling parameters for both $\delta g/g = 0$ and $\delta g/g \neq 0$. Next we have analyzed the quenching dynamics resulting from the quenching of the interspecies nonlinear interactions. We find that as

we perform quenching from high to low nonlinear interaction, droplets exhibit breather-like oscillations. However, these breather droplet gets transformed into expanding one as the quenching is executed in the interspecies interaction from low to high values. The behavior of the droplet in the presence of $\delta g/g$ was observed to be dynamically more stable than those for $\delta g/g = 0$. Finally, we have analyzed the collisional dynamics of the droplets by giving equal and opposite velocities to the component and found that while the collision is inelastic for $\delta g/g = 0$, it is elastic for $\delta g/g \neq 0$.

In this Chapter, we have presented an extensive analysis of the QDs for $N = 1$. Increasing N has been observed to lead to a transition from a Gaussian-like droplet to a flat-top droplet, which we have also observed for higher $\delta g/g$ for the binary droplet. In the next Chapter we will extend the analysis of the droplet presented in the Chapter to large droplets ($N > 1$).

Chapter 5

Spectrum and quench-induced dynamics of spin-orbit coupled quantum droplets

In Chapter 3 we considered the SO coupled setup with a vanishing MF contribution, $\delta g = 0$, and thus solely analyzed the dynamics of the soliton structures. Following this in Chapter 4 we investigated the impact of interactions on droplet configurations for a fixed atom number. In this Chapter, we extend the analysis of Chapter 3 and 4 by considering the finite δg as well the effect of the change in the particle number on the shape and size of the droplet. The structure of the Chapter is as follows: first, we present a very brief literature survey pertaining to the effect of the exchange of the particle on the shape and size of the droplet. Further, we provide the numerical simulation results based on the MF simulation. The work described here is published in Physical Review A [96].

5.1 Introduction

We already provided an extensive literature review on QDs in Chapter 1. In this section, we provide a very brief introduction of the QD with a main focus on the role of the change in number of atoms and effective mean-field interaction in dictating the structure and dynamics of the droplet. For instance, it was shown that a decreasing intercomponent attraction or larger particle number leads to a transition from Gaussian (or soliton-like) droplet distributions to flat-top ones [14, 58, 97]. Specifically, when flat-top is reached by loading more atoms renders the configuration wider while maintaining the same peak density, manifesting droplet incompressibility. Another interesting feature of droplets is

their well-defined surface tension, which, together with their kinetic energy, plays a crucial role in achieving their stability when the former dominates [32, 58, 62]. Moreover, basic properties of their underlying excitation spectrum [31, 98], triggering of modulational instability events [66, 99] and the impact of nonlinear excitations such as dark solitons [100, 101] and vortices [102, 103] were discussed. Very recently, other generically unstable bound states called bubbles [98, 100] existing at more negative chemical potentials have been identified. On the other hand, notable examples of the droplet dynamical response include their collision properties in one- [32, 98], two- [104] and three-dimensions [62]. It was showcased that mainly slow-moving droplets merge, and fast ones feature quasi-elastic collisions. Especially in 1D, they can even fragment [32], while their interactions can be explained through an effective particle picture [98]. Additionally, scattering processes of 1D droplets against a potential well in terms of their velocity and particle number were analyzed [34].

To appreciate the role of intercomponent interactions, the first steps towards the two-component system have been taken recently without [105, 106] and with SO coupling [33, 80, 93, 94, 107]. An immediate additional feature that SO coupling brings into play is the formation of stripe patterns [108, 109, 110], which here build upon the droplet background as it was shown for varying MF interactions in Chapter 4. For instance, in 2D Sachdeva et al. demonstrated the transition from the supersolid stripe phase to the zero-momentum droplet upon increasing the Rabi coupling for fixed SO coupling [111]. This characteristic poses fundamental questions related to the underlying excitation spectrum that remains elusive and could allow us to infer the structural stability of SO coupled droplets. In this context, also alterations between phononic and rotonic-like excitations could be revelead. Along the same lines, the behaviour of the surface energy of the stripe droplet is not yet understood.

Another intriguing direction concerns the dynamical response of these droplet configurations. For vanishing MF interactions, where soliton structures take place [See details in Chapter 3], it was argued that their dynamics, following velocity perturbations or interaction quenches, exhibit breathing oscillations, moving states, spin flipping or generation of secondary solitons. For finite interactions, the droplet was shown to be more stable against perturbations [See Chapter 4].

It is, however, still open whether, for finite interactions, other response regimes can be entered, such as droplet fragmentation or spontaneous generation of stripe droplets due to the interplay of different energy contributions. In the present work, we tackle these issues by employing a 1D symmetric SO coupled bosonic mixture, which one could describe within a corresponding two-component eGPE model.

We find that for large SO coupling and finite interactions, stripe QDs occur, and their density background saturates to a flat-top for increasing atom number. On the other hand, at small SO coupling, it is possible to tune the transition from Gaussian to flat-top droplet distributions for larger (smaller) atom numbers (due to intercomponent attraction) [32]. We have performed the spectral stability of symmetric droplets appearing in short-range interacting bosonic mixtures, which results are inline with the recent analytical works [31, 98]. We have demonstrated that the dynamical response of the SO coupled droplets is dictated by the interplay of the involved energy contributions. We mainly consider four distinct situations: (i) initial velocity imprinted on the droplet components as well as quenches on (ii) the intercomponent attractive coupling, (iii) the Rabi coupling, and (iv) the SO coupled wave number.

The structure of this Chapter is as follows. In Sec. 5.2, we describe the bosonic mixture and the eGPEs used to capture SO coupled QDs. Next, we discuss the SO coupled ground state QD configurations for different parametric variations together with the underlying excitation spectrum identifying the stability properties in Sec. 5.3. Sec. 5.4 narrates the dynamical response of the droplets utilizing velocity perturbations but also quenches on the interaction or SO and Rabi coupling parameters. We conclude our work in Sec. 5.5.

5.2 Beyond mean-field model for spin-orbit coupled droplets

We consider a 1D pseudo-spin-1/2 bosonic gas experiencing strong transverse confinement such that the motion in these directions is frozen [108]. For a detailed description of the corresponding dynamical equation, readers are referred to Eq. 1.54. The involved spin states feature the same intracomponent repulsion $g_{\downarrow\downarrow} = g_{\uparrow\uparrow} \equiv g$, $\delta g = g + g_{\uparrow\downarrow}$ and intercomponent attraction of strength $g_{\uparrow\downarrow}$ the eGPEs [Eq. 1.54] in the dimensionless units [33, 80, 93] reads

$$\begin{aligned}
\mathrm{i}\partial_t\psi_\uparrow = \Big[&-\frac{1}{2}\partial_x^2 - \mathrm{i}k_L\partial_x + \frac{\delta g}{2}\left(|\psi_\uparrow|^2 - |\psi_\downarrow|^2\right) + g|\psi_\uparrow|^2 + g_{\uparrow\downarrow}|\psi_\downarrow|^2 \\
&- \frac{g_{\mathrm{LHY}}^{3/2}}{\pi}\sqrt{|\psi_\uparrow|^2 + |\psi_\downarrow|^2}\Big]\psi_\uparrow + \Omega\psi_\downarrow, \qquad (5.1a)\\
\mathrm{i}\partial_t\psi_\downarrow = \Big[&-\frac{1}{2}\partial_x^2 + \mathrm{i}k_L\partial_x + \frac{\delta g}{2}\left(|\psi_\downarrow|^2 - |\psi_\uparrow|^2\right) + g_{\downarrow\uparrow}|\psi_\uparrow|^2 + g|\psi_\downarrow|^2 \\
&- \frac{g_{\mathrm{LHY}}^{3/2}}{\pi}\sqrt{|\psi_\uparrow|^2 + |\psi_\downarrow|^2}\Big]\psi_\downarrow + \Omega\psi_\uparrow. \qquad (5.1b)
\end{aligned}$$

Here, $\psi_\uparrow$ ($\psi_\downarrow$) denotes the 1D wave function of the spin-up (down) component, k_L is the SO coupled wave number, and Ω refers to the Rabi coupling frequency among the aforementioned spin states. The assumption of equal intracomponent repulsions and atom number per component leads to $|\psi_\uparrow| = |\psi_\downarrow|$. For this reason, we choose to discuss below the features of the total wave function of the SO coupled system. Moreover, the strength of the LHY quantum correction is $g_{\rm LHY} = g$ while $\delta g = g_{\uparrow\downarrow} + g$ is the MF balance point. Additionally, we employ the following condition on the system wave function [32]

$$\int_{-\infty}^{\infty} \left[|\psi_\uparrow|^2 + |\psi_\downarrow|^2 \right] dx = 2N, \tag{5.2}$$

where $2N$ is the normalization constant. It determines the normalized number of particles in the droplet (see also the discussion below).

The energy of the system is measured in terms of $\hbar\omega_\perp$, with $\omega_\perp$ being the trap frequency in the transverse direction. In this sense, the characteristic length scale is set by the transverse harmonic oscillator length $a_\perp = \sqrt{\hbar/(m\omega_\perp)}$ and time is expressed in units of $\omega_\perp^{-1}$. Also, $g = 2\mathcal{N}a_{\uparrow\uparrow}/a_\perp$ and $g_{\uparrow\downarrow} = 2\mathcal{N}a_{\uparrow\downarrow}/a_\perp$, where $a_{\uparrow\uparrow}$ ($a_{\uparrow\downarrow}$) refers to the 3D intracomponent (intercomponent) s-wave scattering length which is tunable via Feshbach resonances [24]. $\mathcal{N}$ denontes the total particle number. The SO coupled wave number and intensity (Rabi coupling) are rescaled as $k_L \to \tilde{k}_L a_\perp$ and $\Omega \to \tilde{\Omega}/\omega_\perp$ respectively, while the wave function as $\psi_{\uparrow,\downarrow} = \tilde{\psi}_{\uparrow,\downarrow}\sqrt{a_\perp}$. Here, the tilde quantities represent the dimensionfull ones.

Experimentally, our setup is realizable with a binary mixture consisting of the hyperfine states $|\uparrow\rangle \equiv |F = 1, m_F = -1\rangle$ and $|\downarrow\rangle \equiv |F = 1, m_F = 0\rangle$ of ^{39}K [15, 23, 62]. The validity of the 1D geometry is ensured by employing strong transverse confinement of frequency $\omega_\perp = 2\pi \times 800$Hz resulting in $a_\perp = 0.568\,\mu$m, while along the axial direction either a box potential or a relatively suppressed confinement e.g. $\omega_x = 2\pi \times 50$ Hz can be used [23]. Moreover, the total particle number in the droplets herein is assumed to take values in the interval $\mathcal{N} \sim [10^4, 10^6]$, which is achieved by varying the normalization constant of Eq. (5.2) within the range $N = [1, 300]$. On the other hand, by choosing the scattering length values $a_{\uparrow\uparrow} = a_{\downarrow\downarrow} = 0.5367a_0/N$, where a_0 is the Bohr radius, a nearly negligible MF interaction (i.e. $\delta g \approx 0$) is attained leading to a dimensionless intracomponent coupling $g = g_{\rm LHY} = 1$. Turning to a finite δg, the intercomponent interaction takes values $g_{\uparrow\downarrow} = [-0.99, -0.6]$, allowing for $\delta g = [0.01, 0.4]$ that can be obtained with $a_{\uparrow\downarrow} = 1/N[-0.5313a_0, -0.322a_0]$.

The Rabi coupling frequency (Ω) depends on the intensity of the underlying Raman

lasers [46, 112], and can be typically adjusted in the experiment within the interval $\tilde{\Omega} = 2\pi \times [0.8, 24]$kHz. The latter corresponds to a dimensionless Rabi coupling frequency $\Omega = [1, 30]$. Additionally, the wavenumber of the spin-orbit coupling (k_L) is tunable via either the laser's geometry or wavelength [46, 108, 109]. Below, we consider values of the dimensionless SO coupled wave number $k_L = [0.1, 3]$, related to variations of the laser wavelength from $\lambda_L = 25.23$ μm to 841nm [46].

To address the ground state properties of the SO coupled droplet setting described by Eqs. (5.1a) and (5.1b), we employ an imaginary-time propagation method using a split-step Crank-Nicolson scheme [71, 85, 86]. In the adopted dimensionless units, the considered box size corresponds to $L = 307$ with spatial resolution $dx = 0.025$, and for the dynamics, a fixed time step $dt = 10^{-5}$ is utilized. A Gaussian initial ansatz with anti-symmetric profiles between the components, i.e., $\psi_\uparrow(x) = -\psi_\downarrow(-x)$ is used.

5.3 Spin-orbit coupled droplet configurations and their spectrum

5.3.1 Different droplet and stripe phases

As explicated above, it is known that QDs of binary short-range bosonic mixtures, in the absence of SO coupling, assemble in different phases upon variations of the system parameters, namely the atom number [32, 67], the MF interactions [31, 65] but also the trap strength [101]. For instance, using fixed interactions and a larger particle number, the QD experiences a transition from a quasi-Gaussian soliton-like structure to a flat-top configuration [32]. However, in Chapter 4, it was demonstrated that the presence of SO coupling is responsible for spatial undulations, so-called stripes, of the droplet for different interactions and keeping the remaining system parameters fixed. Below, we analyze emergent ground state properties of SO coupled droplets, especially focusing on the interplay between the involved MF interactions and the normalized atom number.

Initially, we study the ground state density behaviour of QDs for varying normalized atom number but fixed interaction strengths, i.e. $\delta g/g = 0.1$ with $g = 1$, and $g_{\uparrow\downarrow} = -0.9$, as well as constant Rabi-coupling $\Omega = 1$, and SO coupled wave number $k_L = 0.5$, see Fig. 5.1(a). Notice that the choice of small $k_L = 0.5$, satisfying $k_L^2 < \Omega$, ensures a non-spatially modulated (i.e., absence of stripe) structure in the droplet and thus the emergent configurations are similar to the ones in the absence of SO coupling [80, 86, 93]. Indeed, the QD shows a transition from a quasi-Gaussian shape for small N, e.g. $N = 10$,

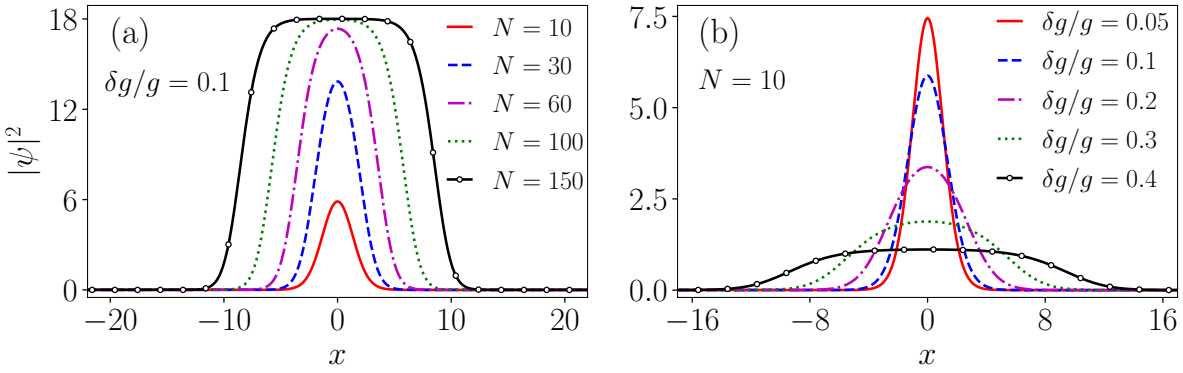

Figure 5.1: Density deformation of a non-modulated QD with $\Omega = 1$ and $k_L = 0.5$. The total density is presented for (a) fixed MF interactions $\delta g/g = 0.1$ and varying normalized atom number N and (b) for constant $N = 10$ and different $\delta g/g$. The droplet transforms from the Gaussian-like configuration to a flat-top one for larger N featuring a saturation peak density in the flat-top regime. The transition threshold value dictated by N decreases for larger $\delta g/g$. However, increasing $\delta g/g$ while N held constant leads to a decrease of the peak density and a flattened profile, e.g. in the case of $N = 10$ for $\delta g/g \gtrsim 0.3$. The displayed results in all figures are in dimensionless units.

towards a profile for larger N. Specifically, increasing N leads to a gradual broadening of the width and the peak amplitude of the QD. After a certain normalized particle number threshold being here $N \gtrsim 100$, the flat-top (peak density) of the QD saturates, and solely the width increases. The latter behaviour is a manifestation of the incompressible nature of the QD [14, 28, 58], while the abovementioned threshold value depends, of course, on $\delta g/g$.

Next, we examine the impact of the effective mean-field interaction parameter, namely $\delta g/g$, on the QD shape. The remaining system parameters are held fixed as in the previous case while $N = 10$ is considered. Fig. 5.1(b) presents the respective QD density profiles for different $\delta g/g$, where since $g = 1$ a larger $\delta g/g$ refers to a decreasing magnitude of intercomponent attraction $g_{\uparrow\downarrow}$. It can be readily deduced that for relatively small $\delta g/g$, for instance, $\delta g/g = 0.05$, the relevant density distribution is Gaussian-like. However, as $\delta g/g$ acquires larger values or equivalently, the intercomponent attraction becomes smaller in magnitude, and the QD size tends to increase, accompanied by simultaneous reduction of the peak density. The latter saturates for further increasing $\delta g/g$, see for example, $\delta g/g = 0.4$, displaying a flat-top shape that persists for larger values of $\delta g/g$ where only the width of the QD keeps expanding. Overall, we once more observe that the droplet undergoes a transition from a quasi-Gaussian to a flat-top profile while attaining an intermediate broader Gaussian state, either for larger N and fixed $\delta g/g$ or by increasing $\delta g/g$ for constant N.

The appearance of the three above-described structural regimes for distinct N indicates

the decisive competition between the individual energy contributions. In general, the existence of a self-bound state can be attributed to the balance between destabilizing and stabilizing terms in the system. For example, the attractive SO coupling and LHY terms attempt to destabilize the droplet, while the repulsive MF and kinetic energies could assist its stability. Indeed, at low N, the kinetic energy dominates over the MF one, resulting in a narrow Gaussian-shaped QD. Meanwhile, at intermediate N, the MF energy surpasses the kinetic one, leading to broader Gaussian-like droplets. Following a further increase of N, there is a corresponding increase in the repulsive MF energy and vanishing kinetic energy, ultimately leading to a flat-top QD structure [32].

We confirm these intriguing characteristics of the distinct droplet states by examining the competition of the system's energy terms. As a first step, we provide in Fig. 5.2 the total chemical potential and the underlying kinetic energy of both components as a function of N. It is evident that μ becomes more negative for larger N, and eventually, depending on the value of $\delta g/g$, it tends to a constant value [Fig. 5.2(a)]. For instance, in the case of $\delta g/g = 0.05$, the saturation of μ takes place at a higher N as compared to $\delta g/g = 0.1$. This implies that for larger N, the system attains a stronger bound state. Conversely, the kinetic energy initially increases as long as the QD refers to a narrow Gaussian; it reaches a maximum when the droplet acquires a broader Gaussian distribution and decreases in the flat-top region [Fig. 5.2(b)]

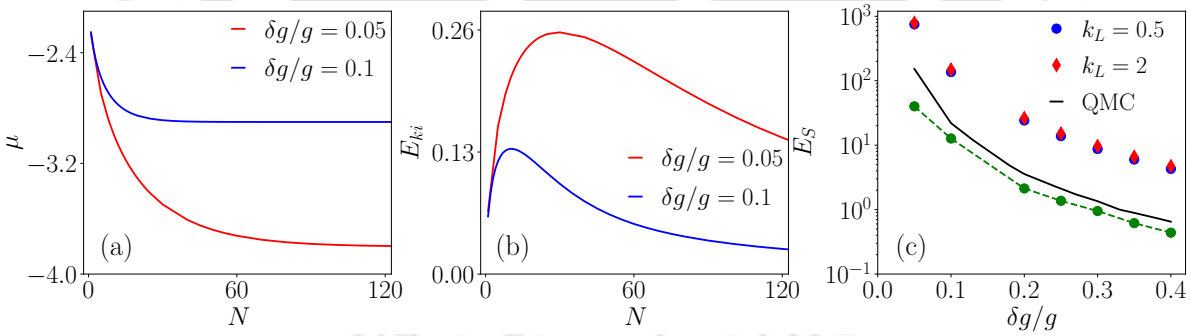

Figure 5.2: (a) The total chemical potential, μ, and (b) the total kinetic energy with respect to N for different interaction strengths $\delta g/g$ (see legend), with the other parameters being the same as in Fig. 5.1. The chemical potential shows a decreasing trend for larger N in the quasi-Gaussian droplet regime and saturates above a threshold value N_c, beyond which a flat-top structure occurs. The aforementioned saturation value of μ becomes larger for increasing $\delta g/g$. The E_{ki} attains its maximum at the transition N_c. (c) The behaviour of the surface energy E_s in terms of $\delta g/g$ is shown. Upon fitting, it is found that the surface energy satisfies $E_s \sim (\delta g/g)^{-2.47}$. The green-dotted line with empty squares presents the difference of E_s among the cases with SO coupled wave numbers $k_L = 0.5$ and $k_L = 2$. The black-solid line represents the many-body results reported for a binary short-range droplet using Quantum Monte Carlo Simulation (QMC) by Parisi and Giorgini [67]. The observed deviations with the eGPE predictions are partly attributed to the presence of SO coupling (in the current setup) but also to residual beyond-LHY correlations that are taken into account within QMC.

To further understand the modifications of the QD distribution, it is quite relevant to explore the so-called surface energy term. Recall that at large $\delta g/g$, the droplet reaches a flat-top profile with its density maximum being insensitive to larger $\delta g/g$, and only its width becomes wider. The surface energy of the QD, in 1D, can be estimated through the standard liquid drop model, namely expressing the total energy per particle within the large N limit [32, 67] as follows

$$\frac{E}{N} = E_v + \frac{E_s}{N}. \tag{5.3}$$

The first term, E_v, represents the bulk energy, and the second one is the correction due to the finite atom number, which scales as $1/N$ and depends on the surface energy coefficient E_s. Determining the energy per particle, E/N, for fixed $\delta g/g$ yields that it obeys a linear trend with increasing $1/N$. Since the slope of E/N is proportional to E_s, we next determine the latter with respect to $\delta g/g$ for the SO coupled wave number $k_L = 0.5$ as well as $k_L = 2$ (stripe phase) of the droplet, see Fig. 5.2(c). It is found that E_s features a power-law dependence on $\delta g/g$ with an exponent of -2.47. This behaviour signals the reduction of E_s in the flat-top region and is attributed to the respective incompressible character. The difference of E_s between $k_L = 0.5$ and $k_L = 2$ is significant at relatively small $\delta g/g$, and it decreases for $\delta g/g > 0.25$, where the flat-top background becomes more prominent, see in particular the green-dotted line with empty squares in Fig. 5.2(c).

Subsequently, we employ a larger SO coupled wave number, such as $k_L = 2$, which enforces significant spatial undulations in the droplet density and thus allows us to access the stripe phase [80]. For simplicity, we use $\Omega = 1$, and examine the ground state of the stripe QD as a function of N for a fixed $\delta g/g = 0.1$, as depicted in Fig. 6.3(a). Apparently, the SO coupled wave vector utilized imprints stripe patterns in the droplet density almost irrespective of N. However, the number of these stripes crucially depends on N and, in particular, increases for larger N, as shown in Fig. 6.3(b) as well. This is expected, as an increasing N leads to a wider background, which can naturally host more stripes. Interestingly, beyond an interaction-dependent normalized particle number threshold (e.g., for $\delta g/g = 0.1$, it refers to $N \gtrsim 100$), the peak density of the central stripes attains that of the bulk density and remains unaltered for larger N. Similar to the non-modulated droplet phase, only the width (size) of the bulk density increases for higher N, while the central distribution features a flattened behaviour. Therefore, the number of stripes in the droplet continues to increase. This is explicitly shown in Fig. 6.3(b) for distinct interactions. Accordingly, the number of stripes is also enhanced at a given N (especially for $N > 10$) for larger $\delta g/g$, which favors a more spatially

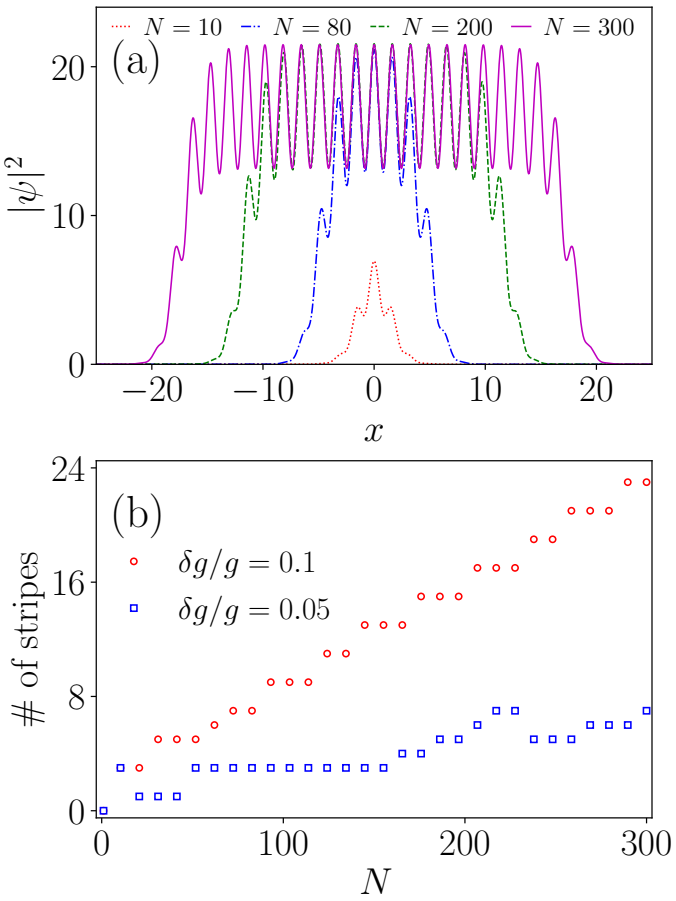

Figure 5.3: (a) Total density profiles of the quantum stripe droplet at $\delta g/g = 0.1$ for several values of N (see legend). The droplet configuration accommodates a larger number of stripes as N increases, and eventually, its background flattens. (b) The number of resulting stripes as a function of the normalized atom number N for various interactions $\delta g/g$ (see legend). Other system parameters are $g = 1$, $\Omega = 1$, and $k_L = 2$.

extended background.

5.3.2 Excitation spectrum of the spin-orbit coupled droplet phases

To extract the excitation spectrum and analyze the stability properties of the previously discussed SO coupled droplet solutions, we perturb the latter according to

$$\Psi_j(x,t) = \mathrm{e}^{-\mathrm{i}\mu_j t}\left[\psi_j(x) + u_j(x)e^{-i\omega t} + v_j^*(x)\mathrm{e}^{\mathrm{i}\omega^* t}\right]. \tag{5.4}$$

In the above expression, ψ_j and μ_j denote the complex ground state wave function and chemical potential of the $j = (\uparrow,\downarrow)$ component. Furthermore, u_j and v_j denote the Bo-

goliubov amplitudes (i.e., the resulting eigenvectors), while ω refers to the eigenfrequency of the perturbation. Upon substituting the ansatz of Eq.(5.4) into the eGPEs [Eq.(5.1)], we obtain the following linearized eigenvalue problem:

$$\mathcal{L}\begin{pmatrix} u_\uparrow \\ v_\uparrow \\ u_\downarrow \\ v_\downarrow \end{pmatrix} = \omega \begin{pmatrix} u_\uparrow \\ v_\uparrow \\ u_\downarrow \\ v_\downarrow \end{pmatrix}, \tag{5.5}$$

where the matrix

$$\mathcal{L} = \begin{pmatrix} f_1 & Y_1 & Z_1 & Z_2 \\ -Y_1^* & -f_1^* & -Z_2^* & -Z_1^* \\ Z_1^* & Z_2 & f_2 & Y_2 \\ -Z_2^* & -Z_1 & -Y_2^* & -f_2^* \end{pmatrix}.$$

The individual matrix elements of Eq. (5.5) exploiting the symmetries of the system read

$$Y_1 = \left[\frac{\delta g}{2} + g - \alpha\right]\psi_\uparrow^2, \quad Y_2 = \left[\frac{\delta g}{2} + g - \alpha\right]\psi_\downarrow^2 \tag{5.6}$$

$$Z_1 = \left[\frac{\delta g}{2} - g - \alpha\right]\psi_\uparrow\psi_\downarrow^* - \Omega, \quad Z_2 = \left[\frac{\delta g}{2} - g - \alpha\right]\psi_\uparrow\psi_\downarrow \tag{5.7}$$

and

$$f_1 = -\frac{1}{2}\partial_x^2 - \mathrm{i}k_L\partial_x + (2g + \delta g - 3\alpha)|\psi_\uparrow|^2 + \left(\frac{\delta g}{2} - g - 2\alpha\right)|\psi_\downarrow|^2 - \mu_\uparrow \tag{5.8}$$

$$f_2 = -\frac{1}{2}\partial_x^2 + \mathrm{i}k_L\partial_x + \left(\frac{\delta g}{2} - g - 2\alpha\right)|\psi_\uparrow|^2 + (2g + \delta g - 3\alpha)|\psi_\downarrow|^2 - \mu_\downarrow, \tag{5.9}$$

where $\alpha = g_{\mathrm{LHY}}^{3/2}/\left(2\pi\sqrt{|\psi_\uparrow|^2 + |\psi_\downarrow|^2}\right)$. The chemical potentials of the individual components assume the forms [80]

$$\mu_\uparrow = \frac{1}{N_\uparrow}\int\left[\frac{1}{2}\left|\frac{\partial\psi_\uparrow}{\partial x}\right|^2 + \tilde{H}_\uparrow + \left(k_L\frac{\partial\psi_\uparrow^I}{\partial x} + \Omega\psi_\downarrow^R\right)\psi_\uparrow^R - \left(k_L\frac{\partial\psi_{\uparrow R}^R}{\partial x} - \Omega\psi_\downarrow^I\right)\psi_\uparrow^I\right]dx, \tag{5.10a}$$

$$\mu_\downarrow = \frac{1}{N_\downarrow}\int\left[\frac{1}{2}\left|\frac{\partial\psi_\downarrow}{\partial x}\right|^2 + \tilde{H}_\downarrow - \left(k_L\frac{\partial\psi_\downarrow^I}{\partial x} - \Omega\psi_\uparrow^R\right)\psi_\downarrow^R + \left(k_L\frac{\partial\psi_\downarrow^R}{\partial x} + \Omega\psi_\uparrow^I\right)\psi_\downarrow^I\right]dx, \tag{5.10b}$$

where

$$N_j = \int |\psi_j|^2 dx, \quad j = \uparrow, \downarrow, \tag{5.10c}$$

$$\tilde{H}_\uparrow = \left[g|\psi_\uparrow|^2 + g_{\uparrow\downarrow}|\psi_\downarrow|^2 + \frac{\delta g}{2}\left(|\psi_\uparrow|^2 - |\psi_\downarrow|^2\right) - \frac{g^{3/2}}{\pi}\sqrt{|\psi_\uparrow|^2 + |\psi_\downarrow|^2} \right] |\psi_\uparrow|^2, \tag{5.10d}$$

$$\tilde{H}_\downarrow = \left[g|\psi_\downarrow|^2 + g_{\downarrow\uparrow}|\psi_\uparrow|^2 + \frac{\delta g}{2}\left(|\psi_\downarrow|^2 - |\psi_\uparrow|^2\right) - \frac{g^{3/2}}{\pi}\sqrt{|\psi_\uparrow|^2 + |\psi_\downarrow|^2} \right] |\psi_\downarrow|^2. \tag{5.10e}$$

In these expressions, the real and imaginary parts of the mixture wave function are denoted by $\psi^R_{\uparrow,\downarrow}$ and $\psi^I_{\uparrow,\downarrow}$, respectively. Using the normalization condition $\int \left(|u_j|^2 - |v_j^*|^2\right) dx = 1$, we obtain the eigenspectrum by numerically solving $\det(\mathcal{L}) = 0$.

Figure 5.4 shows the variation of the real and the imaginary parts of few low lying eigenvalue (ω) with respect to N for different SO coupled wave numbers, namely $k_L = 0.5$ [Fig. 5.4(a)] and $k_L = 2$ [Fig. 5.4(b)], with fixed $\Omega = 1$. Focusing on $k_L = 0.5$, we observe that the eigenvalues remain purely real (with the imaginary part being zero) regardless N, i.e., for both the Gaussian and the flat-top droplet phases. This behavior affirms the dynamically stable nature of the droplet which has been shown already for the binary

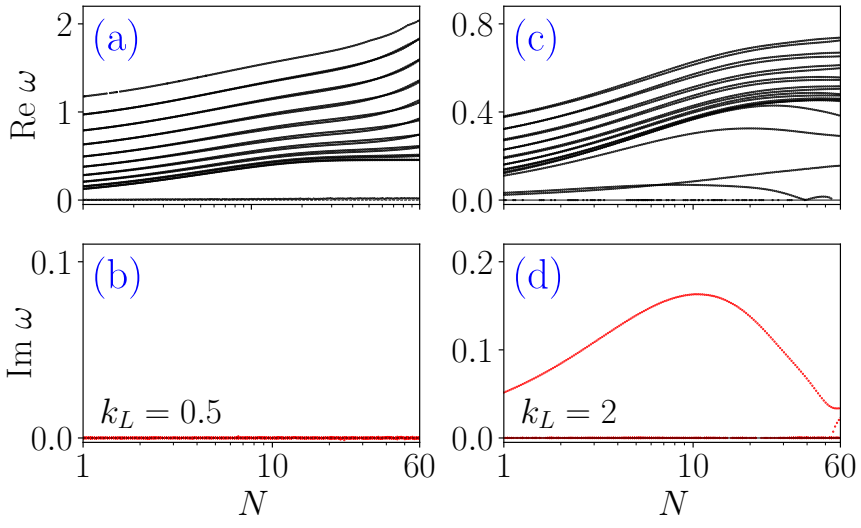

Figure 5.4: The real (upper panels), Re ω, and the imaginary (lower panels), Im ω, parts of the first twenty lower lying eigenvalues of Eq. (5.5) as a function of N for (a), (b) $k_L = 0.5$ and (c), (d) $k_L = 2$ (stripe phase). Here, the parameters $\delta g/g = 0.1$ and $\Omega = 1$ are kept fixed. Apparently, when $k_L = 0.5$ the eigenvalues remain purely real, indicating the dynamical stability of the SO coupled droplet. However, imaginary contributions of the eigenvalue exist for $k_L = 2$ independently of N, suggesting the dynamical instability of the stripe droplet.

short-range interacting droplet setting without SO coupling [31, 98, 101]. However, for the stripe phase ($k_L = 2$) of the droplet, the eigenvalues exhibit a non-negligible imaginary contribution for all N [cf. Fig. 5.4 (c) and (d)], indicating the involvement of dynamical

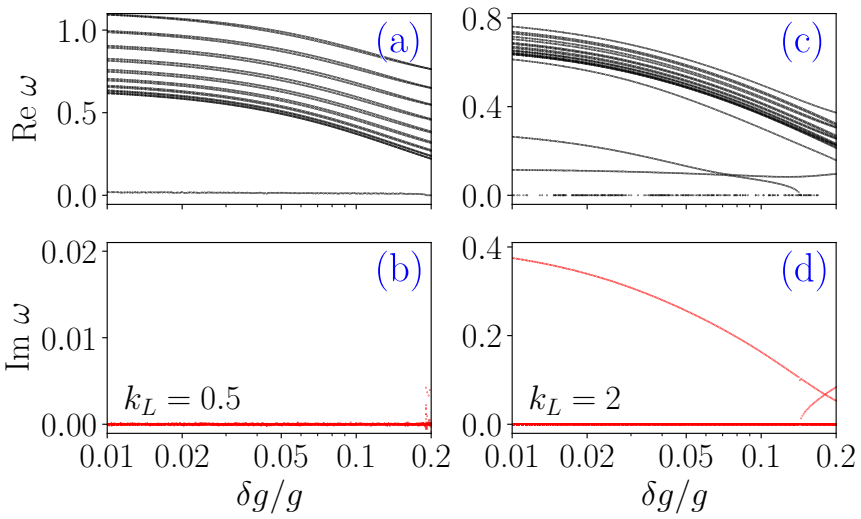

Figure 5.5: (Upper panels) Real, Re ω, and (lower panels) imaginary, Im ω, parts of the eigenvalues of Eq. (5.5) with varying $\delta g/g$ for (a), (b) $k_L = 0.5$, and (c), (d) $k_L = 2$. In all cases $N = 10$ and $\Omega = 1$. For $k_L = 0.5$ the spectrum remains purely real, implying the dynamical stability of the droplet for all $\delta g/g$, while for $k_L = 2$ the presence of imaginary eigenvalues evinces the dynamical instability of the stripe droplet.

instabilities in this case. In a similar vein, analyzing the eigenvalues for $k_L = 0.5$ and $k_L = 2$ by keeping the normalization of the droplet fixed ($N = 10$) and varying $\delta g/g$, we find that the eigenvalues remain purely real in the former case and are complex in the latter phase, as depicted in Fig. 5.5. Interestingly, an increase in $\delta g/g$ results in the decrease of the magnitude of the real and imaginary parts of the eigenvalue for $k_L = 0.5$ and $k_L = 2$, respectively. This feature of ω for increasing $\delta g/g$ can be attributed to the accompanied decrease of the chemical potential also realized for the binary droplet in the absence of SO coupling [98]. A more detailed analysis of the underlying instabilities and their effects as well as their dependence on the remaining system parameters is a fruitful prospect for future work. Finally, notice here that also the case of nonzero quasi-momenta can be taken into account with multiplying the term $\sim \mathrm{e}^{\mathrm{i}kx}$ in the linearization ansatz of Eq. (5.4) which will reveal the presence of the zero-momentum and plane wave [113, 114, 115] besides the stripe one that we find in the present analysis.

5.4 Dynamics of spin-orbit coupled quantum droplets

Having analyzed the ground state properties of the droplet phases under the influence of SO coupling, we next proceed to study the dynamical response of these entities subjected

to different external perturbations. These include (i) imprinting an initial velocity to the droplet through a uniform change in the phase of its ground state wave function, (ii) following a quench of the MF interaction parameter, or (iii) applying a quench to the Rabi coupling. The time evolution of both the standard droplet and the striped one is examined. As in Chapter 3, we studied the case of vanishing MF interactions ($\delta g = 0$), dominant emergent features are breathing motion and dynamical fragmentation of the droplet into multiple fragments as well as droplet splitting for increasing magnitude of its initial velocity is found.

5.4.1 Impact of the initial velocity: transition from breather to fragmented droplets

Here, we explore the response of droplets subjected to a phase shift on the ground state wave function of the individual components, namely $\psi(x, t = 0) = \psi_{\uparrow} \exp(-ivx) + \psi_{\downarrow} \exp(+ivx)$. As a case example, a flat-top droplet containing $N = 120$ atoms and characterized by $\Omega = 1$, $k_L = 0.5$, $g = 1$, and $g_{\uparrow\downarrow} = -0.9$ ($\delta g/g = 0.1$) is employed. The resultant dynamics of such a droplet are presented in Fig. 5.6(a)-(c) for different velocities, namely $v = 0$, $v = 0.17$, and 1. In the case of $v = 0$, the droplet remains unperturbed throughout the evolution, thus confirming its stable nature [Fig. 5.6(a)]. However, for finite velocities, the droplet response is drastically modified [see Figs. 5.6(b) and (c)]. For instance, at $v = 0.17$, the phase perturbation triggers internal excitations of the droplet that are predominantly of breathing type, as can be seen in Fig. 5.6(b). Interestingly, the breathing droplet splits into two parts around $t \sim 40$, which then recombine at $t \sim 180$ into a single droplet. In the vicinity of the droplet splitting, the kinetic energy contribution dominates. Afterwards, $t \sim 180$, the single excited droplet separates again into two oppositely moving and not equally mass ones. Notice here that a smaller normalized atom number which is related to a quasi-Gaussian droplet undergoes solely a breathing motion. A further increase of the initial velocity, e.g. $v = 1$ depicted in Fig. 5.6(c), leads to a dynamical fragmentation process of the flat-top droplet. Indeed, the fragmented density parts here consist of four outer counterpropagating droplets featuring breathing-like oscillations and an inner quasi-stationary droplet residing around $x = 0$. The number of fragmented droplets depends strongly on the involved normalized particle number, e.g. it is three for $N = 80$ and five for $N = 120$.

Turning to the effect of velocity perturbations on the stripe droplet state we observe a somewhat modified response [see Fig. 5.6(d)-(f)]. Here, the employed ground state stripe droplet waveform is characterized by $N = 200$, $\Omega = 1$ and $k_L = 2$, while the

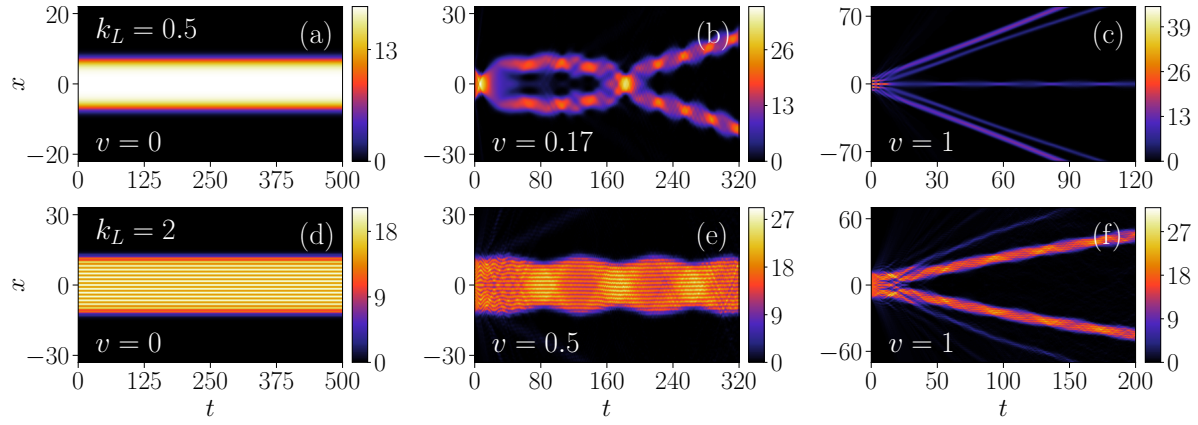

Figure 5.6: Total density evolution of different SO coupled QDs subjected at $t = 0$ to velocity perturbations (a), (d) $v = 0$, (b) $v = 0.17$, (c), (f) $v = 1$ and (e) $v = 0.5$. The droplets are characterized by SO coupled wave number (a)-(c) $k_L = 0.5$ for $N = 120$ and (d)-(f) $k_L = 2$ for $N = 200$. They are initiated in the ground state where $g = 1$, $g_{\uparrow\downarrow} = -0.9$ ($\delta g/g = 0.1$) and $\Omega = 1$. When $v = 0$, the QD propagates undistorted, while for finite velocity, it features a gradual transition from a breather [panel (e)] to moving [panels (c), (f)], i.e. multiple fragmented ones due to the dominant kinetic term contribution. The number of fragmented QDs increases for larger N. Colorbar indicates the total density.

interaction parameters are the same as in the above discussion. For these parameters, the respective ground state configuration turns out to contain nineteen stripes. As expected, for $v = 0$, the stripe droplet (independently of N) is unchanged in both size and shape in the course of the evolution verifying the stability of the state [Fig. 5.6(d)]. However, for finite velocities (e.g. $v = 0.5$), the droplet stripe experiences internal excitations corresponding to the vibrational motion of the participating stripes [see Fig. 5.6(e)]. This, in turn, results in an overall breathing motion of the entire background accompanied by the emission of density portions that become more pronounced for a higher number of atoms. This dynamical response will be referred to in the following as *breather-like* droplet; it occurs also for the standard droplet described above (not shown). Importantly, upon considering higher velocities, namely $v = 1$ here, there is a transition to the so-called *fragmented droplet* dynamical stage as can be clearly seen in Fig. 5.6(f). This fragmentation process is associated with the dominance of the attractive SO coupled energy term, and it means that the initial droplet breaks into several smaller ones whose specific number and behaviour are dictated by the particle number. For instance, when $N = 200$ at short evolution times ($t < 20$), the strong perturbation causes stripe collisions and coalescence. As a result, there is a burst of density emission (radiation) from the "surface" of the droplet accompanied by the nucleation of four counterpropagating stripe droplets featuring breathing excitation. These outer moving droplet stripes retain their nature for long evolution times. In contrast, for $N = 180$ (not shown), the perturbation-induced initial stripe collisions lead to the droplet breaking into three parts, with the

central one resembling a breather stripe droplet and the outer ones traveling outwards.

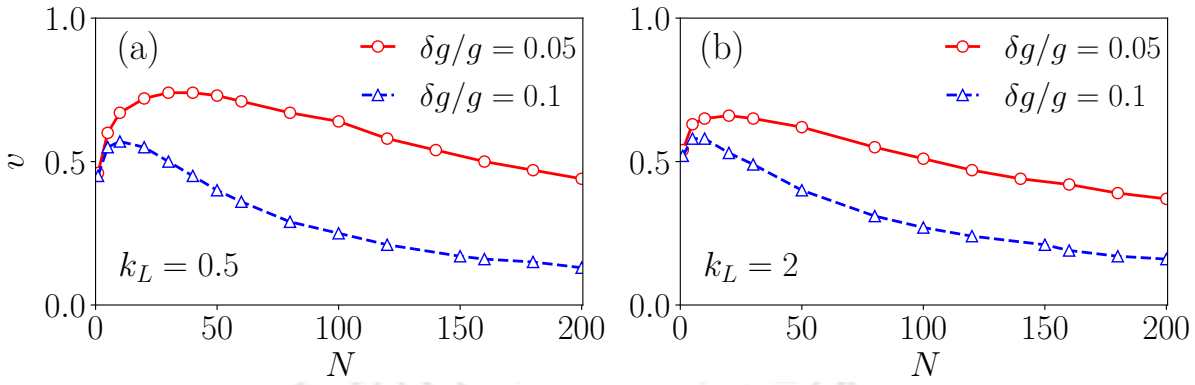

Figure 5.7: Critical velocity, v_c, of the droplet above which it dynamically transforms from a breather to a fragmented (moving) one with respect to N and different $\delta g/g$ (see legends). The droplet is characterized by $\Omega = 1$ and a SO coupled wave number (a) $k_L = 0.5$ (non-modulated solution) and (b) $k_L = 2$ (stripe state). The v_c decreases with increasing N reaching an interaction-dependent maximum where the droplet is more stable against velocity perturbations. Here v_c corresponds to the minimum of the total energy.

The transition from the breather to the fragmented or moving droplet regime is naturally characterized by a critical velocity, v_c, above which this structural deformation occurs. This critical velocity is determined by identifying the velocity at which the total energy at $t > 0$ attains its minimum value for a given set of parameters. Recall that the total energy of a stripe ground state droplet decreases for a larger amount of stripes. The behaviour of v_c for $k_L = 0.5$ (droplet) and $k_L = 2$ (stripe droplet) as a function of the normalized atom number N for $\delta g/g = 0.05, 0.1$ is depicted in Fig. 5.7(a) and (b), respectively. In both cases, i.e. striped or not droplet, v_c has an increasing trend with N, showing a maximum at the normalized particle number at which the transition from the broader Gaussian to the flat-top droplet state takes place. Eventually, v_c decreases as the flat-top regime is reached. For example, in the case of $k_L = 0.5$ for $\delta g/g = 0.05$ ($\delta g/g = 0.1$), the critical velocity exhibits a maximum around $N \sim 30$ ($N \sim 10$) and afterwards decreases. This particular feature indicates that the droplet at the maximum value of v_c is more stable against velocity perturbations as compared to droplets of different sizes [32].

5.4.2 Droplet breathing frequency

Next, we explore the parametric dependence of the droplet breathing frequency on the involved atom number and interactions. The breathing frequency, ω_{bf}, is identified in the spectrum of the time-evolved width of the droplet wavepacket [105], i.e. $\langle\psi|x^2(t)|\psi\rangle$, after a weak velocity perturbation with $v = 0.05$. The cases of both the quasi-Gaussian

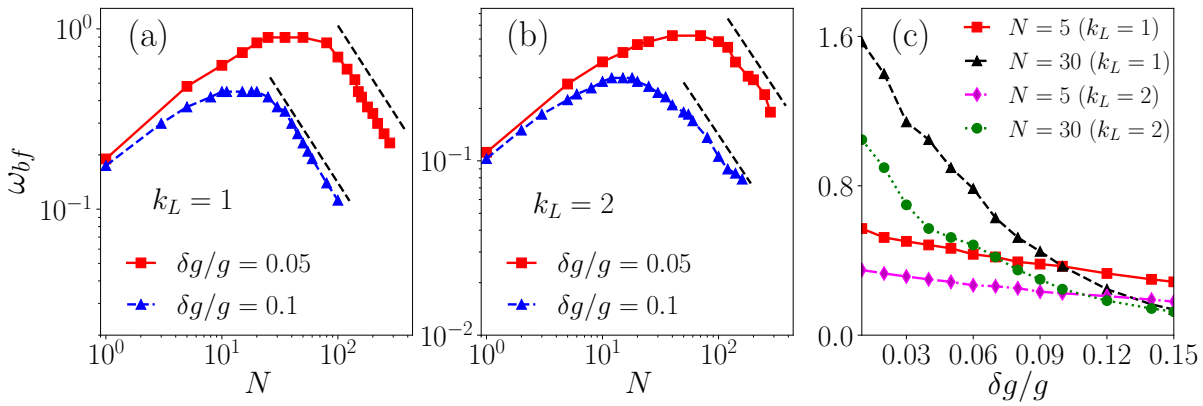

Figure 5.8: (a) Behavior of the droplet breathing frequency (ω_{bf}) with respect to N for (a) $k_L = 1$ and (b) $k_L = 2$ as well as different interactions $\delta g/g$ (see legends). The ground state droplet characterized by $g = 1$ and $\Omega = 1$ is perturbed with the initial velocity $v = 0.05$. The dotted lines provide a guide to the eye illustrating the behaviour of $\omega_{bf} \sim N^{-1}$ at large N where flat-top droplets form. Also, ω_{bf} is generically smaller for stripe droplets as can be inferred by comparing panels (a) and (b). (c) ω_{bf} as a function of $\delta g/g$ for distinct N and k_L (see legend).

with $k_L = 1$ [Fig. 5.8 (a)] and the stripe droplet with $k_L = 2$ [Fig. 5.8 (a)] are studied for completeness. It is apparent that ω_{bf} exhibits similar characteristics in both regimes. In particular, independently of $\delta g/g$, the breathing frequency features an overall increasing trend with N until it reaches a maximum and subsequently decreases at larger N. The value of N, at which ω_{bf} maximizes, appears to be smaller for stronger $\delta g/g$. Also, ω_{bf} is higher for lower $\delta g/g$ and fixed N meaning that flat-top structures possess a smaller ω_{bf} in accordance with observations for non SO coupled droplet configurations [67, 68]. Furthermore, the decreasing behaviour of ω_{bf} at large N is to a good approximation inversely proportional to the atom number, namely it scales as N^{-1}, see also the respective fitted black-dotted lines. This is consistent with the fact that the droplet displays phonon-like excitations once it reaches a flat-top background, as it was also reported in [32].

Another interesting observation is that the magnitude of ω_{bf} for a specific N and $\delta g/g$ is lower when increasing k_L, as can be deduced by comparing Fig. 5.8(a) and (b). To further elucidate this issue, we select $N = 5$ and $N = 30$ for both $k_L = 1$ and $k_L = 2$ and investigate ω_{bf} in terms of $\delta g/g$, as shown in Fig. 5.8(c). Evidently, for $N = 5$, the breathing frequency decreases almost linearly with $\delta g/g$, irrespective of k_L. However, for large N, ω_{bf} shows a non-monotonic behavior. It is higher at smaller $\delta g/g$ and reduces at a faster rate with $\delta g/g$ when compared with the $N = 5$ case. Also, at large values of $\delta g/g$, ω_{bf} is larger for $N = 5$ than for $N = 30$, independently of k_L, since, as explained above, Gaussian structures with smaller widths have an enhanced ω_{bf}.

5.4.3 Dependence of the droplet breathing frequency on the spin-orbit coupling parameters

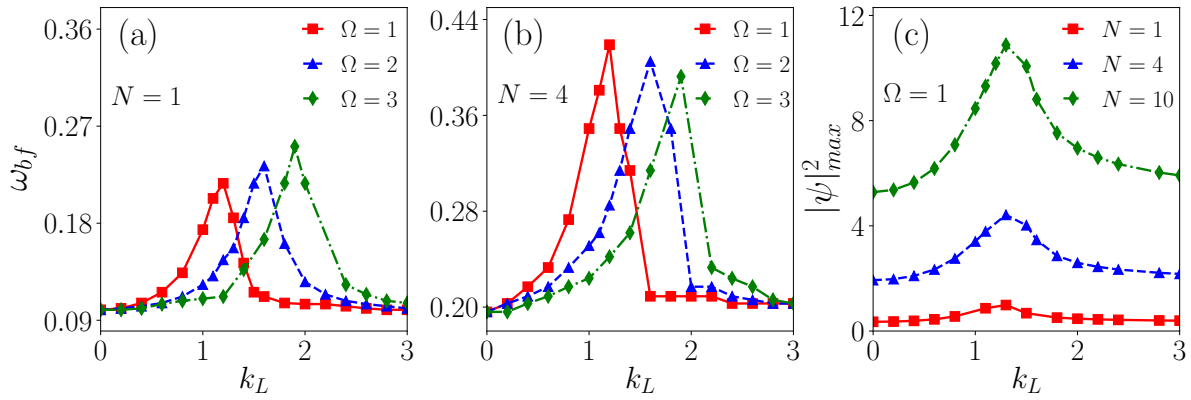

Figure 5.9: Breathing frequency, ω_{bf}, with respect to the SO coupled wave number k_L for various Ω (see legends) at (a) $N = 1$ and (b) $N = 4$. The breathing motion is generated by perturbing the droplet with velocity $v = 0.05$ with the ground state prepared with $\delta g/g = 0.1$. For all N, ω_{bf} first increases for larger k_L below a certain threshold k_L^c and beyond which it decreases. The maximum $\omega_{\rm bf}$ is larger for increased Ω when $N = 1$, while it shows a decreasing behaviour for $N = 4$. (c) The peak density, $|\psi|^2_{max}$, for different k_L and several fixed N (see legend) for fixed $\Omega = 1$. The peak density increases with N and acquires a maximum for all N at the transition where the SO coupled wave number is k_L^c.

Having analyzed the impact of the effective mean-field interaction $\delta g/g$, and atom number N on the breathing frequency ω_{bf}, we proceed to examine in more detail the effect of the SO coupled wave number (k_L) and Rabi-coupling (Ω). Fig. 5.9 presents the behaviour of ω_{bf} as a function of k_L for different Rabi-couplings while maintaining a fixed N in each panel. For small particle number, e.g. $N = 1$ shown in Fig. 5.9(a), it is observed that ω_{bf} increases with k_L until reaching a maximum at a critical k_L value, and then reduces for larger k_L. It eventually approaches the same value as the one at small k_L, i.e. $k_L \sim 0$. The increase in the maximum breathing frequency at the transition point can be attributed to the enhanced rigidity resulting from the higher density at that particular point. Moreover, increasing Ω leads to an elevation in the maximum $\omega_{\rm bf}$, and the same holds for the critical k_L^c above which $\omega_{\rm bf}$ starts to decrease. The exact opposite behaviour in terms of the maximum breathing frequency with increasing Ω is found for larger N. For instance, at $N = 4$, the maximum $\omega_{\rm bf}$ at critical k_L^c exhibits a decreasing tendency with Ω [Fig. 5.9(b)], and this behaviour persists as N is further increased to a higher value, e.g., $N = 10$. In order to understand the origin of the maximum breathing frequency at the critical SO coupled wave number, k_L^c, for different N, we provide the peak density (i.e. $|\psi|^2_{max}$) with k_L for different $N = 1, 4$, and 10 by fixing $\Omega = 1$. It is found that for a fixed N, the total density acquires a maximum, $|\psi|^2_{max}$, at the critical

SO coupled wave number. This feature occurs independently of N[See Fig. 5.9(c)].

5.4.4 Intercomponent interaction quench dynamics of the spin-orbit coupled quantum droplet

Our next focus is to explore the non-equilibrium dynamics of the droplet after a sudden change of the interaction parameter $\delta g/g$. To be more concrete, we keep the intracomponent repulsion constant at $g = 1$, and we quench the intercomponent interaction $g_{\uparrow\downarrow}$ to either larger or smaller attractive strengths compared to the original value of $g_{\uparrow\downarrow} = -0.9$, corresponding to $\delta g/g = 0.1$. The response of the system is exemplary monitored through the total density of the SO coupling setting with $k_L = 2$ and $\Omega = 1$. Similar patterns to the ones presented below also occur for $k_L = 0.5$.

Initially, we examine the effect of quenches towards larger values of $\delta g/g$, which essentially correspond to less attractive intercomponent couplings, as shown in Fig. 5.10(a)-(c). In the ground state of the system, this means that the solution tends to the flat-top regime, as illustrated, for instance, in Fig. 5.1(b). Naturally, this type of quench, due to the reduced post-quench attraction, leads, generally, to an overall expansion of the stripe droplet, but the explicit patterns depend on the specific interaction value. This is evident for all three $(\delta g/g)_{\mathrm{f}}$ values presented in Fig. 5.10(a)-(c). In particular, a relatively large post-quench amplitude, e.g., $(\delta g/g)_{\mathrm{f}} = 0.2$, results in a continuum expansion of the droplet in terms of its width and a reduction of its amplitude since the flat-top is dynamically attained [Fig. 5.10(a)]. Here, the kinetic and attractive SO coupled energy terms are the most prominent ones and thus responsible for the observed dynamics. Notice that such a droplet expansion can be equally observed in short-range attractive interacting bosonic mixtures, as reported in Ref. [105].

However, a slightly smaller quench amplitude, e.g. $(\delta g/g)_{\mathrm{f}} = 0.13$ or 0.12, is accompanied by richer dynamical patterns [see Figs. 5.10(b) and 5.10(c)]. Besides the expansion of the background, a droplet-splitting process takes place, which is less pronounced for interactions closer to the original ones. The splitting events are caused by the progressively dominant contribution of the attractive LHY energy term over the remaining ones in time. For instance, at $(\delta g/g)_{\mathrm{f}} = 0.13$, we observe the generation of three droplets from the initial structure. The two outer ones are counterpropagating, having equal velocities, and they simultaneously experience breathing motion, while the inner droplet remains at the center, showing splitting and merging events [Fig. 5.10(b)]. We remark that, in the process, excitations also propagate from the surface to the bulk. Accordingly, for a comparatively smaller increment of the interactions, e.g., $(\delta g/g)_{\mathrm{f}} = 0.12$, solely two coun-

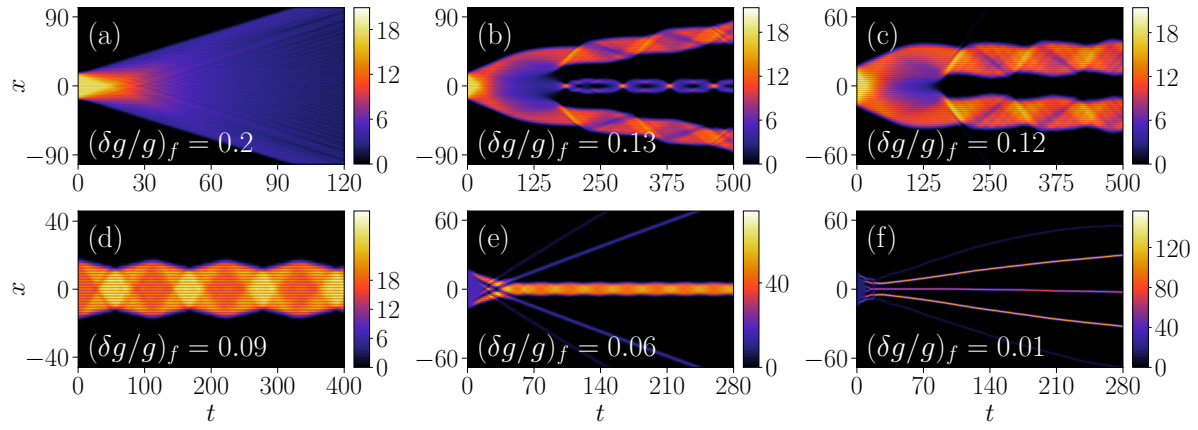

Figure 5.10: Temporal evolution of the stripe droplet density following an intercomponent interaction quench from $(\delta g/g)_{\rm in} = 0.1$ to different values of $(\delta g/g)_{\rm f}$ (see legends). The initial ground state is prepared with $\Omega = 1$, $k_L = 2$, $N = 280$, $g = 1$, and $g_{\uparrow\downarrow} = -0.9$ ($\delta g/g = 0.1$). Quenching to less attractive intercomponent interactions leads to droplet expansion [panel (a)] and splitting [panels (b), (c)]. In contrast, for quenches to stronger attractions, the droplet either performs a breathing motion [panel (d)] or fragments [panels (e), (f)]. The explicit post-quench interaction values correspond to (a) $g_{\uparrow\downarrow} = -0.8$ ($\delta g/g = 0.2$), (b) $g_{\uparrow\downarrow} = -0.87$ ($\delta g/g = 0.13$), (c) $g_{\uparrow\downarrow} = -0.88$ ($\delta g/g = 0.12$), (d) $g_{\uparrow\downarrow} = -0.91$ ($\delta g/g = 0.09$), (e) $g_{\uparrow\downarrow} = -0.94$ ($\delta g/g = 0.06$) and (f) $g_{\uparrow\downarrow} = -0.99$ ($\delta g/g = 0.01$). Similar features can also be observed for $k_L = 0.5$. The colorbar refers to the total density of the SO coupled droplet.

terpropagating droplets with relatively smaller velocity are emitted [Fig. 5.10(c)]. These emitted droplets, being closer to each other, especially as compared to the ones in the $(\delta g/g)_{\rm f} = 0.13$ quench, feature an attraction soon after their creation. This behaviour is in line with one of the closely placed short-range droplets whose effective attractive force can be explained by constructing an effective particle picture[98].

On the other hand, applying interaction quenches towards lower $(\delta g/g)_{\rm f}$ values or equivalently more attractive intercomponent interactions than the pre-quench one favours, in general, the dynamical fragmentation of the stripe droplet, see Figs. 5.10(d)-(f). Referring to the respective ground state configuration, the waveform of the post-quench interaction is a Gaussian with reduced width. Specifically, for small quench amplitudes, the stripe droplet experiences a breathing motion with the individual stripes featuring vibrational modes [Fig. 5.10(d)]. This response changes drastically for larger post-quench attractions where at short times, the destructive interference of the involved stripes generates radiation and structures resembling dark solitons at the vicinity of $x = 0$. These structures suffer further collisions leading to eventual fragmentation into multiple highly localized droplets, a process that is more pronounced for smaller $(\delta g/g)_{\rm f}$, see Figs. 5.10(e) and (f). Such violent fragmentation events are inherently related to the prevailing strong attractive LHY energy contribution. We remark that at these suppressed δg values, where MF interactions cancel out, and solely quantum fluctuations are present, the system is

close to the LHY fluid [79], which has been experimentally realized [61] in the absence of SO coupling and occurs at $\delta g = 0$. A similar droplet breaking mechanism into multiple ones was also found to occur in the context of dipolar droplets [116].

5.4.5 Effect of the Rabi coupling

A natural next question that arises concerns the impact of the SO coupling parameters, i.e. the Rabi coupling and the SO coupled wave number, on the dynamical stability of the QD. Here, we first consider sudden changes of the Rabi coupling and, in particular, divide our analysis into two parts: i) examine the time-evolution upon quenching from $\Omega = 0$ to a finite one $\Omega_\mathrm{f} > 0$ and ii) quench Ω from a finite value to a larger one. We remark that keeping all other system parameters constant and increasing Ω is associated with a decrease of the ground state energy towards more negative values.

The resulting dynamics of the QD total density after applying a quench of the Rabi coupling from $\Omega = 0$ to distinct finite values are demonstrated in Fig. 5.11. The QD is initially in its ground state, where $g = 1$, $g_{\uparrow\downarrow} = -0.95$ ($\delta g/g = 0.05$), $\Omega = 0$, $k_L = 2$, and $N = 300$. We note in passing that quenches in Ω for smaller N mainly result in breathing-like oscillations of the droplet and will not be discussed below. The droplet is left to freely evolve for a finite time, and subsequently, at $t \sim 20$, Ω is quenched. As expected, until $t = 20$, the QD maintains its shape [Fig. 5.11(a), (b)] since it corresponds to the unperturbed ground state of the system. However, around $t \sim 20$, the QD structurally deforms due to the modified Ω, and, in particular, stripes build upon the density background resembling a stripe QD.

In the case of a post-quench $\Omega_\mathrm{f} = 1$, the emergent striped pattern appears to be robust in the course of the evolution [Fig. 5.11(a)]. Namely, it retains its overall structure with the individual stripes performing weak amplitude oscillations after their nucleation and later on remaining quasi-stationary. This density pattern is reminiscent of the respective ground state configuration for $\Omega = 1$ and $k_L = 2$.

In sharp contrast, a larger Rabi coupling, e.g., $\Omega_\mathrm{f} = 5$, leads to a more complex evolution in terms of the fate of the generated configurations. Indeed, after the quench, we observe a fragmentation of the QD into several counterpropagating ones outwards and a central one, see Fig. 5.11(b). It is worth noting that the outer droplets appear to accelerate over time (see the bending behaviour of each density branch), and the inner one moves at an almost constant velocity. Additionally, as time progresses, most outer droplets merge, and the central one maintains a constant velocity accompanied by weak amplitude breathing-like oscillations. This final configuration is completely different from

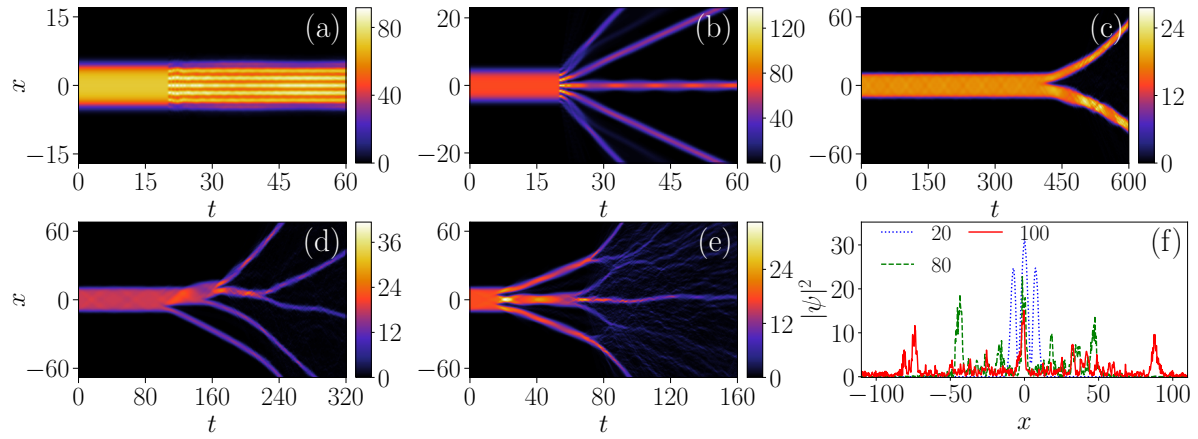

Figure 5.11: Dynamics of the QD following quenches of the Rabi-coupling Ω. Density evolution of the QD after a sudden change of $\Omega = 0$ at $t = 20$ to (a) $\Omega_f = 1$ and (b) $\Omega_f = 5$. The initial ground state is characterized by $g = 1$, $g_{\uparrow\downarrow} = -0.95$ ($\delta g/g = 0.05$), $\Omega = 0, k_L = 2$ and $N = 300$. The quench triggers either the dynamical generation of a quantum stripe droplet [panel (a)] or a fragmented droplet configuration [panel (b)]. Time-evolution of the quenched droplet density starting from $\Omega = 1$ to (c) $\Omega_f = 4$, (d) $\Omega = 11$, and (e) $\Omega = 30$. (f) Characteristic density profiles at different time instants (see legend) of panel (e). The remaining parameters are $g = 1$, $g_{\uparrow\downarrow} = -0.9$ ($\delta g/g = 0.10$), $k_L = 0.5$ and $N = 180$. The quench gives rise to an unstable evolution associated with multiple droplet-breaking events into asymmetrically moving QDs. Emitted radiation accompanies the dynamics, especially for larger Ω_f. The colorbar corresponds to the total density of the droplet.

what is expected at the ground state level of the system and appears to possess lower energy than the ground state. Specifically, the breaking into multiple droplets is attributed to the energetically unstable nature of the ground state for large values of Ω, which is otherwise dynamically stable. A similar fragmentation behaviour was observed in binary short-range droplets in [66], triggered by the modulational instability phenomenon.

On the other hand, the quench-induced droplet response changes drastically for post-quench Rabi couplings satisfying $\Omega_{\rm f} > k_L^2$. This is demonstrated below in the general case of an initially finite Rabi coupling $\Omega \neq 0$. Fig. 5.11(c)-(e) depicts the time-evolved QD densities regarding quenches at $t = 0$ from $\Omega = 1$ to higher values, e.g., $\Omega_f = 4, 11, 30$. Here, the initial state is characterized by $\Omega = 1$, $k_L = 0.5$, and $N = 180$, while the interactions are $g = 1$ and $g_{\uparrow\downarrow} = -0.9$ ($\delta g/g = 0.10$). Interestingly, it is found that this quenching process gives rise to a quite different structural deformation of the original QD compared to the previous case. This is attributed to the dominant Rabi energy term, which is more negative than the previous quench scenario from $\Omega = 0$ to a finite $\Omega_{\rm f}$.

At the initial stages of the evolution, the QD features internal excitations which, after a finite amount of time, lead to the breaking of the droplet into multiple ones whose arrangement and time of creation depend crucially on $\Omega_{\rm f}$. For instance, at $\Omega_f = 4$, the underlying instability gets activated around $t \sim 450$, triggering the breaking of the

droplet into two outgoing ones possessing equal and opposite velocities, which keep on increasing with time as depicted in Fig. 5.11(c). On the contrary, a relatively larger post-quench Rabi coupling, such as $\Omega_f = 11$, is associated with three asymmetric breaking events with respect to $x = 0$, and an eventual erratic dynamical droplet arrangement, see Fig. 5.11(d). Indeed, the first splitting occurs at $t \sim 120$, where a heavy and slow-moving droplet emerges, traveling to the left, and a lighter one with arguably much larger velocity accelerates towards the right edge. Note the earlier time of the fragmentation process than the one for $\Omega_f = 4$ [Fig. 5.11(d)]. Afterwards, this latter heavy droplet suffers a subsequent fragmentation around $t \sim 180$, where left and right-moving daughter droplets arise. Another splitting event generating two droplets takes place at $t \sim 250$, and this splitting process continues for larger evolution times.

Along the same lines quenches, see Fig. 5.11(e), to even larger $\Omega_f = 30$ result in a similar fragmentation procedure occurring at faster timescales, e.g. at $t \sim 20$ where the original droplet breaks into three droplets. Namely, the two outer droplets accelerate towards the left and right edges, respectively, and a central droplet with zero velocity. Here, a non-negligible density emission accompanies this process. Moreover, the droplet at the center undergoes at later times $t \sim 80$ a further splitting where again three highly localized moving droplets appear asymmetrically while simultaneously emitting additional small density portions. The emitted density parts accumulate during the dynamics and, eventually, at longer timescales, the spatial distribution becomes highly delocalized. The above-described density delocalization caused by an instability of the droplet upon quenching Ω is better visualized in the corresponding density snapshots provided in Fig. 5.11(f) for $\Omega_f = 30$. Notice that the energy of the ground state for $\Omega = 4, 11, 30$ is higher than that of the post-quench state during the evolution, which is probably an admixture of excited states. For this reason, the source of the observed instability here can be attributed to the presence of an energetically unstable ground state [117].

5.4.6 Response to spin-orbit coupled wave number modifications

Finally, we analyze the droplet dynamics after quenching the SO coupled wave number, k_L, as shown in Fig. 5.12. Assuming $g = 1$, $\delta g/g = 0.1$, $\Omega = 1$, $N = 180$, and an initial $k_L = 0.5$, the droplet resides in the flat-top region with no spatial undulations. In this case, the unstable droplet dynamics manifest differently as compared with the Ω-quench shown in Fig. 5.11(a) and (b). Focusing on the quench to $k_L = 1.28$ [Fig. 5.12(a)], we observe that the original droplet breaks into distinct ones already at short timescales

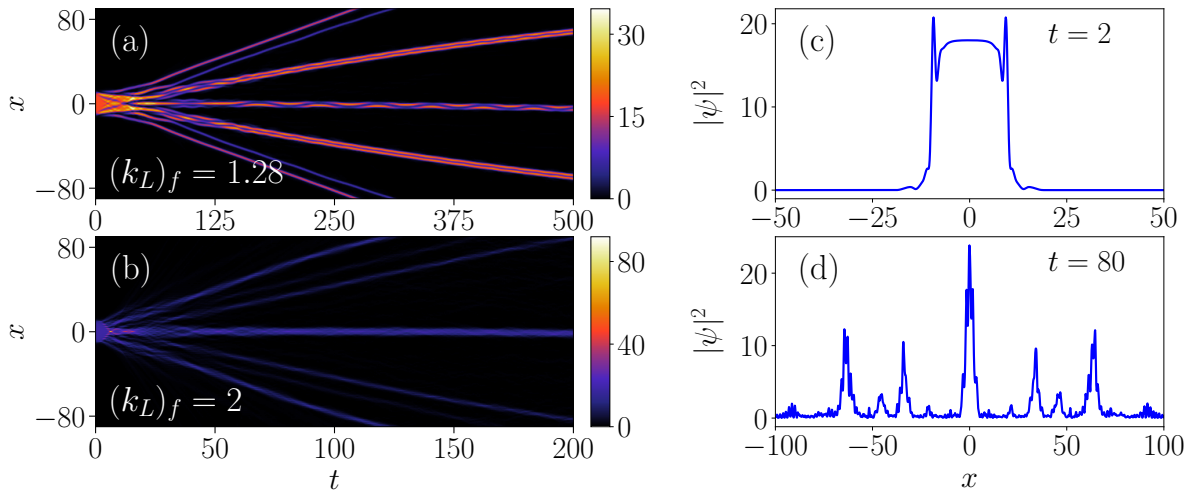

Figure 5.12: Total density evolution (see the colorbar) of the SO coupled droplet upon quenching the SO coupled wave number from $k_L = 0.5$ to (a) $(k_L)_f = 1.28$ and (b) $(k_L)_f = 2$. (c), (d) Profiles of the total density of panel (b) at specific time-instants (see legends). Depending on the quench amplitude, the droplet fragments either into an admixture of counterpropagating single and stripe droplets [panel (a)] or solitary wave patterns exhibiting an overall strong delocalization [panel (b)]. The interactions of the droplet are $g = 1$ and $g_{\uparrow\downarrow} = -0.9(\delta g/g = 0.1)$, while the Rabi coupling is fixed to $\Omega = 1$ and $N = 180$.

$t \sim 20$. This is a consequence of the prevailing contribution of the SO coupled attractive term. Namely, two outer droplets move towards the left and right edges, two travel with opposite velocities towards $x = 0$, and a heavier one remains at the center, shrinking in size. During this process, further emission events from the outer droplets occur, and later on, a collision of the central droplet with its neighboring droplets is observed around $t \sim 40$. This collision subsequently leads to the generation of a multitude of stripe droplets, i.e. density branches containing stripes. Soon after their nucleation, these stripe droplet patterns feature internal collisions, due to their excited nature, which give rise to mass transfer phenomena among the individual stripes. After this collisional stage ($t > 150$), the individual droplet branches possess a definite shape. Specifically, there are two outer counterpropagating droplet pairs, each with a single stripe droplet and almost equal velocities, two slower oppositely moving droplet stripe branches, and a central single droplet that remains more or less stationary. All the above-mentioned droplet fragments feature breathing-like excitation. This latter phenomenon results in mass exchange among the droplets within the slow-moving stripe branches.

Increasing the quench amplitude, e.g. to $(k_L)_f = 2$, is associated with a faster breaking (around $t \sim 5$) of the initial droplet and a more prominent eventual delocalization of the droplet density, as shown in Fig. 5.12(b). In contrast to the previous scenario, stripe droplet branches do not form, which is attributed to the larger quench amplitude causing more excitations into the system. The central droplet appears to be the most excited

and experiences a pronounced breathing behaviour. Here, the long-time localized density branches show solitary wave characteristics in shape, as we have confirmed by fitting them to bright soliton solutions [118]. To demonstrate the spatial delocalization of the droplet distribution, Figs. 5.12(c) and (d) illustrate corresponding density profiles at different instants. It becomes clear that initially, the unstable behaviour develops near the surface of the droplet [Fig. 5.12(c)], and over time, it spreads in space leading to several highly localized symmetric density branches with respect to $x = 0$, featuring a delocalized background due to multiple emissions (radiation), see Fig. 5.12(d). The above-discussed unstable behavior of the SO coupled droplet following the quench in k_L can be attributed, at least partially, to the dynamically unstable phase (for $\Omega < k_L^2$) of the droplet in the final state as suggested by the excitation spectrum presented in Fig. 5.4. We also note the absence of dynamical instability for quenches at which the final state satisfies $\Omega > k_L^2$. This is in line with the observations made in the respective excitation spectrum.

5.4.7 Generation of stripe droplet fragments

In the previous subsection, we discussed the dynamical response of a standard (non-modulated) droplet following a quench of the Rabi-coupling term. Here, for reasons of completeness, we aim to briefly analyze the effect of the abrupt change in Ω when the original (at $t = 0$) configuration is a stripe droplet. As such, a SO coupled setup is prepared with $g = 1$, $\delta g/g = 0.1$, $N = 280$, $\Omega = 1$ and $k_L = 2$. Applying a quench to $\Omega_f = 2.2$, see Fig. 5.13(a), leads to internal, mainly breathing-like, excitations of the

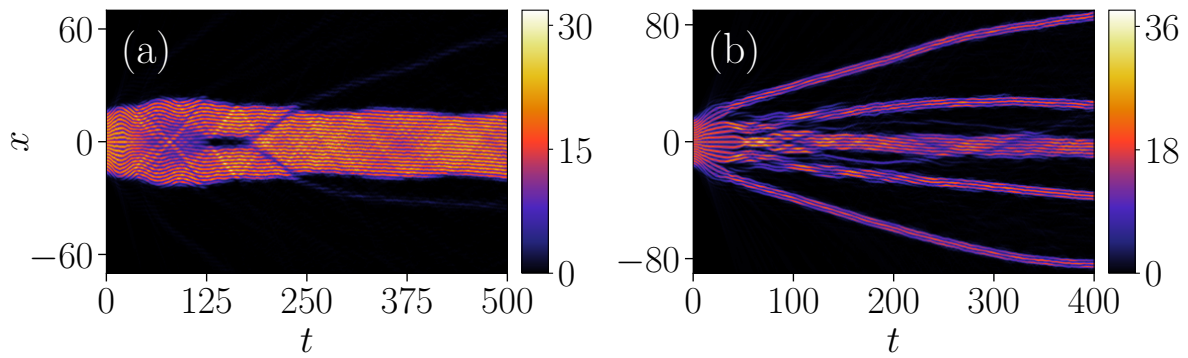

Figure 5.13: Time-evolution of the density of a stripe QD subjected, at $t = 0$, to sudden change of the Rabi coupling from $\Omega = 1$ to (a) $\Omega_f = 2.2$ and (b) $\Omega_f = 2.8$. It becomes clear that a weak amplitude quench on Ω [panel (a)] gives rise to internal excitations as well as droplet breaking and subsequent merging. However, larger quench amplitudes [panel (b)] lead to a pronounced breaking into multiple counterpropagating stripe droplets showing breathing-like oscillations. The remaining system parameters correspond to $g = 1$, $g_{\uparrow\downarrow} = -0.9$ ($\delta g/g = 0.10$), $N = 280$ and $k_L = 2$. Colorbar visualizes the total density of the stripe droplet.

stripe droplet. As time evolves, these excitations allow the splitting of the entire stripe structure, around $t \sim 125$, into two symmetric ones, which naturally contain a smaller amount of stripes. Later on, $t \sim 180$, they merge into a huge breather-striped droplet, which remains as such during the evolution. This merging process is accompanied by the simultaneous emission of two counterpropagating (with nearly equal velocity) density branches towards the edges.

On the other hand, the emergent dynamical response appears to be drastically altered when utilizing a quench to larger Rabi coupling such as $\Omega_f = 2.8$ as can be seen in Fig. 5.13(b). The modification in Ω causes the internal excitation of the original striped pattern, which after some time evolution, emits density fractions. This latter event initiates collisions between the nearest neighboring stripes and, afterwards, the breaking of the entire structure into multiple counterpropagating fragments consisting of stripe droplets. These striped density branches suffer breathing motion and mass transfer among themselves, but they survive during evolution.

5.5 Summary and Conclusions

In this Chapter, we have numerically and analytically investigated the stationary properties and nonequilibrium dynamics of SO and Rabi coupled droplets in 1D. We vary the MF interactions, number of atoms, and SO coupling parameters and have analyzed their impact on the structure and dynamics of the droplet. We have demonstrated that for small SO coupling a transition from a Gaussian to a flat-top structure takes place for either increasing atom number or decreasing intercomponent attraction. For larger SO coupling and finite interactions, we showcase the appearance of stripe patterns upon the droplet distribution and the eventual saturation of the background density to a flat-top. To further understand the transition behaviour, we calculate the system's chemical potential and kinetic energy. The kinetic energy attains its maximum value at the transition threshold, with the respective particle number being smaller for decreasing the magnitude of intercomponent attraction. Furthermore, we estimate the surface energy of the droplet, which is found to obey a power-law dependence on the relative interaction ratio, and it is the same independent of the stripe character of the droplet. We have used Bogoliubov-de-Gennes analysis to compute the collective excitation spectrum of different phases of the droplet while for small SO coupled wave numbers, Gaussian-shaped and flat-top droplets are stable upon variations of the intercomponent attractive interaction and the atom number. However, for larger SO coupled wave numbers, the stripe droplets are unstable configurations as dictated by the emergence of complex eigenvalues in the

excitation spectrum independently of the particle number or intercomponent attraction.

For velocity perturbations, we find that the droplet undergoes breathing-like oscillations for small post-quench velocities and for large velocity breaks into several moving droplets independent of the SO coupled wave number (same for non-modulated and stripe phase of the droplet). The critical velocity for the transition from the breathing to the moving droplet is maximal around the particle number threshold at which the ground state makes a transition from the Gaussian to flat-top. The breathing frequency of the droplet, generally smaller for stripe droplets, shows increasing trend with the atom number reaching a maximum at the transition from Gaussian to flat-top droplets and afterwards satisfies a power-law decrease inversely proportional to the particle number for both non-modulated and stripe phase of the droplet. The latter feature is the indication of the phononic spectrum of flat-top droplets, irrespective of the SO coupled wave number.

Upon intercomponent interaction quenches we have observed a large variety of interesting dynamics. In the case of reduced attraction, the droplet either expands or splits into two counterpropagating fragments. However, for stronger attractions quenching results in a breathing droplet, and for larger amplitudes, the droplet breaks into several fragments whose number increases with larger attraction. Employing quenches of the Rabi coupling leads to a structural deformation from a smooth droplet to a striped one for relatively small quench amplitudes. Additionally, asymmetric droplet fragmentation occurs for increasing post-quench Rabi coupling, where the latter exceeds the SO coupled wave number. Interestingly, abrupt changes of the SO coupled wave number again allow the breaking of the original droplet due to the dominance of the attractive SO coupling contribution and leading to admixtures of single and striped droplet branches or erratic spatial distributions at large SO coupling.

So far, in the previous three Chapters, we have focused to analyze the structure and dynamics of the droplet considering the equal intraspecies interactions. In the next Chapter, we will consider the unequal intraspecies interaction that leads to exhibit an interesting structural change in the SO coupled droplet including the variation in the population among the spin components.

Chapter 6

Interaction imbalanced spin-orbit coupled quantum droplets

In previous Chapters 3, 4, 5, the analysis of the droplet was based upon the equal population of the component. In this Chapter, we consider the effect of the unequal population of the spin-component by imposing the unequal intraspecies interaction on the structure and dynamics of the SO coupled droplet. We have obtained many interesting phenomena, such as controlling population imbalance with SO coupling and structural modifications of the droplet phases by tuning the interaction imbalance both without and with the harmonic trap. The plan of the Chapter is as follows. First, we present a very brief literature review pertaining to imbalanced QD and the motivation of the present work. Further, we provide the numerical simulation results based on the eGPEs of imbalanced SO coupled droplet.

6.1 Introduction

Attractive interacting many-body systems are historically intriguing and challenging to tackle since they are structurally unstable. However, recent advances in cold atoms allow nowadays to enter this regime which, under specific circumstances, can sustain bound states such as QDs [58, 119], bubbles [98, 100] and extreme nonlinear waves, e.g. the Peregrine soliton [120]. Droplets are highly incompressible states which have already been observed in the laboratory using short-range bosonic mixtures [15, 23, 24, 25, 62, 121], as well as long-range dipolar gases [12, 20, 22, 122]. For short-range settings that we are interested in this work, quantum fluctuations, customarily modeled by the LHY correction term [123], provide the key mechanism to support droplet formation [14, 58]. A

frequently employed framework to describe the properties of these configurations, including stationary states [101, 124], collisions [62, 104], collective [31, 125] and nonlinear [101, 102, 126] excitations, refers to a system of suitably eGPE taking into account the dimension [127, 128, 129] and system [28] dependent LHY term. Despite pure bosonic systems, droplets can also exist in Bose-Fermi [63, 130, 131] and SO coupled settings [93, 96, 107].

Yet, droplets have been mainly studied by leveraging the fixed intracomponent interaction to density ratio [14, 97] where the system reduces to a single-component one. The breaking of this condition where the two components are prominently distinguishable has been only very recently considered [68, 69, 132, 133, 134], including also lattice [135] and ring [136] geometries where more complex phases have been identified. On the other hand, the inclusion of SO coupling into the two-component droplet setting brings additional features such as the build-up of stripe droplet configurations [93, 96] and the emergence of spin transfer is prohibited in the absence of Rabi coupling [137]. Hence, the SO coupling parameters (wave number and Rabi-coupling) may be exploited to demonstrate the controllability of the ensuing unexplored two-component droplet phases. To address these open questions, we employ a two-component bosonic droplet system in one dimension with unequal short-range intracomponent interactions. We aim to examine the interplay of intracomponent repulsion and SO coupling parameters on the generation of droplet phases, their nonequilibrium dynamics, and accompanying spin-demixing processes.

We find a variety of different ground state droplet structures sharing intercomponent miscibility while exhibiting stripe (non-modulated) shapes for large (small) SO coupled wave number. Overall droplet background deforms from Gaussian to flat-top for increasing (decreasing) atom number (interaction). Interestingly, a gradual distortion from the stripe to non-modulated Gaussian and afterwards to flat-top droplets occurs for increasing Rabi coupling. It is also explicated that the intercomponent population imbalance can be controlled through the aforementioned parametric variations, e.g. it increases for either larger interactions or SO coupled wave number, but it vanishes for increasing Rabi coupling. An external trap enforces Gaussian stripe droplet distributions of increasing size and peak density for larger atom numbers and, importantly, a transition from a self-bound to a trapped gas reflected in the sign change of the system's chemical potential. The respective transition region exists at lower (larger) atom numbers for tighter traps (stronger repulsions). We explore the lowest excitation in the form of breathing oscillation by quenching the trap. Following this, we analyze the dynamical stability of the imbalanced droplets for different types of perturbations and observe different sorts of novel features like spin-mixing, spin-demixing, and generation of fragmented droplets, etc.

The rest part of the Chapter is organized as follows. Section 6.2 introduces the interaction imbalanced SO coupled droplet setting and the respective coupled eGPEs used to describe both the ground states and the dynamics. In Sec. 6.3, we analyze the ground state phases and spin transfer processes of the two-component SO coupled droplets both in the stripe and the non-modulated states in terms of the interactions, atom number, and SO coupling parameters. The impact of an external trap is also discussed. Section 6.4 elaborates on the dynamical response of the SO coupled droplets after quenching either the trap frequency to induce collective breathing evolution or the SO coupling parameters triggering either fragmentation or a directed droplet motion and spin-mixing whose degree depends on the quench amplitude. In Sec. 6.5, we summarize our main findings.

6.2 Imbalanced spin-orbit coupled droplet setting and equations of motion

We consider a 1D two-component bosonic system in the presence of SO coupling characterized by wave number k_L, and Rabi coupling Ω between the involved spin-$\uparrow$ and spin-$\downarrow$ states. The atoms in each spin state interact repulsively, i.e., $g_{\uparrow\uparrow} \neq g_{\downarrow\downarrow} > 0$, and the coupling among the spin states is attractive $g_{\uparrow\downarrow} < 0$. This condition may give rise to a SO coupled QD in the presence of quantum fluctuations whose effect is taken to first-order via the LHY correction term. The main characteristic of our setup is that the spin states are assumed to feature different intracomponent repulsions ($g_{\uparrow\uparrow} \neq g_{\downarrow\downarrow}$) which in turn result in intercomponent particle imbalance ($N_\uparrow \neq N_\downarrow$) due to Rabi coupling. The SO coupled QD is described by the appropriate set of coupled eGPEs as given in Eq. 1.54. For the sake of completeness here we provide the dynmaical equations [33, 80, 93, 96] which in dimensionless units read

$$\mathrm{i}\partial_t\psi_\uparrow = \Bigg[-\frac{1}{2}\partial_x^2 - \mathrm{i}k_L\partial_x + g_{\uparrow\uparrow}|\psi_\uparrow|^2 - \sqrt{g_{\uparrow\uparrow}g_{\downarrow\downarrow}}|\psi_\downarrow|^2 + \frac{2\sqrt{g_{\uparrow\uparrow}g_{\downarrow\downarrow}}\delta g}{(g_{\uparrow\uparrow}+g_{\downarrow\downarrow})^2}\left(g_{\downarrow\downarrow}|\psi_\uparrow|^2 + \sqrt{g_{\uparrow\uparrow}g_{\downarrow\downarrow}}|\psi_\downarrow|^2\right) - \frac{g_{\uparrow\uparrow}}{\pi}\sqrt{g_{\uparrow\uparrow}|\psi_\uparrow|^2 + g_{\downarrow\downarrow}|\psi_\downarrow|^2}\Bigg]\psi_\uparrow + \Omega\psi_\downarrow, \tag{6.1a}$$

$$\mathrm{i}\partial_t\psi_\downarrow = \Bigg[-\frac{1}{2}\partial_x^2 + \mathrm{i}k_L\partial_x + g_{\downarrow\downarrow}|\psi_\downarrow|^2 - \sqrt{g_{\uparrow\uparrow}g_{\downarrow\downarrow}}|\psi_\uparrow|^2 + \frac{2\sqrt{g_{\uparrow\uparrow}g_{\downarrow\downarrow}}\delta g}{(g_{\uparrow\uparrow}+g_{\downarrow\downarrow})^2}\left(g_{\uparrow\uparrow}|\psi_\downarrow|^2 + \sqrt{g_{\uparrow\uparrow}g_{\downarrow\downarrow}}|\psi_\uparrow|^2\right) - \frac{g_{\downarrow\downarrow}}{\pi}\sqrt{g_{\uparrow\uparrow}|\psi_\uparrow|^2 + g_{\downarrow\downarrow}|\psi_\downarrow|^2}\Bigg]\psi_\downarrow + \Omega\psi_\uparrow, \tag{6.1b}$$

where $\psi_\uparrow$ ($\psi_\downarrow$) is the 1D spin wave function. Also, $\delta g = g_{\uparrow\downarrow} + \sqrt{g_{\uparrow\uparrow} g_{\downarrow\downarrow}}$ is the MF balance point [28]. Since below the system fulfills either $N_\uparrow \neq N_\downarrow$ or $g_{\uparrow\uparrow} \neq g_{\downarrow\downarrow}$ the two-components should behave differently and we aim to probe their deviations when SO coupling is present. For convenience, we use the normalization condition [32] on the system wave function $\int_{-\infty}^{\infty} [|\psi_\uparrow|^2 + |\psi_\downarrow|^2]\, dx = N$. Here, the constant N specifies the normalized total number of particles in the droplet with the population of the individual components given by $N_{\uparrow,\downarrow} = \int_{-\infty}^{\infty} |\psi_{\uparrow,\downarrow}|^2 dx$.

The energy unit of the system is expressed with respect to $\hbar\omega_\perp$, where $\omega_\perp$ is the transverse trap frequency. Accordingly, the time and length scales are measured in units of $\omega_\perp^{-1}$ and $a_\perp = \sqrt{\hbar/(m\omega_\perp)}$ respectively. The effective 1D intracomponent interaction strengths $g_{\uparrow\uparrow} = 2\mathcal{N}_\uparrow a_{\uparrow\uparrow}/a_\perp$ and $g_{\downarrow\downarrow} = 2\mathcal{N}_\downarrow a_{\downarrow\downarrow}/a_\perp$, while the intercomponent one is $g_{\uparrow\downarrow} = 2\mathcal{N}_\uparrow a_{\uparrow\downarrow}/a_\perp$ with $\mathcal{N}_{\uparrow,\downarrow}$ being the particle number in each component. In these expressions, ($a_{\uparrow\uparrow}$, $a_{\downarrow\downarrow}$) is the set of intracomponent 3D s-wave scattering lengths and $a_{\uparrow\downarrow}$ signifies the intercomponent one. These can be tuned in the experiment through Feshbach resonances [24]. The 1D wave function is rescaled as $\psi_{\uparrow,\downarrow} = \tilde{\psi}_{\uparrow,\downarrow}\sqrt{a_\perp}$, while the SO coupling $k_L \to \tilde{k}_L a_\perp$ and intensity (Rabi-coupling) $\Omega \to \tilde{\Omega}/\omega_\perp$. All tilde quantities refer to dimensionful ones.

In a corresponding experiment the two spin states can be emulated, for instance, with the hyperfine states $|\uparrow\rangle \equiv |F = 1, m_F = -1\rangle$ and $|\downarrow\rangle \equiv |F = 1, m_F = 0\rangle$ of ^{39}K [15, 23, 62], while considering a total number of atoms $\mathcal{N} \sim [10^4, 10^6]$. The quasi-1D geometry is achieved via a tight confinement of frequency $\omega_\perp = 2\pi \times 600$Hz in the transverse directions, which leads to $a_\perp = 0.657\,\mu$m. Also, across the elongated direction, a box potential using a digital micromirror device can be used [138]. Moreover, the intervals of 3D scattering lengths $a_{\uparrow\uparrow} = 2/N[0.1242a_0, 0.3104a_0]$ and $a_{\downarrow\downarrow} = 2/N[0.1242a_0, 2.4831a_0]$, where a_0 is the Bohr radius, can be used to reach the effective couplings $g_{\uparrow\uparrow} = [0.2, 0.5]$ and $g_{\downarrow\downarrow} = [0.2, 4]$ allowing for ratios $g_{\downarrow\downarrow}/g_{\uparrow\uparrow} = [1, 20]$. Along the same lines, $a_{\uparrow\downarrow} = 2/N[-0.0621a_0, -0.8070a_0]$ in order to have $g_{\uparrow\downarrow} = [-0.1, -1.3]$ for $\delta g = 0.1$. The dimensionless Rabi coupling frequency interval $\Omega = [0, 30]$ can be realized by tuning the Raman laser intensity [46, 112] in the range $\tilde{\Omega} = 2\pi \times [0 - 18]$kHz, and the SO coupled wave number interval $k_L = [0.1, 12]$ corresponds to variations of the laser wavelength [46, 108, 109] from $\lambda_L = 29.19\ \mu$m to 243.25nm [46].

To numerically obtain the ground state of the interaction imbalanced SO coupled droplets described by the time-independent version of Eqs. (6.1a) and (6.1b), we use the imaginary time propagation method exploiting a split-step Crank-Nicolson scheme [71, 74, 85]. On the other hand, to investigate the nonequilibrium dynamics of the SO coupled droplets, we rely on the real-time propagation method. In dimensionless units, the utilized

box size has length $L = 307$ and features spatial resolution $dx = 0.025$, while the time step of the integrator is fixed to $dt = 10^{-5}$. For all the simulations to be presented below, we employ a Gaussian initial ansatz for each component, simultaneously imposing the anti-symmetric condition, i.e., $\psi_\uparrow(x) = -\psi_\downarrow(-x)$ on the components which facilitates the numerical identification of the SO coupled droplet ground state [139].

6.3 Ground states of the imbalanced spin-orbit coupled droplets

A pertinent question concerns the structure of the droplet configurations and their control by varying relevant system parameters. Recently, it has been demonstrated that an imbalanced bosonic mixture in the droplet regime (where the components preserve their atom number) may arrange in miscible flat-top or Gaussian type QD distributions with distorted tails upon tuning the intracomponent interactions [68, 69]. However, in the presence of SO coupling, particle exchange can occur due to the Rabi coupling, and interestingly, the QDs can also assemble in the so-called stripe configurations. Below, we exploit different intracomponent interaction imbalances in order to characterize various ground-state QD configurations featuring intercomponent atom exchange.

6.3.1 Spin-orbit coupled droplets in free space

To understand the impact of the intracomponent interaction imbalance quantified by the ratio $g_{\downarrow\downarrow}/g_{\uparrow\uparrow}$ on the SO coupled QD structures without a trap, we initially employ the densities $|\psi_\uparrow|^2$ and $|\psi_\downarrow|^2$ of the individual components. We first focus on SO coupling parameters $\Omega = 0.5$, $k_L = 0.5$ implying the absence of spatially modulated stripe phases since $k_L^2 < \Omega$. Figure 6.1(a) presents the component density profiles for different $g_{\downarrow\downarrow}/g_{\uparrow\uparrow}$, while the remaining system parameters ($N = 100$, $\delta g = 0.1$) including the SO coupling ones are held fixed. As it can be seen, upon increasing $g_{\downarrow\downarrow}/g_{\uparrow\uparrow}$ there are two important structural modifications in the QD distributions. Namely, a gradual transition from flat-top to Gaussian-type miscible droplets takes place. This is understood by the fact that an increase in $g_{\downarrow\downarrow}/g_{\uparrow\uparrow}$ implies a stronger intercomponent attraction for maintaining the δg constant. This stronger intercomponent attraction is responsible for the spatial localization of the droplets and hence their deformation to Gaussian-type configurations which has also been discussed in two-component droplets without SO coupling [68]. Additionally, to identify the interaction threshold value beyond which the aforementioned transition occurs, we calculate the total kinetic energy of the droplet as a function $g_{\downarrow\downarrow}/g_{\uparrow\uparrow}$

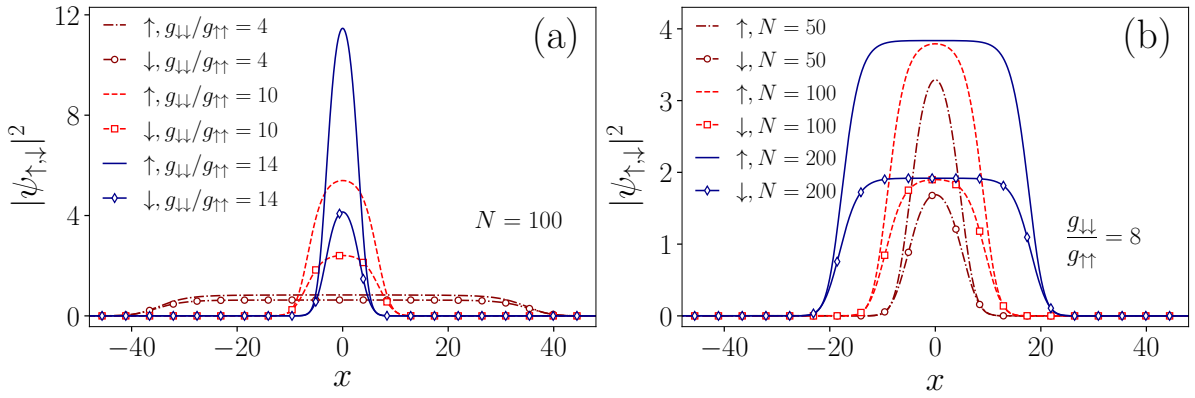

Figure 6.1: Ground state densities of the spin-up (down) component of the SO coupled QD (a) for different intracomponent interaction ratio $g_{\downarrow\downarrow}/g_{\uparrow\uparrow}$ keeping the total atom number $N = 100$ and (b) for varying N and fixed $g_{\downarrow\downarrow}/g_{\uparrow\uparrow} = 8$. Each component droplet densities transit from flat-top to Gaussian profiles upon increasing $g_{\downarrow\downarrow}/g_{\uparrow\uparrow}$ or decreasing N. The droplets among the components are miscible, and the distribution of the stronger interacting spin-down one becomes wider for larger (smaller) $g_{\downarrow\downarrow}/g_{\uparrow\uparrow}$ (N). In all cases, the SO coupled QD is characterized by $\Omega = 0.5$, $k_L = 0.5$, $\delta g = 0.1$, and $g_{\uparrow\uparrow} = 0.2$.

as depicted in Fig. 6.2(a). The sharp increase of the kinetic energy beyond $g_{\uparrow\uparrow}/g_{\downarrow\downarrow} \sim 8$ signifies the transition from the flat-top to the Gaussian droplet. Indeed, flat-top droplets being highly incompressible should minimize their kinetic energy [28].

Another observation is that both components having droplet character remain miscible independently of $g_{\downarrow\downarrow}/g_{\uparrow\uparrow}$ with the spin-down featuring the stronger repulsion to be wider. Notice here that suppressing $g_{\downarrow\downarrow}/g_{\uparrow\uparrow}$ leads to almost identical droplets in both components, thus recovering the symmetric droplet case which has been mainly explored so far [58, 97]. Importantly, a larger $g_{\downarrow\downarrow}/g_{\uparrow\uparrow}$ yields transfer of atoms among the spin components which

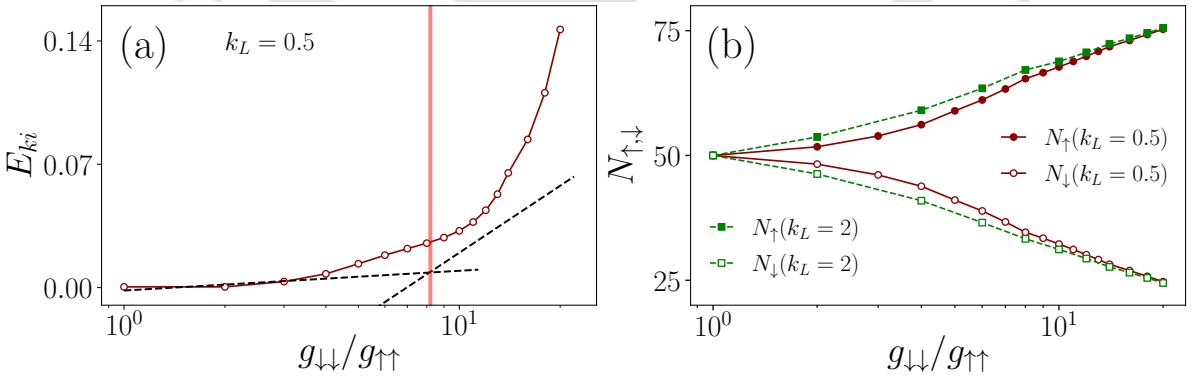

Figure 6.2: (a) Total kinetic energy, $E_{\rm ki}$, with respect to $g_{\downarrow\downarrow}/g_{\uparrow\uparrow}$ and SO coupled characteristics $k_L = 0.5$ and $\Omega = 0.5$. The increasing tendency of $E_{\rm ki}$ with a finite rate for larger $g_{\downarrow\downarrow}/g_{\uparrow\uparrow}$ indicates the deformation of the droplets to a Gaussian shape. (b) Variation of each component atom number as a function of $g_{\downarrow\downarrow}/g_{\uparrow\uparrow}$ for different k_L (see legend). Population transfer occurs from the strongly interacting spin-down to the weakly spin-up components, and it is enhanced for larger $g_{\downarrow\downarrow}/g_{\uparrow\uparrow}$. The remaining system parameters are the same with Fig. 6.1.

can also be testified by monitoring the component populations as a function of $g_{\downarrow\downarrow}/g_{\uparrow\uparrow}$ shown in Fig. 6.2(b). Indeed, atoms migrate from the strongly interacting component towards the weaker interacting one, and the particle imbalance is enhanced for increasing $g_{\downarrow\downarrow}/g_{\uparrow\uparrow}$.

For completeness, we illustrate the effect of the total atom number N on the QD ground states in Fig. 6.1(b) while fixing all other parameters and considering $g_{\downarrow\downarrow}/g_{\uparrow\uparrow} \sim 8$. In all cases, we observe that the droplet components assemble in a miscible fashion, with the strongly interacting spin-down component being wider and accommodating a smaller number of atoms [see Fig. 6.2(a)]. Moreover, for larger N, the QD becomes broader both in amplitude and width and transforms from a Gaussian shape (e.g. $N = 50$) to a flat-top (e.g. $N \gtrsim 100$) one. We remark that such a transition with respect to the atom number has also been discussed in the context of single-component droplets in Chapter 5.

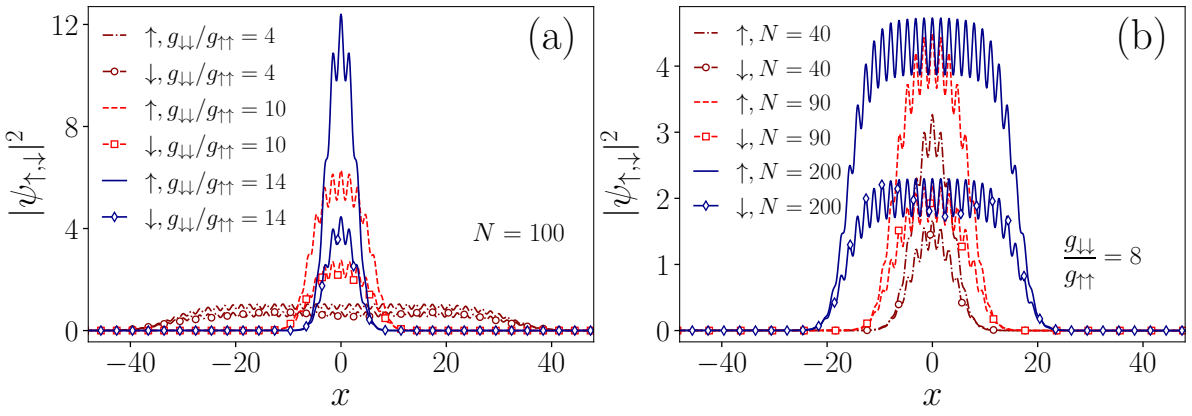

Figure 6.3: Densities of the ground state stripe droplets of the spin-up and spin-down components (a) in terms of $g_{\downarrow\downarrow}/g_{\uparrow\uparrow}$ while considering $N = 100$ and (b) for different N having $g_{\downarrow\downarrow}/g_{\uparrow\uparrow} = 8$. As it can be seen, a decreasing (increasing) $g_{\downarrow\downarrow}/g_{\uparrow\uparrow}$ (N) leads to the formation of stripe flat-top SO coupled droplets in each of the components with the latter maintaining their miscible character and hosting a larger number of stripes. The stripe SO coupled droplets are prepared with $\Omega = 0.5$, $k_L = 2$ $\delta g = 0.1$, and $g_{\uparrow\uparrow} = 0.2$.

Similar ground state QD configurations exist also when the SO coupling parameters become more important, i.e., for $k_L^2 > \Omega$, where stripe droplets build up in both components. To demonstrate this situation we employ a SO coupled wave number $k_L = 2$ and Rabi coupling $\Omega = 0.5$, while investigating variations of the interaction ratio $g_{\downarrow\downarrow}/g_{\uparrow\uparrow}$ [Fig. 6.3(a)] and the total atom number [Fig. 6.3(b)]. The other system parameters remain fixed. It becomes evident that either decreasing $g_{\downarrow\downarrow}/g_{\uparrow\uparrow}$ or increasing N a deformation from a Gaussian-type stripe droplet to a flat-top one occurs. Naturally, flat-top droplets can host a larger number of stripes since they are substantially elongated. As in the $k_L = 0.5$ case, the weakly interacting component has relatively smaller width and larger peak density. Finally, the transfer of atoms takes place from the strongly interacting

spin-down to the weakly interacting spin-up component, see Fig.6.2(b). This population transfer is almost the same both in magnitude and trend with the $k_L = 0.5$ scenario.

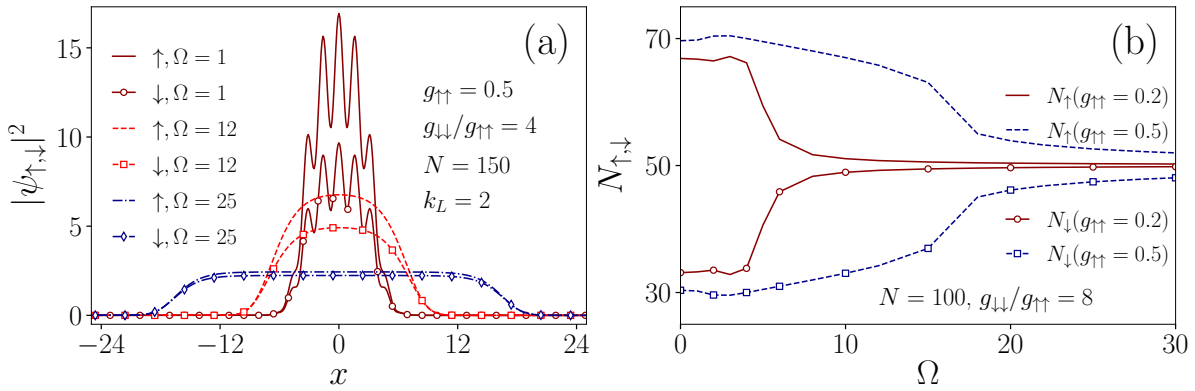

Figure 6.4: Ground state densities of the spin-up and spin-down droplet components for different Rabi couplings Ω (see legend) and fixed $g_{\downarrow\downarrow}/g_{\uparrow\uparrow} = 4$, $N = 150$, and $k_L = 2$. An increasing Ω results in the deformation from stripe to standard and afterwards wider droplets with more pronounced flat-top and almost equal intercomponent population. (b) The population of each spin component as a function of Ω for different intracomponent interactions $g_{\uparrow\uparrow} = 0.2$ and $g_{\uparrow\uparrow} = 0.5$ with fixed $N = 100$, $k_L = 2$ and $g_{\downarrow\downarrow}/g_{\uparrow\uparrow} = 8$. The Ω threshold above which the components become almost equally populated depends on the interactions.

As a next step, we analyze the impact of the Rabi coupling on the shape and population imbalance of the two-component droplet. Characteristic density profiles of both droplet components are depicted in Fig. 6.4(a) with respect to the Rabi coupling. It can be seen that a larger Ω results in the structural modification from the stripe to standard droplets close to the threshold $k_L^2 = \Omega$. Further increasing Ω enforces a broadening of the non-modulated droplet distributions towards flat-top profiles and simultaneous suppression of the intercomponent population imbalance. Such density deformations upon Rabi coupling variations have also been reported in single-component droplets in Chapter 5. Hence, an increasing Ω tends to balance the population among the components, which is attributed to the dominance of the Rabi coupling energy term as compared to the kinetic, MF and LHY energy contributions in the droplet.

Moreover, we find that the intercomponent atom transfer from the majority to the minority component is minimized for high Ω [140]. This can be directly inferred from the spin populations shown in Fig. 6.4(b) in terms of Ω for different interactions and $k_L = 2$. The spin populations remain nearly constant for low Ω, namely before the transition from stripe to standard configurations occurs. Afterwards, they start to be significantly modified and become almost the same for high enough Ω. This process depends on the intracomponent interactions, and in particular, the Ω interval where the spin imbalance is enhanced is larger for stronger interactions which are in accordance to the behaviour

of a spin-1/2 repulsive gas [137, 141]. Therefore, the interactions can be used as a knob to control the spin imbalance. It is worth noting that a similar behaviour of the spin populations takes place also for other values of the SO coupled wave number k_L, and especially the imbalance at relatively small Ω is more prominent for increasing k_L (not shown for brevity).

6.3.2 Impact of a harmonic trap: transition from droplet to gas

Having explicated the effect of the intracomponent interaction imbalance, the atom number, and the Rabi coupling on the two-component SO coupled droplet configurations in free space, we move to understand the impact of an external harmonic trap on the ensuing ground states. Specifically the eGPE Eqs. (3.1a), (6.1b) contain the additional $V(x)\psi_{\uparrow,\downarrow}$ term with the same trap $V(x) = (1/2)M\lambda^2x^2$ (where $m_\uparrow = m_\downarrow \equiv M$) acting on both spin states. This external confinement imposes the harmonic oscillator length, $a_{\rm ho} = \sqrt{\hbar/(m\lambda)}$, across the axial direction as another relevant length scale which certainly delays the formation of flat-top structures as it has already been reported for single-component droplets [68]. However, the presence of an external trap is common in corresponding experimental settings [23, 24, 25].

Density profiles of ground state SO coupled droplets are presented in Fig. 6.5(a) for varying atom number and an exemplary relatively weak trap frequency $\lambda = 0.04$, while $g_{\downarrow\downarrow}/g_{\uparrow\uparrow} = 6$, $\Omega = 0.5$, and $k_L = 2$ are kept fixed. It can be readily seen that the finite trap acts against the formation of flat-top droplets for increasing atom number. Notice that for the same parameters but without the trap, both components feature a transition towards a flat-top with stripe shape as N increases (not shown for brevity) [see Fig. 6.1(b)]. Instead, here, for larger N, the stripe droplet density becomes wider, featuring a striped Gaussian shape whose peak value increases [Fig. 6.5(a)]. The striped droplet components remain miscible, and the stronger interacting component has a slightly larger width and lower peak density. As expected, upon considering a tighter trap, the Gaussian profile of the striped droplet becomes more pronounced (not shown), a behaviour that remains consistent for larger atom numbers.

To shed further light on the role of the external trapping potential for the droplet configurations and their bound character, we subsequently calculate the total chemical potential (μ) of the two-component system for varying atom numbers. As an example, we employ an interaction ratio of $g_{\downarrow\downarrow}/g_{\uparrow\uparrow} = 6$ illustrated in Fig. 6.5(b) for different values of λ. In the case of $\lambda = 0.01$, μ initially (namely for quite small atom numbers, $N < 20$) exhibits a decreasing tendency (i.e., it becomes more negative) for increasing N, and

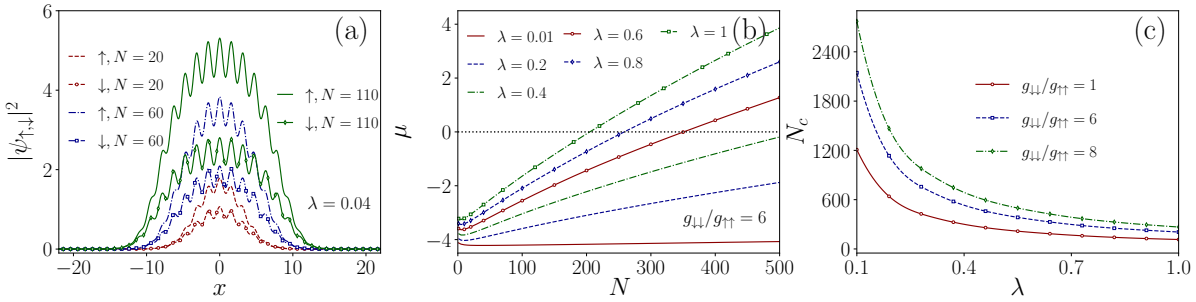

Figure 6.5: (a) Ground state density profile of the droplet components for different N (see legends) in the presence of a harmonic trap with strength $\lambda = 0.04$ and $g_{\downarrow\downarrow}/g_{\uparrow\uparrow} = 6$. The stripe distributions of both components become wider for larger, N while flat-top signatures are suppressed due to the trap. (b) Total chemical potential, μ, of the binary stripe droplet as a function of N for different trap strengths (see legend) when $g_{\downarrow\downarrow}/g_{\uparrow\uparrow} = 6$. A transition from a negative to a positive system's energy exists for increasing N, becoming more prominent for tighter confinement. (c) Critical atom number, N_c for the droplet to gas transition with respect to λ and various $g_{\downarrow\downarrow}/g_{\uparrow\uparrow}$ (see legend). The transition takes place at larger N_c for increasing $g_{\downarrow\downarrow}/g_{\uparrow\uparrow}$ and fixed λ. In all cases the SO coupling parameters $\Omega = 0.5$, and $k_L = 2$, while the interaction strengths $g_{\uparrow\uparrow} = 0.2$ and $\delta g = 0.1$.

eventually after reaching a certain atom number it saturates. This behavior indicates that the many-body state maintains its self-bound droplet character throughout the N variation. On the other hand, as the confinement becomes tighter (namely for larger λ) the aforementioned chemical potential trend changes drastically. Specifically, μ starts to decrease for relatively small atom number acquiring a minimum and afterwards features a clean increasing tendency, which is more pronounced for larger λ. However, irrespectively of N, it holds that $\mu < 0$, and hence the system maintains its self-bound nature as long as λ is not noticeable, e.g. $\lambda \leq 0.2$. The chemical potential minimum with respect to N, is a consequence of the balance of the kinetic, MF, and LHY energy contributions at the specific N depending on λ. We also observe that this minimum value of μ shifts towards lower N for larger λ due to the increasing influence of the potential energy.

Interestingly, there is a critical value of the trap strength e.g., $\lambda \geq 0.4$ in our setting at which μ crosses from negative to positive values, see also the green dash-dotted line in Fig. 6.5(b). This suggests a transition of the two-component bosonic system from a self-bound droplet phase ($\mu < 0$) towards a trapped gas where $\mu > 0$ [69, 142]. It is also evident that this transition occurs at smaller N for increasing λ since the energy of the trap becomes more prominent.

The droplet-to-gas transition quantified through μ can be also clearly seen for different interaction imbalances that we have checked, see e.g., Fig. 6.5(c). In particular, the stronger the imbalance the larger the negative μ interval. Otherwise stated, for stronger intracomponent interactions the droplet character is sustained for a broader atom number, which is important especially for tighter traps. The critical number of atoms, N_c, where

the transition point occurs is explicitly shown in Fig. 6.5(c) for varying λ and specific interaction ratios verifying our previous arguments. Indeed, we find that N_c increases for larger $g_{\downarrow\downarrow}/g_{\uparrow\uparrow}$, while it decreases with λ in a power-law fashion with an exponent close to -1.

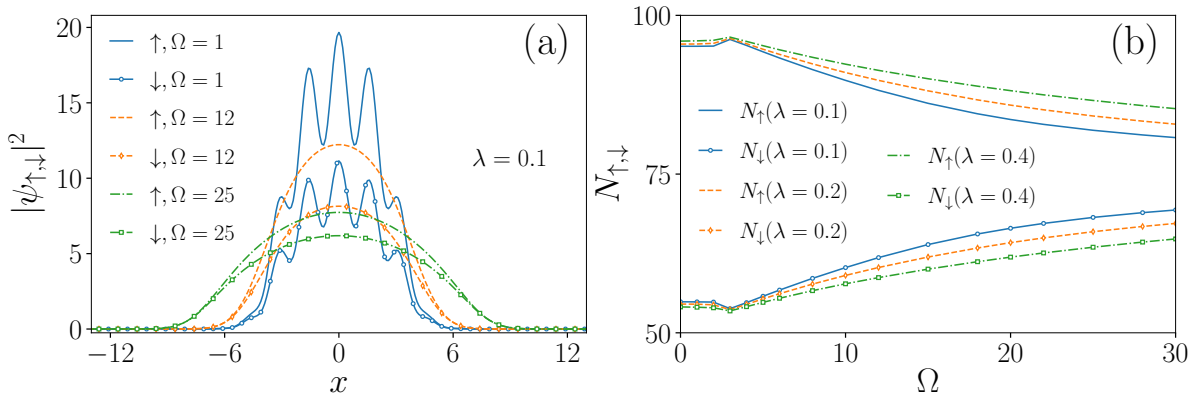

Figure 6.6: (a) Trapped ground state droplet components for several Ω (see legend) and fixed atom number $N = 150$ and $\lambda = 0.1$. A deformation from stripe to Gaussian-type droplets occurs followed by broadening of the droplet width and peak density reduction. (b) Atom number in each spin state for varying Ω and distinct λ (see legend). The intracomponent interaction ratio is $g_{\downarrow\downarrow}/g_{\uparrow\uparrow} = 4$ with $g_{\uparrow\uparrow} = 0.5$ and $\delta g = 0.1$, the SO coupled wave number $k_L = 2$.

Turning to the impact of the Rabi coupling on the ground state phases of the trapped droplets, we observe that it is the same as in free space, see Fig. 6.6. Specifically, Fig. 6.6(a) presents the droplet density profiles for different Ω and fixed $g_{\downarrow\downarrow}/g_{\uparrow\uparrow} = 4$, $N = 150$ and $\lambda = 0.1$. The size (width) of the droplets increases while their peak densities decrease for larger Ω. Interestingly, the droplet components also transform from stripe distributions for $\Omega = 1$ to standard (i.e. non-modulated) droplet structures for increasing Ω where $k_L^2 < \Omega$ holds. Yet also in this case, flat-top signatures are diminished when compared to the un-trapped case. It is, however, worth noting that the total chemical potential remains negative independently of Ω and, in particular, becomes more negative for larger Ω, verifying the bound nature of the system. Of course, for a fixed Ω and varying λ, μ features an increasing trend towards positive values. Moreover, the population difference among the components becomes gradually smaller for increasing Ω and depends on λ, see also Fig. 6.6(b). Namely, the spin balance process with Ω is delayed for larger λ.

6.4 Quench dynamics of the imbalanced spin-orbit coupled droplets

6.4.1 Collective breathing mode

To develop a preliminary understanding of the dynamical response of imbalanced SO coupled droplets, we examine the properties of one of their fundamental collective excitations, namely the breathing mode. To generate this collective mode, we prepare the two-component droplet configuration in its ground state under the influence of a weak trap strength $\lambda = 0.01$ while fixing the SO coupling parameters $\Omega = 0.5$ and $k_L = 0.5$. Subsequently, a quench of the trap strength to $\lambda = 0.03$ is applied, inducing an overall expansion and contraction dynamics of each droplet component distribution manifesting the ensuing breathing mode evolution. Notably, the latter is accompanied by an underlying spin-mixing dynamics among the components as captured through $N_\uparrow(t) - N_\downarrow(t)$. This process is traced back to the existence of SO coupling (and, in fact, the Rabi coupling) and can be easily deduced by monitoring the instantaneous population of each spin state depicted in Fig. 6.7(a). The component populations undergo an out-of-phase oscillatory behaviour, while both the oscillation amplitude and frequency depend on the interactions. We find that at weak interactions (e.g. $g_{\downarrow\downarrow}/g_{\uparrow\uparrow} = 1$), the spin-mixing is negligible and becomes more pronounced at intermediate interactions (e.g. $g_{\downarrow\downarrow}/g_{\uparrow\uparrow} = 6$) while it again reduces for stronger interactions (e.g. $g_{\downarrow\downarrow}/g_{\uparrow\uparrow} = 10$). Moreover, it is possible to associate the aforementioned out-of-phase oscillatory behaviour of the populations with the different stages of breathing evolution. In particular, during the expansion interval, atoms get transferred from the spin-down to the spin-up component and vice versa in the course of the contraction stage. In all cases, independently of $g_{\downarrow\downarrow}/g_{\uparrow\uparrow}$ or the SO coupling parameters, the total atom number is conserved.

The interaction-dependent behaviour of the breathing mode frequency, ω_{bf}, is explicitly provided in Fig. 6.7(b) for different atom numbers and constant SO coupling parameters $\Omega = 0.5$ and $k_L = 2$. Notice that ω_{bf} is calculated through the spectrum of the time-evolved droplet width of each component, namely $\langle\psi_{\downarrow,\uparrow}|x^2|\psi_{\downarrow,\uparrow}\rangle$ [105] which can be experimentally assessed through in-situ absorption images [143]. For the analysis below, ω_{bf} is the same for both components since, within the parameter regime considered, the droplets are not strongly particle imbalanced. Specifically, ω_{bf} remains almost constant around ~ 0.05 for all parameter sets (N, $g_{\downarrow\downarrow}/g_{\uparrow\uparrow}$) which correspond to flat-top droplet distributions. However, beyond the interaction threshold where the droplets acquire a Gaussian-type distribution, ω_{bf} starts to feature an increasing tendency. This

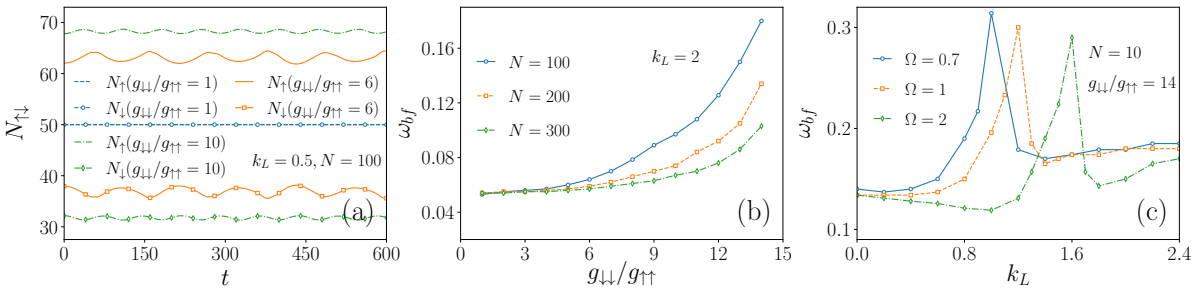

Figure 6.7: (a) Time-evolution of the spin populations of the droplet for distinct $g_{\downarrow\downarrow}/g_{\uparrow\uparrow}$ (see legend) in the course of the collective breathing dynamics of the droplets with fixed $k_L = 0.5$ and $\Omega = 0.5$. (b) Breathing mode frequency, ω_{bf} of the droplet as a function of $g_{\downarrow\downarrow}/g_{\uparrow\uparrow}$ for (b) $k_L = 2, \Omega = 0.5$ and (c) different SO coupled wave numbers k_L at various Ω (see legend). The almost constant ω_{bf} in panel (b) refers to flat-top structures transforming into Gaussian droplets whose ω_{bf} increases with $g_{\downarrow\downarrow}/g_{\uparrow\uparrow}$. Also, at the threshold from standard to stripe droplets, ω_{bf} is maximized in terms of k_L. In all the panels the initial droplet state is characterized by $g_{\uparrow\uparrow} = 0.2$ and $\delta g = 0.1$. The dynamics is triggered following a quench of the trap strength from $\lambda = 0.01$ to $\lambda = 0.03$ in panel (a,b) and $\lambda = 0.01$ to $\lambda = 0.05$ in panel (c).

increasing behaviour of ω_{bf} is caused by the substantially shrunk droplet distributions for larger $g_{\downarrow\downarrow}/g_{\uparrow\uparrow}$ [see Fig. 6.3(a)], which lead to a reduced period of the ensuing breathing evolution. A similar phenomenology of ω_{bf}, in terms of $g_{\downarrow\downarrow}/g_{\uparrow\uparrow}$, occurs also for different SO coupled wave numbers that we have checked, e.g. also for $k_L = 0.5$ where standard non-modulated droplets exist. Recall that such an increasing tendency of ω_{bf} with respect to the interactions has also been reported for the symmetric droplet in the previous Chapter 3.

To reveal the interplay of the SO coupling parameters on ω_{bf} we next examine how it depends on k_L variations for distinct Ω and fixed $g_{\downarrow\downarrow}/g_{\uparrow\uparrow} = 14$ and $N = 10$, see Fig. 6.7(c). It can be seen that at a given Rabi coupling ω_{bf} exhibits an increasing trend reaching a maximum at SO coupled wave numbers for which $\Omega \gtrsim k_L^2$. Recall that this refers to the threshold set by the SO coupling parameters where the droplet transits from the standard to a stripe configuration. Indeed, for $k_L^2 > \Omega$, the breathing frequency decreases until it attains an almost saturated value of around $\omega_{bf} \sim 0.15$ for all Ω at sufficiently large k_L. We remark here that such a behavior of ω_{bf} in terms of k_L at fixed Ω has also been discussed in Chapter 5 for the case of symmetric droplets.

6.4.2 Droplets fragmentation by Rabi coupling quenches

Next, we examine the dynamics of the SO coupled two-component droplet subjected to sudden changes of the Rabi coupling with and without an external trap, see Fig. 6.8. In particular, we start with the ground state of the SO coupled droplets characterized by

$\Omega = 15$, $g_{\downarrow\downarrow}/g_{\uparrow\uparrow} = 4, g_{\uparrow\uparrow} = 0.5, k_L = 2$, $N = 150$ and quench to either $\Omega_f = 4$ or $\Omega_f = 25$. On the ground state level, it is known that in the former case of $\Omega_f = 4$, the droplets have the tendency to form stripes since the Rabi coupling becomes comparable to the SO coupled wave number and their population imbalance may increase [Fig. 6.4 and Fig. 6.6]. However, for $\Omega_f = 25$ it is anticipated that in their ground state, the droplets will acquire a flat-top non-modulated shape with vanishing intercomponent atom imbalance, see also Fig. 6.4 and Fig. 6.6.

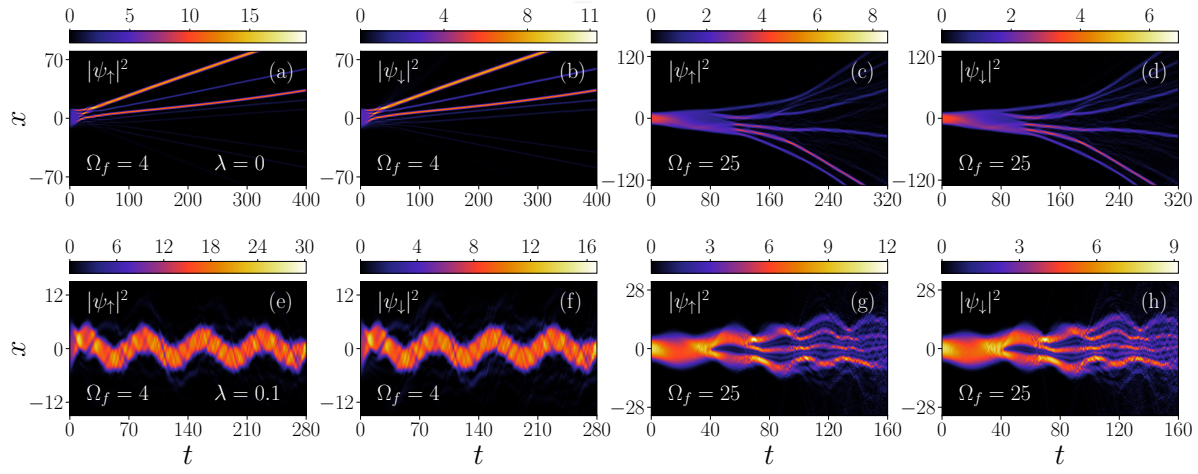

Figure 6.8: Dynamical evolution of each component SO coupled droplet density after quenching the Rabi coupling from $\Omega_i = 15$ to $\Omega_f = 4$ in the (a), (b) absence of a trap and (e), (f) presence of a trap with strength $\lambda = 0.1$. The same as above but for $\Omega_i = 15$ to $\Omega_f = 25$ (c), (d) without and (g), (h) with the trap having $\lambda = 0.1$. In the absence of the trap, a quench on Ω_f towards lower values results in the formation of fragmented moving droplets (panels (a), (b)), while quenches to higher Ω_f lead to erratic fragmented patterns (panels (c), (d)). The postquench state in the former (latter) quench is dynamically (energetically) unstable, as was shown in Chapter 5. In the trap, the SO coupled droplets oscillate with frequency equal to the one of the confinement. The ground state of the SO coupled droplet is prepared for $g_{\downarrow\downarrow}/g_{\uparrow\uparrow} = 4$, $g_{\uparrow\uparrow} = 0.5$, $\delta g = 0.1$, $k_L = 2$ and $N = 150$.

For quenches to $\Omega_f = 4$, we observe that in the absence of a trap, both SO coupled droplet components acquire the same finite velocity towards positive x and fragment into several parts as illustrated Fig. 6.8(a), (b). As argued above, the fragmentation process is traced back to the ground state density favoring the build-up of stripe structures on top of the background which is dynamically unstable. Interestingly, both components retain their initial miscible character in contrast to the expectations on the post-quench ground state level. Moreover, intercomponent atom exchange is evident in the spin populations shown in Fig. 6.9(a) which from $N_\uparrow \approx 82$ and $N_\downarrow \approx 68$ fluctuates around $N_\uparrow \approx 89$ and $N_\downarrow \approx 61$ during the evolution. In the presence of the trap, the time evolution of the SO coupled droplets is altered. Indeed, both components after the quench gain the same finite velocity (as in the un-trapped scenario), they reach the trap edge and subsequently

undergo an oscillatory motion around $x = 0$ dictated by the trap frequency, see Fig. 6.8(e), (f). Notice also the pronounced density disturbances of both spin states which essentially reflect the excited nature of the droplets due to the quench. The spin transfer is once again relatively weak as shown in Fig. 6.9(b), while performing an overall oscillatory behavior on top of the vanishing amplitude oscillations, which are an imprint of the excited droplet character. Finally, once again, and in contrast to the ground state behavior the droplets remain miscible in the course of the dynamics.

On the other hand, a quench to larger Ω_f, e.g. $\Omega_f = 25$, leads to droplets breaking into different left and right moving ones in an erratic manner, see Fig. 6.8(c), (d). This behavior is attributed to the most probably energetically unstable character of the postquench state. For this reason, the droplet breaks erratically as time evolves, allowing the system to reach a lower energy state. Specifically, at short evolution times ($t \lesssim 30$), the droplets take a velocity towards the negative x direction accompanied by an asymmetric with respect to $x = 0$ broadening of their profiles ($30 \lesssim t \lesssim 90$) and consecutive fragmentation into smaller sized ones traveling in both directions as time evolves. As above, the components

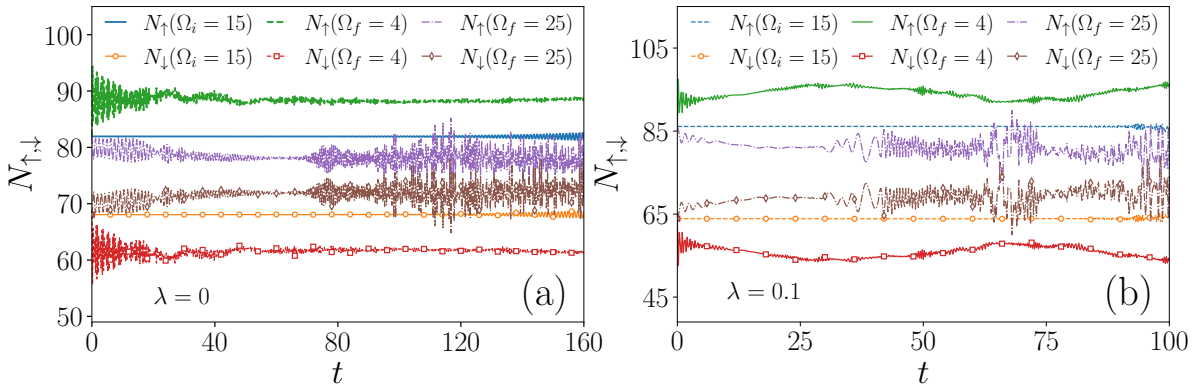

Figure 6.9: Time-evolution of the SO coupled droplet spin populations upon considering different quenches of the Rabi coupling (see legends) (a) with and (b) without an external harmonic trap of strength $\lambda = 0.1$. Despite the fluctuations in the individual atom numbers the populations do not feature significant exchange.

are miscible throughout the dynamics, and their populations are only slightly changed tending to become almost equal at longer evolution times as depicted in Fig. 6.9(a). The highly oscillatory small amplitude behavior of $N_\uparrow(t)$ and $N_\downarrow(t)$ reflects the excited nature of the droplets. For such quenches to larger Rabi couplings, a similar droplet response takes place also upon considering an external trap, see Fig. 6.8(g), (h). However, in this case, the droplet components initially ($t \lesssim 40$) tend to oscillate within the trap and afterwards fragment as in the previous case. Naturally, the dispersion trend of the fragments is less compared to the un-trapped case since the trap sustains the droplet

background. As a consequence, a more prominent interference occurs among the fragments since they lie close to one another. The quench-induced spin transfer is relatively small and at long evolution times, $t \gtrsim 90$, the components tend to acquire the same population. Also, miscibility is observed between the components in the course of the evolution as anticipated from the postquench ground state.

6.4.3 Spin-demixing and counterpropagating droplets after quenching the spin-orbit coupled wave number

Let us now turn our attention to the impact of the SO coupled wave number on the dynamical response of the two-component interaction imbalanced droplets both in the presence and absence of an external harmonic trap. Below, the droplet setting is initiated in each two-component ground state with parameters $g_{\downarrow\downarrow}/g_{\uparrow\uparrow} = 10$, $\delta g = 0.1$, $k_L = 0.5$, $\Omega = 0.5$ and $N = 50$. Focusing on the un-trapped case, we show the density evolution of each droplet component upon considering a quench to relatively small [Fig. 6.10(a), (b)] or large [Fig. 6.10(c), (d)] SO coupled wave numbers quantified by $(k_L)_f^2 < \Omega$ and $(k_L)_f^2 > \Omega$ respectively. Independently of the final value of the SO coupled wave number, each droplet

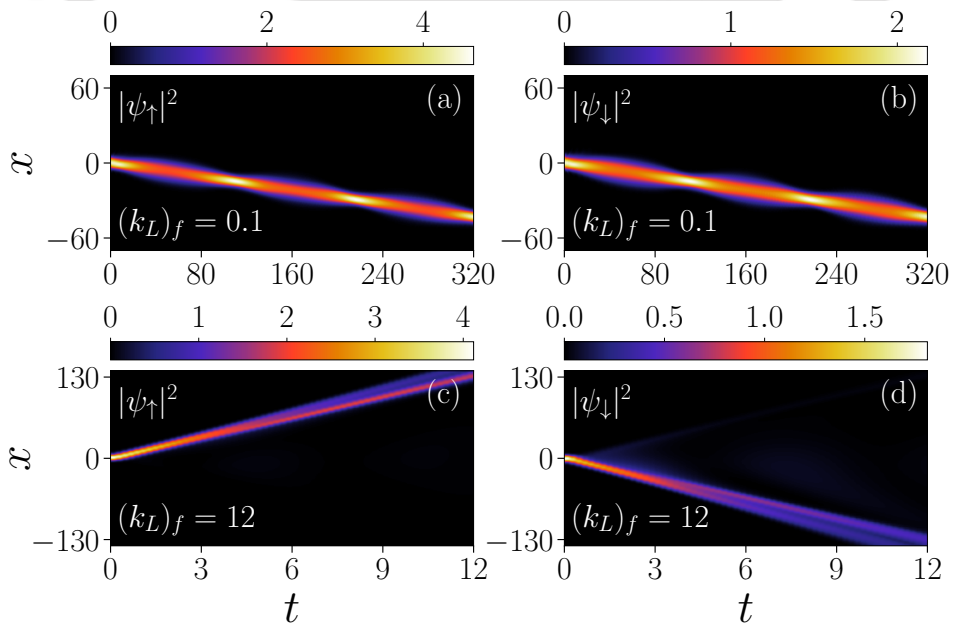

Figure 6.10: Temporal evolution of each droplet component (see legends) density profile after quenching the SO coupled wave number from $(k_L)_i = 0.5$ to (a), (b) $(k_L)_f = 0.1$ and (c), (d) $(k_L)_f = 12$. It is observed that for large postquench SO coupled wave numbers such that $(k_L)_f^2 > \Omega$ [panels (c), (d)], the components demix during the evolution and move in opposite directions. Otherwise, the components are miscible and head towards the same direction. The two-component Bosonic system is prepared in its ground state with $g_{\downarrow\downarrow}/g_{\uparrow\uparrow} = 10$, $g_{\uparrow\uparrow} = 0.2$, $\delta g = 0.1$, $k_L = 0.5$, $\Omega = 0.5$ and $N = 50$.

component experiences a momentum "kick" since k_L is related to the system's momentum, and hence the droplets become moving. In particular, in the case of $(k_L)_f^2 < \Omega$ depicted in Fig. 6.10(a), (b) we observe that both components feature a breathing oscillation while moving in the negative x-direction with a constant velocity. As such, we conclude that the droplet components remain mixed during the course of evolution. We also mention in passing that a relatively weak periodic population transfer among the components of maximum amplitude $\sim 6\%$ takes place (not shown) following the aforementioned droplets breathing.

In contrast, quenching to $(k_L)_f^2 > \Omega$ leads to a different droplet arrangement. Indeed, as illustrated in Fig. 6.10(c), (d), the droplet components become counterpropagating and show a gradual spatial delocalization tendency during the evolution. This delocalization trend is reminiscent of the droplet fragmentation in the case of a symmetric mixture as in Chapter 3. The fact that the droplets move oppositely is attributed to the dominant SO coupling contribution here, which appears with opposite signs in the eGPEs (6.1), imparting opposite velocities to the different components. Evidently, the components are demixed since their overlap is vanishing throughout the propagation, while there is a small periodic population exchange accompanying the dynamics (not shown).

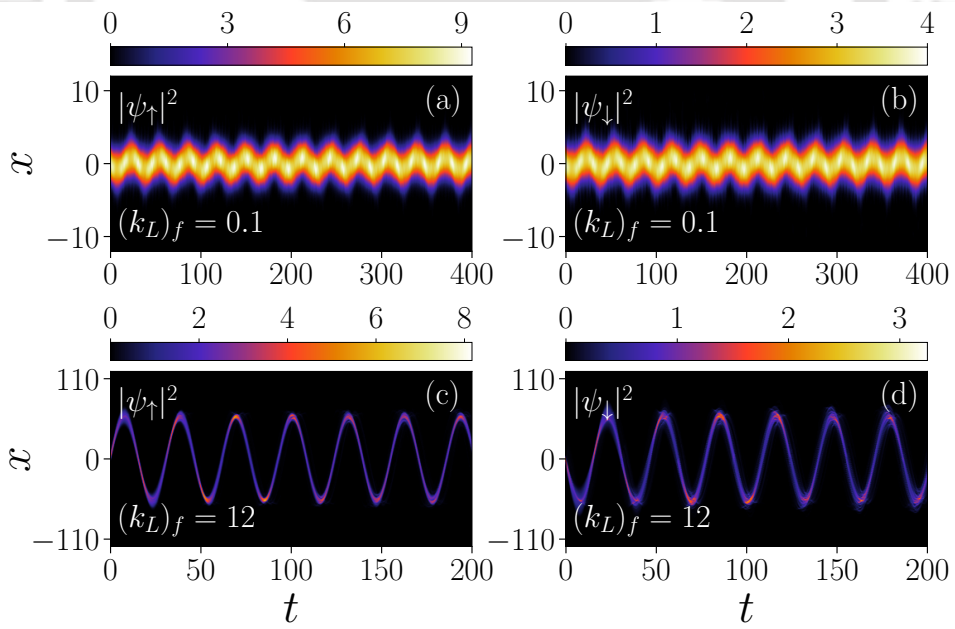

Figure 6.11: Density dynamics of the different harmonically trapped droplet components following a sudden change of the SO coupled wave number from $(k_L)_i = 0.5$ to (a), (b) $(k_L)_f = 0.1$ and (c), (d) $(k_L)_f = 12$. As it can be seen, for postquench values satisfying $(k_L)_f^2 > \Omega$ [panels (c), (d)], the droplets oscillate out-of-phase within the trap; otherwise they oscillate in-phase. The imbalanced droplet setting is initialized in its ground state configuration where $\lambda = 0.2$, $g_{\downarrow\downarrow}/g_{\uparrow\uparrow} = 10$, $g_{\uparrow\uparrow} = 0.2$, $\delta g = 0.1$, $\Omega = 0.5$ and $N = 50$.

The existence of an external harmonic trap does not substantially alter the droplet response in terms of spin-demixing but rather induces an oscillatory droplet motion, see Fig. 6.11. For completeness, again, we consider quenches, both to smaller and larger SO coupled wave numbers, while the remaining system parameters remain the same as in the un-trapped scenario. An overall prevailing feature is that the specific quench triggers a directed droplet in-trap oscillatory motion, which depends further on the postquench k_L value. For instance, when $(k_L)_f = 0.1 < \sqrt{\Omega}$ the droplet components oscillate in sync with the same frequency as the trap frequency [Fig. 6.11(a), (b)]. They also retain their miscible character during the entire evolution, and intercomponent atom transfer is suppressed. However, for $(k_L)_f^2 = 12 > \Omega$, the droplet components exhibit out-of-phase oscillations [Fig. 6.11(c), (d)] and therefore become immiscible during the dynamics. The oscillation period is dictated by the external trap, whilst the spin exchange population is relatively weak of maximum amplitude $\sim 15\%$ and not regular. We remark that a similar spin-mixing and spin-demixing dynamics was reported for the SO coupled solitons after the sudden introduction of SO coupling into the system [87].

6.5 Summary and Conclusions

In this Chapter, we have investigated the ground state phases and the quench dynamics of interaction-imbalanced SO coupled droplets in one dimension both in the presence and absence of an external harmonic trap. In the ground state, we found a variety of different droplet configurations bearing miscible characters among the components, and ranging from standard non-modulated to stripe patterns having either flat-top or Gaussian shapes. A key feature of our setup is the SO coupling parameters, where, in particular, the Rabi coupling favors population transfer between the involved spin states, which may thus experience atom number imbalance.

Specifically, the droplet components deform from flat-top to Gaussian distributions by increasing (decreasing) the intracomponent interaction ratio (total atom number). The spatially modulated droplet character depends on the SO coupled wave number. A higher SO coupled wave number (roughly larger than the Rabi coupling) promotes the formation of stripes atop the droplet. Spin imbalance increases with larger interaction strength, higher SO coupled wave number, or lower Rabi coupling. Conversely, increasing the Rabi coupling while keeping other parameters constant leads to a gradual transition from stripe to Gaussian, then to flat-top droplets, suppressing imbalance. In the stripe region, spin populations exhibit a nearly constant imbalance, which decreases in the Gaussian regime and becomes almost uniform in the flat-top regime.

On the other hand, in the presence of a trap, the stripe droplets feature Gaussian profiles with their size and peak density increasing for larger atom numbers or decreasing interactions. Importantly, a transition from a self-bound to a trapped gas phase occurs for increasing atom number as captured by the total chemical potential which changes from negative to positive. The underlying critical region shifts to smaller atom numbers for increasing trap frequency or to a larger number of atoms for fixed trap frequency and stronger intracomponent repulsions. A similar phenomenology to the un-trapped case in terms of the Rabi coupling takes place also in the presence of a trap but instead of reaching flat-top configurations Gaussian ones are attained.

Turning to the dynamics we have first examined the behavior of the collective breathing motion of the two-component droplet system after a quench of the trap strength. This process induces a relatively small population transfer. It is found that the breathing mode frequency increases for larger intracomponent interaction ratio, while it features a maximum in terms of the SO coupled wave number at the location of the transition from a standard non-modulated to the stripe droplet. Additionally, a sudden reduction or increase of the Rabi coupling is associated with minor intercomponent population exchange and the formation of fragmented moving droplets in the absence of the trap and oscillating ones with the trap frequency in its presence. On the other hand, following a quench of the SO coupled wave number leads to a drastically different dynamical response. In particular, independently of the postquench SO coupled wave number the droplets acquire finite momentum and feature a directed motion. In the absence of a trap, this motion refers to the same direction or opposite ones for small and large post-quench amplitudes respectively. This process is accompanied by spatial mixing or de-mixing of the droplet components, which simultaneously exhibit breathing and spatial delocalization respectively. The presence of the trap leads to similar characteristics but enforces an oscillatory droplet motion with the same frequency as the one of the trap. Droplets oscillate out-of-phase (in-phase) in the trap for larger (weak) quench amplitudes while being immiscible (miscible).

Chapter 7

Conclusions and future scope

7.1 Main conclusions of the thesis

In this thesis, we have performed analytical and numerical studies to investigate the structure and dynamics of the ultra-dilute SO coupled QDs in one dimension. Broadly, we have considered two types of SO coupled droplets: in the first case, we have maintained the equal population among the components, while in the second case, we have considered the unequal population among the components. For the first case, we have systematically analyzed the individual effect of BMF contribution. Further, we have extended it in the presence of both BMF and MF and variation of the total number of atoms. For the second case we have explored the particle imbalance droplet. The main conclusion of our studies is as follows.

In **Chapter 3**, we have explored the structure and dynamics of the one-dimensional droplet for vanishingly small MF contribution, which is achieved by taking equal and opposite intra- and inter-species interaction, which results the appearance of QD in the form of quantum soliton. We have derived an analytical soliton solution for non-zero SO coupling that matches quite well with the numerical results. Further, we have investigated the dynamical stability of these solitons by adopting three protocols, such as (i) adding initial velocity to each component, (ii) quenching the SO and Rabi coupling parameters at initial and finite time, and (iii) allowing collision between the two spin-components by giving equal and opposite direction velocity to them. For small velocity perturbation, the soliton has the presence of the breathing oscillation, while large velocity perturbations transform the soliton into moving solitons. The maximum breathing frequency exhibits power law dependence on the Rabi coupling frequency with an exponent ~ 0.16. The quenching of SO and Rabi couplings results in several interesting dynamical features,

such as dynamical phase transition from plane to stripe phase, dynamical flipping of the spin state, and secondary solitonic modes. In the absence of the SO and Rabi couplings, depending upon the velocity of the up-spin and down-spin components, the collision between them is either elastic or inelastic, which is consistent with the earlier numerical and experimental observation. However, in the presence of coupling parameters, the collision appears to be inelastic and quasi-elastic in nature.

In **Chapter 4**, we have extended the analysis of QDs presented in the previous chapter by considering the effect of the finite effective mean-field interaction. For this case, we found that QD exhibits remarkably different natures in compare to those for zero effective mean-field interaction. For zero effective mean-field interaction, it exhibited a bright sech-like droplet nature, while with finite effective mean-field interaction, we found the flattened sech-like shape of the droplet. Further, we have analyzed the effect of velocity perturbation on the dynamics of the QDs. We obtained a systematic change from the solitonic droplet nature to the breathing droplet which finally has a moving droplet feature upon increasing the velocity. We noticed a transition from breather to moving droplet happens at lower velocity upon an increase in the effective mean-field interaction. Finally, we have investigated various dynamics that ensued in the QD due to the quenching of the interaction parameters, coupling parameters, or allowing the droplet to undergo collisions. The collisional dynamics of the droplets are greatly modified by considering the effective mean-field interaction. The collision between the droplets is inelastic in the absence of MF interaction, while it is elastic in the presence of effective mean-field interaction. We have realized that the presence of effective mean-field interaction makes droplets more dynamically stable than those in the absence of the effective mean-field interaction.

In **Chapter 5**, we have explored the effect of the atom variation with finite effective mean-field interaction on the structure, stability, and dynamics of the SO coupled droplet. As the SO coupled wave number increases, stripe droplet patterns emerge, with a flat-top background, for larger particle numbers. The surface energy of the droplet decays following a power-law with respect to the interactions. At small SO coupled wave numbers, we found a transition from Gaussian to flat-top droplets either by increasing the number of atoms or by reducing intercomponent attraction. We ascertain the stability of the droplet using the excitation spectrum, which shows that droplets for relatively small SO coupling wave numbers are stable, otherwise stripe droplets feature instabilities as a function of the particle number or the interactions. We also witness rich droplet dynamical features using velocity imprinting and abrupt changes in the intercomponent interaction or the SO coupling parameters. Characteristic responses include breathing oscillations, expansion, symmetric and asymmetric droplet fragmentation, admixtures of single and stripe

droplet branches, and erratic spatial distributions suggesting the triggering of relevant instabilities.

In chapter **6**, we have explored the ground states and quench dynamics of SO coupled one-dimensional two-component QDs featuring intracomponent interaction imbalance. We have obtained a plethora of miscible ground state stripe and standard flat-top or Gaussian droplets, which depend on the interplay between the SO coupled wave number and interactions. Our study revealed how population exchange among spin components of the droplet is influenced by changes in Rabi or SO coupling. Quenching Rabi coupling to high values can destabilize the droplet and result in the formation of the chaotic state of the droplet, while quenching SO coupling leads to a spin-mixing demixing state. This particular dynamical feature suggests the control over the individual component dynamics. We have provided a detailed analysis of how trapping affects imbalanced droplets. Our findings indicate that increasing particle numbers can transition the system from a bound state to a trapped gas many-body state.

7.2 Scope for future work

Based on the results in the thesis, there is a multitude of intriguing extensions that may be followed in the future. An immediate step is to construct an effective potential picture in the case of large particle imbalance where the majority stripe droplet component plays the role of an external lattice potential for the minority one as was done in Ref. [132] but in the absence of SO coupling. Another direction would be to analyze the dynamics of SO coupled dipolar droplets in the similar line adopted in the present thesis work [116]. Another interesting pathway is to calculate the excitation spectrum of these two-component droplet structures, especially focusing on the stripe configurations and their crossover to non-modulated droplets. [96, 110, 144]. Moreover, it would be worth examining the correlation patterns [105] associated with the stripe droplets, shedding light on the underlying two-body processes participating in the respective many-body states. The generalization of our setup in two dimensions in order to reveal the phases of two-component stripe droplets and their relation with supersolids [12] is desirable. Finally, it would be interesting to study the impact of optomechanical couplings [145, 146] in the identified droplet states.

Bibliography

[1] C. J. Pethick and H. Smith, *Bose–Einstein condensation in dilute gases*. Cambridge university press, 2008.

[2] Bose, "Plancks gesetz und lichtquantenhypothese," *Zeitschrift für Physik*, vol. 26, no. 1, pp. 178–181, 1924.

[3] A. Einstein, "Quantum theory of the monatomic ideal gas," *Sitzungsberichte der Preussischen Akademie der Wissenschaften, Physikalisch-mathematische Klasse*, vol. 261, 1924.

[4] P. Kapitza, "Viscosity of liquid helium below the λ-point," *Nature*, vol. 141, no. 3558, pp. 74–74, 1938.

[5] J. F. Allen and A. Misener, "Flow of liquid helium ii," *Nature*, vol. 141, no. 3558, pp. 75–75, 1938.

[6] F. London, "On the bose-einstein condensation," *Phys. Rev.*, vol. 54, no. 11, p. 947, 1938.

[7] L. Landau, "Theory of the superfluidity of helium ii," *Phys. Rev.*, vol. 60, p. 356, 1941.

[8] O. Penrose, "Cxxxvi. on the quantum mechanics of helium ii," *The London, Edinburgh, and Dublin Philosophical Magazine and Journal of Science*, vol. 42, no. 335, pp. 1373–1377, 1951.

[9] O. Penrose and L. Onsager, "Bose-einstein condensation and liquid helium," *Phys. Rev.*, vol. 104, no. 3, p. 576, 1956.

[10] M. H. Anderson, J. R. Ensher, M. R. Matthews, C. E. Wieman, and E. A. Cornell, "Observation of bose-einstein condensation in a dilute atomic vapor," *Science*, vol. 269, no. 5221, pp. 198–201, 1995.

[11] K. B. Davis, M.-O. Mewes, M. R. Andrews, N. J. van Druten, D. S. Durfee, D. Kurn, and W. Ketterle, "Bose-einstein condensation in a gas of sodium atoms," *Phys. Rev. Lett.*, vol. 75, no. 22, p. 3969, 1995.

[12] L. Chomaz, I. Ferrier-Barbut, F. Ferlaino, B. Laburthe-Tolra, B. L. Lev, and T. Pfau, "Dipolar physics: a review of experiments with magnetic quantum gases," *Rep. Prog. Phys.*, vol. 86, no. 2, p. 026401, 2023.

[13] G. Modugno, "Anderson localization in Bose-Einstein condensates," *Rep. Prog. Phys.*, vol. 73, no. 10, p. 102401, 2010.

[14] D. S. Petrov, "Quantum mechanical stabilization of a collapsing bose-bose mixture," *Phys. Rev. Lett.*, vol. 115, p. 155302, 2015.

[15] C. Cabrera, L. Tanzi, J. Sanz, B. Naylor, P. Thomas, P. Cheiney, and L. Tarruell, "Quantum liquid droplets in a mixture of bose-einstein condensates," *Science*, vol. 359, no. 6373, pp. 301–304, 2018.

[16] T. D. Lee, K. Huang, and C. N. Yang, "Eigenvalues and eigenfunctions of a bose system of hard spheres and its low-temperature properties," *Phys. Rev.*, vol. 106, no. 6, pp. 1135–1145, 1957.

[17] T. Lee and C. Yang, "Many-body problem in quantum mechanics and quantum statistical mechanics," *Phys. Rev.*, vol. 105, no. 3, p. 1119, 1957.

[18] H. Kadau, M. Schmitt, M. Wenzel, C. Wink, T. Maier, I. Ferrier-Barbut, and T. Pfau, "Observing the rosensweig instability of a quantum ferrofluid," *Nature*, vol. 530, no. 7589, pp. 194–197, 2016.

[19] I. Ferrier-Barbut, H. Kadau, M. Schmitt, M. Wenzel, and T. Pfau, "Observation of quantum droplets in a strongly dipolar bose gas," *Phys. Rev. Lett.*, vol. 116, no. 21, p. 215301, 2016.

[20] M. Schmitt, M. Wenzel, F. Böttcher, I. Ferrier-Barbut, and T. Pfau, "Self-bound droplets of a dilute magnetic quantum liquid," *Nature*, vol. 539, no. 7628, pp. 259–262, 2016.

[21] I. Ferrier-Barbut, M. Schmitt, M. Wenzel, H. Kadau, and T. Pfau, "Liquid quantum droplets of ultracold magnetic atoms," *J. Phys. B: At. Mol. Opt. Phys*, vol. 49, no. 21, p. 214004, 2016.

[22] L. Chomaz, S. Baier, D. Petter, M. Mark, F. Wächtler, L. Santos, and F. Ferlaino, "Quantum-fluctuation-driven crossover from a dilute bose-einstein condensate to a macrodroplet in a dipolar quantum fluid," *Phys. Rev. X*, vol. 6, no. 4, p. 041039, 2016.

[23] P. Cheiney, C. R. Cabrera, J. Sanz, B. Naylor, L. Tanzi, and L. Tarruell, "Bright soliton to quantum droplet transition in a mixture of bose-einstein condensates," *Phys. Rev. Lett.*, vol. 120, p. 135301, 2018.

[24] G. Semeghini, G. Ferioli, L. Masi, C. Mazzinghi, L. Wolswijk, F. Minardi, M. Modugno, G. Modugno, M. Inguscio, and M. Fattori, "Self-bound quantum droplets of atomic mixtures in free space," *Phys. Rev. Lett.*, vol. 120, p. 235301, 2018.

[25] C. D'Errico, A. Burchianti, M. Prevedelli, L. Salasnich, F. Ancilotto, M. Modugno, F. Minardi, and C. Fort, "Observation of quantum droplets in a heteronuclear bosonic mixture," *Phys. Rev. Res.*, vol. 1, p. 033155, 2019.

[26] A. Burchianti, C. D'Errico, M. Prevedelli, L. Salasnich, F. Ancilotto, M. Modugno, F. Minardi, and C. Fort, "A dual-species Bose-Einstein condensate with attractive interspecies interactions," *Condens. Matter*, vol. 5, no. 1, p. 21, 2020.

[27] J. C. Smith, D. Baillie, and P. B. Blakie, "Quantum droplet states of a binary magnetic gas," *Phys. Rev. Lett.*, vol. 126, p. 025302, 2021.

[28] D. Petrov and G. Astrakharchik, "Ultradilute low-dimensional liquids," *Phys. Rev. Lett.*, vol. 117, no. 10, p. 100401, 2016.

[29] L. Lavoine and T. Bourdel, "Beyond-mean-field crossover from one dimension to three dimensions in quantum droplets of binary mixtures," *Phys. Rev. A*, vol. 103, no. 3, p. 033312, 2021.

[30] A. Frölian, C. S. Chisholm, E. Neri, C. R. Cabrera, R. Ramos, A. Celi, and L. Tarruell, "Realizing a 1d topological gauge theory in an optically dressed BEC," *Nature*, vol. 608, no. 7922, pp. 293–297, 2022.

[31] M. Tylutki, G. E. Astrakharchik, B. A. Malomed, and D. S. Petrov, "Collective excitations of a one-dimensional quantum droplet," *Phys. Rev. A*, vol. 101, p. 051601, 2020.

[32] G. E. Astrakharchik and B. A. Malomed, "Dynamics of one-dimensional quantum droplets," *Phys. Rev. A*, vol. 98, p. 013631, 2018.

[33] A. Tononi, Y. Wang, and L. Salasnich, "Quantum solitons in spin-orbit-coupled Bose-Bose mixtures," *Phys. Rev. A*, vol. 99, p. 063618, 2019.

[34] A. Debnath, A. Khan, and B. Malomed, "Interaction of one-dimensional quantum droplets with potential wells and barriers," *arXiv preprint arXiv:2302.13367*, 2023.

[35] E. Cornell, "Very cold indeed: The nanokelvin physics of bose-einstein condensation," *Journal of research of the National Institute of Standards and Technology*, vol. 101, no. 4, p. 419, 1996.

[36] J. Dalibard, "Collisional dynamics of ultra-cold atomic gases," in *Bose-Einstein Condensation in Atomic Gases*, pp. 321–349, IOS Press, 1999.

[37] C. Chin, R. Grimm, P. Julienne, and E. Tiesinga, "Feshbach resonances in ultracold gases," *Reviews of Modern Physics*, vol. 82, no. 2, pp. 1225–1286, 2010.

[38] E. P. Gross, "Structure of a quantized vortex in boson systems," *Il Nuovo Cimento (1955-1965)*, vol. 20, no. 3, pp. 454–477, 1961.

[39] L. P. Pitaevskii, "Vortex lines in an imperfect bose gas," *Sov. Phys. JETP*, vol. 13, no. 2, pp. 451–454, 1961.

[40] C. Myatt, E. Burt, R. Ghrist, E. A. Cornell, and C. Wieman, "Production of two overlapping bose-einstein condensates by sympathetic cooling," *Phys. Rev. Lett.*, vol. 78, no. 4, p. 586, 1997.

[41] E. A. Cornell, D. Hall, M. Matthews, and C. Wieman, "Having it both ways: Distinguishable yet phase-coherent mixtures of bose-einstein condensates," *Journal of low temperature physics*, vol. 113, no. 3, pp. 151–165, 1998.

[42] D. Stamper-Kurn, M. Andrews, A. Chikkatur, S. Inouye, H.-J. Miesner, J. Stenger, and W. Ketterle, "Optical confinement of a bose-einstein condensate," *Phys. Rev. Lett.*, vol. 80, no. 10, p. 2027, 1998.

[43] J. Stenger, S. Inouye, D. Stamper-Kurn, H.-J. Miesner, A. Chikkatur, and W. Ketterle, "Spin domains in ground-state bose–einstein condensates," *Nature*, vol. 396, no. 6709, pp. 345–348, 1998.

[44] H.-J. Miesner, D. Stamper-Kurn, J. Stenger, S. Inouye, A. Chikkatur, and W. Ketterle, "Observation of metastable states in spinor bose-einstein condensates," *Phys. Rev. Lett.*, vol. 82, no. 11, p. 2228, 1999.

[45] D. Stamper-Kurn, H.-J. Miesner, A. Chikkatur, S. Inouye, J. Stenger, and W. Ketterle, "Quantum tunneling across spin domains in a bose-einstein condensate," *Phys. Rev. Lett.*, vol. 83, no. 4, p. 661, 1999.

[46] Y.-J. Lin, K. Jiménez-García, and I. B. Spielman, "Spin-orbit-coupled Bose–Einstein condensates," *Nature*, vol. 471, no. 7336, pp. 83–86, 2011.

[47] Y. A. Bychkov and E. I. Rashba, "Oscillatory effects and the magnetic susceptibility of carriers in inversion layers," *J. Phys. C: Solid State Phys.*, vol. 17, no. 33, p. 6039, 1984.

[48] G. Dresselhaus, "Spin-orbit coupling effects in zinc blende structures," *Phys. Rev.*, vol. 100, pp. 580–586, 1955.

[49] P. Wang, Z.-Q. Yu, Z. Fu, J. Miao, L. Huang, S. Chai, H. Zhai, and J. Zhang, "Spin-orbit coupled degenerate fermi gases," *Phys. Rev. Lett.*, vol. 109, no. 9, p. 095301, 2012.

[50] T.-L. Ho, "Spinor Bose condensates in optical traps," *Phys. Rev. Lett.*, vol. 81, pp. 742–745, 1998.

[51] M. Z. Hasan and C. L. Kane, "Colloquium: topological insulators," *Reviews of modern physics*, vol. 82, no. 4, pp. 3045–3067, 2010.

[52] X.-L. Qi and S.-C. Zhang, "Topological insulators and superconductors," *Reviews of modern physics*, vol. 83, no. 4, pp. 1057–1110, 2011.

[53] Y. K. Kato, R. C. Myers, A. C. Gossard, and D. D. Awschalom, "Observation of the spin hall effect in semiconductors," *Science*, vol. 306, no. 5703, pp. 1910–1913, 2004.

[54] I. Žutić, J. Fabian, and S. D. Sarma, "Spintronics: Fundamentals and applications," *Reviews of modern physics*, vol. 76, no. 2, p. 323, 2004.

[55] M. Johanning, A. F. Varón, and C. Wunderlich, "Quantum simulations with cold trapped ions," *J. Phys. B: At. Mol. Opt. Phys.*, vol. 42, no. 15, p. 154009, 2009.

[56] I. Bloch, J. Dalibard, and S. Nascimbene, "Quantum simulations with ultracold quantum gases," *Nature Physics*, vol. 8, no. 4, pp. 267–276, 2012.

[57] I. Ferrier-Barbut, "Ultradilute quantum droplets," *Physics Today*, vol. 72, no. 4, pp. 46–52, 2019.

[58] Z.-H. Luo, W. Pang, B. Liu, Y.-Y. Li, and B. A. Malomed, "A new form of liquid matter: Quantum droplets," *Frontiers of Physics*, vol. 16, pp. 1–21, 2021.

[59] S. Papp, J. Pino, R. Wild, S. Ronen, C. E. Wieman, D. S. Jin, and E. A. Cornell, "Bragg spectroscopy of a strongly interacting rb 85 bose-einstein condensate," *Phys. Rev. Lett.*, vol. 101, no. 13, p. 135301, 2008.

[60] N. Navon, S. Piatecki, K. Günter, B. Rem, T. C. Nguyen, F. Chevy, W. Krauth, and C. Salomon, "Dynamics and thermodynamics of the low-temperature strongly interacting bose gas," *Phys. Rev. Lett.*, vol. 107, no. 13, p. 135301, 2011.

[61] T. G. Skov, M. G. Skou, N. B. Jørgensen, and J. J. Arlt, "Observation of a Lee-Huang-Yang fluid," *Phys. Rev. Lett.*, vol. 126, no. 23, p. 230404, 2021.

[62] G. Ferioli, G. Semeghini, L. Masi, G. Giusti, G. Modugno, M. Inguscio, A. Gallemí, A. Recati, and M. Fattori, "Collisions of self-bound quantum droplets," *Phys. Rev. Lett.*, vol. 122, p. 090401, 2019.

[63] D. Rakshit, T. Karpiuk, M. Brewczyk, and M. Gajda, "Quantum Bose-Fermi droplets," *SciPost Phys.*, vol. 6, p. 079, 2019.

[64] M. R. Pathak and A. Nath, "Dynamics of quantum droplets in an external harmonic confinement," *Sci. Rep.*, vol. 12, no. 1, 2022.

[65] S. I. Mistakidis, T. Mithun, P. G. Kevrekidis, H. R. Sadeghpour, and P. Schmelcher, "Formation and quench of homonuclear and heteronuclear quantum droplets in one dimension," *Phys. Rev. Res.*, vol. 3, p. 043128, 2021.

[66] T. Mithun, A. Maluckov, K. Kasamatsu, B. A. Malomed, and A. Khare, "Modulational instability, inter-component asymmetry, and formation of quantum droplets in one-dimensional binary Bose gases," *Symmetry*, vol. 12, no. 1, p. 174, 2020.

[67] L. Parisi and S. Giorgini, "Quantum droplets in one-dimensional Bose mixtures: A quantum Monte Carlo study," *Phys. Rev. A*, vol. 102, no. 2, p. 023318, 2020.

[68] I. A. Englezos, S. I. Mistakidis, and P. Schmelcher, "Correlated dynamics of collective droplet excitations in a one-dimensional harmonic trap," *Phys. Rev. A*, vol. 107, no. 2, p. 023320, 2023.

[69] T. A. Flynn, N. A. Keepfer, N. G. Parker, and T. P. Billam, "Harmonically trapped imbalanced quantum droplets," *Phys. Rev. Res.*, vol. 6, no. 1, p. 013209, 2024.

[70] E. Chiquillo, "Low-dimensional self-bound quantum rabi-coupled bosonic droplets," *Phys. Rev. A*, vol. 99, no. 5, p. 051601, 2019.

[71] P. Muruganandam and S. K. Adhikari, "Fortran programs for the time-dependent Gross–Pitaevskii equation in a fully anisotropic trap," *Comput. Phys. Commun.*, vol. 180, no. 10, pp. 1888–1912, 2009.

[72] R. K. Kumar and P. Muruganandam, "Numerical studies on vortices in rotating dipolar Bose-Einstein condensates," in *J. Phys. Conf. Ser.*, vol. 497, p. 012036, 2014.

[73] R. K. Kumar, L. E. Young-S, D. Vudragović, A. Balaž, P. Muruganandam, and S. K. Adhikari, "Fortran and c programs for the time-dependent dipolar gross–pitaevskii equation in an anisotropic trap," *Comput. Phys. Commun.*, vol. 195, pp. 117–128, 2015.

[74] R. Ravisankar, D. Vudragović, P. Muruganandam, A. Balaž, and S. K. Adhikari, "Spin-1 spin-orbit- and Rabi-coupled Bose-Einstein condensate solver," *Comput. Phys. Commun.*, vol. 259, p. 107657, 2021.

[75] S. Koonin and D. Meredith, "Computational physics art (fortran version)," 1990.

[76] W. F. Ames, *Numerical methods for partial differential equations*. Academic press, 2014.

[77] R. Dautray and J.-L. Lions, *Mathematical analysis and numerical methods for science and technology: volume 3 spectral theory and applications*. Springer Science & Business Media, 2012.

[78] J. Denschlag, J. E. Simsarian, D. L. Feder, C. W. Clark, L. A. Collins, J. Cubizolles, L. Deng, E. W. Hagley, K. Helmerson, W. P. Reinhardt, *et al.*, "Generating solitons by phase engineering of a bose-einstein condensate," *Science*, vol. 287, no. 5450, pp. 97–101, 2000.

[79] N. B. Jørgensen, G. M. Bruun, and J. J. Arlt, "Dilute fluid governed by quantum fluctuations," *Phys. Rev. Lett.*, vol. 121, p. 173403, 2018.

[80] S. Gangwar, R. Ravisankar, P. Muruganandam, and P. K. Mishra, "Dynamics of quantum solitons in Lee-Huang-Yang spin-orbit-coupled Bose-Einstein condensates," *Phys. Rev. A*, vol. 106, p. 063315, 2022.

[81] S. Sahu and D. Majumder, "Collective excitation of two-dimensional bose–einstein condensate in liquid phase with spin–orbit coupling," *J. Phys. B: At. Mol. Opt. Phys.*, vol. 53, no. 9, p. 095301, 2020.

[82] E. Chiquillo, "Quasi-one-dimensional spin-orbit- and Rabi-coupled bright dipolar Bose-Einstein-condensate solitons," *Phys. Rev. A*, vol. 97, p. 013614, 2018.

[83] J.-R. Li, J. Lee, W. Huang, S. Burchesky, B. Shteynas, F. Ç. Top, A. O. Jamison, and W. Ketterle, "A stripe phase with supersolid properties in spin-orbit-coupled Bose-Einstein condensates," *Nature*, vol. 543, no. 7643, pp. 91–94, 2017.

[84] L. E. Young-S. and S. Adhikari, "Deep inelastic collision of two-dimensional anisotropic dipolar condensate solitons," *Commun. Nonlin. Sci. Num. Simulat.*, vol. 106, p. 106094, 2022.

[85] L. E. Young-S, D. Vudragović, P. Muruganandam, S. K. Adhikari, and A. Balaž, "OpenMP Fortran and C programs for solving the time-dependent Gross–Pitaevskii equation in an anisotropic trap," *Comput. Phys. Commun.*, vol. 204, pp. 209–213, 2016.

[86] R. Ravisankar, T. Sriraman, R. K. Kumar, P. Muruganandam, and P. K. Mishra, "Influence of Rashba spin-orbit and Rabi couplings on the spin-mixing and ground state phases of binary Bose-Einstein condensates," *J. Phys. B: At. Mol. Opt. Phys.*, vol. 54, no. 22, p. 225301, 2021.

[87] R. Ravisankar, T. Sriraman, L. Salasnich, and P. Muruganandam, "Quenching dynamics of the bright solitons and other localized states in spin-orbit coupled Bose-Einstein condensates," *J. Phys. B: At. Mol. Opt. Phys.*, vol. 53, no. 19, p. 195301, 2020.

[88] J. Denschlag, J. E. Simsarian, D. L. Feder, C. W. Clark, L. A. Collins, J. Cubizolles, L. Deng, E. W. Hagley, K. Helmerson, W. P. Reinhardt, *et al.*, "Generating solitons by phase engineering of a bose-einstein condensate," *Science*, vol. 287, no. 5450, pp. 97–101, 2000.

[89] A. Di Carli, C. D. Colquhoun, G. Henderson, S. Flannigan, G.-L. Oppo, A. J. Daley, S. Kuhr, and E. Haller, "Excitation modes of bright matter-wave solitons," *Phys. Rev. Lett.*, vol. 123, no. 12, p. 123602, 2019.

[90] C.-H. Li, C. Qu, R. J. Niffenegger, S.-J. Wang, M. He, D. B. Blasing, A. J. Olson, C. H. Greene, Y. Lyanda-Geller, Q. Zhou, *et al.*, "Spin current generation and relaxation in a quenched spin-orbit-coupled Bose-Einstein condensate," *Nat. Commun.*, vol. 10, no. 1, p. 375, 2019.

[91] S. Mardonov, M. Modugno, and E. Y. Sherman, "Dynamics of a macroscopic spin qubit in spin–orbit coupled bose–einstein condensates," *J. Phys. B: At. Mol. Opt. Phys.*, vol. 48, no. 11, p. 115302, 2015.

[92] Y. Cheng, G. Tang, and S. K. Adhikari, "Localization of a spin-orbit-coupled Bose-Einstein condensate in a bichromatic optical lattice," *Phys. Rev. A*, vol. 89, p. 063602, 2014.

[93] S. Gangwar, R. Ravisankar, P. Muruganandam, and P. Mishra, "Exploring the role of beyond mean-field interaction in the structure and dynamics of one-dimensional quantum droplets," *J. Phys. B: At. Mol. Opt. Phys.*, vol. 56, p. 165302, 2023.

[94] Y. Li, Z. Luo, Y. Liu, Z. Chen, C. Huang, S. Fu, H. Tan, and B. A. Malomed, "Two-dimensional solitons and quantum droplets supported by competing self- and cross-interactions in spin-orbit-coupled condensates," *New J. Phys.*, vol. 19, no. 11, p. 113043, 2017.

[95] H. Sakaguchi, B. Li, and B. A. Malomed, "Creation of two-dimensional composite solitons in spin-orbit-coupled self-attractive Bose-Einstein condensates in free space," *Phys. Rev. E*, vol. 89, p. 032920, 2014.

[96] S. Gangwar, R. Ravisankar, S. I. Mistakidis, P. Muruganandam, and P. K. Mishra, "Spectrum and quench-induced dynamics of spin-orbit-coupled quantum droplets," *Phys. Rev. A*, vol. 109, p. 013321, 2024.

[97] S. I. Mistakidis, A. G. Volosniev, R. E. Barfknecht, T. Fogarty, T. Busch, A. Foerster, P. Schmelcher, and N. T. Zinner, "Few-body Bose gases in low dimensions—a laboratory for quantum dynamics," *Phys. Rep.*, vol. 1042, pp. 1–108, 2023.

[98] G. C. Katsimiga, S. I. Mistakidis, B. A. Malomed, D. J. Frantzeskakis, R. Carretero-Gonzalez, and P. G. Kevrekidis, "Interactions and dynamics of one-dimensional droplets, bubbles and kinks," *Condens. Matter*, vol. 8, no. 3, p. 67, 2023.

[99] T. Mithun, S. I. Mistakidis, P. Schmelcher, and P. G. Kevrekidis, "Statistical mechanics of one-dimensional quantum droplets," *Phys. Rev. A*, vol. 104, no. 3, p. 033316, 2021.

[100] M. Edmonds, "Dark quantum droplets and solitary waves in beyond-mean-field Bose-Einstein condensate mixtures," *Phys. Rev. Res.*, vol. 5, p. 023175, 2023.

[101] G. C. Katsimiga, S. I. Mistakidis, G. N. Koutsokostas, D. J. Frantzeskakis, R. Carretero-González, and P. G. Kevrekidis, "Solitary waves in a quantum droplet-bearing system," *Phys. Rev. A*, vol. 107, no. 6, p. 063308, 2023.

[102] Y. Li, Z. Chen, Z. Luo, C. Huang, H. Tan, W. Pang, and B. A. Malomed, "Two-dimensional vortex quantum droplets," *Phys. Rev. A*, vol. 98, no. 6, p. 063602, 2018.

[103] Y. V. Kartashov, V. M. Lashkin, M. Modugno, and L. Torner, "Spinor-induced instability of kinks, holes and quantum droplets," *New J. Phys.*, vol. 24, no. 7, p. 073012, 2022.

[104] Y. Hu, Y. Fei, X.-L. Chen, and Y. Zhang, "Collisional dynamics of symmetric two-dimensional quantum droplets," *Frontiers of Physics*, vol. 17, no. 6, p. 61505, 2022.

[105] S. I. Mistakidis, T. Mithun, P. G. Kevrekidis, H. R. Sadeghpour, and P. Schmelcher, "Formation and quench of homonuclear and heteronuclear quantum droplets in one dimension," *Phys. Rev. Res.*, vol. 3, no. 4, p. 043128, 2021.

[106] J. Vallès-Muns, I. Morera, G. E. Astrakharchik, and B. Juliá-Díaz, "Quantum droplets with particle imbalance in one-dimensional optical lattices," *arXiv preprint arXiv:2306.12283*, 2023.

[107] X. Cui, "Spin-orbit-coupling-induced quantum droplet in ultracold Bose-Fermi mixtures," *Phys. Rev. A*, vol. 98, no. 2, p. 023630, 2018.

[108] J. Hou, X.-W. Luo, K. Sun, T. Bersano, V. Gokhroo, S. Mossman, P. Engels, and C. Zhang, "Momentum-space Josephson effects," *Phys. Rev. Lett.*, vol. 120, no. 12, p. 120401, 2018.

[109] C. Qu, C. Hamner, M. Gong, C. Zhang, and P. Engels, "Observation of Zitterbewegung in a spin-orbit-coupled Bose-Einstein condensate," *Phys. Rev. A*, vol. 88, no. 2, p. 021604, 2013.

[110] R. Ravisankar, H. Fabrelli, A. Gammal, P. Muruganandam, and P. K. Mishra, "Effect of Rashba spin-orbit and Rabi couplings on the excitation spectrum of binary Bose-Einstein condensates," *Phys. Rev. A*, vol. 104, no. 5, p. 053315, 2021.

[111] R. Sachdeva, M. N. Tengstrand, and S. M. Reimann, "Self-bound supersolid stripe phase in binary Bose-Einstein condensates," *Phys. Rev. A*, vol. 102, p. 043304, 2020.

[112] J.-Y. Zhang, S.-C. Ji, Z. Chen, L. Zhang, Z.-D. Du, B. Yan, G.-S. Pan, B. Zhao, Y.-J. Deng, H. Zhai, *et al.*, "Collective dipole oscillations of a spin-orbit coupled bose-einstein condensate," *Phys. Rev. Lett.*, vol. 109, no. 11, p. 115301, 2012.

[113] Y. Li, L. P. Pitaevskii, and S. Stringari, "Quantum tricriticality and phase transitions in spin-orbit coupled Bose-Einstein condensates," *Phys. Rev. Lett.*, vol. 108, no. 22, p. 225301, 2012.

[114] M. Khamehchi, Y. Zhang, C. Hamner, T. Busch, and P. Engels, "Measurement of collective excitations in a spin-orbit-coupled Bose-Einstein condensate," *Phys. Rev. A*, vol. 90, no. 6, p. 063624, 2014.

[115] Y. Chen, H. Lyu, Y. Xu, and Y. Zhang, "Elementary excitations in a spin–orbit-coupled spin-1 Bose-Einstein condensate," *New J. Phys.*, vol. 24, no. 7, p. 073041, 2022.

[116] M. Edmonds, T. Bland, and N. Parker, "Quantum droplets of quasi-one-dimensional dipolar Bose-Einstein condensates," *J. Phys. Commun.*, vol. 4, no. 12, p. 125008, 2020.

[117] T. Ozawa, L. P. Pitaevskii, and S. Stringari, "Supercurrent and dynamical instability of spin-orbit-coupled ultracold Bose gases," *Phys. Rev. A*, vol. 87, no. 6, p. 063610, 2013.

[118] P. G. Kevrekidis, D. J. Frantzeskakis, and R. Carretero-González, *Emergent nonlinear phenomena in Bose-Einstein condensates: theory and experiment*, vol. 45. Springer, 2008.

[119] F. Böttcher, J.-N. Schmidt, J. Hertkorn, K. S. Ng, S. D. Graham, M. Guo, T. Langen, and T. Pfau, "New states of matter with fine-tuned interactions: quantum droplets and dipolar supersolids," *Rep. Prog. Phys.*, vol. 84, no. 1, p. 012403, 2020.

[120] A. Romero-Ros, G. C. Katsimiga, S. I. Mistakidis, S. Mossman, G. Biondini, P. Schmelcher, P. Engels, and P. G. Kevrekidis, "Experimental realization of the peregrine soliton in repulsive two-component Bose-Einstein condensates," *Phys. Rev. Lett.*, vol. 132, p. 033402, 2024.

[121] Z. Guo, F. Jia, L. Li, Y. Ma, J. M. Hutson, X. Cui, and D. Wang, "Lee-huang-yang effects in the ultracold mixture of na 23 and rb 87 with attractive interspecies interactions," *Phys. Rev. Res.*, vol. 3, no. 3, p. 033247, 2021.

[122] A. Trautmann, P. Ilzhöfer, G. Durastante, C. Politi, M. Sohmen, M. Mark, and F. Ferlaino, "Dipolar quantum mixtures of erbium and dysprosium atoms," *Phys. Rev. Lett.*, vol. 121, no. 21, p. 213601, 2018.

[123] I. L.-T. Properties, "Eigenvalues and eigenfunctions of a Bose system of hard spheres," *Selected Papers (1945-1980) Of Chen Ning Yang (With Commentary)*, vol. 36, p. 212, 2005.

[124] G. Bougas, G. Katsimiga, P. Kevrekidis, and S. Mistakidis, "Stability and dynamics of nonlinear excitations in a two-dimensional droplet-bearing environment," *Phys. Rev. A*, vol. 110, no. 3, p. 033317, 2024.

[125] Y. Fei, X. Du, X.-L. Chen, and Y. Zhang, "Collective excitations in two-dimensional harmonically trapped quantum droplets," *Phys. Rev. A*, vol. 109, no. 5, p. 053309, 2024.

[126] S. Chandramouli, S. I. Mistakidis, G. C. Katsimiga, and P. G. Kevrekidis, "Dispersive shock waves in a one-dimensional droplet-bearing environment," *Phys. Rev. A*, vol. 110, no. 2, p. 023304, 2024.

[127] P. Zin, M. Pylak, T. Wasak, M. Gajda, and Z. Idziaszek, "Quantum Bose-Bose droplets at a dimensional crossover," *Phys. Rev. A*, vol. 98, no. 5, p. 051603, 2018.

[128] T. Ilg, J. Kumlin, L. Santos, D. S. Petrov, and H. P. Büchler, "Dimensional crossover for the beyond-mean-field correction in Bose gases," *Phys. Rev. A*, vol. 98, no. 5, p. 051604, 2018.

[129] J. C. Pelayo, G. Bougas, T. Fogarty, T. Busch, and S. I. Mistakidis, "Phases and dynamics of quantum droplets in the crossover to two-dimensions," *arXiv preprint arXiv:2407.16383*, 2024.

[130] J. C. Pelayo, T. Fogarty, T. Busch, and S. I. Mistakidis, "Phases and dynamics of few fermionic impurities immersed in two-dimensional boson droplets," *Phys. Rev. Res.*, vol. 6, p. 033219, 2024.

[131] D. Rakshit, T. Karpiuk, P. Zin, M. Brewczyk, M. Lewenstein, and M. Gajda, "Self-bound Bose–Fermi liquids in lower dimensions," *New J. Phys.*, vol. 21, no. 7, p. 073027, 2019.

[132] I. A. Englezos, P. Schmelcher, and S. I. Mistakidis, "Particle-imbalanced weakly interacting quantum droplets in one dimension," *Phys. Rev. A*, vol. 110, p. 023324, 2024.

[133] T. A. Flynn, L. Parisi, T. P. Billam, and N. G. Parker, "Quantum droplets in imbalanced atomic mixtures," *Phys. Rev. Res.*, vol. 5, p. 033167, 2023.

[134] Y. V. Kartashov and D. A. Zezyulin, "Multipole quantum droplets in quasi-one-dimensional asymmetric mixtures," *Phys. Rev. A*, vol. 110, p. L021304, 2024.

[135] J. Vallès-Muns, I. Morera, G. E. Astrakharchik, and B. Juliá-Díaz, "Quantum droplets with particle imbalance in one-dimensional optical lattices," *SciPost Phys.*, vol. 16, no. 3, p. 074, 2024.

[136] M. N. Tengstrand and S. M. Reimann, "Droplet-superfluid compounds in binary bosonic mixtures," *Phys. Rev. A*, vol. 105, no. 3, p. 033319, 2022.

[137] M. Abad and A. Recati, "A study of coherently coupled two-component Bose-Einstein condensates," *Eur. Phys. J. D*, vol. 67, pp. 1–11, 2013.

[138] N. Navon, R. P. Smith, and Z. Hadzibabic, "Quantum gases in optical boxes," *Nature Physics*, vol. 17, no. 12, pp. 1334–1341, 2021.

[139] S. K. Sarkar, R. Ravisankar, T. Mishra, P. Muruganandam, and P. K. Mishra, "Signature of reentrant localization in collisional inhomogeneous spin-orbit coupled condensates," *arXiv preprint arXiv:2403.02027*, 2024.

[140] H. Deng, T. Wan, Y. He, T. Han, J. Huang, S. Ding, Y. Li, D. Lei, C. Jiang, M. Yao, *et al.*, "The population transfer and superflow associated with the spatiotemporal bloch states for a high-frequency driven spin–orbit coupled Bose–Einstein condensate," *Results Phys.*, vol. 31, p. 104926, 2021.

[141] S. I. Mistakidis, G. M. Koutentakis, F. Grusdt, P. Schmelcher, and H. R. Sadeghpour, "Inducing spin-order with an impurity: phase diagram of the magnetic Bose polaron," *New J. Phys.*, vol. 24, no. 8, p. 083030, 2022.

[142] X. Du, Y. Fei, X.-L. Chen, and Y. Zhang, "Ground-state properties and bogoliubov modes of a harmonically trapped one-dimensional quantum droplet," *Phys. Rev. A*, vol. 108, no. 3, p. 033312, 2023.

[143] T. Fukuhara, A. Kantian, M. Endres, M. Cheneau, P. Schauß, S. Hild, D. Bellem, U. Schollwöck, T. Giamarchi, C. Gross, *et al.*, "Quantum dynamics of a mobile spin impurity," *Nature Physics*, vol. 9, no. 4, pp. 235–241, 2013.

[144] S. K. Gangwar, R. Ravisankar, H. Fabrelli, P. Muruganandam, and P. K. Mishra, "Emergence of unstable avoided crossing in the collective excitations of spin-1 spin-orbit-coupled bose-einstein condensates," *Phys. Rev. A*, vol. 109, p. 043306, 2024.

[145] N. Pradhan, P. Kumar, R. Kanamoto, T. N. Dey, M. Bhattacharya, and P. K. Mishra, "Ring bose-einstein condensate in a cavity: Chirality detection and rotation sensing," *Phys. Rev. A*, vol. 109, p. 023524, 2024.

[146] N. Pradhan, P. Kumar, R. Kanamoto, T. N. Dey, M. Bhattacharya, and P. K. Mishra, "Cavity optomechanical detection of persistent currents and solitons in a bosonic ring condensate," *Phys. Rev. Res.*, vol. 6, p. 013104, 2024.